UNIVERSITÀ DEGLI STUDI DI PAVIA
DOTTORATO DI RICERCA IN FISICA – XXXI CICLO

DNA damage by charged and neutral radiation at different spatial and temporal scales: integrating Monte Carlo simulations with *in vitro* experiments.

Sofia Barbieri

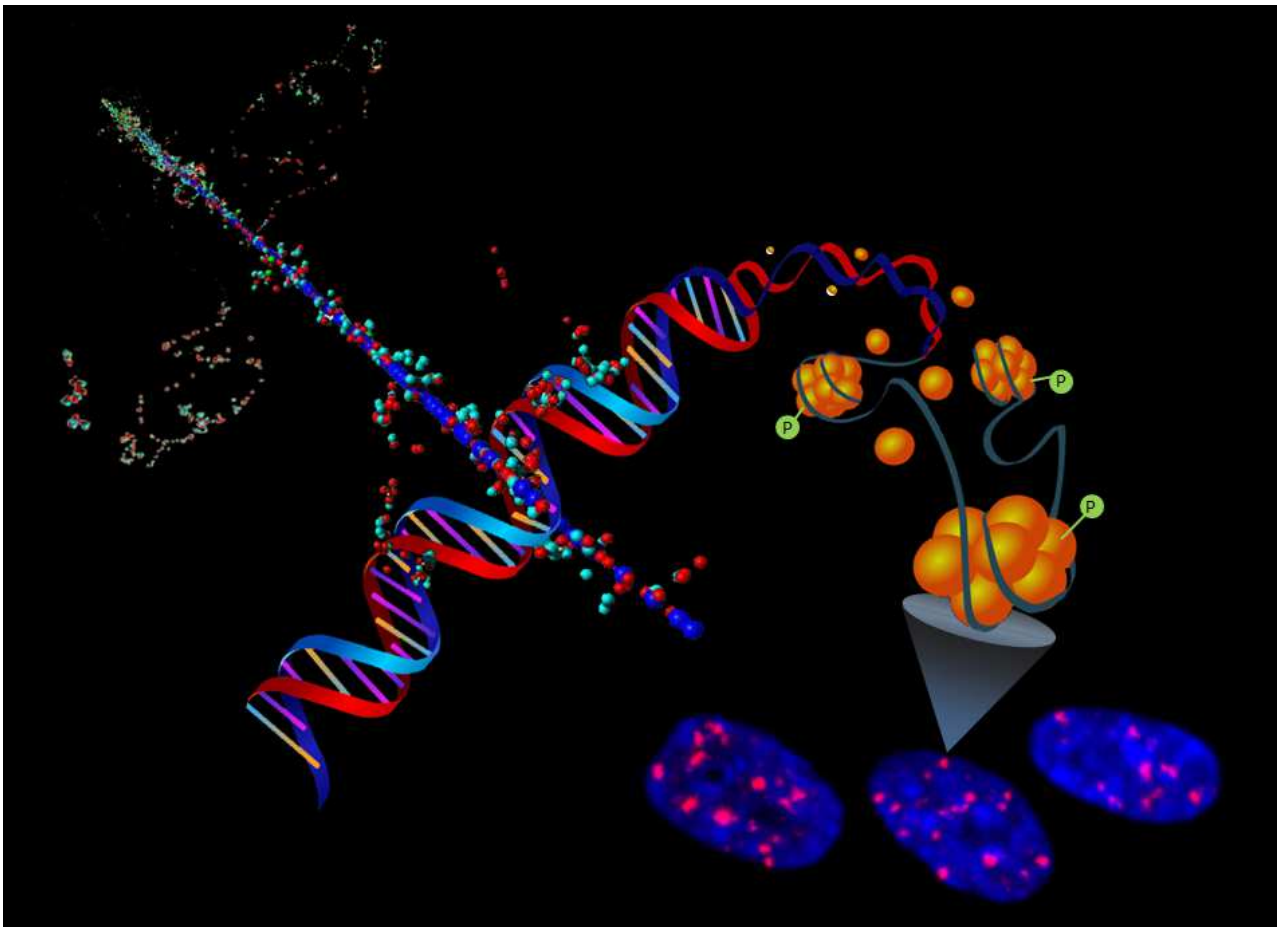

Tesi per il conseguimento del titolo

Università degli Studi di Pavia
Dipartimento di Fisica

DOTTORATO DI RICERCA IN FISICA – XXXI CICLO

DNA damage by charged and neutral radiation at different spatial and temporal scales: integrating Monte Carlo simulations with *in vitro* experiments

Sofia Barbieri

Submitted to the Graduate School of Physics in partial fulfilment of the requirements for the degree of

DOTTORE DI RICERCA IN FISICA

DOCTOR OF PHILOSOPHY IN PHYSICS

at the

University of Pavia

Supervisor: Prof. Andrea Davide Ottolenghi
Referees: Dr. Mark Hill (University of Oxford, UK)
Dr. Carmen Villagrasa (IRSN, France)

Cover

Left: track structure simulation of a 10MeV α particle impinging on a schematics of the DNA macromolecule.
(Credits for the ion track: Dr. Werner Friedland)

Right: condensation of the DNA into nucleosomes, and radiation-induced phosphorylation of the H2AX histone. γ-H2AX foci in irradiated IMR90 cells are shown in the picture taken with a fluorescent microscope in the bottom-right corner.

DNA damage by charged and neutral radiation at different spatial and temporal scales: integrating Monte Carlo simulations with in vitro experiments

Sofia Barbieri

PhD thesis - University of Pavia
Pavia, Italy, January 2019

Contents

Abbreviations and acronyms

2D 2 Dimensions

3D 3 Dimensions

ANDANTE Multidisciplinary evaluation of the cancer risk from neutrons relative to photons using stem cells and the analysis of second malignant neoplasms following paediatric radiation therapy

ARS Acute Radiation Syndrome

ASI Italian Space Agency

BFO Blood Forming Organs

bp Base Pairs

BSA Bovine Serum Albumin

CNAO National Centre of Oncological Hadrontherapy

CNS Central Nervous System

CRR Center for Radiological Research

DAPI 4',6-Diamidino-2-Phenylindole

DDR DNA Damage Response

DMEM Dulbecco's Modified Eagle Medium

DOF Depth Of Field

DNA Deoxyribonucleic Acid

DSB Double Strand Break

DT Doubling Time

ECSS European Commission for Space Standardization

EDTA Ethylenediaminetetraacetic Acid

EMEM Eagle's Minimal Essential Medium

ESA European Space Agency

ESP Emission of Solar Protons

EVA Extra Vehicular Activity

EtOH Ethanol

FBS Foetal Bovine Serum

FLUKA FLUktuierende KAskade

Geant GEometry ANd Tracking

GCR Galactic Cosmic Ray

GDML Geometry Description Markup Language

GOES Geostationary Operational Environmental Satellite)

GRAS Geant4 Radiation Analysis for Space

HR Homologous Recombination

HZE High Z and Energy particles

ICC Immunocytochemistry

ICRP International Committee for Radiation Protection

IMP Interplanetary Monitoring System

INITIUM Track structures and initial events: an integrated approach to assess the issue of radiation quality dependence

IR Ionizing Radiation

IRIF Ionizing Radiation Induced Foci

IVA Intra Vehicular Activity

ISS International Space Station

LEO Low Earth Orbit

LET Linear Energy Transfer

LQ Linear Quadratic

MC Monte Carlo

MSL Mars Science Laboratory

NASA National Aeronautic and Space Administration

NHEJ Non-Homologous End-Joining

NIBIB National Institute for Biomedical Imaging and Bioengineering

OMERE Outil de Modélisation de l' Environnement Radiatif Externe

ONERA Office National d'Etudes et de Recherches Aérospatiales, Toulouse-France)

PBS Phosphate-Buffered Saline

PE Plating Efficiency

PERSEO PErsonal Radiation Shielding for intErplanary missiOns

PFA Parafolmaldehyde

PFGE Pulsed Field Gel Electrophoresis

PLD Potentially Lethal Damage

RAD Radiation Assessment Detector

RARAF RAdiological Research Accelerator Facility

RBE Relative Biological Effectiveness

RBM Red Bone Marrow

REID Risk of Exposure-Induced Death

ROI Region Of Interest

RT Room Temperature

ROS Reactive Oxygen Species

SEM Standard Error of Mean

SF Surviving Fraction

SF_2 Surviving Fraction after 2 Gy irradiation

SOBP Spread Out Bragg Peak

SPE Solar Particle Event

SPENVIS SPace ENVironment Information System

SRIM Stopping and Range of Ions in Matter

SSB Single Strand Break

TREND TRacking damage at ions' track ENDs

TRIM TRansport of Ions in Matter

US-NRC US - Nuclear Regulatory Commission

Chapter 1

Introduction and objectives

Radiation action in cells has been studied to understand the mechanisms behind the onset of biological damage in targets of relevance, such as the DNA macromolecule. The characterization of DNA damage following radiation exposure represents a fundamental knowledge for *e.g.* the use of radiation for therapy and for diagnostics, for radiation protection of the general population (and workers) against the hazards deriving from environmental and occupational exposure or from the use of nuclear power and weaponry, as well as for radiation protection for manned space exploration. Such a large variety of applications is reflected in the many exposure scenarios to be considered, including exposures to mixed radiation fields. As a matter of fact, radiation (especially particles) can undergo many different interactions in the biological target, as a result of which a mixed field is generated and particles of different types are ultimately responsible for energy deposition. This is always the case for neutrons, that are themselves an unavoidable by-product *e.g.* of particle-beams used for therapy, of nuclear devices, or of space-radiation interactions with spacecraft walls.

In vitro experiments are a powerful tool to investigate radiation-induced DNA damage and the consequent cellular responses. However, technical and practical limitations reasonably exist, that prevent obtaining experimental information at the spatial scale interested by radiation energy deposition (the nanometre scale of the DNA double helix) and at the temporal scale at which initial events occur (with energy depositions within $\approx 10^{-15}$ s from the passage of radiation). In case of exposure to a mixed field, it is also impossible to experimentally distinguish which component of the field is actually responsible for the damage. On the other side, the complexity of the response of cell systems (also in interaction with each other in an *in vitro* culture) can be reproduced and investigated with such experiments.

Mechanistic approaches and Monte Carlo (MC) simulations of radiation interactions come to great help for the interpretation of radiobiological data and prediction of radiation effectiveness: information on initial events at the nanoscopic scale in the DNA (and also other potential initial targets) can be

obtained, as well as on the separate contribution to the damage of different radiation qualities in a mixed field. Integrating Monte Carlo simulation with *in vitro* experiments will therefore deliver insight on biological mechanisms at the basis of radiation response of cellular systems, offering the opportunity to see "behind" experimental findings, overcoming technical limitations and finally allowing for a thorough comparison of the effectiveness of radiation qualities in inducing biological damage. The flexibility of simulation approaches in being adapted to different spatial scales also offers the unique opportunity to make the bridge between effects at the cellular and sub-cellular level and the macroscopic description of the radiation field *e.g.* at the tissue/organ level or even of the radiation environment found in space.

The purpose of this Ph.D. thesis is to contribute to the investigation on the mechanisms underlying the induction of DNA damage by different radiation qualities, using both experimental measurements with different *in vitro* systems and modelling approaches to quantify and characterize the damage. In each Chapter, specific exposure scenarios are addressed, offering examples of the possible applications that could benefit from results and approaches developed in this study, such as, among others, clinical treatments, biodosimetry and space radiation protection.

In **Chapter 2**, MC simulations for radiation transport and tracks have been carried out to investigate how different radiation qualities impact the final biological outcome, in terms of spatial distribution of the energy depositions and of the characteristics of the final DNA lesions, intimately related to the biological effectiveness.
The characterization of the DNA damage complexity as a function of the Linear Energy Transfer (LET) is firstly addressed: this work was carried out in the framework of the DoReMi INITIUM ("Track structures and initial events: an integrated approach to assess the issue of radiation quality dependence") and TREND ("TRacking damage at ions' track ENDs") projects, and my contribution was the simulation of clustered DNA damage due to light (such as protons) and heavy charged particles (up to neon ions), by means of the biophysical track-structure code PARTRAC. A wide range of particle energies has been tested, up to the low energies found in the distal end of the Bragg peak used in therapy.
The formalism behind the concept of LET was then investigated in more detail, starting with its usual definition and going to the lineal energy as its microdosimetric equivalent. It is recognised that a microdosimetric approach offers a better description of the stochastic pattern of energy depositions at the microscopic scale with respect to averaged macroscopic LET values. My contribution was on the derivation of these two quantities from proton tracks at different energies simulated with PARTRAC.
This work contributed to the development of a model for the neutron relative

biological effectiveness (RBE), calculated in terms of clustered DNA lesions with respect to low-LET X-rays, with the aim to trace back the variation of RBE as a function of neutron energy to initial physical events. The characterization of neutron RBE is still subject of debate and the available recommendations for the neutron weighting factors w_R are constantly under revision to keep track with the experimental findings and measurements. This work has been carried out in the framework of the ANDANTE ("Multidisciplinary evaluation of the cancer risk from neutrons relative to photons using stem cells and the analysis of second malignant neoplasms following paediatric radiation therapy") project. ANDANTE included experimental and theoretical work to estimate the risk of secondary tumours following proton-therapy in paediatric patients, where secondary neutrons might play a role. My contribution in this project concerned the simulation of neutron transport with PHITS and of particle tracks with PARTRAC, to be coupled to predict neutron RBE as a function of neutron energy.

In **Chapter 3**, the simulation of DNA damage was extended to the reproduction of DNA repair foci, originating from the recruitment of DNA repair proteins at the damage site. This Chapter represents the main core of the experimental and modelling activities I performed during my Ph.D. work. The phosporylated form of histone H2AX (γ-H2AX focus) was considered, since this has been demonstrated to be one of the early events following the induction of DNA double strand breaks (DSBs) and to play a key role in the recruitment of repair factors by the DNA damage repair (DDR) system. γ-H2AX foci measured at the earliest time-points can therefore be directly correlated with initial DNA damage. The aim of the modelling was to reproduce the observer's point of view, starting from the simulation of damage at the nanometre level, but finally delivering the read-out of the endpoint, which is necessarily affected by the physical extension of the region in the genome interested by the phosporylation and by the chosen experimental technique to visualize and score foci. To this aim, taking advantage of the modelling approaches largely discussed in Chapter 2, a clustering algorithm was developed that starts from initial damage and takes account of both these factors. This approach has been applied to different exposure conditions, with X-rays, neutrons and carbon ions.
Dedicated data have been obtained from experimental measurements with *in vitro* systems (normal human lung fibroblasts and mouse breast cancer cells) for the benchmark of the newly developed modelling approach. Measurements for neutrons and X-rays were carried out at the Radiological Research Accelerator Facility (RARAF) - Center for Radiological Research (CRR), Columbia University Medical Center, New York, USA, where I spent six months of the Ph.D. program. An analogue of the neutron field generated by the Hiroshima bomb at 1.5 km from the hypocentre of the explosion is available at RARAF for radiobiological experiments and physical measurements. Exposure to carbon ions was carried out at the National Centre of Oncological Hadrontherapy

- CNAO in Pavia, using a treatment plan for ^{12}C ions in a water phantom, to mimic the irradiation of tumour cells in a patient using a Spread Out Bragg Peak (SOBP). The induction of foci has been measured through immunocytochemistry (ICC) and results from both conventional fluorescence microscopy and confocal microscopy (performed, respectively, at RARAF/the "RadBioPhys Lab" of the Physics Department, Pavia, and at the "Centro Grandi Strumenti", Pavia) have been compared, to highlight the differences in the quantification of foci (and of underlying initial DNA damage) due to technical limitations related to the read-out system.

Finally, in **Chapter 4**, selected applications to the space radiation environment are presented. Biological effects of space radiation are of great interest also in view of future manned exploration missions in deep space. Space radiation exposures can lead to both long-term detrimental health consequences, but also short-term effects in case of acute exposures as the ones due to solar phenomena.
In the first part of the Chapter results from a preliminary study are presented, focused on the modelling of DNA clustered damages due to the neutron field expected at the surface of Mars, taking advantage of the simulation of neutron transport and damage induction elaborated in the previous Chapters. The analysis aimed at unravelling the resulting biological effectiveness of Martian neutrons.
Finally, selected results of the PERSEO ("PErsonal Radiation Shielding for intErplanetary missiOns") project are presented. PERSEO is funded by the Italian Space Agency (ASI), and led to the construction and test of a demonstrator for a personal radiation protection device, in form of a water-filled garment, to be worn by the astronaut in a space habitat to mitigate the harmful effects of cosmic radiation, in particular during solar particle events (SPEs). Being the focus here the development of countermeasures for acute effects, dose calculations are performed at the tissue/organ level, without going to the level of detail of DNA damage. This set of results provides therefore an example of application of modelling radiation transport at the macroscopic scale only. In the framework of this project, I contributed to the Monte Carlo simulations carried out to evaluate the dose reduction achieved thanks to the PERSEO garment in organs that can display the onset of non-cancer short-term effects.

The measurements and modelling results presented in each Chapter concern the experimental and theoretical activities I personally carried out for this Ph.D. work. At the end of each "Objective" Section in the introductory Paragraphs, there is reference to the main papers in which the work has been finalized, that include additional data and results for the interest of the reader.

Finally, **Chapter 5** summarizes the conclusions of this Ph.D. thesis.

Chapter 2

Initial events at the nanoscopic level

2.1 Simulation of radiation-induced initial DNA damage

2.1.1 DNA as a radiation target

The radiation-induced effects to the cellular DNA have represented a hot topic of research since the introduction of radiation in many facilities for research, therapy [1] and industrial purposes.
Energy depositions to the DNA may compromise the functionality and the integrity of the entire cell, influencing its final fate. It has been shown that the degree of damage can be completely different, in frequency and complexity, under different irradiation conditions [2, 3]. This also affects how modifiers (such as oxygenation and radio-sensitizers or protectors) act [4]. The differences in effectiveness for the induction of biological damage are traced back to the so-called radiation quality, a concept strictly related to track-structure, that is the event-by-event pattern of energy depositions in the target (for the purpose of this thesis, the DNA) at the nanometre level [5, 6]. The distribution of these highly organized events within the radiation track is often condensed in averages quantities as the dose or the Linear Energy Transfer (LET, defined in the following), but it is fundamental in determining the spectra and the microscopic features of the resulting damage in cells [5]. The characteristics of molecular damage at the DNA level have been classified by means of computational approaches [7]: Charlton *et al.* (1989) adjusted the probabilities of single-strand breaks (SSBs) induction starting from the energy deposited in critical DNA volumes, obtaining good agreement with radiobiological measurements for cells irradiated with electrons, protons and alpha particles. Double strand beaks (DSBs), obtained when single strand breaks on opposite strands are separated by few (a ten) base pairs, were also considered in the analysis

[8].
Clusters of damages were soon recognized as a critical kind of damage, influencing the severity of the radiation-induced damage: several authors explored the effects of different clustering degrees of energy depositions and associated lesions on the modelling of experimental data, starting from few ionizations in 3-10 nm of the DNA [9, 10, 11]. Goodhead *et al.* (1980) associated a number of 3-9 lesions in 3 nm to simple damages (as the ones from sparsely ionizing radiation - IR), while 10 or more ionizations in 3 nm would generally give rise to more complex and detrimental lesions [12]. 3D descriptional models were also developed by Mozuder and Magee in 1966, by proposing the structures known as "spurs", "blobs" and "short tracks" [13], and by Butts and Katz in 1967, with the amorphous track description [14]. These studies confirmed that highly clustered energy depositions, typically induced by ionizing radiation, are more detrimental to the biological matter than lesions from other endogenous factors. The difference in the energy depositions (and therefore DNA breaks) propagates furthermore at the micrometer (nuclear/cellular) scale, affecting more compacted structures of the DNA like the chromosomes [15, 16, 17].
However, despite sophisticated experimental techniques have been developed in order to detect initial damages in many cellular compartments, including DNA [18, 19], sensitivity limitations always affect an accurate quantification of the damage, and underestimation of closely spaced DNA lesions is very likely to happen [20]. This is particularly true for the study of mechanisms and damages following low-dose exposures. When going to risk evaluation, most often risks due to low doses of radiation are extrapolated from the available data at higher doses, meaning that the risk estimation for radiation protection purposes is affected by significant uncertainties.
An additional practical limitation, often hindering the quantification of the initial response, is related to the fact that some assays are carried out minutes after the exposure of the biological samples (like the γ-H2AX assay, discussed later). When studying initial DNA damage and its repair, this means that the first measurement will take place when DNA repair might have already been initiated, even if cooling samples prior the irradiations can be adopted to prevent/slow-down the initiation of repair pathways.
As anticipated, modelling approaches and, in particular, Monte Carlo (MC) simulations can support radiobiological measurements, for both the study of low-dose effects and for the evaluation of the initial damage. MC codes have been widely adopted to simulate radiation-induced damages in biological targets starting from the physical interactions of the radiation track [21, 22, 23].

2.1.2 Monte Carlo calculation of radiation-induced damage

Depending on the length scale over which radiation energy depositions are averaged, MC codes can be distinguished in radiation transport codes and

track-structure codes: for charged particles, transport codes consider average values of multiple energy depositions (due to inelastic collisions with atomic electrons in the target) in track segments (*condensed-history* approach), while track-structure codes deal with all single events produced by radiation, taking account of the kind of interaction (ionization/excitation), the energy deposited and the event spatial distribution (*event-by-event*). In modern track-structure codes this can be done for charged particles down to energies of few electronvolts. For both cases, secondary particles that are generated by primary particle interactions (*e.g.* products of nuclear reactions in transport codes, or accelerated electrons in track-structure codes) are in turn followed in their history with the same approach used for primary ones.
When coupled to a software reproduction of the biological target, MC simulations provide the possibility to investigate biological damages starting from physical events, allowing to estimate parameters of relevance for both mechanistic studies, practical applications as radiation therapy [24], and the undertanding of processes at more systemic level [25]. To this aim, further steps are necessary to relate track-structure calculations to biological damage: i) the implementation in the simulation of the generation and diffusion of free radicals by radiation energy depositions in the cellular micro-environment (mostly consisting of water) [26]; ii) the implementation of the target geometry (the DNA, in our case); iii) based on energy depositions in the target (either by diffusing radicals or directly by radiation), a series of rules/assumptions to evaluate resulting damages to bases, to the sugar-phosphate backbone (*e.g.* SSBs and DSBs); iv) finally, a scoring scheme to quantify the overall damage complexity.
Nikjoo *et al.* reported in 2001 on the complexity and frequency spectra of the simple and complex DNA lesions, proposing a modelling approach of strand breaks based on Monte Carlo track simulations in liquid water and coupling the resulting pattern of interactions to a canonical model of the B-DNA. They characterized the spectrum of strand breaks per unit dose for energetic electrons and ions, also providing useful information on the percentage of damage to the bases and their combination with other kinds breaks: they found out that the majority of damage is represented by single breaks, and that for the radiation types under investigation their total yield of damage (Gy^{-1}) remains almost constant; yields of base damages vary according to the radiation quality, and they often accompany single breaks; more interestingly, they highlighted that, at low energies, electrons cause double-strand breaks and more complex types of lesions in $\approx 30\%$ of cases, with the percentage increasing for alpha particles [27].
Different track-structure codes have been developed following a similar approach, some for different specific purposes and optimized for single radiation types, and others as PARTRAC (PARticle TRACks) [28] and more recently Geant4-DNA (in the Geant4 - GEometry ANd Tracking - environment) [29, 30, 31, 32] able to deal with several radiation qualities.

For the purpose of this work, the biophysical track-structure code PARTRAC has been extensively used. PARTRAC has been mainly developed at the Helmholtz Zentrum München, in collaboration with the University of Pavia [6]. In its current version, it gives the possibility to simulate different kinds of radiation-induced lesions in a realistic atom-by-atom representation of the human genome for fibroblast- or lymphocyte-like cells [33] in their G_0/G_1 state. The software replica of the genome comprises all organization levels, from the simplest deoxynucleotide pair, to the whole structures of the double helix and its condensation from nucleosomes to chromatin loops and territories. The DNA is implemented in a single compactness state, that is in heterochromatin.
PARTRAC has been also recently upgraded in order to properly deal with interaction cross sections for full slowing down ions [34]. A more detailed description of the code is provided in Par.2.1.5
Geometrical aspects of the DNA organization will play an important role for a large part of the results presented in this thesis. DNA geometry regulates the yield of damages (*e.g.* strand breaks) and also influences the availability of scavengers in proximity to the damaged site [35]. In particular, DNA damage repairability has been shown to be strongly influenced by both the geometrical and the "genomic" distance between strand breaks [24], which is ultimately correlated to the amount of energy deposited in the target per unit length, therefore to radiation quality. Also, damage distribution in space is at the basis of our ability to detect and quantify DNA damage with radiobiological assays. All these issues will be specifically faced in this work.

2.1.3 Introduction of basic quantities

The linear energy transfer (LET) was introduced to quantify the average energy $d\epsilon$ imparted to the medium in electronic collisions by a charged particle traversing a distance of dl [36]:

$$\frac{d\epsilon}{dl}\left[\frac{keV}{\mu m}\right] \tag{2.1}$$

For photons and other neutral particles, a LET can be equally defined as the one of the accelerated secondary charged particle species. By definition, LET is an averaged quantity, and the underlying local energy deposition at the microscopic scale can be subject to great variability, as later discussed. The LET depends both on properties of the impinging radiation and of the traversed medium: in particular, it is proportional to the squared charge of the incident particle and inversely dependent on its squared velocity (according to the Bethe-Bloch formula):

$$LET \propto \frac{Z^2}{\beta^2}, \tag{2.2}$$

where β is the ratio of particle velocity to the speed of light.
Particles change their energy while traversing the target material, and more

particle types can be accelerated (or can be present from the beginning in a mixed field): this results in a LET distribution in the target. To characterize the field by a single parameter, different average values can be used, as later detailed, which may however provide little information on a complex field.
Overall, this quantity reflects the spatial density of energy deposition events by radiation, and it is intimately related to the effectiveness in producing biological damage. Generally speaking, a higher LET, as it is found for charged particles with respect to photons, is associated to an increase in biological damage. The use of the LET is therefore common in fields such as radiation therapy and radiobiology to characterize the radiation quality.
To compare the effectiveness of different radiation qualities, the relative biological effectiveness RBE is defined as the ratio of the dose from a low-LET reference radiation (250 kVp X-rays or high energy γ-rays as suggested in [37]) required for a given biological effect, to the dose that would produce the same effect with the radiation under investigation s [38]:

$$RBE = \frac{D_X}{D_s} \tag{2.3}$$

Though the formula is simple, the RBE is not easily evaluated and its use requires attention: RBE itself depends on a large variety of parameters, such as dose, dose-rate, biological target (*e.g.* cell lines), biological endpoint, kind of particle, LET and reference radiation.
As it will be discussed also in Par.2.2, the optimization of treatment plans in heavy ion therapy is based on the concept of biological dose, defined as physical dose $\times$ RBE, so that different biological effectiveness at equal physical dose are taken into account.

2.1.4 Objective

A mechanistic study relying on track-structure Monte Carlo calculations has been undertaken to characterize different radiation qualities in terms of DNA damage induction (from simple SSBs to clustered lesions), as a function of their LET.
This study was carried out in the framework of the DoReMi - INITIUM ("Track structures and initial events: an integrated approach to assess the issue of radiation quality dependence") and TREND ("TRacking damage at ions' track ENDs") projects [1]. In this section we present systematic results for charged particles from protons to ^{20}Ne ions, simulated over a wide energy spectrum, from the very high energies (low-LET) used in hadrontherapy down to the stopping energies (very high-LET) corresponding to the Bragg peak region. The MC biophysical code PARTRAC has been used. RBE estimates can be derived based on these results.

[1] Project n. 249689

Publications for the topic

- "Comprehensive track-structure based evaluation of DNA damage by light ions from radiotherapy-relevant energies down to stopping", W. Friedland, E. Schmitt, P. Kundrát, M. Dingfelder, G. Baiocco, **S. Barbieri**, A. Ottolenghi. Scientific Reports, 2017.
- "The origin of neutron biological effectiveness as a function of energy", G. Baiocco, **S. Barbieri**, G. Babini, J. Morini, D. Alloni, W. Friedland, P. Kundrát, E. Schmitt, M. Puchalska, L. Sihver, A. Ottolenghi. Scientific Reports, 2017.

2.1.5 Material and methods

PARTRAC: DNA damage yields from different radiation qualities

PARTRAC simulations were carried out using a fibroblast cellular model, exposed to particles of energies of interest for medical applications, to quantify the induction of DNA damages as a function of LET.
In the code, a software replica of the DNA is implemented atom-by-atom, and recursive looping of stackable chromatin fibre elements of the DNA (each contained in a volume of 50 × 50 × 50 nm^3 and consisting in 5-6 kbps) is introduced to create the condensation levels from chromatin loops to chromosomes domains. Each atom is considered as a sphere with doubled van Der Waals radius, to remove empty space between atoms. The semi-axes of the ellipsoidal nucleus were of 10, 5.3 and 2.7 μm in x, y and z respectively. The cytoplasmic compartment was instead reproduced as a rectangular box of side 14, 14 and 10.2 μm along the three directions.
^{1}H, ^{2}He, ^{12}C, ^{14}N, ^{16}O and ^{20}Ne ions were generated with energies from 0.025 to 256 MeV/u. All secondary electrons are followed down to energies of 10 eV [26]. Nuclear interactions were neglected and only Coulomb interactions were considered in the calculations.
According to their energy, particles were simulated in two different ways, in order to have a homogeneous irradiation of the target volume:

- for energies implying a range longer than the transversal dimension of the nucleus along z, particles were generated from a grid of 5×3 voxels (each of 16 μm^2), positioned at 0.3 μm of distance below the nuclear surface along the z-axis. For each run, 15 particles (one per pixel) were generated, for a fluence of 0.0625 particles/μm^2. In this case, the following relation between LET and dose holds:

$$LET[kev/\mu m] = \frac{D[Gy]}{0.1602 \cdot fluence[\mu m^{-2}]}, \tag{2.4}$$

  where D represents the dose deposited in the target in the run and it is provided by PARTRAC as an output parameter. No electronic equilibrium is provided with the following setup, especially for highly energetic

particles emitted by the fixed grid along the z-axis. As a partial mitigation, a *mirroring* effect was implemented to act along the cytoplasm surfaces only in the x and y directions: all the particles leaving the cytoplasmic volume in these directions are reflected back inside the cytoplasm, as if a new particle of the same energy as the one escaping the nucleus would enter the cell;

- short-range particles could not be emitted by a fixed source, so they were randomly and isotropically generated in the nucleus (even if that might not mimic some experimental arrangements, where particles are shot perpendicularly): in this way they are free to stop wherever inside the nucleus. Particles generated close to the surface can escape the nucleus. A fixed number of 0.08 particles per μm^{-3} for particle starting points was chosen. The LET in this case was estimated by using:

$$LET[keV/\mu m] = \frac{E_{dep}[keV]}{range[\mu m]}, \tag{2.5}$$

i.e. dividing the energy deposited by the particle (E_{dep}) by its range in water, in continuous slowing down approximation, as from SRIM/TRIM ("Stopping and Range of Ions in Matter"/"TRansport of Ions in Matter" [39]) tables.

In both cases, fluences were adjusted in order to have damages due to a single particle, as also later discussed.
In PARTRAC, lesions to the DNA are obtained by superimposing the energy depositions calculated using liquid water onto the DNA model, and using determined probabilities for the induction of DNA damage.
The chemical stage has been thoroughly implemented in PARTRAC, using experimental data on the diffusion and reaction coefficients [28]. Reactive species that arise from the interactions with water molecules are transported in their diffusion path and all the reactions with other radicals and the DNA are taken into consideration. The lifetime of $^{\cdot}$OH radicals, the most abundant radio-induced reactive oxygen species (ROS), is however influenced by the presence of further scavengers [40], whose scavenging capacity was estimated to be around $4 \cdot 10^8$ s^{-1} [41]. Since the chemistry module of PARTRAC does not include reactions with these molecules, the removal of $^{\cdot}$OH radicals in the code was introduced by means of a characteristic time of 2.5 ns.
No clear-cut distinction has been drawn between direct and indirect effects: the first have been defined as damages strand breaks which are not removed by scavengers, including interactions within the inner hydration shell, while indirect effects are breaks that can be suppressed by the addition of radical scavengers. The energy parameters for the cross sections were optimized trying to reproduce the number of breaks after low-LET irradiation such as ^{60}Co γ- or 220 kVp X-rays: according to Ref.[42, 43], a resulting number of ≈ 1000 strand breaks (Gy^{-1} cell^{-1}) can be expected, with a ratio of 35:65 between direct and

indirect effects. Using a probability of SSB induction linear up to 37.5 eV, but with a threshold at 5 eV (before which it is null) the data on direct effects were successfully reproduced [44, 45, 33, 46], even if higher energy values (57.6 eV) were considered to take into account the role of DNA on track-structures [47] and the fact that heat-labile sites were neglected from the count of strand breakage [48]. This represents an alternative approach from what previously done by Nikjoo *et al.*, who used a threshold energy of 17.5 eV to model SSBs [27].
For what concerns the indirect strand break induction due to low-LET irradiation, the calculations were in agreement with the aforementioned results when 65% of the ·OH interactions with deoxyribose lead to SSBs. This fraction corresponds to 13% of all ·OH-DNA interactions (values $\sim$ 20% were found for the percentage of ·OH-deoxyribose interactions), while the remaining fraction corresponds to interactions with the bases.
As for DSBs, the threshold has not been enhanced with respect to the one for SSBs, but a radical transfer mechanism was proposed, in 1% of the cases a single interaction may lead to a DSB [28]. Exposure to different radiation qualities implies that yields and complexity of the damages vary significantly, so a characterization of different kinds of DNA damages was carried out: the focus was on the distribution of the SSBs and DSBs as "simple" damages, while yields of DSBs clusters (defined as lesions comprising 2 or more DSBs within a genomic distance of 25 bps) were investigated, under the hypothesis that these clusters are complex lesions that could influence the fate of a cell. Their multiplicity (the mean number of DSBs in a cluster) was also considered.
DNA fragment distributions were obtained, where the majority of these fragments is induced by 2 DSBs from a single track, since the particle fluence inside the target was adjusted to minimize fragments from multiple particles. All the results are presented as averages (Gy^{-1}, per cell) over a variable number of simulation runs, from 64 to 256 according to the energy of particles, and the errors are presented as standard errors of the mean (SEM) among different runs.

Software for plot elaboration

Unless specified in the text, all the plots shown in this thesis were obtained by means of GraphPad Prism version 6.01 for Windows, GraphPad Software, La Jolla California USA [49].

2.1.6 Results and discussion

The first set of results, shown in Fig.2.1, concerns the conversion of particle energy in MeV/u into LET. Similar results always obtained with PARTRAC are presented for different nuclear model geometries and irradiation setups in [50].

Two different LET curves are presented for each particle: the curves labelled

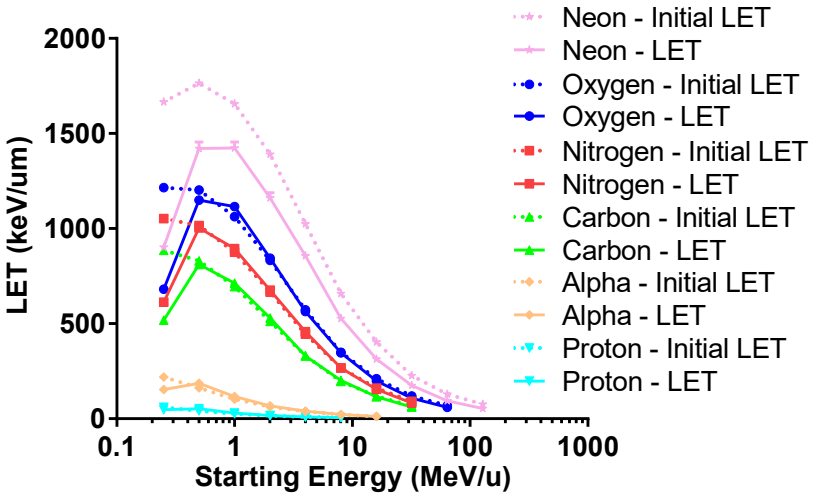

Figure 2.1: LET values as a function of particle initial energy (MeV/u), calculated from energy deposited within the cell nucleus (solid lines, drawn to guide the eye) and comparison with stopping powers from ICRU [36, 51] (dotted lines).

with "LET" were obtained according to Eq.2.4 and 2.5, applied to the specific irradiation setup, while the curves labelled with "Initial LET" refer to the stopping power of particles at their initial energy, as provided by ICRU [36, 51].
The average LET can be used to describe radiation clustering properties in track segments along which there are no significant changes of the particle energy. In case of very low energy particles, whose range is smaller than the transversal thickness of the nucleus, the LET has been calculated as the ratio of the total energy deposited in the target to the particle range. The LET in the low energy range is lower with respect to ICRU nominal values. At the lowest energy range, depending on the species, calculated LET ranges from $\sim$ 45 to 900 keV/μm.
By definition of LET (and stopping power), at equal energy, the LET is higher for heavier ions. Decreasing the energy per nucleon, the values of the LET initially increase up to an inversion point (around 0.5 MeV/u) for all the species, even if the effect is less pronounced for the lighter ions. Thereafter the LET starts to bend down and to decrease very steeply for all the radiations. The Bragg peak corresponds to the region of the curve where the LET reaches its maximum. Despite having the same LET, two particles at the proximal

and distal edge of the Bragg peak have different velocity, hence different track structures. It has to be recalled that in the low energy region, the Bethe-Bloch formalism breaks down, which is due to several factors, including charge changing reaction for slowing down particles. LET values here derived are specific of the irradiation setup and are average values over the nuclear model under consideration.

Fig.2.2 shows the yields of SSBs, DSBs, total number of strand breaks and

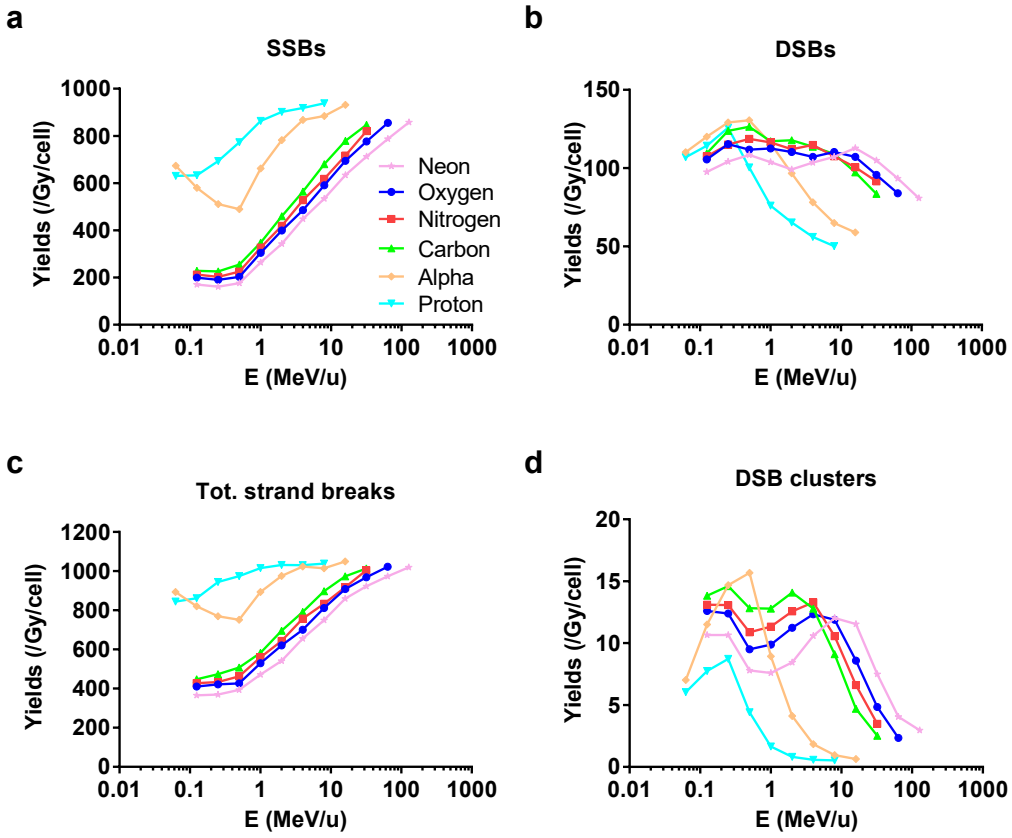

Figure 2.2: DNA damage as a function of particle initial energy: yields of (a) SSBs; (b) DSBs; (c) total strand breaks; (d) DSB clusters. Lines are drawn to guide the eye. Error bars are SEM values from different simulation runs.

DSB clusters for all the species as a function of their initial energy; Fig.2.3 reports the same data as a function of the LET, using the relationship between the starting energy and the LET shown in the previous plot. In the count of DSBs, we also include all DSBs that might be clustered in higher complexity lesions: *e.g.* DSB clusters contribute multiple DSBs corresponding to their multiplicity (number of DSB per cluster).

The interpretation of the results as a function of energy and LET is not straightforward, due to the non-monotonic dependency between these two latter quantities. In general, SSB yields are much higher for the light-particles,

and they increase with the energy, except for α particles, which display a deep valley. Higher energies mean lower LET and sparse distribution of damages, which translates into more simple damages than clustered ones, as also clearly visible in the plots in Fig.2.3(a).

On the contrary, for DSBs the trend is quite different: the number of these

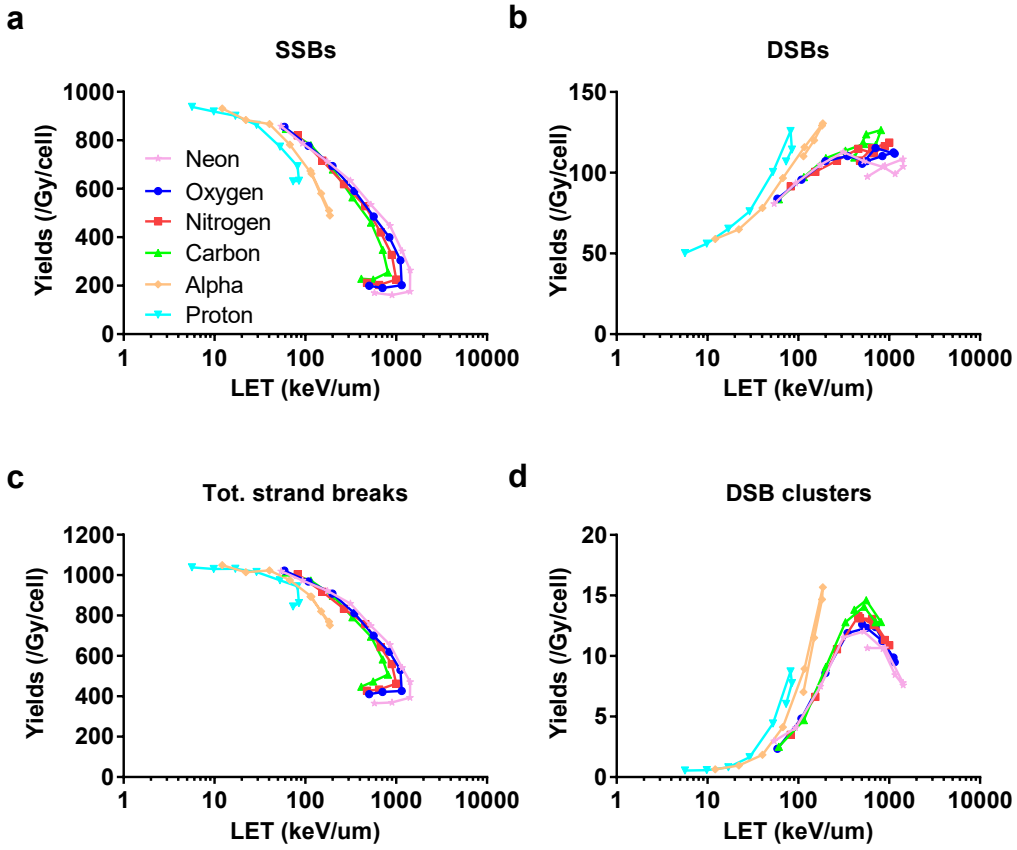

Figure 2.3: DNA damage as a function of particle LET: yields of (a) SSBs; (b) DSBs; (c) total strand breaks; (d) DSB clusters. Lines are drawn to guide the eyes. Error bars are SEM values from different simulation runs.

lesions slightly increases with the energy, but then this trend is inverted and DSB yields decrease (Fig.2.2(b)). As a function of LET, the yield of DSBs increases almost monotonically: a higher energy deposition per unit length translates into closer breaks.

Different ions at the same LET induce damage of different complexity, due to the energy of secondary electrons. At equal LET, lighter species induce more DSBs: from the Z^2/β^2 dependence of LET, the same linear energy transfer for ions of different charge implies that the lighter one must have a lower velocity. As the velocity of secondary electrons is proportional to the velocity of the primary particles, secondary electrons will be less energetic in this case. But if the LET is the same, this means that more electrons have to be accelerated

per unit path lenght. This results in denser interactions, hence more localized damage [52]. In particular, the final part of the track of a δ-ray is usually the site for very clustered lesions, as simple damages are condensed in few nanometers of distance [53]. The difference among the heavier species at equal LET is less evident, because of the similar charge.
For both SSBs and DSBs, a common feature at very low energies/high-LET is manifest, that is an inversion of the trend in the yields, resulting in hooks in the curves connecting simulation points. This can be explained by Fig.2.1, where the LET stops increasing for lower energies and it falls off beyond the point of maximum. If we consider the curves for the total strand breaks (Fig.2.2(c) and Fig.2.3(c)), calculated as the sum of SSBs and twice the yield of DSBs, it is immediate to notice the resemblance to the plots for SSBs, as these latter dominate in the count of total damages.
For targets at the order of magnitude of the nanometre, the induction of DNA complex lesions deserves specific attention, as indicator of radiation clustering properties, as already introduced in the pioneering work of Nikjoo *et al.* [54, 55]. In Figg.2.2(d) and 2.3(d) we show the yield of DSB clusters as a function of energy and LET, respectively. The definition of DSB clusters adopted in this work is of > 2 DSBs within 25 bps, which means within few helical turns of the DNA, according to the definition of DSB++ given by Nikjoo *et al.* [8, 56] (the notation DSB+ referred instead to a DSB in close proximity of a SSB). This specific definition of DSB cluster is an operational definition to allow quantification of complex damage.
The trend is non-monotonous for the heavier charged particles under investigation: the number of clusters starts bending down before the maximum LET is reached, as the damage becomes more spatially localized when the energy decreases. Again, the curves connecting simulation points show hooks, with DSB cluster yields that are going back to values close to those obtained with a lower LET. This means that differences in the complexity of damage induced by two particles with the same LET but at the proximal and distal sides of the Bragg peak are somewhat hidden when DSB clusters are scored. In Par.2.3.5 we address the issue that, given the observed trend of DSB clusters *vs* LET, a single DSB cluster yield can be approximately associated to a single LET value.
For the purpose of this study, different definitions of DNA cluster damage could have been adopted, *e.g.* by means of different degrees of complexity or lesions comprising a DSB plus a second type of DNA damage (bases). In fact, there is no standard approach to relate the energy deposition pattern in a chosen sensitive volume at the nanometer scale to the biological outcome of the exposure. This would obviously result in different damage spectra and a different asessment of radiation effectiveness, based on different endpoints. However, it is common knowledge that DSBs are the typical signature of radiation passage in matter, and the biological correlation between complex lesions (like DSB clusters) and impaired cellular repair mechanisms is well recognized within the

radiation research community [57, 58, 59]. It is therefore reasonable to adopt DSB clusters to evaluate the radiation effectiveness (this will be discussed in Chap.2.3 of this thesis, where clustered DNA damage is used to quantify the neutron RBE).
It must be also noted that PARTRAC is one of the track-structure codes nowadays available within the radiation research community, but other tools may rely on different implementations of the DNA macromolecule and cross-sections, leading to different ways to calculate clustered damage. Examples of track-structure codes exploiting a geometrical model of the DNA are:

- the MOCA-15 code by Paretzke and Wilson (1987) [60], where the energy depositions simulated in water vapour of unit density were superimposed to the DNA model proposed by Charlton and Humm (1988) [61, 62]. The sequence of bases was described as a 1-nm-diameter cylinder, surrounded by the sugar phosphates as 0.34-nm-thick and 2.3-nm-diameter half-annuli, each one rotated by 36°.

- the KURBUC code, introduced by Nikjoo *et al.* in 1993 [63], which allowed the simulation of electron and ion transport and it exploited a geometrical model similar to the one from Charlton: a cylinder divided into regions for the bases and the sugar-phosphate moiety, helically wrapped around the central cylinder. The resulting diameter of the DNA was of 2.3 nm, and the model included the first hydration shell.

Although a good approximation, these models are far from the atomic resolution of single events obtained nowadays in the models used in PARTRAC or Geant4-DNA. Nevertheless, the genomic distances between lesions were converted into geometric ones (measured in nm), to recreate sequences of nucleotide pairs. The cross-sections used in these codes for both direct damage and the reactions involving the $^{\cdot}OH$ radicals were adjusted taking into account the chosen DNA geometry (*e.g.* the implemented van der Waals radius), to match the experimental measurements (as explained in the "Material and Methods" of this Paragraph for the PARTRAC code) [64].
DNA fragment yields are another important endpoint, often investigated experimentally by means of *e.g.* pulsed-field gel electrophoresis. The reliability of PARTRAC results has often been checked through the comparison with experimental results on the fragmentation induced in human fibroblasts. For example, fragments from iron ions were simulated for different size ranges and then compared to experimental results, as reported in Ref.[65]. Moreover, PARTRAC calculations allowed to support the interpretation of experimental findings on the PFGE data and DSB yields following irradiation with other radiation qualities (see Fig.2.4) [66]. This proves the robustness of the track-structure code.
As a further benchmark of the code, in Ref.[50] (Supplementary Material) Friedland *et al.* show the RBE calculated for the DSB induction from the analysis of the DNA fragments (considering the detectable fragment size intervals)

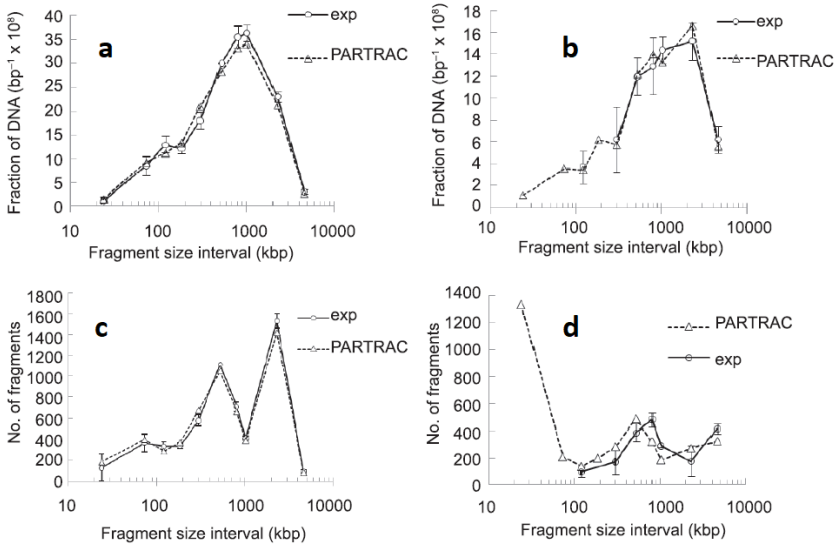

Figure 2.4: Comparison between experimental and PARTRAC data on initial DNA mass distribution (upper) and DNA fragment spectrum (lower), as a function of fragment size, following exposure to (a-c) 150 Gy of 60Co γ-rays and (b-d) 64 Gy of ^{14}N ions (LET = 80 keV/μm). Adapted from Ref.[66].

after exposure to LET particles in a lymphocyte nucleus. For the estimation, 128 MeV protons were chosen as reference radiation, as they yielded the lowest value for the endpoint with respect to other radiation qualities (*i.e.* being of the lower biological effectiveness). The predictions for the theoretical RBE are found in good agreement with experimental results [67, 68].

The results for yields of fragments per cell per Gy, are shown in the Fig.2.5 for four different size intervals ($0 \leq$ bps ≤ 30; $30 \leq$ bps ≤ 1000; $1000 \leq$ bps ≤ 9000; and $9000 \leq$ bps ≤ 23100). The first size interval can be directly correlated to the number of fragments generated within a DSB cluster: a cluster containing only two DSBs (multiplicity = 2) will result in a single fragment with length ≤ 25 bps, while more complex clusters from high-LET IR (multiplicities > 2) will enclose many shorter fragments. In Tab.2.1, the values of the multiplicity of DSB clusters are reported for all the charged ions under investigation, at the different energies/LET, obtained as:

$$\text{Average multiplicity} = \frac{\text{Average number of DSBs in a cluster}}{\text{Average yield of DSB clusters}} \tag{2.6}$$

The yield of fragments in a DSB cluster is calculated as the average multiplicity minus one, and it is also reported in the same Table. For light ions, the number of fragments is, on average, always close to 1 for all LET values, even if a dependence on the LET can still be observed, with higher LET values corresponding to the higher fragment yields. For heavier ions, DSB cluster multiplicity reaches maximum values of approximately 5, 6, 7 and 9 for C, N, O and Ne ions at their highest LET values. In Fig.2.5(a), the yield of DNA

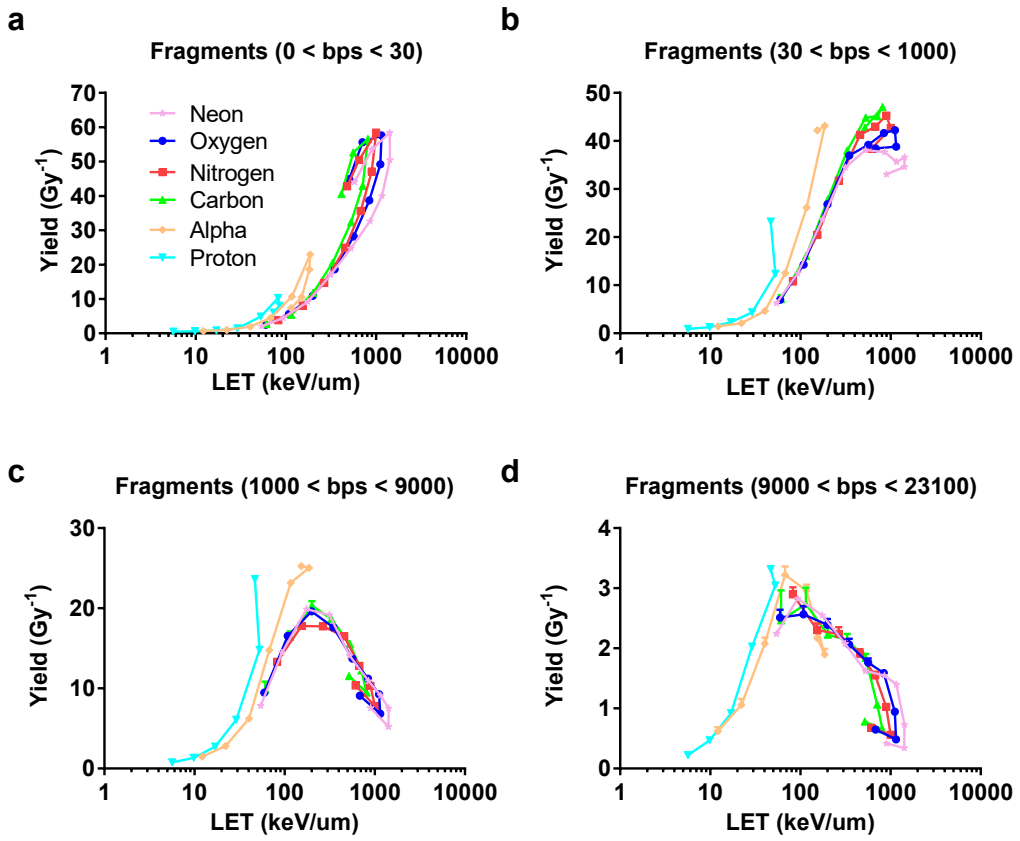

Figure 2.5: Yields of DNA fragments in different size intervals: (a) 0-30 bps; (b) 30-1000 bps; (c) 1000-9000 bps; (d) 9000-23000 bps. Lines are drawn to guide the eyes. Error bars are the SEM values from different runs.

fragments shorter than 30 bps is shown: for protons and α's, the trend is close to the one for DSB clusters, with average cluster multiplicity of ~ 2. The number of fragments becomes higher as the LET increases, and, unlike DSB clusters, there's no bending point. Coupling these results, it becomes evident that with increasing LET, the number of DSB clusters decreases because the lesions are so close to each other that they contribute to single, large clusters, with higher average multiplicity. However, as later discussed in (Par.2.3.5), hooks connecting simulation points observed for the heavier ions (C, N, O) imply that a fragment yield cannot be unambiguously associated to a given LET value.

Yields of longer fragments in wider size intervals are shown in (2.5(b-d)): yields of longer fragments are lower than the one related to the first size interval ($\leq$ bps ≤ 30), meaning that most of the fragments are created by high-proximity damages.

These ranges give an idea of the trend of fragments at spatial scales corresponding to fragments sizes experimentally measurable [69, 65].

For the range ($30 \leq$ bps ≤ 1000), the yield initially increases with increasing LET. The plots for the last two size intervals seem to show an enhancement of the effectiveness in inducing fragments with increasing LET only for protons and α-particles. For heavier species and increasing LET, the number of fragments displays a decreasing trend, and only small fragments will be produced. The maximum is however well below with respect to peak values observed before (almost $\frac{1}{3}$ for fragments in the range [1-9 kbps], and $\frac{1}{20}$ for the size range [9-23 kbps], if compared to the range [0-30 bps]).
All the data presented in this section give an insight on the effectiveness of different radiation qualities in inducing damage to the DNA. Results are necessarily dependent on the particular cell model and setup implemented for the track-structure simulations. However, they might be useful *e.g.* for the creation of a DNA damage database, which could be used for many applications without resorting to new track structure calculations. An example in this sense will be presented in Par.2.3 of this Chapter.
As it will be later discussed in Chap.3, several biological endpoints commonly detected in the lab are essentially related to the energy depositions in the genetic material of a cell and to initial DNA damage. Information from this kind of calculations might be coupled with studies addressing damage on a "visible" (hence larger) spatial scale.

Table 2.1: Average multiplicity and number of fragments generated per DSB cluster (Gy^{-1} $cell^{-1}$) due to different IRs.

		MeV/u	0.0625	0.125	0.25	0.5	1	2	4	8	16	32	64	128
Proton		LET	73.53	85.03	82.24	52.59	29.13	17.01	9.80	5.65				
	DSB clust.		6.04	7.76	8.73	4.42	1.65	0.81	0.58	0.54				
	Multipl.		2.09	2.12	2.15	2.08	1.85	2.02	2.02	2.00				
	# Fragm.		1.09	1.12	1.15	1.08	0.85	1.02	1.02	1.00				
Alpha		LET	114.16	149.25	182.15	186.65	116.82	67.48	40.40	22.14	12.17			
	DSB clust.		7.02	11.51	14.68	15.68	8.93	4.12	1.84	0.96	0.63			
	Multipl.		2.14	2.27	2.36	2.42	2.17	2.07	2.04	2.01	2.04			
	# Fragm.		1.14	1.27	1.36	1.42	1.17	1.07	1.04	1.01	1.04			
Carbon		LET		413.22	560.75	811.45	712.27	529.77	330.37	201.33	115.07	61.11		
	DSB clust.			13.83	14.61	12.81	12.79	14.08	12.79	9.11	4.71	2.52		
	Multipl.			3.91	4.54	5.34	4.28	3.23	2.58	2.25	2.12	2.05		
	# Fragm.			2.91	3.54	4.34	3.28	2.23	1.58	1.25	1.12	1.05		
Nitrogen		LET		476.84	650.56	1003.04	894.64	676.67	457.73	266.43	154.21	82.64		
	DSB clust.			13.11	13.07	10.88	11.33	12.56	13.29	10.56	6.62	3.48		
	Multipl.			4.25	4.86	6.21	5.04	3.75	2.85	2.37	2.18	2.07		
	# Fragm.			3.25	3.86	5.21	4.04	2.75	1.85	1.37	1.18	1.07		
Oxygen		LET		503.78	707.97	1149.46	1115.21	843.51	563.88	347.18	199.04	107.99	59.47	
	DSB clust.			12.60	12.39	9.50	9.88	11.24	12.33	11.89	8.59	4.85	2.35	
	Multipl.			4.53	5.39	6.88	5.82	4.33	3.22	2.53	2.24	2.12	2.04	
	# Fragm.			3.53	4.39	5.88	4.82	3.33	2.22	1.53	1.24	1.12	1.04	
Neon		LET		576.04	902.20	1421.14	1423.80	1161.36	856.17	526.88	313.23	174.86	93.50	54.27
	DSB clust.			10.66	10.66	7.79	7.59	8.44	10.59	12.03	11.54	7.49	4.06	2.97
	Multipl.			5.17	5.91	8.53	7.43	5.59	3.99	2.99	2.46	2.20	2.07	1.68
	# Fragm.			4.17	4.91	7.53	6.43	4.59	2.99	1.99	1.46	1.20	1.07	0.68

2.2 Energy transfer from the micro- to the macroscopic scale

2.2.1 LET evaluation for proton therapy

Results given in Par.2.1.6 have been reported as a function of LET, as it is usually done to discern the effects of radiation quality.
In particle therapy, the LET can be advantageously used to plan the enhancement of the biological dose in the target region, given its relation to increasing RBE at the distal end of the Bragg peak. As a matter of fact, this is currently done for carbon ion therapy, but not for proton therapy. As known, proton beams allow a better dose conformation to the tumour region than conventional photon radiotherapy. Concerning their biological effectiveness, in clinical practice they are assumed to be more effective than photons, and their RBE has been parametrised as a constant factor of 1.1, not dependent on the depth in the tissues [70]. In the plateau of the Bragg curve, protons and secondary electrons are as biologically effective as photons, but secondary hadrons account for the increase in the effectiveness. The hadronic component disappears in the Spread Out Bragg Peak (SOBP) [71], however proton LET starts to vary along the path of the beam, dramatically increasing with depth in passing from the proximal to the distal part of the Bragg peak [72].
This might give rise to LET/RBE hotspots, entailing the risk of damage induction in tissues close to the target region.
As a matter of fact, little is known about the possible clinical impact of neglecting such change in treatment planning, leading to suboptimal exploitation of the technique. First clinical evidence starts to appear on the correlation between high-LET for end-of-range protons and harbinger signals of normal tissue damage [73].
This is of great relevance, considering that proton therapy is still preferably used for tumours located in proximity of highly sensitive organs or structures, and in paediatric patients, for whom the probability of complications or secondary malignancies is also higher due to the longer life expectancy.
The optimization of proton treatment planning thanks to the inclusion of LET variations in the target and in normal tissues has been suggested [74]. The so-called LET-painting approach [75] has been proposed, to modulate the LET over the tumor, maximizing tumour cell killing and sparing at most normal tissues [76].
However, to consider LET variations in the planning, robust calculations have to be made available for the clinical practice, requiring development of calculation methods, experimental data for benchmark and finally development of analytical formulations for fast implementation in planning systems. As known however, LET itself is, by definition, an average quantity, and it might be not suited to describe the biological effectiveness of radiation in very small sensitive regions of the target. A most precise characterization of energy transfer on a

small spatial scale is desirable. Nevertheless, when going to practical clinical applications, quantities given at the voxel size for treatment plan implementation are needed [77], and the more general issue of linking quantities describing radiation energy deposition at different spatial scales will be addressed in this section.

2.2.2 Formalism for the linear energy transfer

Averaging energy depositions per unit track length might hide a huge variability in the actual distribution of energy depositions, that becomes higher the smaller the spatial scale we are considering.
We recall in the following the formalism elaborated by Keller [78] that is at the basis of the so-called microdosimetry.
Starting from LET, we can first distinguish two different definitions to condense the information of a whole LET distribution, as the one due to a mixed field, in a single representative value, namely:

- the frequency average LET, defined based on particle fluence, using the probability density function of LET in fluence f(L):

$$\overline{L}_F = \int L \cdot f(L) \cdot dL \tag{2.7}$$

- the dose average LET, defined in terms of the absorbed dose delivered by particles with given LET, using the probability density function of LET in dose d(L):

$$\overline{L}_D = \int L \cdot d(L) \cdot dL \tag{2.8}$$

Both quantities can be averaged in macroscopic regions of any size and related to absorbed dose for the same macroscopic region. Going to small spatial scales, we can introduce the notion of the so-called sensitive site, *i.e.* a site of fixed dimensions, possibly related to a biological structure of interest. A sensitive site can be defined *e.g.* as a sphere with diameter 1 μm, roughly corresponding to the linear size of a chromosome domain. Energy deposition by radiation in such site is a stochastic quantity, to which we can associate probability distributions and expectation values.
Such probability distributions will depend on the characteristics of the site and, most importantly, on the radiation quality under study. We will speak of "event" in a site, when statistically correlated particles are depositing energy in the site. By definition, an event requires energy deposition: the mere passage of a charged particle without energy transfer to the site is therefore not counted as an event.
The energy imparted ϵ is the sum of all energy transfers ϵ_i within a specified site S:

$$\epsilon = \sum \epsilon_i \tag{2.9}$$

It is a random variable, fluctuations are larger for smaller sites, for densely ionizing radiation and for small doses.
Energy imparted has a uniquely defined value in a specified region after an exposure has taken place. From this quantity, the specific energy z can be defined, in analogy with the macroscopic dose, as the energy imparted divided by the mass m of the specified region: $z = \epsilon/m$, expressed in Gy.
We can then define the probability density f(z; D), that is the probability of having a specific energy z in a microscopic site when the macroscopic dose is D.
The single-event distributions for energy imparted are defined in an analogous way, under the condition that exactly one event has taken place in the site.
The lineal energy y is defined as the energy imparted in one event divided by the mean chord length $\bar{l}$ of the site, that is the length resulting from the random interception of the site by a straight line:

$$y = \frac{\epsilon}{\bar{l}} \tag{2.10}$$

The lineal energy is the microdosimetric analogue of LET, and it is expressed in keV/ μm.
The mean chord length $\bar{l}$ is equal to $4 \cdot \frac{V}{S}$ for a convex site of volume V and surface S.
The average lineal energy produced by an event in the site is called frequency mean lineal energy and it is given by:

$$\overline{y}_F = \int_0^\infty y \cdot f(y) \cdot dy, \tag{2.11}$$

The frequency mean lineal energy is therefore analogous to the frequency mean LET.
When energy loss straggling and the lateral escape of secondary electrons out of the site are negligible, and when the range of the ionizing particle is sufficiently large, the two mean values $\overline{L}_F$ and $\overline{y}_F$ are approximately equal.
In analogy to the definitions of the LET distributions one can consider also the dose distributions of the lineal energy, determining the fraction of absorbed dose that is associated with certain values of y.
The dose distribution of y can be obtained by using the formula:

$$d(y) = \frac{y}{\overline{y}_F} f(y) \tag{2.12}$$

Such distribution is relevant to link the effectiveness of radiation to the local energy concentration in microscopic sites.
Dose average value of y is defined as dose mean lineal energy, according to the following equation:

$$\overline{y}_D = \int y \cdot d(y) \cdot dy \tag{2.13}$$

2.2.3 Objective

In this section results on the characterization of proton energy transfer at different spatial scales are presented, using average LET values and microdosimetric quantities, starting from simulated particle tracks.
The MC code PARTRAC was used for the simulation of the full topology of proton tracks in water for different proton energies. We focused our efforts on the *ab-initio* derivation of microdosimetric quantities, particularly $\overline{y}_D$, trying to make the bridge with equivalent macroscopic quantities ($\overline{L}_D$).

2.2.4 Material and methods

Proton LET and $\overline{y}_D$

Proton tracks for different energies (20, 40 and 70 MeV) were simulated with PARTRAC in water phantoms of increasing dimension, namely cubic boxes with side of 134, 200 and 550 μm, respectively. The dimensions were chosen considering a rough estimate for the maximum range of secondary electrons accelerated by primary protons, so that all secondary electrons are stopped in the water phantom and enter in the calculation of energy transfer.
Protons were generated from a single point source at the center of the bottom surface of the water phantom, and directed perpendicularly upwards (z axis). The coordinate system's origin was placed in the middle of the water phantom. PARTRAC output files contain information on the spatial coordinates of all energy deposition events, as well as the corresponding amount of energy deposited in each interaction point. In the simulations, sub-excitation electrons were neglected, that is electrons with energies below $\sim$ 10 eV.
Spheres of diameter d 1 or 2 μm were considered as microdosimetric sensitive sites. To calculate microdosimetric quantities, we need to sample the track with randomly placed sites, and to score the amount of imparted energy. As we want to associate the microdosimetric quantity to a single proton energy (as much as this is possible) the sampling could not be done for the whole length of the track. Only a portion of the track was sampled, falling in a slice at the center of the water phantom, with thickness 7 μm (-3.5 $\leq$ z $\leq$ 3.5 μm) and 9 μm (-4.5 $\leq$ z $\leq$ 4.5 μm), respectively for the smaller and larger site diameters. A schematic picture of the setup is shown in Fig.2.6.
The sampling is done according to the following algorithm:

1. an interaction point among those of the track is randomly selected. Since the large majority of energy deposition events are concentrated along the track core and close to it, the probability of selecting regions with a dense concentration of events is considerably higher. To compensate for this bias in the sampling, a weight factor is later introduced (see step 5);

2. a spherical surface is built, centred on the selected interaction point, with radius r drawn randomly in the interval $0 \leq r \leq d$, where d is the sensitive site diameter;

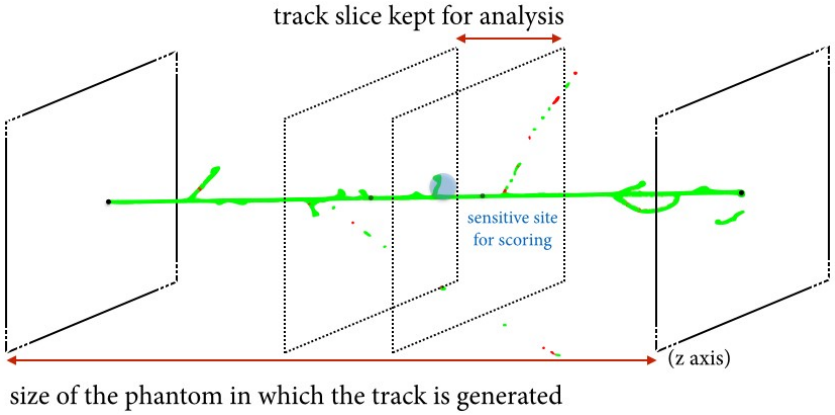

Figure 2.6: A schematics of the setup used for the calculation of proton LET and microdosimetric quantities.

3. a new point is randomly selected on such spherical surface. This point will be the centre of the sampling region (sensitive site). By construction, the sampling region will therefore always include at least one energy deposition (the one associated to the interaction point selected in the first step of the algorithm), thus avoiding the creation of empty sampling sites;

4. interactions occurring within the sampling site are counted, and the deposited energy of each interaction is recorded in a vector for further analysis;

5. a weight is defined as:

$$\frac{N_{\text{tot. events}}}{N_{\text{events in the scoring region}}}, \tag{2.14}$$

where the numerator is the total number of energy deposition events in the track portion under consideration, and the denominator is the number of events falling in the sampling site. This is done to correct the bias in the sampling, as explained in the first step of the algorithm;

6. frequency histograms for the number of interactions in the scoring region (multiplicity), total energy deposited in the site (ϵ), and lineal energy y are created, where histogram entries are weighted with the factor calculated in the previous step;

7. dose distribution of y is obtained using Eq.2.12;

8. frequency mean lineal energy $\overline{y}_F$ and dose mean lineal energies $\overline{y}_D$ are given as calculation outputs.

The algorithm was applied for the generation of one scoring sphere per track, for a number of tracks equal to 10^4 for 20 and 40 MeV protons, $5 \cdot 10^3$ for the

highest energy of 70 MeV.
To obtain an estimation of LET, all the energy depositions in the selected portion of the track were summed up, and then divided for the corresponding track length ($\mathrm{LET_{track}}$). To introduce a dose weight in this scheme, it is enough to record the dose imparted by each of the simulated track portion, and apply a dose weight to the LET when averaging on all tracks ($\mathrm{LET_{dose}}$).

2.2.5 Results and discussion

Results are summarized in Tab.2.2 for the three proton energies. Dose average LET values are generally found to be higher than track average values. Results for LET can be compared to SRIM/TRIM tables, considering protons of the same energy in water. For the same initial energies, SRIM gives LET values of 2.65, 1.51 and 0.97 keV/μm for 20, 40 and 70 MeV protons, respectively. Values obtained from particle tracks are averaged over the portion of the track under consideration rather than associated to the initial energy, but still close to SRIM results, and the dependency on the energy is maintained.
From the energy depositions ϵ in the scoring regions, the lineal energy y has been obtained through Eq.2.10, being $y = \epsilon \cdot \frac{3}{2}$ for a sphere of radius of 0.5 μm, and $y = \epsilon \cdot \frac{3}{4}$ for r = 1 μm.
The frequency mean lineal energy $\overline{y}_F$ and the dose mean lineal energy $\overline{y}_D$ are reported in the Table for the two scoring regions. As expected, $\overline{y}_F$ decreases for increasing proton energies, due to the lower linear energy transfer of the more energetic particles. These values can be correlated the $\mathrm{LET_{track}}$. Similar

Table 2.2: For different proton energies (MeV), values of $\overline{y_F}$, $\overline{y}_D$ and LET values ($\mathrm{LET_{track}}$ and $\mathrm{LET_{dose}}$), calculated on the 7 μm track slice (keV/mum) (see Fig.2.6).

Scoring region	**E(MeV)**	$\overline{y}_F$	$\overline{y}_D$	$\mathbf{LET_{track}}$	$\mathbf{LET_{dose}}$
1μm sphere	20	2.30 ± 0.09	3.57 ± 0.08		
	40	1.33 ± 0.04	2.61 ± 0.10		
	70	0.86 ± 0.03	2.15 ± 0.12		
2μm sphere	20	2.72 ± 0.06	3.52 ± 0.07		
	40	1.51 ± 0.02	2.37 ± 0.09		
	70	0.96 ± 0.02	1.83 ± 0.09		
Whole track slice	20			2.22 ± 0.02	2.59 + 0.02
	40			1.26 ± 0.04	1.73 ± 0.11
	70			0.76 ± 0.03	1.17 ± 0.11

data were found by Cortes-Giraldo *et al.* (2015), for a 160 MeV proton beam at a depth of 16.5 cm in a cylinrical water phantom, corresponding to a proton mean energy of approximately 35.1 MeV: the Geant4-DNA calculations in a scoring site with a radius of 5 μm provided a $\overline{y}_D$ of 2.06 keV/μm [77]. Anderson *et al.* (2017) measured the proton microdosimetric spectra in water using a

solid-state micro-detector, obtaining, for a 4×4 cm^2, 71.3 MeV proton beam, a $\overline{y}_D$ = 1.92 keV/μm and a $\mathrm{LET}_{\mathrm{dose}}$ of 1.15 keV/μm, at a depth of 2.5 cm in water [79]. Pan *et al.* (2015) combined measurements by means of a mini-TEPC detector and simulations with the FLUKA (FLUktuierende KAskade) code [80] for 30 MeV protons from a cyclotron, showing a good agreement converging to a $\overline{y}_D$ of almost 4 keV/μm [81]. They also reported data from Borak *et al.* (2004) [82], in agreement with our findings for the 40 and 70 MeV protons.
$\overline{y}_D$ values are higher than the ones for the $\mathrm{LET}_{\mathrm{dose}}$, as expected from theoretical considerations formulated by Kellerer [78]. However, simulations at more energies are needed, to test the overall $\overline{y}_D$ *vs* $\mathrm{LET}_{\mathrm{dose}}$ interrelation for different sizes of the sensitive site. The final aim would be to derive analytical functions to describe the $\overline{y}_D$ as a function of the LET, that might be useful for practical applications where the LET is usually used as estimator of radiation quality, along with the RBE.

The work giving the preliminary results presented in this section led to the development of the algorithm to derive microdosimetric quantities from PARTRAC tracks, and it opened to the investigation of the interrelations between energy depositions at different spatial scales, always starting from simulated tracks.

2.3 Neutron biological effectiveness

2.3.1 Implications due to secondary fields in therapy

Up to now, only damage due to electronic collisions by primary particles (and their secondary electrons) has been discussed and considered. However, radiation can undergo nuclear reactions, as a result of which radiation quality is modified [83], *i.e.* different secondary charged particle species are generated and are in turn responsible for electronic energy loss and damage induction.
Radiation therapy is an example of a general context in which this represents a specific concern [84], because the onset of by-product particle fields might lead to energy depositions outside the target region. This can happen both as a consequence of interactions of the primary beam in elements of the setup for beam transport, focusing or shaping, or directly with traversed biological tissues. The improvement of irradiation methodologies, as in particular the introduction of active scanning beamlines for particle therapy, has led to the reduction of by-products fields generated because of beam transport. However, secondary field production in tissues cannot be avoided.
For conventional radiotherapy with photons, the concern exists only when energies used for the treatment are high enough ($\gtrsim$ 8 - 10 MeV) [85] to induce photonuclear reactions, where mainly neutrons (but also other charged particles) can be produced. Nuclear reactions induced by proton beams include fragmentation of target nuclei, producing low energy secondary particles, and acceleration of secondary neutrons, which is kinematically favoured due to the very similar masses of protons and neutrons. Carbon projectiles can also undergo fragmentation, as a result of which the so-called fragmentation tail appears after the Bragg peak in the dose deposition profile, as lighter fragments have longer penetration depths in tissue (the range scales as $\frac{A}{Z^2}$) [86].
In general, a constant build-up of secondary species occurs, while the primary ion intensity is gradually attenuated in matter.
The biological effects of secondary particle fields have to be considered when comparing the outcome of different treatments, because they might play a major role in the induction of long-term complications and effects as second primary cancers. Generally speaking, long-term effects deserve today high attention, also because the chance of success in tumour eradication and long-term survival following radiation and particle therapy have noticeably increased over the past years [87].
In this context, the concern particularly exists for secondary neutrons depositing energy outside the target region, and basically throughout the patient body: though the dose delivery is orders of magnitude smaller than the prescribed tumour dose [88], neutron biological effectiveness can be high, and this is not currently included in any system for treatment planning. The production of secondary fields represents also a problem from a radiation protection point of view, and it has to be considered when designing appropriate shielding strategies, as it is the case *e.g.* for shielding against space radiation, discussed in a

separate chapter of this thesis.

2.3.2 Mechanisms behind neutron-induced damages

Patients treated with protons are likely to receive neutron doses, generated both in the medical accelerator and beam transport system (especially if passive scanning is used) and in the patient's body [89, 90, 91, 92]. In the practice, neutrons are seldom produced for targeted purposes, limited possibilities exist for the generation of mono-energetic neutron beams, and they are difficult to focus. Fast neutrons have been proposed for use in radiotherapy, because of their higher penetration depth and their enhanced tumour-control probability, but their use has been abandoned since the depth-dose distribution was comparable to the one for photons. Neutrons are always a by-products of nuclear interactions, therefore usually characterized by broad energy and angular distributions. This is true also for neutron production in particle therapy.
The effectiveness of neutrons in causing human carcinogenesis and other biological consequences is still the subject of theoretical [93] and experimental studies with *in vitro* or *in vivo* measurements. Epidemiological data from the A-bomb survivors hardly allow to draw clear-cut conclusions on this matter, due the predominance of γ-ray contributions and uncertainties in neutron dose reconstruction.
The evolution of knowledge on neutron biological effectiveness is reflected in the choices of the International Committee for Radiation Protection (ICRP), that gives recommendations for neutron radiation weighting factors w_R's as a function of energy based on available data from radiation biology, epidemiology and physics [93]. Recommendations given in 1990 were revised in 2007: neutron w_R's were dimished by a a factor of almost 2 for the lowest neutron energies, to account for the previously neglected effect of the change in size when translating animal data to humans, for whom a higher contribution of the lower effectiveness photon component of the neutron dose has to be expected. Also, a continuous function of w_R *vs* energy has replaced fixed values in discrete energy intervals. A maximal effectiveness, with $w_R \approx 20$, is agreed upon for neutrons of energies around 1 MeV [37].
However, available data analyzed to set radiation protection standards can be themselves much varied, and also subject to large uncertainties, so that different recommendations can be formulated by different committees, as in the case of the US - Nuclear Regulatory Commission (US-NRC) [94].
Within this general context, new efforts to study neutron biological effects are needed.

2.3.3 Objective

In the framework of the European project ANDANTE ("Multidisciplinary evaluation of the cancer risk from neutrons relative to photons using stem cells and

the analysis of second malignant neoplasms following paediatric radiation therapy") [2], the neutron RBE and the risk of secondary cancers due to neutron production in proton-therapy for paediatric patients were investigated.
Radiobiological measurements with neutron beams on stem cells of the thyroid, salivary glands and breast (possible targets for the incidence of secondary tumours) were performed and data on the RBE were correlated with model predictions [95].
Part of the work presented in this thesis has been carried out as a contribution to this project, particularly concerning MC simulations to develop a mechanistic model for neutron RBE as a function of energy, using as an endpoint the induction of complex DNA damage calculated with PARTRAC.
In PARTRAC no neutron cross-sections are currently available, thus simulating neutron-induced DNA damage requires an additional modelling step, that is the systematic characterization, by means of radiation transport codes, of the physical properties of neutron-induced secondary charged particle fields.
For this purpose, a novel coupling approach has been developed: we first used the code PHITS (Particle and Heavy Ion Transport code System, v. 2.82) [96] to evaluate *i.e.* the dose mean lineal energy and the relative contribution to the total neutron dose of secondary charged species; we then fed these results as input parameters for track-structure calculations with PARTRAC, to obtain neutron-induced initial DNA damage and RBE.

Publications for the topic.

- "At the physics-biology interface: the neutron affair", G. Baiocco, **S. Barbieri**, G. Babini, J. Morini, W. Friedland, P. Kundrát, E. Schmitt, M. Puchalska, U. Giesen, R. Nolte, A. Ottolenghi. Radiation Protection Dosimetry, 2017.

- "The origin of neutron biological effectiveness as a function of energy", G. Baiocco, **S. Barbieri**, G. Babini, J. Morini, D. Alloni, W. Friedland, P. Kundrát, E. Schmitt, M. Puchalska, L. Sihver, A. Ottolenghi. Scientific Reports, 2017.

2.3.4 Material and methods

Transport calculations of secondary fields from mono-energetic neutrons

The Monte Carlo code PHITS is a well-established tool for radiation transport simulations. It can simulate continuous energy loss, collisions and it is provided with reaction models and cross-section data libraries to simulate decays and nuclear interactions. It also provides a wide spectrum of physical

[2]ANDANTE was funded by the European Commission (Directorate General - EURATOM), in the 7th Framework Programme for Community Research. EU contract number: 295970

and radiobiological parameters of importance relatively to any flagged particle species.
We used PHITS for the simulation of neutron transport in matter: for neutron-induced reactions below 20 MeV, the Event Generator Mode is switched on, thus delivering information on an event-by-event basis using the cross-sections from Evaluated Nuclear Data libraries. For high energy neutrons (and other particles), the JAM4 and JQMD5 models are implemented to simulate particle-induced reactions up to 200 GeV and the nucleus-nucleus collisions, respectively.
A 15-cm-diameter sphere (ICRU sphere geometry), made of ICRU 44 soft tissue, was simulated to reproduce a simplified model of the human body; the phantom is exposed to an isotropic source of mono-energetic neutrons. Different energies were tested, namely: 10^{-5}, 10^{-3}, 10^{-2}, 0.1, 0.3, 0.5, 1, 1.5, 2, 3, 5, 10, 15, 20, 25, 30, 50, 100 MeV, to study how neutron biological effectiveness depends on energy.
Neutrons can undergo a plethora of different interactions in matter, strongly depending on the energy of the incoming particle and on the nature of the target. Following these reactions, the initial field characteristics are altered, and new particles with different radiobiological properties appear. Neutron biological effectiveness is therefore determined by all the radiation qualities accelerated or produced during the exposure, that are the main players in the dose deposition. A characterization of the mixed particle field is necessary, considering all possible reactions elicited by neutrons.
The change in the cross-sections for nuclear reactions, as neutrons lose energy in the target, also requires to study how neutron effectiveness varies with the position in the phantom. To this aim, we implemented three different scoring regions: each one is a small sphere of radius 1.5 cm, one concentric to the spherical phantom (*inner*), and the other two centred at 7.5 (*intermediate*) and 13.5 cm (*outer*) from the center of the phantom, respectively.
PHITS records characteristics of the secondary particles in the three scoring regions according to specified tallies.
Being the soft tissue mostly made of hydrogen, oxygen, carbon and nitrogen (respectively 10.12, 76.18, 11.10 and 2.60 %), results for these heavy particles were obtained, as well as for α particles and deuterons as possible products of nuclear reactions. We also scored results for electrons, because they deliver energy to the tissue when photons are produced.
To apply the coupling scheme proposed for this study, two parameters are required for each species in the three scoring regions, as input for further track-structure calculations with PARTRAC: the relative dose deposited in the target by each secondary species and its dose-mean lineal energy. These two parameters are proposed to condense all the information concerning the neutron-induced radiation field.
We also calculated the saturation-corrected dose-mean lineal energy, proposed itself as an indicator of biological effectiveness, to be compared with the dose-

mean lineal energy and to extract alternative RBE values without using track-structure results, as later detailed.
In the following, we give more details on how these quantities can be calculated with PHITS:

- analytical functions implemented in PHITS [97, 98] allow the calculation of probability densities of microdosimetric quantities in macroscopic regions. A specific tally (T-SED) provides the distribution $d(y)$. The distribution $d(y_s)$ was obtained for each species s in the three scoring regions, for a spherical sensitive site with diameter 1 μm (roughly corresponding to the linear dimension of chromosome domains).
  The dose-mean lineal energy $\overline{y}_D$ is then calculated as:

$$\overline{y}_D = \frac{\int_0^\infty y \cdot d(y) \cdot dy}{\int_0^\infty d(y) \cdot dy} \tag{2.15}$$

  where the integral is replaced by a sum over binned $d(y)$ distributions. The distribution $d(y_n)$ for the whole field, not distinguished in its components, can also be calculated;

- for all particle species, the dose to the sensitive site can be computed as the integral of the dose distribution of the lineal energy $d(y_s)$ over the explored lineal energy range. The relative contribution is obtained further normalizing such integral to the corresponding one for $d(y_n)$;

- the saturation-corrected dose-mean lineal energy is defined as:

$$y^* = \frac{y_0^2 \cdot \int_0^\infty [1 - exp[-(y/y_0)^2]] \cdot f(y) dy}{\int_0^\infty f(y) dy} \tag{2.16}$$

  where the saturation parameter y_0 can be fixed to a value equal or higher than 100 keV/μm, thus reducing the weight of higher y component in the field.

To test the validity of the coupling scheme, we compared microdosimetric dose mean lineal energies to macroscopic dose average LET calculated with PHITS for the same scoring region: for this setup and given the irradiation conditions, the averaging in dose and over a macroscopic region of the microdosimetric quantity lead to a numerical agreement between these two quantities (see also the discussion in 2.2.5).
PHITS results were always obtained with a statistics of at least 10^7 neutrons per run (10^4 neutrons per batch per 10^3 batches), and were averaged over up to 5 runs when energy deposits are low (for $E_n \leq 0.1$ MeV), to decrease statistical fluctuations. The errors were obtained as standard deviations among results for different runs.
Simulations for photons, necessary for the evaluation of the RBE, were run with the same geometrical setup and the most external scoring region only. The spectrum of X-rays generated by a Xstrahl-200 machine was used (220 kV field, 2 mm Cu filter) [95].

Coupling neutron transport to track-structure calculations

DSB clusters were chosen as the endpoint to evaluate the energy-dependent neutron RBE. Yields of DNA fragments (length $\leq$ 30 bps), due to complex DNA lesions, were also considered. We used the results on DNA damage yields given as a function of LET (operational definitions given by Eq.2.4 and Eq.2.5 (Par.2.1.6), for a dose delivery of 1 Gy (cell^{-1}).
The curves for DNA fragments or DSB clusters *vs* LET previously shown (Fig.2.5(a) and Fig.2.3(d)) were fitted with analytical functions, as later detailed, to be able to associate a single value for both endpoint to an input LET value.
In particular, values of $\overline{y}_D$ calculated with PHITS were given as input to the analytical functions, to obtain the yield of damage generated by secondary particles of that specific linear energy. The relative dose, always calculated with PHITS, was instead used to normalize the damage yield to the contribution of each species in the neutron field. All damage contributions were finally summed up, thus obtaining the yield of neutron-induced damage.
The X-ray spectrum from the Xstrahl-200 machine was implemented in PARTRAC, to get the yields of DSB clusters and DNA fragments for the estimation of the RBE.
Errors on the yields of short DNA fragments were calculated assuming a Poisson counting for the overall statistics. Errors on DSB cluster yields per run were obtained as standard deviations among results for different runs. The standard deviations among doses to the nucleus in different runs were also calculated, and error propagation was used to account for variations in the damage yield per Gy.

2.3.5 Results and discussion

An indicator of biological effectiveness for a mixed particle field. Fig.2.7(a) shows the neutron $\overline{y}_{D,n}$ as a function of neutron initial energy in the three scoring regions in the soft tissue phantom. For the most external region, the neutron energy is approximately the same as the initial one from the source, while to reach the inner sphere, particles have to travel deep into the target and they loose energy. The energy spectrum seen in this scoring regions is therefore "shifted" towards lower energies, implying different cross-sections for nuclear reactions.
In the most external region, the correspondent curve shows two peaks for neutrons of about 1 and 20 MeV.
For the two deeper regions, the low energy neutrons are easily moderated, causing a decrease in the onset of secondary charged particles in the target, which is instead hit by the photon component, resulting in a lower lineal energy of the mixed field.

In the higher neutron energy range, $\overline{y}_{D,n}$ reaches values higher than 100 keV/μm, that can be reached only by ions with Z $\geq$ 2, which means that slow

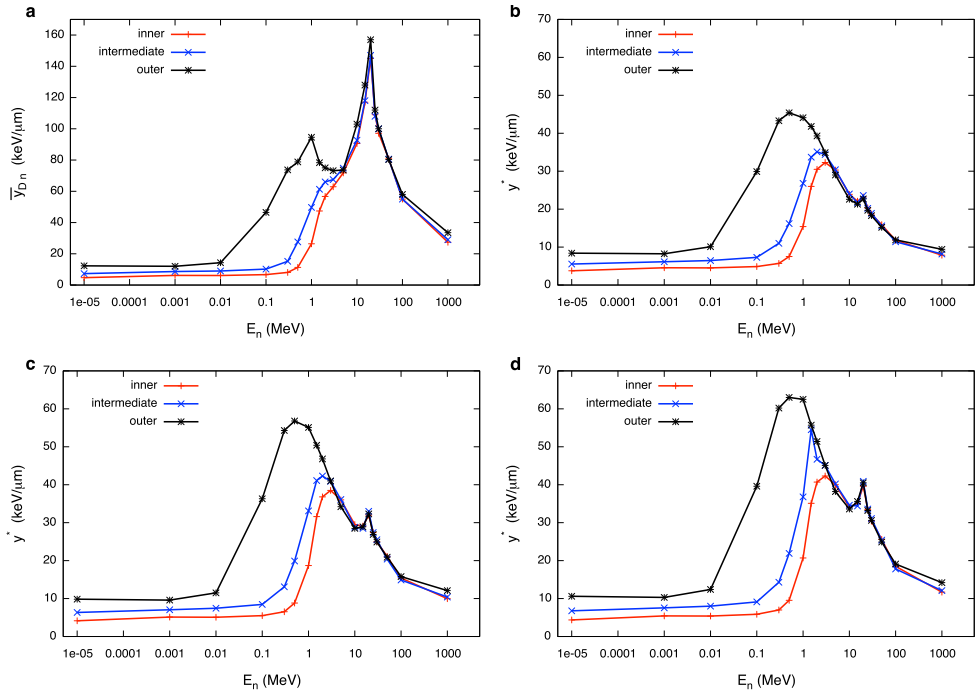

Figure 2.7: Variation with neutron energy and location in the phantom of neutron dose-mean lineal energy (a) and saturation-corrected dose-mean lineal energy (b-d). The latter has been calculated for saturation parameters of y_0 = 100 (b), 150 (c) and 200 keV/μm (d). Error bars are standard deviations among different PHITS runs. Lines are drawn to guide the eye.

recoiling nuclei or nuclei produced in nuclear reactions weigh a lot in the estimation of the overall dose-mean lineal energy.
It is worth noticing that, at such high linear energy transfer, the biological effectiveness measured in terms of survival-related endpoints is lower, since a lowest fraction of cells survives when hit by high-LET radiation (overkill effect) due to the large energy depositions, and averaging across the whole cell population may be misleading.
This can be taken into account, at least phenomenologically, introducing the saturation-corrected dose-mean lineal energy y^* (Eq.2.16). Results for y^* as a function of neutron energy and position in the phantom are given in Fig.2.7(b-d), for different values of the saturation parameter: y_0 = 100, 150 and 200 keV/μm.
The lower the saturation parameter, the lower weight of the high y component of the distributions, hence the lower the increase of the peak for neutron energies around 20 MeV.
The position of the peak of maximal effectiveness is found at 1 MeV when initial neutron energy corresponds to the actual one in the scoring region (outer), while it is shifted to higher energies for deeper-seated targets.

Secondary particle contributions to the neutron dose. We now go back to the characterization of secondary species. We first recall that the photon component of the neutron dose is scored as energy depositions of the tertiary electrons accelerated by the neutron-induced secondary photons.
Heavier species with atomic number $Z \geq 8$ are not included, because they appear as recoils only for the highest neutron energies; still such species contribute up to few per cent to the total dose (e.g. $\approx 3.5\%$ for neutron energy of 100 MeV).
Fig.2.8 shows the relative dose deposited in the three targets for the secondary species under investigation, always as a function of neutron energy. It can be observed that there is a large variation in relative dose contributions by different species as the depth increases. The largest percentage of deposited

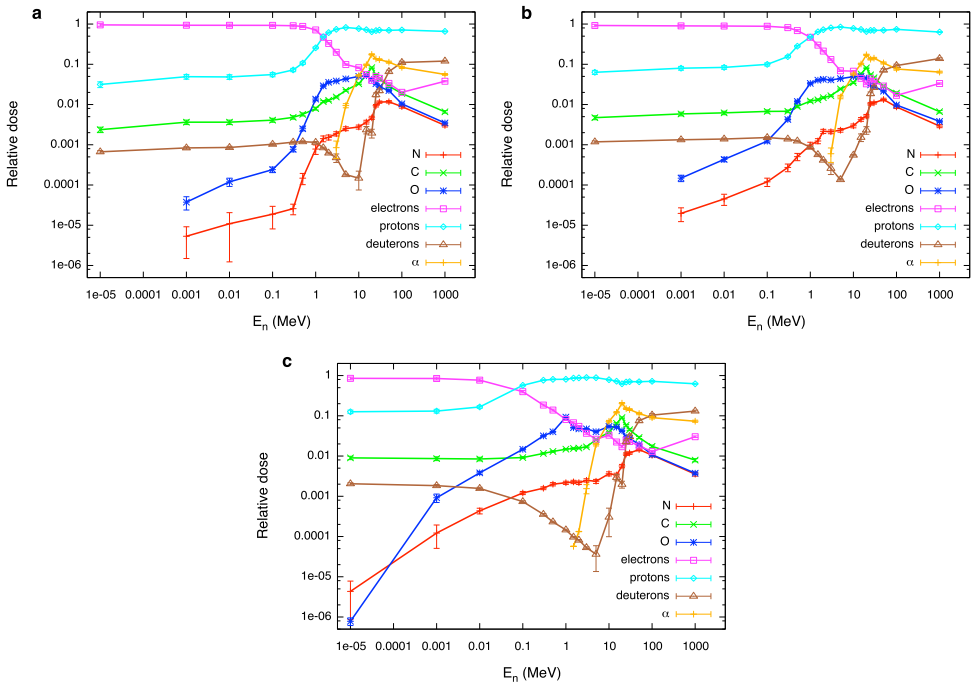

Figure 2.8: Variation with neutron energy and location in the phantom of the relative contribution of secondary species to the total neutron dose: (a) *inner*; (b) *intermediate*; (c) *outer* scoring region. Error bars are standard deviations among results for batches in a single run as given by PHITS. Lines are drawn to guide the eye.

dose is either due to electrons or secondary protons. The electron component stems from the 2.2 MeV photons that arise from neutron capture processes on hydrogen - p(n,γ)d - where also the recoiling deuteron deposits energy to the target. Neutron capture cross-section related to this reaction decreases

with increasing neutron energy, as it is clear from the drop of the electron contribution. Of course, the drop happens at a neutron energy that depends on the depth, and it is lower for the most external scoring region (Fig.2.8(c)), when less neutrons are moderated down to energies where the capture process is dominant.
The dose contribution due to recoiling deuterons is instead less significant (of several orders of magnitude), and it falls down in the same way as the electron component. After the drop, new reaction channels open with increasing neutron energy, either photons (electron dose) or deuterons can be newly produced, and the corresponding dose contributions may rise again.
Always at low neutron energies, when the electron component is the major contribution, a small proton contribution derives from the ^{14}N(n,p)^{14}C capture processes, with the products sharing the gain in energy of 626 keV.
At neutron energies below 10-5 MeV down to thermal neutrons, no significant differences are expected, as the no-threshold neutron capture reactions on target H and N nuclei are largely dominant.
For higher neutron energies, protons represent largely the dominating component to the neutron dose, because they can acquire the maximal energy in a single collision with a neutron, following the formula:

$$E_{max} = \frac{4 \cdot m_t \cdot m_n \cdot E_n}{(m_n + m_t)^2} \tag{2.17}$$

where E_n stands for the incoming neutron energy and m_n and m_t are respectively the neutron and the target nucleus mass.
The other heavy elements also contribute to the total neutron dose, and their weight becomes higher as neutron energy increases. Additional factors to take into account are: the relative elemental abundance in the tissue, that influences the probability of being target for neutron interactions; nuclear reactions occur, at energies higher than specific neutron thresholds, *e.g.* $\approx$ 10, 1 and 5 MeV for collisions with C, N, O targets, leading to the production of fragments with charge different than the reaction target (*e.g.* α particles). As can be seen from Fig.2.8, α particles appear for higher neutron energies, depending specifically on possible thresholds for (n, α) reactions on different targets.
When the deeper scoring regions are considered (Fig.2.8(a-b)), the energy dependence of the induced reaction is masked, as neutrons reaching the inner spheres might have lost part of their energy during their path in matter. This is particularly true for neutron energies at which the neutron mean free path is shorter than the path neutrons have to travel to reach the scoring volume.

Energy depositions of secondary species. In Fig.2.9, the dose-mean lineal energies for particles in the secondary mixed field are shown for the three target spheres. For comparison with the values of the neutron dose-mean lineal energy $\overline{y}_{D,n}$ in the same regions we recall the plot shown in Fig.2.7(a).
When $E_n \leq 1$ MeV, secondary protons are characterized by a high and almost

constant value of $\overline{y}_D$. Thereafter, a decrease can be observed for $E_n \geq 1$ MeV. As seen before, for low neutron energies however, the proton dose contribution is low, hence such a high value of the proton lineal energy does not lead to a high neutron $\overline{y}_{D,n}$.

When the proton dose contribution increases, the $\overline{y}_{D,n}$ increases as well, be-

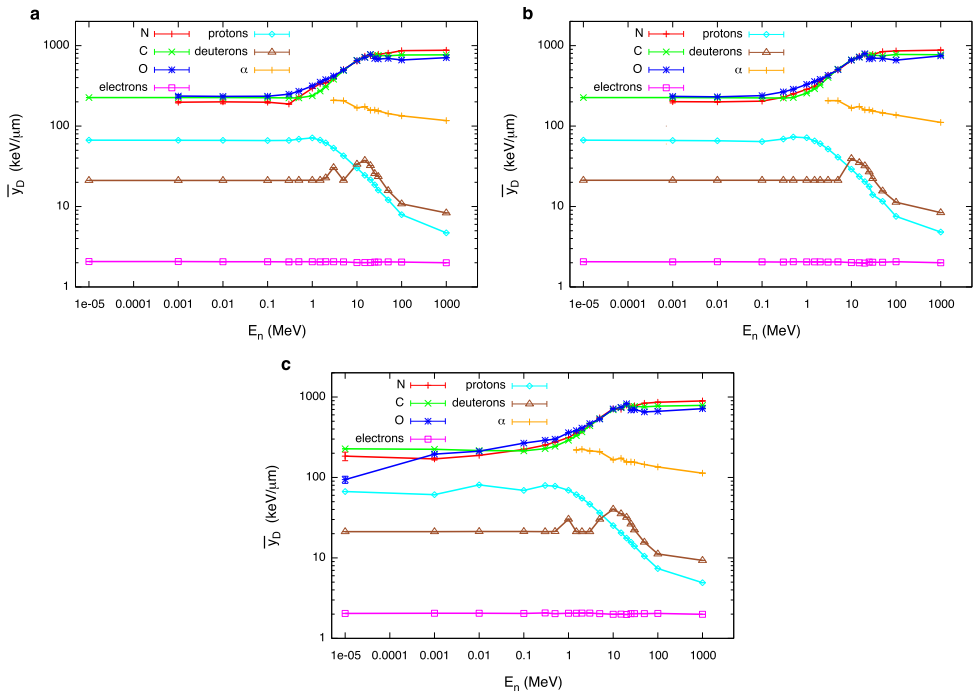

Figure 2.9: Variation with neutron energy and location in the phantom of the dose-mean lineal energy of secondary species: (a) *inner*; (b) *intermediate*; (c) *outer* scoring region. Error bars are standard deviations among different PHITS runs and are in most cases within the symbols. Lines are drawn to guide the eye.

fore the decrease in proton lineal energy itself determines a new decrease of the $\overline{y}_{D,n}$. This is the origin of the first peak of the overall neutron $\overline{y}_{D,n}$ reported in Fig.2.7(a) as a function of neutron energy. The second peak observable in the dose-mean lineal energy can be attributed to the increase of $\overline{y}_D$ for the heavy ions (C, N, O), together with their higher dose weight in the neutron dose, for $E_n \geq 1$ MeV.

Electrons display a constant and rather low dose-mean lineal energy, like the deuterons produced as recoil products from neutron capture reactions on H nuclei (for low neutron energies). However, when deuterons are produced via other reactions (given the much wider energy range in which they can be accelerated and eventually stopped in the target), higher values of the lineal energy can be reached. α particles have a decreasing $\overline{y}_D$, because of their higher initial energy and, consequently, lower stopping power, when produced by neutrons

with higher energies.

DNA damage as a function of LET. Results concerning DNA fragments and DSB cluster are shown in Fig.2.10(a-b), where the data points from Figg.2.5(a) and 2.3(d) are reported.
Starting from DNA fragments, it was previously commented that the curves connecting simulation points show hooks, and for this reason it is impossible to obtain, at least for heavier ions (C, N,O), an unambiguous fragment yield for a given LET value, preventing the coupling to neutron transport based on a linear energy transfer indicator. However, the curves have been fitted with analytic functions approximating the yield of fragments as a function of LET, by means of an exponential function:

$$Y(\text{DNA fragments}) = a_p \cdot LET^{n_p}, \tag{2.18}$$

where a_p and n_p are particle-dependent parameters. Best fit curves are shown in Fig.2.10(a).
In Fig.2.10(b), the yield of DSB clusters as a function of LET is shown, where

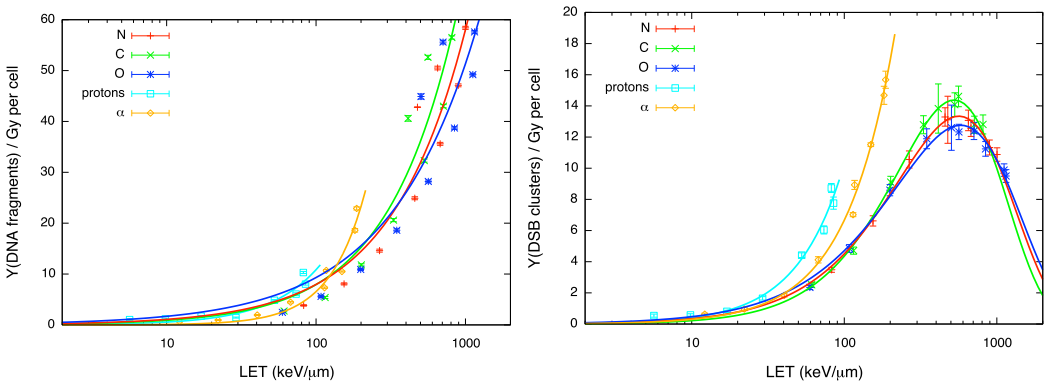

(a) (b)

Figure 2.10: Analytical fit of: induced DNA fragments ($\leq$ 30 bps) with Eq.2.18 (a) and DSB clusters with Eq.2.19 (b) (Gy^{-1} $cell^{-1}$). Error bars are given according to a Poisson counting of the fragment yield for the whole statistics, taking into account propagation with the standard deviation of the dose to the nucleus among different PARTRAC runs.

results were fitted with the analytical function:

$$Y(\text{DSB clusters}) = A_p \cdot LET^{N_p} \cdot exp(-B_p \cdot LET), \tag{2.19}$$

with N_p, A_p and B_p fit parameters that vary according to the particle species. While for protons and α particles the simple power-law function is still suited

for the fit of the DSB clusters yields, a factor is introduced for heavy ions to take into account damage clustering, which dampens the increasing trend and leads to a maximum in the curve.

Coupling transport and track-structure calculations. At this point, the dose-mean lineal energy $\overline{y}_{D,s}$ of a given secondary species s is associated to a damage induced by the same s particles (Gy^{-1} $cell^{-1}$), using Eq.2.18 or Eq.2.19. Then it is weighted with the relative dose contribution, obtaining the s-induced damage per unit neutron dose per cell, for all secondary species.
Deuteron-induced damage as a function of LET is considered similar to the one for protons, and damage from electrons (with almost constant LET) is also calculated with the proton curve (at highest proton energy).
Errors on final damage yields were obtained taking into account errors on relative dose contributions of secondary species as calculated by PHITS.
The overall neutron-induced DNA damage per Gy per cell is calculated summing up all the contributions from secondary species. Fig.2.11 shows neutron-induced DNA fragment production and DSB cluster induction as a function of E_n, for the three different scoring regions.

Unlike predictions for DSB clusters, predictions on neutron-induced DNA

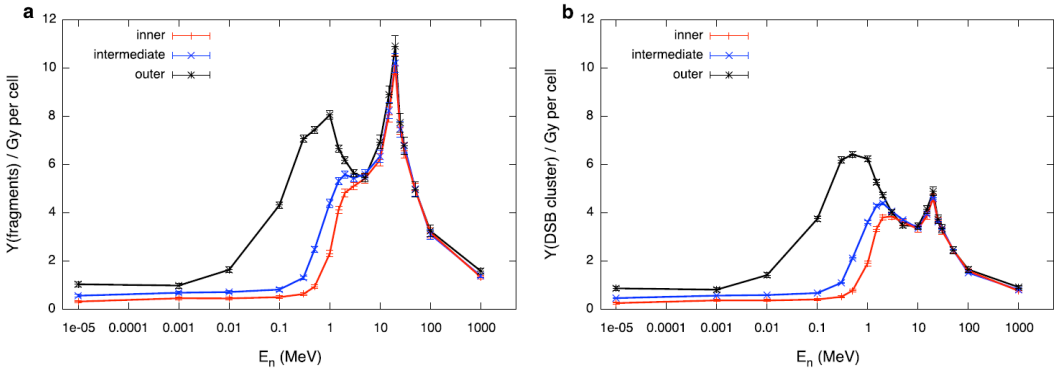

Figure 2.11: Neutron-induced DNA damage (Gy^{-1} $cell^{-1}$) as a function of neutron initial energy in the three scoring regions in the phantom: (a) DNA fragments shorter than 30 bp; (b) DSB clusters. Error bars come from standard deviations among results on doses of secondary species for batches in a single run as given by PHITS. Lines are drawn to guide the eye.

fragment yields are necessarily affected by the fact that Eq.2.18 does not reproduce simulated data of charged-particle-induced fragments *vs* LET.
For this reason, the RBE is later calculated only using clustered damages.
For both plots, the maximal effectiveness is found for neutron energies of about 1 and 20 MeV, mainly due to slow secondary protons [99] and heavy nuclei, respectively.
The overall shape (peaks, heights) of neutron effectiveness depends on the type

of damage under consideration, as it is clear observing the height of the second peak for the two endpoints, which is greatly reduced when spatial clustering of damage is taken into account.
The dependence on where the secondary field is evaluated also emerges from the comparison of data for the three scoring regions. For the outer volume (low neutron moderation) the corresponding damage can be associated to a local evaluation of neutron energy throughout the exposed target.

Evaluations of neutron RBE from y* and DSB cluster induction. For the evaluation of the RBE, photon effectiveness has to be evaluated: for this radiation, $\overline{y}_{D,X}$ does not show a strong dependence on the scoring region, and the average value on the three spheres is of 3.42. The average value of the saturation-corrected dose-mean lineal y* is found to be equal to 3.42 as well. As expected, for low-LET radiations, the correction for the saturation does not influence the results. When the same X-ray radiation source is implemented in PARTRAC, the yield of DSB clusters is found to be approximately 0.38 per cell per Gy.
Neutron RBE values are presented, as calculated for the most external scoring

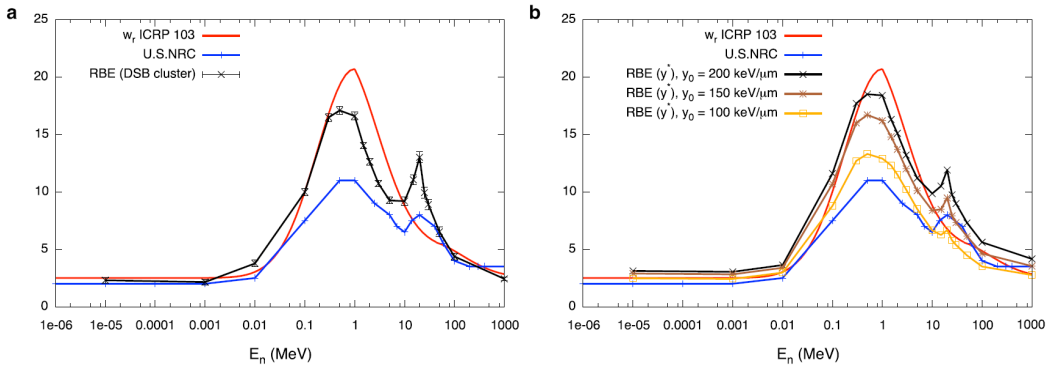

Figure 2.12: Neutron RBE as a function of energy evaluated from: (a) ratio of saturation-corrected dose-mean lineal energies with $y_0 = 100$ (yellow squares), 150 (brown asterisks) and 200 keV/μm (black crosses); (b) DSB cluster induction (black crosses). Lines are drawn to guide the eye. Results are given for the more external scoring region of the phantom. ICRP (red) and U.S. NRC (blue) standards for weighting factors are also plotted. Error bars on RBE in (a) come from standard deviations among different PHITS runs for neutron and X-ray y* values. Error bars on RBE in (b) come from errors on the DSB cluster yields for neutrons and X-rays.

region in the phantom, where neutron energy is closer to nominal energy for an external irradiation. Under the assumption of the linearity of the chosen DNA damage endpoint with dose, neutron RBE can be extracted from the evolution of the measured endpoint as a function of neutron energy, divided

by a measure of the endpoint following exposure to the photon reference field. This is assumed to be true for the DSB cluster endpoint, since the probability of two particle tracks cooperating in inducing damage on such a short genomic length is very low, and the final yield of DSB clusters ultimately depends on the number of tracks traversing the cell nucleus, which is in turn linearly correlated to the dose.
Neutron RBE for DSB cluster induction can therefore be obtained as the ratio of the yield of clusters following neutron irradiation to the photon-induced clusters. This is shown in Fig.2.12(a). Results have been compared with two popular standards for neutron w_R, the ones from the ICRP and the US-NRC: despite the resulting curve is very close in shape and values to the ICRP standard for w_R, especially in the initial region up to the first maximum, it displays a second peak as it is reflected only in the US-NRC standard. To test the goodness of these results with a further approach, the phenomenological estimation of the RBE, using the saturation-corrected dose-mean lineal energy y^*, is also proposed. The saturation-corrected dose-mean lineal energy introduced with Eq.2.16 allows us to neglect explicit consideration of the neutron-induced charged particle field. If we assume a correlation between such indicator for neutrons relative to photons and the corresponding enhancement in biological effect, for all neutron energies the RBE is simply given by the ratio of neutron y^* to the corresponding one for photon irradiation of the phantom. Fig.2.12(b) shows indeed the neutron RBE values obtained from saturation-corrected dose-mean lineal energies. The Figure shows a substantial agreement between the mechanistic RBE model using clustered DNA damage induction as an endpoint and the model based on y^*, offering an independent validation of the fully mechanistic model.

Chapter 3

DNA damage: experimental detection and modelling

3.1 Radiation-induced γ-H2AX foci

3.1.1 DNA repair and γ-H2AX

The nucleosome represents the first level of chromatin organization, and it is composed by *core* histones (H2A, H2B, H3 and H4, in copies to form an octamer), around which $DNA \sim 145$ - 150 bps are tightly wrapped. The *linker* histone H1, binds to "linker DNA" between nucleosomes to condensate the structure into the chromatin fibre.
Histone proteins regulate, structurally and functionally, the transition between active and inactive chromatin states [100]. Chemical post-transcriptional modifications to nucleosome's histones such as phosphorylation, methylation or acetylation are frequently involved during processes such as replication, transcription, recombination and DNA damage repair [101, 102]. These modifications "mark" the histone tails for subsequent functional changes to DNA, triggering the action of specific factors in the chromatin stretch involved by the modification.
In case of DNA repair, the DNA damage response (DDR) system orchestrates the re-localization of proteins to distinct sub-nuclear structures, which can be achieved thanks to the flexible and dynamical nature of the chromatin: this is appropriately modified to facilitate the access and the anchoring to the site [103].
This leads to the formation of the so-called DNA damage foci, whose analysis is fundamental to shed light on the molecular mechanisms underlying the repair.
Exposure of DNA to exogenous agents as IR, for instance, elicits heavy stress on the cellular system, which has to counteract multiple severe DNA lesions. DSBs, in particular, are quite disruptive lesions [104], whose mis-repair is likely

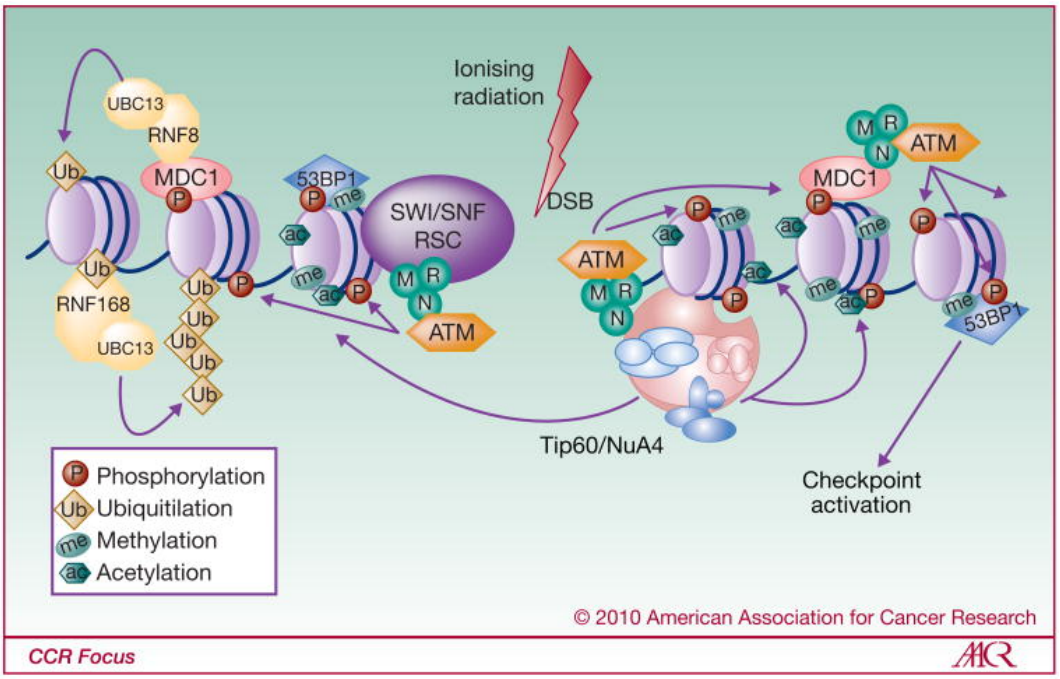

Figure 3.1: Recognition and signalling of a DSB. γ-H2AX plays a key role in DNA-damage signalling, acting as a platform of assembly for the repair factors as well as for checkpoint proteins [101].

to lead either to modifications in the genetic make-up or to cell death [105]. DSBs are promptly sensed by the cell, activating downstream pathways to cope with the damage: the Homologous Recombination (HR) and the Non-Homologous End Joining (NHEJ) repair pathways are the most important [106]. HR repair relies on the presence of homologous but unbroken DNA, which serves as a template to flawlessly copy the original sequence of bases. For this reason, HR often occurs just during and after DNA replication, when the two daughter DNA molecules lie close together. This repair is error-free, but it is a slow process.
On the other hand, NHEJ can be activated throughout any phase of the cell cycle, but it favours the depletion of the damaged site with respect to the conservation of the whole genetic material: the DNA strands hit by radiation are processed and the ends are directly ligated by DNA ligases, usually leaving a mutation at the site at which the DSB is repaired [107].
Sensing and processing DSBs is initiated by the phosphorylation of the H2AX histone, whose pathway has been discovered by E.Rogakou in 1998 [108] and has been demonstrated to be one of the early events following the induction of DSB [109, 110, 111].
The phosphorylation of the serine 139 of the histone subunit H2AX is mediated by three different kinds of kinases, belonging to the family of phosphoinositide-3-kinase-related protein kinases (PIKK): the Ataxia - Telangiectasia mutated (ATM) protein (mediated by the MRN complex), the ATM and Rad3-related

(ATR) protein and the DNA-dependant protein kinases (DNA-PKs) [112]. The first and the last act following IR exposure and throughout all the cell cycle, while the ATR responds to stress due to replication or UV radiation, predominantly during the S-phase [101].
The phosphorylation of H2AX has been demonstrated to not affect chromatin structure, but it acts as a platform for the recruitment of repair factors [113] and cohesins (to keep DNA ends in proximity during the repair [114]), facilitating their accumulation at the break site and leading to the formation of ionizing radiation induced foci (IRIF).
The IRIF are thus created by the co-localization of DDR factors, checkpoint proteins (such as MRN, MDC1, BRCA1, 53BP1, UBC13/RNF8, RNF168, *etc...*) and chromatin-remodelling complexes with the γ-H2AX histones (see Fig.3.1) [115, 116, 117]. Indeed, the phosphorylation is not limited to the first-neighbour histones, but it spreads from few base pairs (a ten is involved in a DSB) to $\sim$ 2 Mbps, creating distinct clusters that amplify the signal and efficiently communicate the presence of the DSB.
This has experimental evidence, as it was shown by Reindl *et al.* [118, 119] that many nanoscopic structures corresponding to Rad51 and/or 53BP1 foci colocalize with a single γ-H2AX focus.
It has been demonstrated that prolonged self-reinforced phosphorylation of H2AX is induced by ATM and MDC1 [120], to allow a continuous accumulation of repair factors to the γ-H2AX site (Fig.3.1) [121, 122].
It might therefore happen that different foci overlap, especially in case of high IR doses or high-LET radiations, making the estimation of the number of foci and its interpretation controversial.
After the successful repair of damage, cells have to recover from checkpoints, so phosphatases (*e.g.* Wip1) dephosphorylate H2AX at the Ser139 and allow the cell to re-enter the cell cycle [123].

3.1.2 Modelling the repair kinetics of DNA damage foci

Some biochemical kinetics models were developed to mechanistically describe and predict DSB repair. These fill the gap left by phenomenological models, because they are able to consider the molecular interactions involved in the pathways individually.
Cucinotta *et al.*, for example, developed a set of non-linear differential equations to model molecular events associated to the NHEJ pathway starting from the recruitment and phosphorylation of DNA repair complex intermediates, and the kinetics of γ-H2AX foci induction/removal, depending on the complexity of the initial damage [124].
The IRIF repair kinetics is often investigated, since it gives an insight on the complexity of the damage and the sensitivity of exposed cells; analytical models have been developed to describe the dynamics as a function for different radiation qualities. The model from Michaelis-Menten (1913) generally describes enzymatic reactions, where a substrate with concentration $[S]$ binds to

an enzyme (of concentration $[E]$), giving rise to the enzyme-substrate complex [ES]. The latter transforms in the product P, releasing the enzyme, which is then available for new enzymatic reactions with S:

$$E + S \underset{k_{-1}}{\overset{k_1}{\rightleftharpoons}} ES \overset{k_2}{\rightarrow} E + P$$

where k_1, k_{-1} are the forward and reverse rate constants, respectively, while catalytic rate constant is labelled as k_2.
This is exactly the case of kinases attaching to the H2AX histone to create its phosphorylated form.
According to the model, the enzymatic reaction rate ν, defined as the formation rate of product P, is proportional to the concentration of the substrate $[S]$ as in the following kinetic equation:

$$\nu = \frac{k_2 \cdot [E] \cdot [S]}{K_M + [S]} = \frac{\nu_{max} \cdot [S]}{K_M + [S]}, \tag{3.1}$$

where ν_{max} is the maximum reaction rate, K_M is the concentration of the substrate at which the reaction rate is $\frac{\nu_{max}}{2}$. A steady state solution can therefore be modelled as a function of time with a saturating curve:

$$f(t) = A \cdot \frac{t}{B + t}, \tag{3.2}$$

where A and B are constants.
For what concern the dephosphorylation of γ-H2AX, the rate at which the complex decays depends on the damage complexity: following exposure to IR it is likely to have a mixture of both simple and complex lesions, thus it is reasonable to hypothesize that the repair kinetics will be driven by two different decay rates, proportional to the efforts to cope with the damage. Hence, the former damage will be easily rejoined, and foci will be quickly disassembled, while clustered lesions from high-LET particles need more time to be repaired. The temporal dynamics of foci removal can be described as a sum of two distinct exponential components:

$$g(t) = C \cdot e^{-D \cdot t} + (1 - C) \cdot e^{-E \cdot t} \tag{3.3}$$

where C is the fraction of simple damages, (1-C) is the fraction of cluster lesions, D is the decay rate for the simple damages and it is higher than E, the repair rate for the complex ones. The total dynamics of foci formation and repair can therefore be described by functions like $N(t) = f(t) \cdot g(t)$.
Mariotti *et al.* proposed a very similar formula to fit experimental data obtained by acute irradiations with X-rays and α particles, substituting $f(t)$ with the following function:

$$f(t) = A \cdot (1 - e^{-B \cdot t}) \tag{3.4}$$

where A is a normalization factor and B drives the dynamics of the IRIF induction.
The resulting function $N(t)$ is therefore given by:

$$A \cdot (1 - e^{-B \cdot t}) \cdot [C \cdot e^{-D \cdot t} + (1 - C) \cdot e^{-E \cdot t}] \tag{3.5}$$

and the function was also adapted to fit foci yields also after fractionated exposure to the same particles, by simply adding the same expression in which the time is substituted by the term $(t - \Delta t)$ [125].
In general, for the γ-H2AX foci the maximum of the curve is usually found 30 min post- (single dose) irradiation, while the tail of the repair kinetics at late time-points is dependent on physical factors as the dose and radiation quality, but also on the cell line considered. Fig.3.2(a) shows the results of

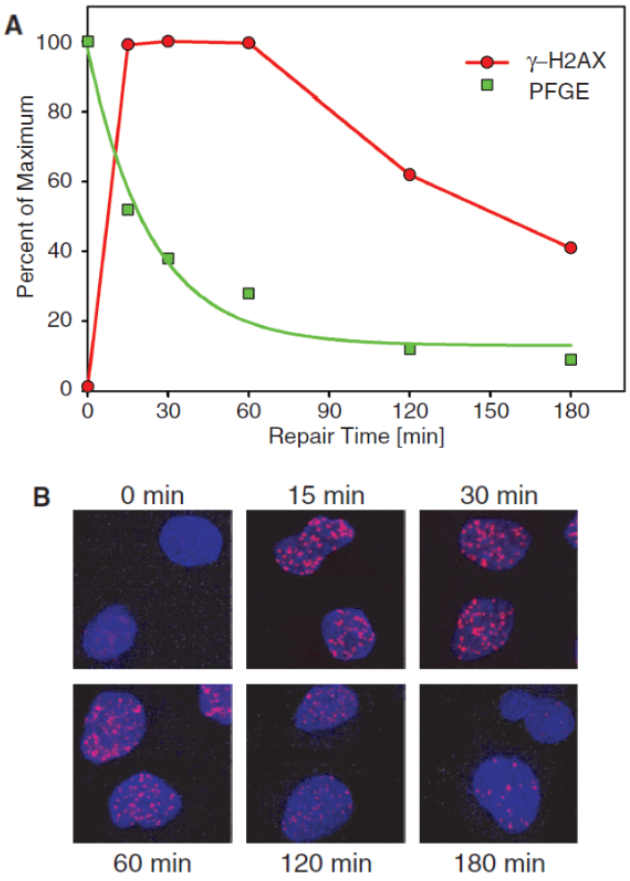

Figure 3.2: Comparison of DSB repair kinetics as measured by PFGE and γ-H2AX foci assay. Plateau-phase A549 cells were exposed to 20 Gy or 1 Gy X-rays and analysed by PFGE or immunofluorescence, respectively. (a) PFGE results (squares) are normalized to the signal measured at 0 h, while the γ-H2AX results (circles) to the maximum number of scored foci. (b) Examples of γ-H2AX immunofluorescence at different times after exposure to IR (1 Gy). Adapted from [109].

a study by Kinner et al. [109], where the yield of DNA fragments measured

through Pulsed Field Gel Electrophoresis (PFGE) is compared to the yield of foci measured by means of ICC: while for PFGE the maximum of the curve is found immediately after irradiation, corresponding to the maximum number of damages, the γ-H2AX assay follows the formation and disappearance of the foci and the delayed kinetics can be explained by the time required to initiate/sustain the biochemical events leading to development of a mature focus.

3.1.3 Detection techniques

The example just shown underlies the intrinsic difficulty of relating DSBs to γ-H2AX foci and the dependence of yield estimation on the chosen detection method. Moreover, quantification of γ-H2AX foci requires to probe hundreds of cells, in order to obtain statistical robustness, making the process costly and time consuming. Flow cytometry represented a turning-point technique, allowing high-throughput analysis of thousands of cells in few seconds. This averages the inter-cellular differences in the IRIF number that are present in the cell population, either due to biological reasons (*e.g.* different cell cycle phases) or inhomogeneous cell irradiation [126]. Flow cytometry only measures the overall average foci fluorescence intensity [127], making the technique blind to the discrete description of the events (yields of foci per cell, spatial distribution and morphological characteristics), necessary to trace out radiation quality and the efficacy of repair pathways.
Visualization of DNA damage foci (and subsequently of the particle track) is known to benefit the quantification of complex lesions [128]; fluorescence microscopy exploits immunoglobulins that bind to specific antigens, and in this way γ-H2AX foci can be selectively tagged and made "visible" by using fluorophores. This represents a semi-quantitative measure of DNA damage even at doses as low as several centigrays [129]. However, this detection strategy relies on visual counting, that comes with limitations about subjectivity and the time costs. Still, it was often adopted because of its reliability to recognize foci regardless of fluorescence intensity levels and variations in both the background and foci, thanks to the analytical abilities of the operator, which offset most of microscopy artefacts.
Automation of the counting process by means of macros written with image analysis software packages eases some of these limitations, allowing the standardization of the analysis for larger samples, and the evaluation of foci properties that can be hardly extracted by manual counting [130, 131, 132].
Only recently, machines integrating flow cytometry (speed and sample size) and microscopy (resolution and sensitivity) have been developed, providing the opportunity to collect both qualitative and quantitative image data of single cells [133].

3.1.4 Objective

In Par.2.3 the neutron RBE was modelled starting from the induction of clusters of DNA damages. Experimental evaluation of the RBE, however, requires measurements of a detectable endpoint.
These reasons fostered the choice to extend the study to the simulation of radiation-induced γ-H2AX foci. On a spatial scale, we move from an ideally point-like event (the DSB) to a spatially defined object, whose extension is exploited to physically detect it and make it visible at the microscopic level.
To investigate the role of radiation quality in the induction of γ-H2AX foci, different neutral and charged particles have been chosen to perform the experiments. Cell cultures of human foetal lung fibroblasts and mouse mammary adenocarcinoma cells have been exposed to neutrons, but other particles have also been considered in the study, namely photons (250 kVp X-rays) and ^{12}C ions (as discussed in Par.3.3). The criterion for the choice of X-rays and C-ions is also the knowledge of their effectiveness for therapeutic purposes, towards optimal dose prescriptions to tumour cells.
As for neutron exposure, its consequences on patients' health were previously described. At the RARAF facility [134], studies at the interface between physics and biology are carried out using a neutron field that mimics the one from the Hiroshima nuclear device, with energies ranging from around 100 keV to 10 MeV. This study may unveil the severity of damage induced by this neutron spectrum, considered to be a reference in radiation biology and epidemiology.

In this digression from MC simulations, the measurements carried out both during a six-month project at the RARAF facility and at the "RadBioPhys" Lab (Physics Department, University of Pavia) will be discussed. Results will provide a radiobiological characterization of the cell lines, in terms of clonogenic survival and of induction/repair of γ-H2AX IRIF. Immunocytochemistry assay has been chosen for the visual detection of foci, and images of samples are acquired with conventional (*i.e.* wide-field) fluorescence microscopy. Parameters on foci morphology (intensity and size) have been extracted as indicators of the damage complexity and/or clustering in space, characteristics that are intimately related to the radiation qualities.

3.1.5 Material and methods

Cell cultures and reagents

IMR90 normal human foetal lung fibroblasts (ATCC) and BALB/c mouse – derived poorly immunogenic mammary carcinoma TS/A cell [135, 136] (kindly provided by Dr. E. B. Golden) were grown at 37°C in a humidified atmosphere with 5% CO_2. TS/A cells have a doubling time (DT) of $\approx$ 24 h, while IMR90 cells show a DT of 36 h.

IMR90 cells were cultured in Eagle's Minimal Essential Medium (EMEM, Corning), supplemented with 12.5% Foetal Bovine Serum (FBS, Sigma-Aldrich), L-glutamine 2mM (Sigma-Aldrich) and 1% Non-Essential Amminoacids (MEM NEAA, Gibco). TS/A cells, instead, were cultured in Dulbecco's Modified Eagle Medium (DMEM, Gibco) with 10% FBS in T75 cm^2 flasks (Falcon); all cell cultures are grown up to the 90% confluence. IMR90 cells between passages 5 and 22 and TS/A cells between passages 1 and 13 were used for experiments. For both cell lines, the day before neutron and X-ray irradiation 10^5 cells in 0.5 ml medium were plated in each well of 4-chamber CultureSlide flasks (Falcon), if ICC had to be performed, while for clonogenic assay 10^5 cells in 1 ml medium were plated in 30-mm Petri dishes (Thermo Fisher Scientific).
Cells cultured for the experiments were not synchronized: differences in foci yields can be expected depending on the cell cycle phase of irradiated cells. However it is known that the irradiation itself causes a redistribution of cells in the cell cycle [137, 138], and a characterization of damage yields for different cell cycle phases is not easily done and goes beyond the purpose of this work.

Irradiation setup

X-ray irradiations. Exposure to low-LET X-ray was carried out using the Westinghouse Coronado X-ray machine (225 kVp, 1 mm Al and 0.5 mm Cu filters in the beamline) available at RARAF, Columbia University (Fig.3.3(a)). The photon beam is emitted perpendicularly to the biological samples. Dosimetry was performed through the Accu-Dose+ (Radcal) ionization chamber, to guarantee a dose-rate of ≈ 1.1 Gy/min; for the purposes of detecting foci by means of immunocytochemistry, doses of 0, 1, 2 and 5 Gy were used, while for survival curves the response at low doses was also studied, and specifically doses of 0, 0.1, 0.25, 0.5, 1, 1.35, 2 and 5 Gy were selected.

Neutron irradiations. Neutron irradiations were carried out using the broad-energy beam available at the RARAF facility, which is produced as described in [139]: a mixture of 5 MeV protons and deuterons from a Singletron accelerator is made to impinge against a 1-mm thick beryllium foil and, through the ^{9}Be(p,n) and ^{9}Be(d,n) nuclear reactions, a neutron field is produced with characteristics similar to those from an improvised nuclear device. In particular, the Hiroshima neutron fluence spectrum at 1.5 km from the hypocentre is reproduced, with energies ranging from 0.1 to almost 10 MeV, with a mean energy of about 2.4 MeV. Measurements verified the agreement between the beam characteristics and the Hiroshima spectrum [140]. As in most neutron irradiations, the total dose to the sample is only in part due to the neutron field (in this case the $\approx 85\%$), and a γ-ray component deriving from other nuclear interactions or nuclei relaxation is always present, imparting the remaining $\sim$ 15% of the dose. The setup used at RARAF for the irradiation is showed in Fig.3.3(b): it consists of a metallic "Ferris" wheel, with multiple rods on which it is possible to hang tubes containing biological samples or small animals.

(a) (b)

Figure 3.3: The Westinghouse Coronado X-ray machine for X-ray irradiations (a) and the rotating metallic wheel installed on the beamline for neutron irradiations (b) of biological samples at RARAF.

The wheel is rotating in the neutron field around the particle beam. The samples are positioned at a forward angle of 60° and at a distance of 10 cm from the incident beam. The rotation assures a homogeneous distribution of the dose inside the samples. For these experiments, we neglect the dose differences along the axial coordinate, being the surface of each well, and in good approximation the area of the whole flask, negligible with respect to the dimensions of the field.
The highest achievable dose-rate of 5 cGy/min was exploited in order to shorten as much as possible the irradiation time. In this perspective, doses of 0, 0.1, 0.5, 1 Gy were selected for ICC. While doses up to 0.5 Gy were delivered in a single shot, 1 Gy of dose was obtained through a fractionated regime, with samples remaining on the beam line during two consequent 0.5 Gy irradiations. As for survival curves, the doses of 0.25 and 1.35 Gy (2×0.5 Gy + 0.25 Gy + 0.1 Gy) were also added. The fractionated regime represents a difference with X-ray irradiations, where doses were delivered in a single shot.
The time between each fraction is nevertheless around 3 minutes, to let the radiation field in the cave cool down and to allow the change of the flasks on the beamline, and it is negligible with respect to the total irradiation time (30-40 min).

Clonogenic assay

The protocol for the clonogenic assay is performed post-irradiation: immediately following the irradiation of the samples, the medium was discarded, cells

were washed with 0.3 ml of PBS (phosphate-buffered saline) and harvested with 0.5% Trypsin-EDTA (Ethylenediaminetetraacetic Acid) (Gibco). Cells were centrifuged for 4 min at 500 g, the supernatant discarded and cells were carefully re-suspended in complete fresh medium, paying attention to break all clumps and have single cell suspensions. A hemocytometer was used to count cells in the suspension.
For each dose, a right dilution was then created to have 1000 cells in 2 ml of medium, which were plated in six-well plates. Technical duplicates were made for each sample. Cells were plated for all doses with the same concentration to avoid sham control for each condition, which was otherwise unavoidable if the different growing rates (due to different densities) were to be taken into account. For IMR90 and TS/A cells, a waiting time of 14 and 7 days, respectively, was necessary in order to have the formation of colonies, intended as clusters of more than 40-50 cells [141].
In case of 14 days of incubation, medium was changed after 1 week, carefully in order to not detach cells that might create satellite colonies. After the incubation time, medium was discarded and cells were washed twice with 0.5 ml PBS. The cells were fixed using 95% ethanol (EtOH) for 10 min at room temperature (RT) and then stained with 2 % (w/v) Crystal Violet in 95% EtOH, for 15 min at RT.
Finally, the stain was removed and the Petri dishes were washed with water until colonies are clearly visible. Colonies, as in groups of more than 40 cells, were scored using a Nikon Eclipse TS100 microscope.

Immunocytochemistry

Cells were fixed at different time-points (15 min, 30 min, 1 h, 2 h, 3 h, 24 h for neutrons/X-rays) post-irradiation with 2% paraformaldehyde (PFA, Electron Microscopic Sciences) in PBS (Gibco) at RT for 20 min. For long exposures (as in case of high neutron doses), time is counted from the moment samples are put in the incubator, in accordance to what done for the other biological samples. Foci were detected by fluorescent staining through the following protocol: permeabilization was performed with 100% methanol for 20 min at -20°C. Cells were washed three times (5 min each) with PBS and they were blocked against non-specific binding in 0.2% bovine serum albumin (BSA, Invitrogen) in PBS at RT, for 15 min. The incubation with 1:500 anti-γ-H2AX rabbit primary antibody (Cell Signaling Technology) in 0.2% BSA/PBS was performed for 1 h, always at RT.
Afterwards, cells were washed as previously described, and incubated with 1:1000 anti-rabbit goat IgG Alexa Fluor 555 conjugated secondary antibody (Invitrogen) in 0.2% BSA/PBS for 45 min, at RT. After washing, samples were finally mounted with VectaShield Mounting Medium containing DAPI (4',6-Diamidino-2-Phenylindole, Vector Laboratories, Inc.), to allow simultaneous nuclei counter-staining.
An IX70 (IX-ILL 100 LH) Olympus fluorescent microscope (magnification of

60X) was used to acquire several fields, to analyse at least 200 - 250 cells per slide, trying to exclude fragmented or pleomorphic cells from the image acquisition. The focus was optimized manually trying to have most cells and foci in the same focal plane (usually the median plane of the nucleus).

Image processing

Each 2D picture was analysed with a macro written with the software ImageJ [142, 143] that was developed from scratch for this kind of analyses (as previously described in Ref.[144]).
The recognition of the regions of interest (ROIs) relies on conventional image processing steps: the images were converted in 16-bit, they underwent histogram-based binarization (conversion in black and white, to distinguish objects from background) by applying "*Otsu*" thresholding [145], which was manually adjusted to select the right regions for the nuclei. The macro then applied a smoothing mask and allowed some discretionary steps, like holes-filling, volume-dilatation or Watershed segmentation (to separate different objects that touch each other), to refine the reconstruction of the nuclei.
Then ROIs for the nuclei were selected by setting some thresholds on morphological parameters as the circularity and the size. For nuclei, 5000 pixel^2 $\leq$ size $\leq$ 10000 pixel^2 and $0 \leq$ circularity ≤ 1); and the ROIs are stored to extract parameters as the intensity, the size, and to determine the foci/cell.
For the selection of foci, the steps were the same, except for the some adjustment to the background, and the application of "*Unsharp Mask*" option, to add a high-pass filtered image and thus to sharpen the image. The recognition of foci ROIs turned out to be tricky, because of a mixture of very small foci, probably generated by the low-LET radiations, with very bright and big foci (that may be assumed as induced by charged particles), making it important to define reasonable thresholds to include all the cases. Moreover, halos from foci not completely at focus were excluded from the analysis by means of threshold processing. The range for focus circularity was left very loose (0-1), while the threshold for the size was of 14 - 750 pixel^2. Optimization of the macro was carried out by the experimenter comparing the results, for different doses of the two radiation qualities, with those obtained by manual scoring of the foci, especially for the adjustment of the thresholds for the foci size, which were kept fixed for all the analyses.
The semi-automatic algorithm allowed to refine some of the parameters image by image, according to visual check with the original picture (*Otsu* thresholding, Watershed segmentation, *Unsharp Mask* parameters...). Nuclei ROIs were stored to allow quantification of the number of foci per cell. Moreover, the average intensity of pixels in each focus was recorded, to have a parameter correlated to the degree of complexity of the damage and/or of the possible overlap of different structures due to their distribution in 3D. The foci size was extracted as well, to be correlated with the intensity and to have a better insight on the morphology of the events.

3.1.6 Results

Survival curves. The number of colonies, normalized to the plating efficiencies and averaged over three independent experiments (each made by a technical duplicate), has been plotted in lin-log scale as a function of the dose for both cell lines under investigation and radiation qualities, as in Fig.3.4. Both cell lines show a higher sensitivity to neutrons with respect to photons,

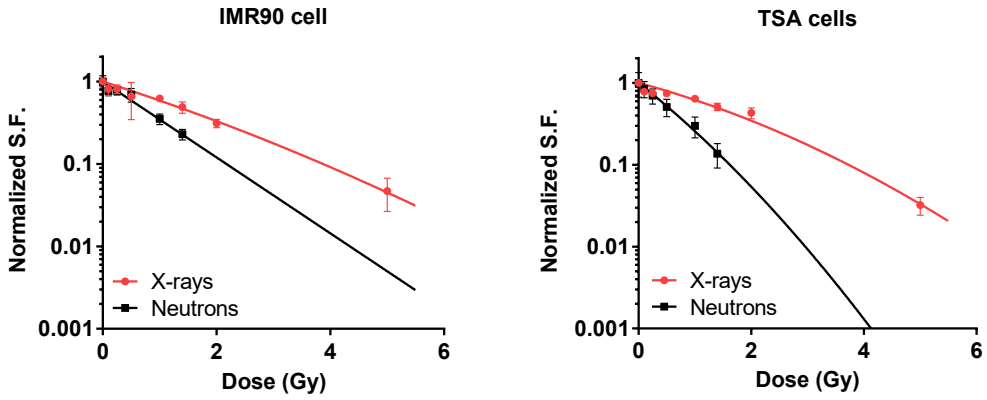

(a) (b)

Figure 3.4: Survival curves for (a) IMR90 and (b) TS/A cells following exposure to X-rays and neutrons. The data points have been fitted with the LQ model. Results are shown as mean of at least 3 independent experiments ± SEM.

despite the dose-rate used for the neutron irradiation was 20 times lower than the one for X-rays.
In Fig.3.4 the fit were obtained by using the Linear-Quadratic (LQ) model, historically used to describe radiation-induced clonogenic cell death, that is the loss of the cellular ability to divide and form clones.
The mathematical formulation of the model as a function of the dose D is given in Eq.3.6:

$$SF(D) = PE \cdot exp(-\alpha \cdot D - \beta \cdot D^2) \tag{3.6}$$

where α is the coefficient for the linear dose term and is the cell kill per Gy, β is the coefficient of quadratic component of the survival curve (on a log-linear plot) and PE is the plating efficiency (the surviving fraction at D = 0 Gy), equal to 1 after normalization. Tab.3.1 shows the parameters extracted from the fit of the curves with their uncertainties, along with the corresponding reduced χ^2_R. However, the available experimental data show that, for some of the curves, there are some discrepancies with the best fit obtained with the LQ model for doses $\leq$ 0.5 Gy, because the survival assumes lower values than the ones at higher doses.
This remark led to the decision to test a second model, the one introduced by Marples and Joiner in 1993, the so-called Induced Repair model, referred

Table 3.1: Values of the α and β parameters, with their uncertainties, as extrapolated from the fit of the experimental data with the LQ model, for both IMR90 and TS/A cells exposed to X-rays and neutrons. Values of the reduced χ^2_R of the fit and the degrees of freedom ν are also reported in Table.

LINEAR-QUADRATIC MODEL												
	IMR90						**TS/A**					
	α	$\Delta\alpha$	β	$\Delta\beta$	χ^2_R	ν	α	$\Delta\alpha$	β	$\Delta\beta$	χ^2_R	ν
X-rays	0.51	0.07	0.02	0.02	2.62	6	0.43	0.05	0.05	0.01	19.57	6
Neutrons	1.06	0.33	0	6.8	2.75	4	1.26	0.52	0.1	0.41	1.03	4

hereinafter as Hypersensitivity (HS) model.
Indeed, a downward "kink" in survival curves of different cell lines was observed following irradiation with X-rays [146, 147, 148] and neutrons [149, 150], usually for doses < 1 Gy.
The mathematical formulations is given by the following formula:

$$SF(D) = exp(-\alpha_r \cdot [1 + (\frac{\alpha_s}{\alpha_r} - 1) \cdot e^{(-\frac{D}{D_c})}] \cdot D - \beta \cdot D^2) \tag{3.7}$$

The parameter α is not unequivocally determined, but it depends on the dose: α_r is the low-dose slope of the survival curve as from the fit with LQ model of the points at high doses; α_s is instead the value of α extrapolated from the hypersensitivity curve at low doses (D $< D_c$). D_c is the dose at which there is either an inflection or a minimum in the curve; β is the coefficient of the quadratic dose component.

The results of these fits are shown in Fig.3.5(a) for the IMR90 cells exposed to neutrons and in Fig.3.5(c) for the TS/A cells exposed to X-rays, while the values of all parameters are reported in Tab.3.2, along with their errors and the reduced χ^2_R. The large uncertainties correlated to the points related to X-rays for IMR90 cells do not allow to draw any conclusions, and the LQ model was applied to this curve. Same stands for the data points related to TS/A cells irradiated with neutrons, where the LQ model already offers a good fit.
Panels labelled as (b) and (d) zoom on the part of the curve for doses up to 1.5 Gy, to better highlight the trend of the experimental points and the agreement with the HS model. An over-agreement of the fit with the data has been found, as shown by the reduced χ^2_R: this is due to the high number of free parameters introduced in the function with respect to the number of data available from the experiments.
The protocol adapted for the experiments on clonogenicty implies the immediate plating of the cells after irradiation. It may be useful to comment on how this influences the repair of the so-called PLD, Potentially Lethal Damage, that is the component of damage that can be modified by manipulating the post-irradiation environmental conditions [151]. It has been found that when

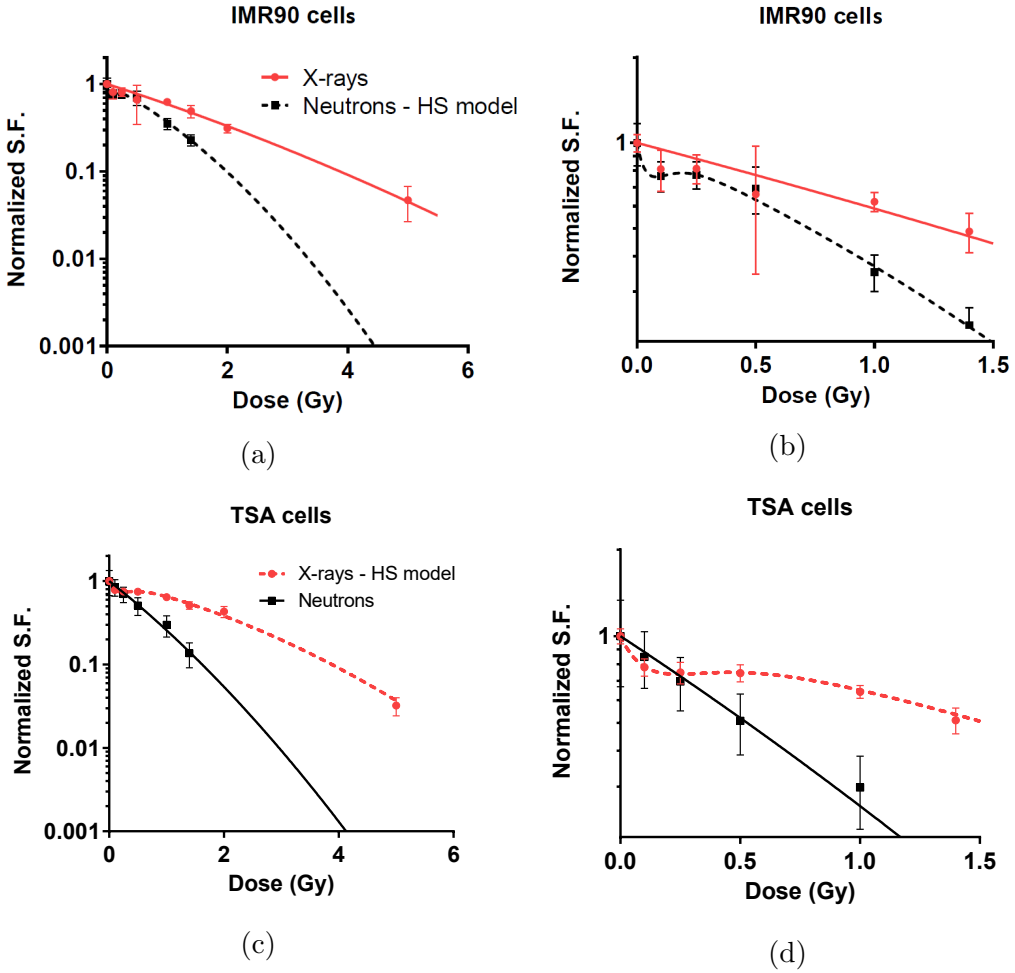

Figure 3.5: Survival curves for IMR90 (a-b) and TS/A cells (c-d) following exposure to X-rays and neutrons. (a) Data for IMR90 cells exposed to X-rays have been fitted with the LQ model, while neutron data have been fitted using the HS model. (c) Data for TS/A cells exposed to X-rays have been fitted with the HS model, while neutron data have been fitted using the LQ model. (b) and (d) are zoom of curves for doses up to 1.5 Gy, for IMR90 and TS/A cells, respectively. Results are shown as mean of at least 3 independent experiments ± SEM.

cells are held in a quiescent state after irradiation, like in the G_0 phase, they are more likely to repair the damage with respect to cells that are free to progress within the cell cycle and proliferate. Following low-LET particle exposure, the survival for quiescent cells has been shown to increase for a relatively wide range of doses [152, 153], while proliferating cells preserve the damage and, presumably, they are more likely to clonogenically die because of additional unrepaired damage [154, 155]. Liu *et al.* (2013) showed that, at same initial yield of DSBs, differences in the survival fraction following X-rays of human fibroblasts between cycling and non-cycling cells could be due to differences

Table 3.2: Values of the α_r, α_s, D_c and β parameters, with their uncertainties, as extrapolated from the fit of the experimental data. Data for IMR90 cells have been fitted with the HS model when irradiated with neutrons, while the model is used for TS/A cells when exposed to X-rays. Values of the reduced χ^2_R of the fits and the degrees of freedom ν are also reported.

HYPERSENSITIVITY MODEL										
	IMR90									
	α_r	$\Delta\alpha_r$	α_s	$\Delta\alpha_s$	D_c	ΔD_c	β	$\Delta\beta$	χ^2_R	ν
Neutrons	0.84	0.41	10.66	24	0.06	0.08	0.16	0.32	0	2
	TS/A									
	α_r	$\Delta\alpha_r$	α_s	$\Delta\alpha_s$	D_c	ΔD_c	β	$\Delta\beta$	χ^2_R	ν
X-rays	0.37	0.6	4.12	1.79	0.17	0.06	0.06	0.015	0.92	4

in the fraction of either mis- or un-rejoined DSBs [156]. Blakely et al. (1985) reported results from experiments with both X-rays and neon ions, showing a significant PLD repair for the former (with survival increased up to 10-fold), and only negligible repair in early and mid G1-phase cells after exposure to the latter radiation [157], demonstrating a dependence on radiation quality [158]. Since cells were harvested and then plated in cell culture flasks immediately after the irradiation at low density, they are stimulated to grow exponentially, potentially increasing the chance of mis-repair of the PLDs. This might hold true for the low-LET X-rays, for which we could expect a higher survival if different post-irradiation conditions were adopted, independently on the chosen fit function. However, as aforementioned, the damage from the more densely ionizing recoil particles from neutrons might be less affected by this phenomenon (LET $\approx$ 45 keV/μm), even if cells are equally free to cycle and grow exponentially.

Tab.3.3 shows the survival fraction at 2 Gy (SF_2) and the doses at 10%, 37% and 60% survival (D_{10}, D_{37}, D_{60}) obtained from the best fit, and used to calculate the RBE. As it can be seen from the table, for the IMR90 cells, the RBE for all the survival levels is ≈ 2, if parameters are extracted from the fit using the LQ model for the neutron data points, but it is slightly higher ($\approx$ 2.5 - 2.8) when the HS model is instead exploited. In both cases the RBE is calculated using the LQ fit for X-ray data. The value of $\frac{\alpha_N}{\alpha_X}$ is calculated using the α values from the LQ models for both neutron and X-ray irradiated cells, and in this case a value of 2.08 has been found.

For TS/A cells, neutron RBE is calculated using the parameters coming from the two different fits of the X-ray data points. Using the LQ model, the neutron RBE ranges from 2.3 to 2.7, for a survival of the 10%, 37% and 60%, respectively. The corresponding values using the parameters extrapolated from the HS model vary from 2.34, quite similar to the previous case, to almost 4 for the 60 % survival.
In this case, the value of $\frac{\alpha_N}{\alpha_X}$ has been found to be of 2.93, always using the α values from the LQ model for both neutron and X-ray irradiated cells.

Table 3.3: For IMR90 and TS/A cells, the values extracted from the fits of surviving fraction at 2 Gy (SF_2), dose at 10% survival (D_{10}), dose at 37% survival (D_{37}), dose at 60% survival (D_{60}) and ratio of the α value for neutrons to the α value of X-rays, and extracted RBE at different survival levels.

Surviving fraction, dose at % survival and RBE values.								
	IMR90							
	SF_2	D_{10}	D_{37}	D_{60}	RBE_{10}	RBE_{37}	RBE_{60}	$\frac{\alpha_N}{\alpha_X}$
X-rays LQ (*)	0.33	3.87	1.81	0.96	\	\	\	\
Neutron LQ	0.06	2.19	0.95	0.49	1.77 (*)	1.91(*)	1.96(*)	2.08(*)
Neutron HS	0.03	1.40	0.70	0.38	2.76(*)	2.59(*)	2.53(*)	
	TSA							
	SF_2	D_{10}	D_{37}	D_{60}	RBE_{10}	RBE_{37}	RBE_{60}	$\frac{\alpha_N}{\alpha_X}$
X-rays LQ (*)	0.35	3.73	1.89	1.06	\	\	\	\
X-rays HS (**)	0.37	3.79	2.01	1.54	\	\	\	\
Neutron LQ	0.05	1.62	0.74	0.39	2.30(*)	2.55(*)	2.72(*)	2.93(*)
					2.34(**)	2.72(**)	3.95(**)	

γ-H2AX foci kinetics. The yields of γ-H2AX foci as a function of time, counted by an *ad hoc* developed macro in ImageJ is shown in Fig.3.6.

The macro to perform extensive image analysis was developed on the basis of

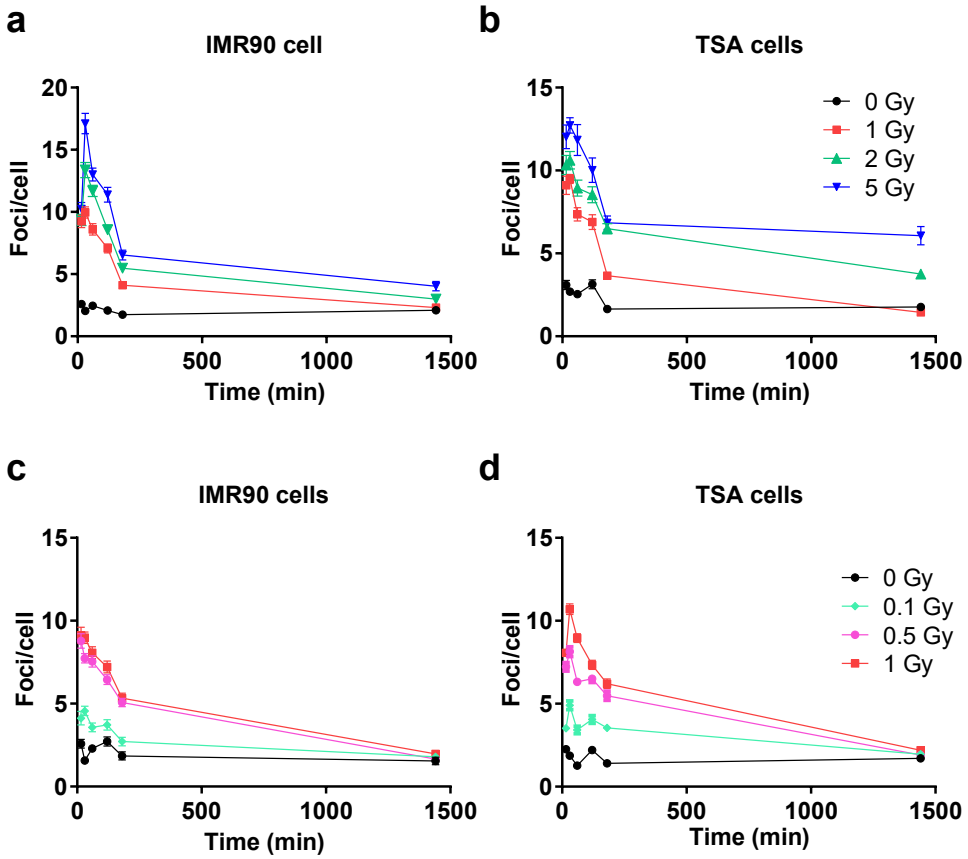

Figure 3.6: Repair kinetics of γ-H2AX foci for IMR90 and TS/A cells, following irradiation with different doses of X-rays (a-b) and neutrons (c-d). The errors represent the SEM of 3 independent experiments. Lines are drawn to guide the eye.

specific criteria on what has to be considered as a focus or not.

First of all, the macro had to be calibrated by comparing the results with foci yields scored "by eye", to minimize errors in the recognition and counting of foci related to the macro implementation, which will however reflect a certain degree of subjectivity. It remains however true that the use of a macro allows the analysis of large amount of data in a quicker and reproducible way.

Our study aims at showing that, when accompanied by a modelling approach, an actual quantification of damage can be derived even if only 2D images are used. To this aim, when analysing images, only the brighter spots that appear as belonging to the focal plane when taking the picture are considered as foci, and neighbouring foci that are not unambiguously distinguishable are merged (examples of pictures taken with the Olympus microscopes are shown

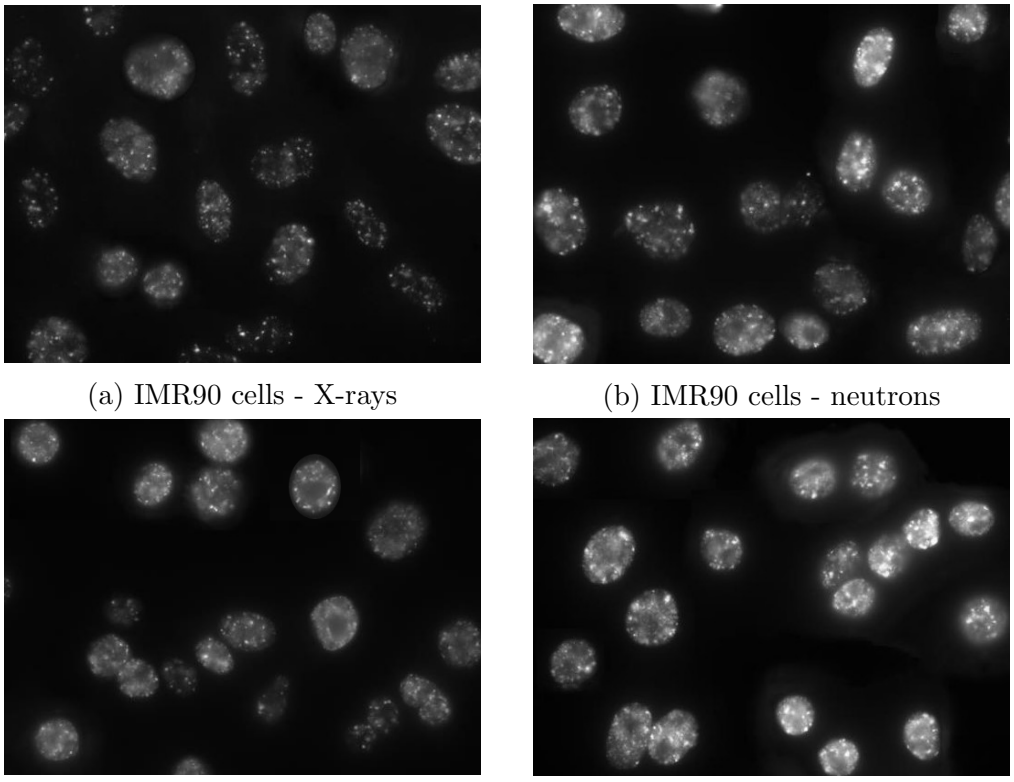

(a) IMR90 cells - X-rays (b) IMR90 cells - neutrons

(c) TS/A cells - X-rays (d) TS/A cells - neutrons

Figure 3.7: Pictures taken with the Olympus conventional fluorescent microscope of: foci resulting from exposure to 1 Gy X-rays (a-c) and 1 Gy neutrons (b-d), for IMR90 and TSA cells, respectively, fixed 1 h post-IR.

in Fig.3.7). The presence of other damages in different planes, and the merging of foci originating from close DSBs can then, on the other hand, be taken into account in the modelling, as it will be discussed in Par.3.2.
An underestimation of foci levels is expected when 2D images are considered. Had the study been limited to 2D images, without any effort in modelling, it would have been reasonable to be less strict, to count all possible foci.
Still, it remains logical that not all foci can be counted in any case, if single 2D images from conventional microscopy are used, this being even more true for higher doses. Moreover, the experimental results for the overall number of foci are to be taken as average yields for all different cell cycle phases, and this could influence the discrepancy between the experimental data and the MC observations presented in next Par.3.2. In Par.3.3 experimental and modelling results in 3D will be presented, to cope with these limitations.
The background of foci is relatively small for the two types of cells considered in this study, and it is constant with the time around a value of two for all conditions. The number of foci increases steeply 30 min post-irradiation with both X-rays and neutrons. As the time goes on, the repair response successfully copes with the damage and the number of foci decreases. It has to be

noted that the slow-dose rate achievable for the neutron irradiations implied an almost 40-minute-long exposure, carried out at RT. Being the temperature not low enough to prevent the initiation of repair processes, presumably the fast component of the DSB repair (half-times of 10–30 min [159, 160]) may be going on during the same irradiation, altering the overall number of foci.
Despite the dose dependency is quite clear for all the conditions for early time-points, 24 h post-irradiation the difference is not that sharp, especially for the samples that have been exposed to neutrons, where the residual damage is completely independent on the imparted dose. This is also true for the data point referring to the samples irradiated with 1 Gy X-rays.
The data for the temporal dynamics have been fitted using the function in Eq.3.5, described by Mariotti *et al.* [125]. The results are shown in Fig.3.8, where the plots have been obtained by means of the ROOT toolkit [161].

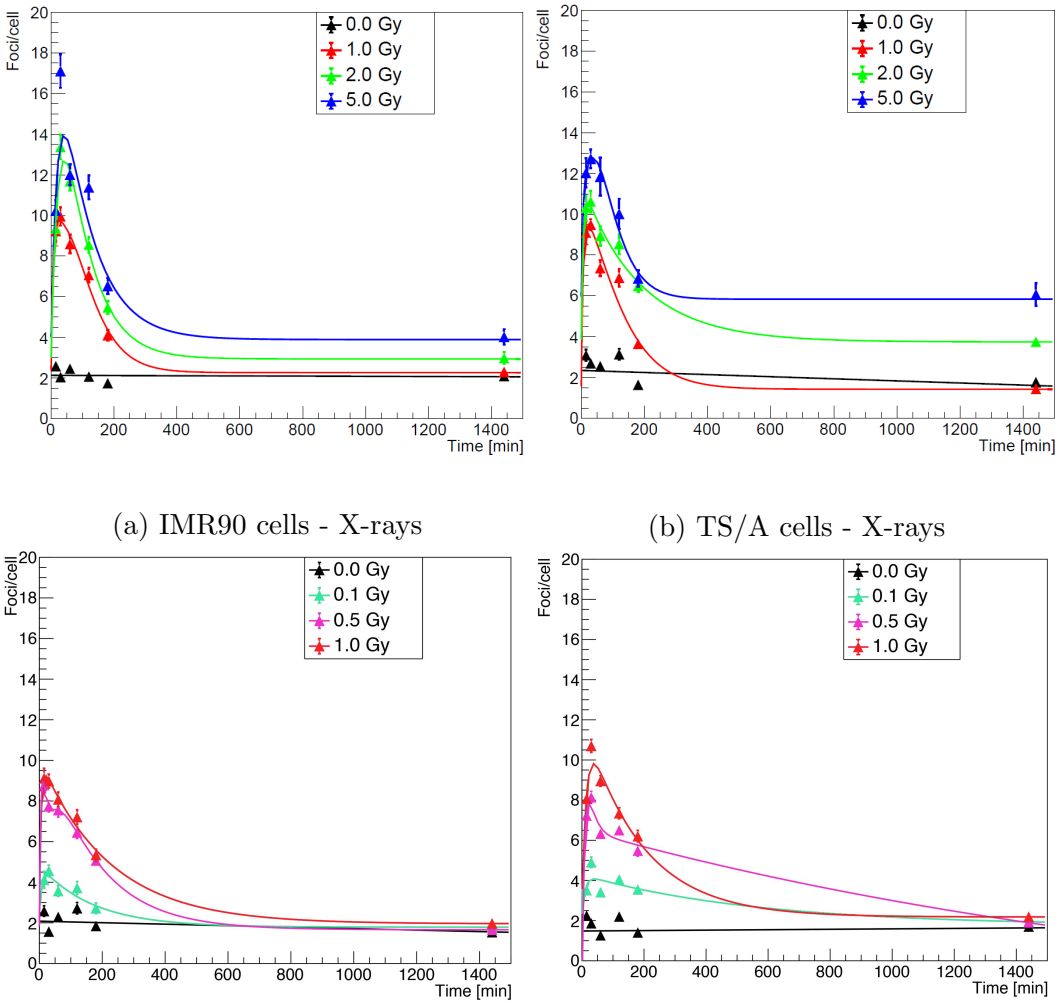

(a) IMR90 cells - X-rays

(b) TS/A cells - X-rays

(c) IMR90 cells - neutrons

(d) TS/A cells - neutrons

Figure 3.8: Fit of foci yields as a function of time, obtained using Eq.3.5 using the ROOT toolkit, for different doses of X-rays (a-b) and neutrons (c-d).

The maximum values are rather low with respect to what reported in the literature, for both considered radiation qualities [162]. This can be explained taking into account that conventional fluorescence microscopy has been resorted to for the image acquisition and scoring has been carried out on one single picture for each field: the visualization of all foci in the nucleus is therefore hampered by the microscope depth of field (DOF), that is the distance from the nearest object plane in focus to the farthest object plane that is simultaneously in focus. Indeed, similar values have been found in other studies using the same technique [163].
It has also to be considered that these counts derive from cells that are not synchronized, but are distributed in different phases of the cell cycle: averaging results from all cells in the population might introduce some biases on the estimation of number of foci per cell, and this has to be considered when experimental data points will be compared to calculation results, that are instead based on cells in G_0/G_1 phase.
However, as already mentioned, the major hinder to a realistic quantification of the initial damages is due to geometrical limitations related to the read-out technique, as only a portion of the damages is at focus at the moment of the image acquisition.
Conventional fluorescence microscopy does not allow a scanning of the specimen along the z direction, and therefore different structures could be present in the image even if at different depths. Thus, other than the physical extension in space of a γ-H2AX focus, being the consequence of extensive phosphorylation of neighbouring H2AX histones, the superimposition of foci that are spatially distributed at different z-coordinates, but that are simply projected on a single 2D plane while observed through the eye-pieces of the microscope, has to be considered.
As it will be discussed in the next Paragraph, confocal microscopy allows a more complete quantification of foci.

γ-H2AX foci yields and morphological characteristics as a function of dose. Fig.3.9 shows that the extra yield of foci ΔFoci (defined as foci yields minus to the sham values) for all the time-points taken into account for the study. While at 24 h is linear with increasing dose, for the earlier time-points, linearity might hold only up to 1-2 Gy following irradiation with X-rays for both IMR90 and TS/A cells, and up to 0.5 Gy when the cell lines have been irradiated with neutrons. At increasing doses for the early time-points, ΔFoci tends to reach a constant plateau. For this reason, a fit function of the type:

$$\Delta Foci(D) = b \cdot (1 - e^{-c \cdot D}) \tag{3.8}$$

has been used in the ROOT framework to better reproduce the saturation, with b and c free parameters of the fit [144].
Linear fits have been applied in many studies to X-ray-induced foci yields at low doses [164, 165]. The saturation following photon irradiation was instead

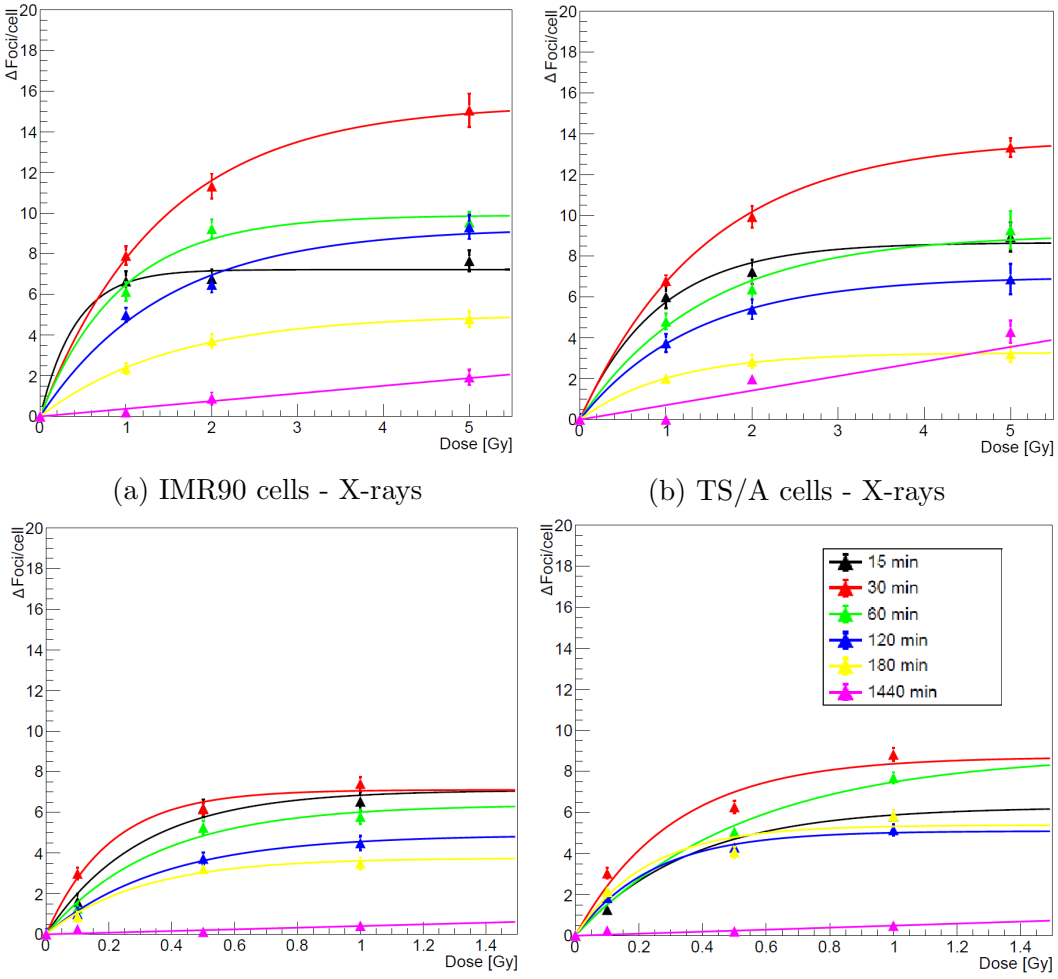

(a) IMR90 cells - X-rays

(b) TS/A cells - X-rays

(c) IMR90 cells - neutrons

(d) TS/A cells - neutrons

Figure 3.9: Dose dependence of the scored yields ΔFoci/cell. The fits have been obtained with Eq.3.8 using the ROOT toolkit. The error bars represent SEM values for 3 independent experiments. Black - 15 min; red - 30 min; green - 60 min; blue - 120 min; yellow - 180 min; pink - 24 h.

assessed in the same dose range of this study when ICC is performed for the scoring [166, 167], while higher saturation thresholds were observed when the overall fluorescence intensity from the whole nucleus is recorded by means of flow cytometry [168]. Being γ-H2AX foci used in many fields as biomarkers of radiation exposure, the first requested characteristics is the capability to predict the irradiation dose [169]. However, the saturation of the signal described up to now hinders a proper quantification of both lesions and foci.
Since this behaviour does not have a physical/biological explanation (especially for X-rays, for which a yield of 30-40 DSB/Gy is expected), it has to be assumed that artefacts related to the detection technique mainly hinder a real quantification of IRIF after relatively high doses of X-rays.
More information about foci has been extracted for all the time-points and the

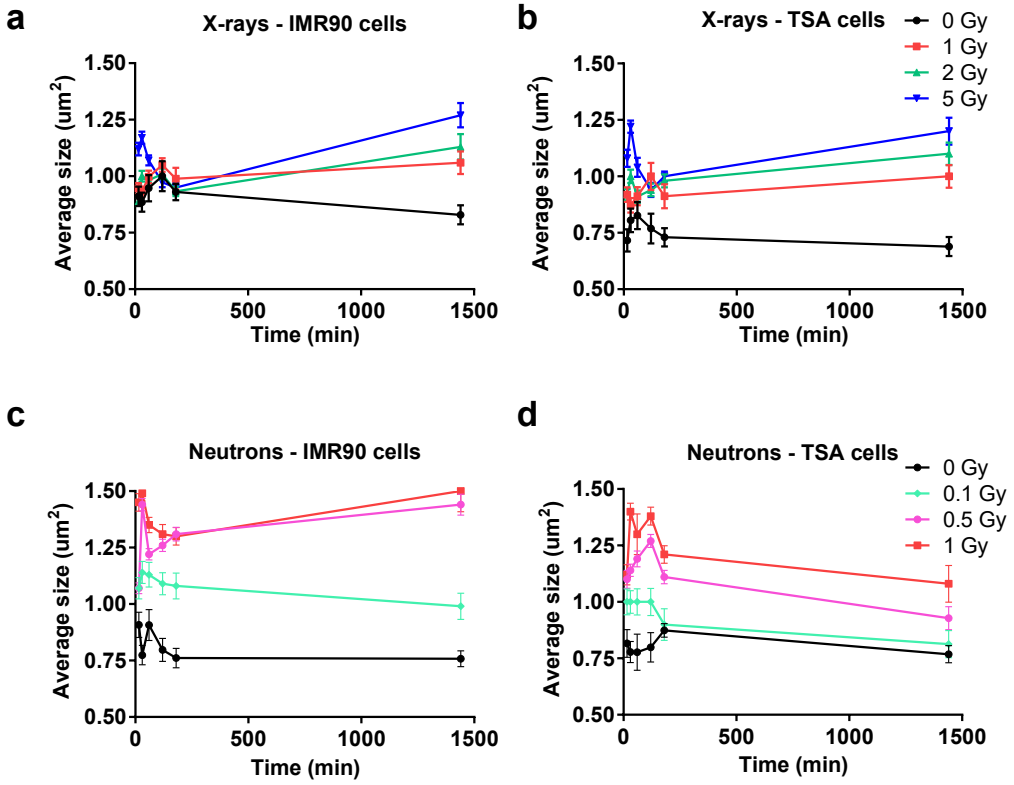

Figure 3.10: Temporal dynamics of γ-H2AX foci planar size, for IMR90 and TS/A cells, following irradiation with different doses of X-rays (a-b) and neutrons (c-d), respectively. The errors bars represent the SEM of 3 independent experiments. Lines are drawn to guide the eye.

doses considered for this assay. In particular, foci dimension and the intensity of single foci have been extracted from the analysis, as indicators of either the overlap of different events close in space, or of increasing damage complexity, due to the close proximity of different DSBs within the lesion and therefore the phosphorylation of more H2AX sites.
Fig.3.10 shows the kinetics of the foci size, for IMR90 and TS/A cells, following irradiation with X-rays (a-b) and neutrons (c-d). The averages have been performed on all the foci of the multiple nuclei acquired in the different fields of the same sample. Since no significant differences have been encountered between the technical replicates, the extracted parameters about foci yields and their characteristics have been pooled and statistically analysed.

The dose response is quite clear for all the time-points following irradiation with neutrons: even with a small dose like 0.1 Gy, there is a 32% of difference between the sizes of the foci in irradiated and sham samples. The enhancement of foci dimension is even more pronounced in case of the two higher doses, which show nevertheless less differences between each other. For all the doses, an initial bump is recorded, meaning that damages different in nature from the ones due to endogenous metabolic processes are occurring, even in mock-irradiated samples.
For IMR90 cells, this is true until maximum 1 h post irradiation, but for TS/A cells in some cases, the sizes stay large even after a couple of hours.
Another difference between the cell lines is the following: for TS/A cells, we have a decrease of the sizes as a function of time after the peak, independently on the dose, meaning that the repair is solving the damages and the planar dimensions of the foci are also decreasing, even though they don't reach the sham level even after 24 h. On the contrary, for large doses (0.5 and 1 Gy) of neutrons, the average foci dimensions in IMR90 cells seem to decrease after the initial peak, but then they start increasing: this could be explained by the fact that we are reporting mean values of the dimensions, and 24 h post-irradiation all the small foci have been coped with and subsequently disappeared, while only the more complex lesions might be still present in the nuclei.
More complex trends have been found for X-rays, with less differences among the different doses for the early time points (up to 180 min).
In general, the same initial peak due to the onset of large radio-induced foci is followed by a decrease in the sizes and then, again an increase as the one discussed for the neutron-irradiated IMR90 cells. In this case, the size of the residual damage is dose-dependent, with larger foci for higher doses.
Furthermore, there is evidence that the repair of major lesions does not occur at the damage site, but most compromised DNA gets relocated to *repair centres*. These sub-domains seem to be located near the boundary between high and low density DNA regions [170].
Although the behaviour was observed for early time-points (30 min for γ-H2AX foci), it can be assumed that the restriction of heavily damaged portions of DNA to certain regions can last until DNA is flawlessly repaired. This may take time in case of high doses of low-LET radiation or for neutron damage.
Being the analysis carried out on 2D images, this might not provide precise information on foci characteristics in other "portions" of the nucleus except for the one at focus. The visible foci do not represent, therefore, single foci but are derived from artefacts due to the superimposition of foci in the third dimension. Confocal microscopy is highly recommended in order to have a better insight on the number of foci in the whole nucleus, especially if high-LET particles are considered (*e.g.*, following neutron irradiation, most damages are imparted by protons of different energies and recoil heavy ions), and damages are densely distributed along the track.
In Fig.3.11, the average intensity of single foci, normalized to sham values,

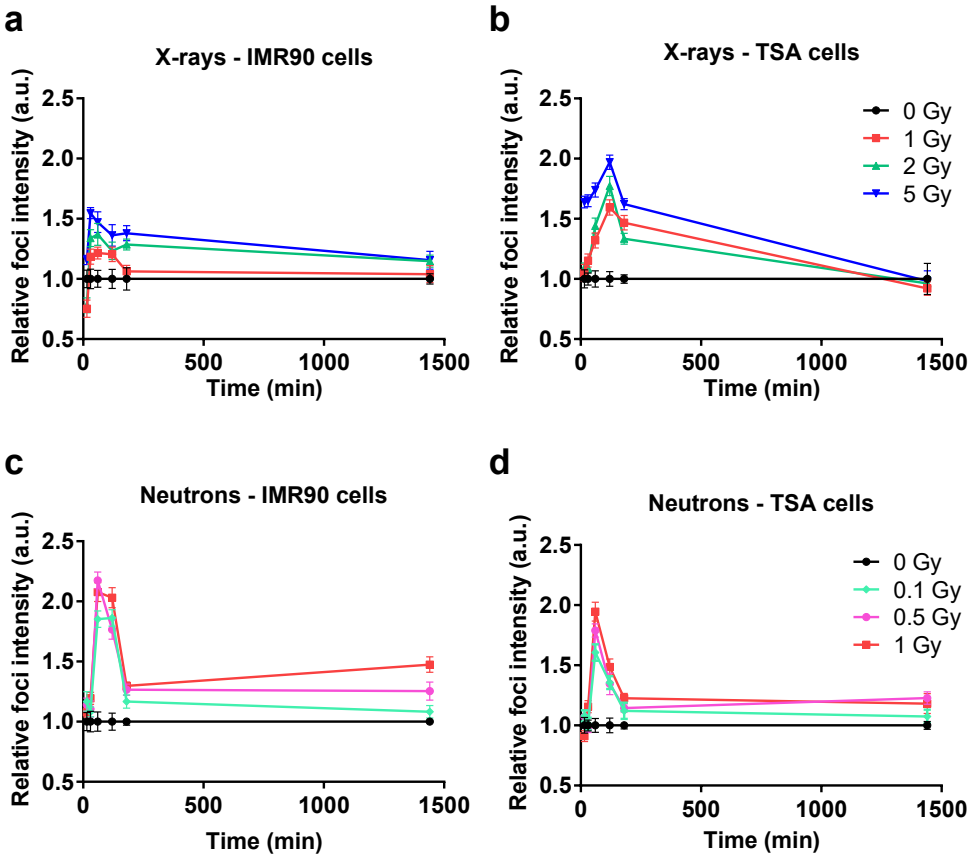

Figure 3.11: Temporal dynamics of γ-H2AX foci intensity, for IMR90 and TS/A cells, following irradiation with different doses of X-rays (a-b) and neutrons (c-d), respectively. The errors bars represent the SEM of 3 independent experiments. Lines are drawn to guide the eye.

is reported. Also in this case, data from the technical duplicates have been pooled together and the points represent the mean ± SEM of three independent experiments.
The dose-dependency can be observed for both cell lines and radiation qualities, and, as recorded for the foci size, also the intensity increases steeply at the early time-points, an evidence of the prompt initiation of IRIF by the cell. The trend as a function of time seems to be modulated by the repair processes like the number of foci per cell. In this case, however the levels of the average intensity for the residual damage are similar to the sham's ones following X-ray exposure, while for neutrons a dose-dependent level of intensity has been found for both cell lines. This might be explained by an increase in the complexity of the lesions, *i.e.* clusters of DSB in space due to protons.
The residual level of damage following 1 Gy of X-rays and neutrons is considerably different from the point of view of the intensity, underlying different complexity and/or enhanced overlap of damages in space.

This suggests that poor resolution of the technique might conceal the realistic number of foci (which saturates as a function of the dose), but dose-dependent differences in the morphological characteristics of γ-H2AX IRIF might provide significant pieces of information on the damage entity. In Fig.3.12 the average size and intensity (normalized to sham values) of single foci in TS/A cells following X-ray irradiation are reported as a function of the dose, for the 30 min and 24 h samples. They have been linearly fitted, and the curve shows that 30 min post-irradiation both quantities increase linearly. At the late time-point, the intensity stays constant as a function of the dose, while the IRIF size is approximately the same as the one for the early time-point. It can be assumed that at early time-points the linear increase might be due to spatial clustering of damages, while foci superimposition is unlikely for IRIF a 24 h post-exposure, which are easily distinguishable. For this reason, the increase could be due to higher complexity.

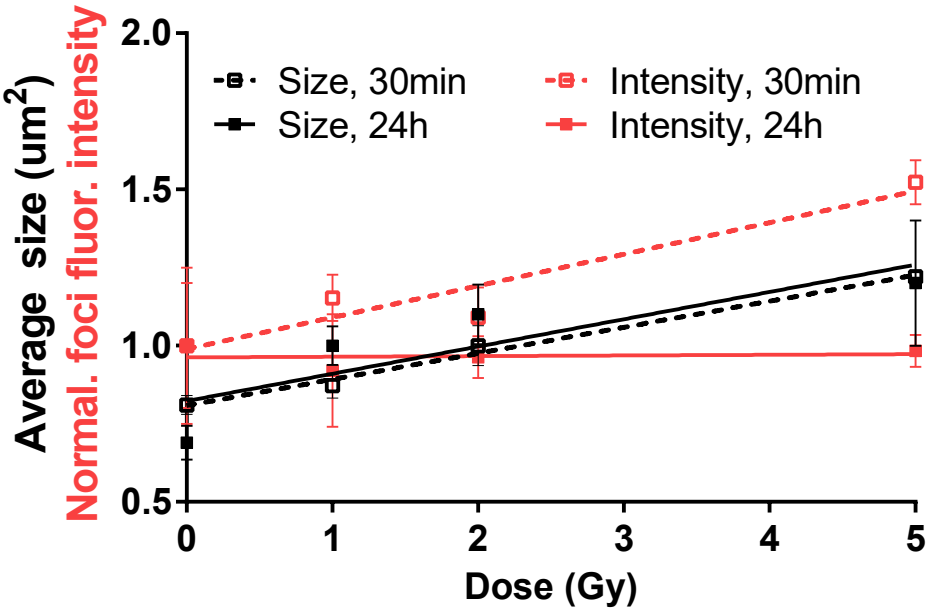

Figure 3.12: Experimental data for foci average size (μm^2) and foci intensity (normalized to the value of the sham) following exposure with X-rays, 30 min and 24 h post-irradiation, in TSA cells. Results are shown as mean of at least 3 independent experiments $\pm$ SEM [144].

3.2 Modelling of γ-H2AX foci and experimental read-out

3.2.1 Why do we need the modelling of γ-H2AX foci?

γ-H2AX foci have been proposed as endpoint for biodosimetry [171, 172], bypassing the low sensitivity intrinsic of other experimental assays [173], *e.g.* micronucleus and comet assays. Detection of γ-H2AX foci was used to quantify damage in blood lymphocytes [174] following conventional fractionated radiotherapy [175], or following exposure to radon [176], given its sensitivity to very low radiation doses. Formation of IRIF was also included in translational studies to monitor the clinical response in patients treated with DNA-targeted therapies, such as some kinds of chemotherapies, radiation or radionuclide therapies or combinations of different treatment modalities [177].
Automatic algorithms to recognize and score foci have been developed to allow high-throughput analyses [166, 178, 179, 180, 181], in the direction of a large scale (routinised) test to scan damage in human genome [173]. However, as discussed in the previous Paragraph, γ-H2AX foci detection is necessarily influenced by the read-out technique, often compromising a straightforward quantification of the yields and their morphological characteristics. It is clear that artefacts in the detection of foci and the signal saturation for increasing dose might hamper the prediction of the imparted dose, or at least introduce large uncertainties in the reconstruction. The same limiting factors apply when γ-H2AX foci are used as endpoint for the comparison of the effectiveness of different radiation qualities.
In this context, help can be offered by modelling, addressing many of the uncertainties related to the biological aspects (how/where foci are induced, how far they extend from the original DNA damage sites, *etc*...) and to the technical limitations of the read-out technique. Depending on the model, the calculation might aim at either the simulation of the induction of foci at early time-point, or at the description of foci evolution, if DNA damage repair mechanisms are included.
Tommasino *et al.* developed a phenomenological model to describe the induction and processing of γ-H2AX foci from X-ray radiation, in chromatin loop structures [168]. The model starts from the simulation of both isolated and clustered DSBs in 2 Mbps loops, and they assume that the phosphorylation of the H2AX histone extends in all such domains, independently on the number of induced DSBs. The number of lesions per loop is determined using the Poisson distribution, and the phosphorylation is extended to a maximum of 10 Mbps, involving other surrounding domains (*activated domains*), to simulate the spread of γ-H2AX foci for high doses.
In the framework of the BioQuaRT project, Villagrasa *et al.* used GEANT4/DNA calculations to compare the simulated number of DSBs per track of protons and α particles from microbeams to the experimental data on IRIF formation

(per track), addressing some of the issues due to the detection and resolution of foci in a x-y plane due to high-LET radiation [182].
In a work by Rabus *et al.* [183] we also present a theoretical model, purely based on combinatorics, to predict foci overlap as a function of dose, both in case of randomly distributed damage following exposure to X-rays and to high-LET α particles microbeams. The model also includes consideration of non-radiation-induced foci, as those due to processes naturally occurring during the cell cycle, that are assumed to be statistically independent from radiation-induced ones, though this can be compromised due to overlapping of events when scored in a 2D observation plane.

3.2.2 Objective

The work presented in this part of the thesis aims at tracing back the phenomenology behind the induction of DNA damage foci, and their characteristics, to radiation quality.
The modelling of γ-H2AX has been carried out through different simulation steps, as detailed in the following. Track-structure calculations with PARTRAC have been performed to simulate the energy depositions in DNA and resulting spatial distribution of DNA lesions. These are the starting point for the simulation of γ-H2AX foci under different irradiation conditions (dose, LET...). In case of neutron exposures, the coupling approach presented in Chap.2, Par.2.3, can be used, and the secondary charged particle field needs to be characterized first with a transport code (PHITS), before going to track-structure calculations.
Once the initial damage is simulated, we applied a machine learning approach to simulate foci based on an unsupervised clustering algorithm. This was done with a C++ macro, reading the output of the PARTRAC code, specifically written for the purpose. Through this algorithm, we take account both of the extension of the phosphorylation of the H2AX histone from a biological point of view, but also of the overlapping of close foci due to the read-out technique, in particular when scoring is performed in 2D images.
Simulations of γ-H2AX foci for both cell lines (IMR90 and TS/A) and all radiation qualities under investigation (X-rays and neutrons) have been carried out, implementing a software replica of the experimental irradiation setups. The proposed modelling approach can be benchmarked with the experimental results presented in Par.3.1.6, in particular foci yields and size at early time-points.
The final aim is to develop a modelling tool able to reproduce induction and read-out of DNA damage foci yields (and other characteristics), also considering artefacts and limitations of the specific read-out technique. Simulating the observer's point of view, this tool allows to trace back experimental foci data to the characteristics of initial DNA damage. This is necessary to use foci induction as an endpoint to compare radiation effectiveness or to reconstruct exposure doses for different radiation qualities.

Publications for the topic

- **S. Barbieri**, G. Baiocco, G. Babini, J. Morini, W. Friedland, M. Buonanno, V. Grilj, D. J. Brenner, A. Ottolenghi. Modelling γ-H2AX foci induction to mimic limitations in the scoring technique. Radiation Protection Dosimetry, online ahead of print, 2018.

3.2.3 Material and methods

PHITS simulation of the irradiation setup

Our coupling approach was adopted to estimate the number of DSBs induced by the mixed secondary field that arises from the interactions of the Hiroshima neutron field with our biological samples.

A simplified mock-up of the setup used for irradiations at the RARAF facility

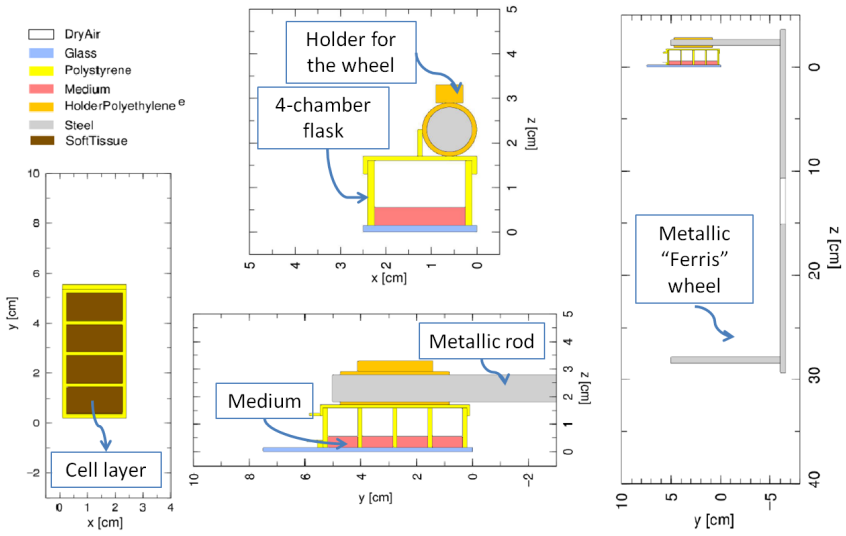

Figure 3.13: Lateral view of the rotating "Ferris" wheel and zoom on the 4-well CultureSlide flask used for neutron irradiations, as implemented in PHITS for the transport simulations. The soft tissue represents the cellular mono-layers.

was recreated with PHITS: the 4-well CultureSlide flask used for the simultaneous irradiation of IMR90 and TS/A cells was reproduced, with the same material and geometry. The four regions with biological material (cell layers) consist of ICRU44 [184] soft tissue, and they are taken as scoring regions for all the physical and radiobiological quantities of interest. The medium (water) and air interfaces were also taken into account. The metallic "Ferris" wheel shown in Fig.3.3(b), together with the rods to sustain the samples, was also implemented. Recoiling heavy charged particles due to neutron interactions in the metal are not expected to reach the scoring region, due to their low penetration power and high stopping in the heavier material. Fig.3.13 shows different views of the simulated setup, with the geometrical reconstruction of

the rotating wheel and of the culture flask.
Instead of reproducing the wheel motion, the setup was simulated in a fixed position but with a rotating source: neutrons were generated perpendicularly from a disk, moving tangentially around a sphere of radius 5 cm, that surrounds the whole CultureSlide flask and the rod on which the flask was hanging. The radius of the disk was equal to the one of the sphere, giving rise to an isotropic neutron field. Particles were emitted from disk with the same energy spectrum that was experimentally measured at the biological sample position [140]. In Fig.3.14(a), a sketch of the irradiation setup used in PHITS is shown, along with the neutron fluence spectrum measured at RARAF (Fig.3.14(b)).
The spectrum implemented as a source in the simulation is missing the lowest

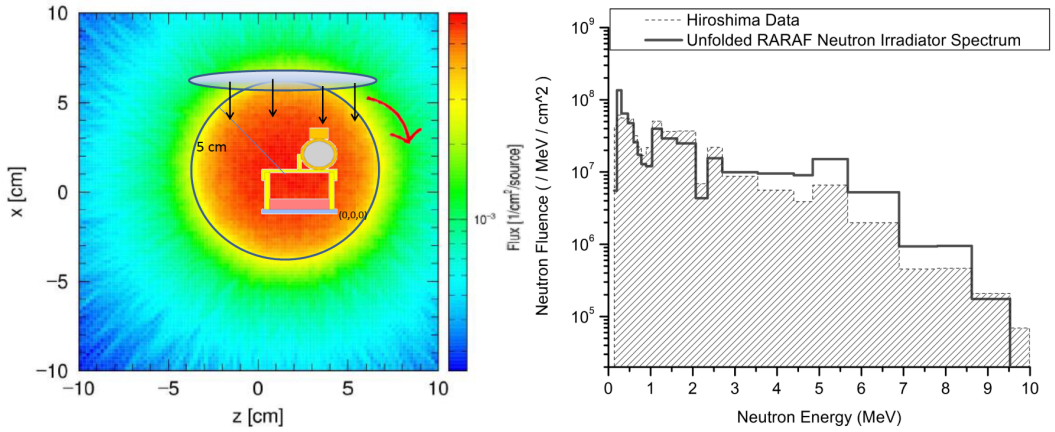

(a) (b)

Figure 3.14: (a) A schematic view of the flask implemented in PHITS, once immersed in the neutron field. Particles are emitted by a disk rotating around a sphere of radius 5 cm. The fluence spectrum was obtained with the [T-Track] tally in PHITS. (b) Measured neutron fluence spectrum (in $\mathrm{MeV}^{-1}\mathrm{cm}^{-2}$) at the RARAF facility [140].

energy component (neutrons below 100 keV), which was invisible to the detector used for the measurement [140]. Instead of introducing an extra source term, without the possibility of an experimental benchmark, we work with the assumption that the missing component is not influencing the final results. As a partial compensation, low energy neutrons can still be generated in the simulation by interactions of the primary neutrons with elements of the setup, and reach the scoring region. Also, photons directly coming from the interaction of the p/d beam on the Be target are not implemented as an extra source term. The contribution to the dose to the sample by this photon component is expected to be of the order of 15 - 20% of the total dose, and this is separately taken into account when analysing simulation results, as later discussed.
Each run consisted in the simulation of 10^9 neutrons, and results were averaged from 5 different runs.

Track-structure simulations

We adopted the lymphocyte-like cell model implemented, with a spherical nucleus of 10 μm of diameter, as software replica of TS/A cell nuclei. The difference between murine and human chromosomal content (10%) is neglected for simplicity, even if this could lead a difference in the DNA damage yields at equal irradiation conditions. Also, in case of TS/A cells, we neglected the heterogeneity in DNA content among different cells, that is expected since we are dealing with tumour cells. The cytoplasmic compartment was simulated as a box centred at the origin of the coordinate system, with sides of 14 μm along the x and y axes, and an extension from -5.1 and 5.1 μm along z [144]. For the IMR90 cell line, we instead used the fibroblast-like cell model, with an ellipsoidal nucleus with axes of 20, 10.6 and 5.4 um along x, y and z. The cytoplasm was reproduced as a box, centred at the origin and containing the nucleus (27 μm along x, 17.6 μm along y, and from -2.8 μm to 5 μm along z). We first carried out simulations with an X-ray source. This is necessary to test the approach for foci predictions and to benchmark the model with data from reference low-LET exposures.
Simulated foci have been compared to the experimental values obtained by ICC 30 minutes post-irradiation, since PARTRAC predicts only initial damage due to IR. Furthermore, the code does not take into account the biological background, that is cell line dependent, so experimental values were normalized to sham values when compared to calculation results. For sparsely ionizing radiation, model results can be more intuitively correlated with experimental foci yields, as no bias due to complex track-structure is expected.
In the neutron irradiation setup, the resulting field used for the experiments has a non-negligible photon component, due to primary p/d beam interactions at the target. Predictions of foci induction due to photons are therefore needed also to interpret experimental data from neutron irradiations.
For the simulations, photons were generated randomly from a plane, positioned at the bottom surface of the cytoplasm, perpendicularly to the cell. The broad energy distribution from the Xstrahl-200 machine was implemented. Calculations were stopped when fixed doses (1, 2 and 5 Gy) were delivered to the nuclei of both lymphocyte [144] and fibroblast cell models. To simulate the effect of neutron exposures, we needed as input results from PHITS on the secondary fields.
As it will be discussed in detail in Par.3.2.4, we found that 98.3% of the dose is deposited by ^{1}H, ^{16}O and ^{12}C ions (in order of relevance, delivering $\approx$ 87.7%, 7.6% and 3% of the total neutron dose, respectively). Since the contribution to the dose from other species is negligible, we implemented in PARTRAC different irradiation setups to simulate exposures to these ions only, with the corresponding $\overline{y}_D$ value as obtained by PHITS. For both protons and heavy ions, different numbers of tracks were simulated, up to a maximum of 15, in order to check the dose-dependency of the endpoint under investigation.
In detail:

- protons with an energy of 60 MeV are generated to mimic the isotropic field of recoil protons accelerated by neutrons at the cell nucleus: the same setup used in Par.2.1.5 was used, with a disk of a radius of 5.046 μm (total surface of 80 μm^2), rotating around the nucleus, and emitting a fixed numbers of protons perpendicularly to the its surface. The simulations were carried out for the spherical nucleus used for the TS/A cells. With this setup, the average proton LET in the nuclear region is of about 45 keV/μm [50]. The same solution cannot be adopted in case of the ellipsoidal nucleus, as a source tangential to an ellipsoidal volume is not implemented in the current version of PARTRAC;

- secondary heavy particles (O, C) are generated uniformly and randomly in both models of cell nuclei. The LET for particle whose range is shorter that the nucleus thickness can estimated with the following formula:

$$LET = \frac{\text{Initial particle energy}}{\text{Particle range at that energy}} \tag{3.9}$$

  Using this expression, we calculated the energies necessary to have an LET equal to $\overline{y}_D$ values calculated with PHITS, namely 1.2 MeV for ^{12}C ions (LET $\sim$ 375 keV/μm) and 875 keV for oxygen ions (LET $\sim$ 350 keV/μm). These energies correspond to a particle range $\approx$ 3.2 μm and 2.5 μm, which further justifies the choice of generating the particles inside the nuclear volume. It is interesting to notice that the dose deposited by a single track for such a high-LET particle is likely to exceed the average dose contribution of the same particle species to the total neutron dose, for all neutron doses considered for the experimental irradiations (see Paragraph "Results" for relative ^{12}C and ^{16}O doses). See later for discussion on this finding.

A minimum number of 64 runs up to 1024 was performed for the X-ray calculations, depending on the dose, while 512 to 2028 runs were performed for all charged particles of interest, according to the statistics of each simulation condition (more runs when fewer particles are generated). Uncertainties are given as standard deviations among results for different runs.

Development of an unsupervised clustering algorithm

PARTRAC offers the possibility to score damages within regions of different size, by clustering damages on a spatial and/or genomic scale. Results already shown in this thesis were based on PARTRAC simulation of DSB clusters, defined as 2 or more DSBs within a genomic distance of 25 bps [185, 50].
For the simulation of foci, we had the option to adopt a clustering criterion based on a genomic scale of 1 - 2 Mbps. This would account for the physical extension of the domain interested by H2AX phosphorylation at the site of DNA damage. However, this would not be enough for the reproduction of

experimental results obtained from 2D images: geometrical effects related to the experimental technique also affect the read-out, as later detailed.
We therefore decided to use parameters based on geometrical distances only, to develop a clustering algorithm able to account both for the physical extension of the domain where a focus appears, and for the artefacts and limitations related to the scoring technique.
γ-H2AX foci are well known to arise following DSB induction. The starting point of the modelling is therefore obtaining results on the spatial distributions (coordinates) of these lesions (or more complex ones). As starting hypothesis, each single DSB or more complex damage (*i.e.* DSB clusters) is seen as the anchoring site for the repair proteins involved in DDR system, implying a 1:1 relationship between foci and DSB yields.
It is reasonable to expect that foci arising from single DSBs are resolvable only for low-LET radiations, for which damage occurs randomly and homogeneously in the target volume. Since, for the neutron spectrum under study in this work, the neutron insult is mainly conveyed by protons and charged particles, it is instead reasonable to expect that damage will be locally clustered. Overlap of phosphorylated proteins might happen, especially considering that phosphorylation takes place over large genetic distances. This is a first cause for a decrease in the yield of detectable foci, breaking the 1:1 relationship with DSBs expected after low-LET exposures. In addition to physical overlap, imaging limitations due conventional microscopy hinder the scoring of single foci: first of all, light coming from different focal planes is collected by the objective, resulting in blurring and overlap of foci. Secondly, a single picture of nuclei (and foci) was taken with the Olympus microscope, and consequently only a fraction of the DSBs happens to be at focus, according to the microscope DOF.
We developed an unsupervised clustering algorithm in C++, reading PARTRAC output file with spatial coordinates of DSBs with nm resolution. Runs with no DSBs/DSB clusters in the nuclear volume were automatically excluded from the analysis, as no foci could be reconstructed. We therefore simulated only cells that are therefore hit by radiation and that contain at least one focus. Both the genomic extension of a focus and artefacts related to microscopy were taken into account in an interdependent way [144]:

- a parameter is introduced to reproduce the DOF of conventional fluorescence microscopes, called *slicing thickness* Δz, which selects a slice of the nucleus and the DSBs therein contained. Being the focus usually chosen in the DAPI channel around the median plane, the slice is symmetrically centred at $z = 0$ μm. Values of Δz between 0.5 and 1 μm were tested, because close enough to DOFs for magnifications of 60X and 40X respectively (*i.e.* 0.4 - 1 μm);

- DSBs contained in the selected slice are projected on the x-y plane, to reproduce the visualization of foci in 2D images;

- after projection, neighbouring DSBs are grouped in the same focus if they lie within a resolution parameter, called *clustering radius* r. For single isolated foci, this radius also represents the spatial extension of the focus domain built around a DSB. For this reason, initial guess values for the *clustering radius* were chosen based on foci size for sham samples, where the few background foci are not expected to overlap in space: r has been chosen to vary in the range of [0.5, 1] μm.

In case of conventional fluorescence microscopy, the main limitations have therefore been traced back to geometrical factors of immediate implementation in the code. The steps of the algorithm are schematically shown in Fig.3.15.
In this work, results are presented as average values of foci yields ($\pm$ SEM) for all the runs in which at least one DSB/DSB cluster survives the selection imposed by the nucleus slicing. Experimental data (used to benchmark the calculations) represent instead the average number of foci over the whole cell population, including cells with no foci.
Foci size has been calculated in two different ways:

- a circular focus is drawn, with radius l equal to the distance between the centroid of the focus resulting from the merging of neighbouring DSBs, and the farthest DSB attributed to it. This is an oversimplified definition, and foci with a single DSB are attributed a zero size. In the following, we will refer to this definition as "circular foci" method [144];

- for each DSB in a focus, a circular area of radius equal to the *clustering radius* r is drawn, representing the "physical" extension of each individual focus around the DSB before the merging due to the projection (see Fig.3.15(b)). When DSBs are merged, their areas overlap and merge in the total focus area (obtained by summing single areas, with overlapping regions counted only once). A "hit-or-miss" MC strategy is then used to calculate the total area of the focus: a rectangle is drawn, containing all DSBs in the focus and associated circles. The centre of the rectangle is the centroid of the focus, and its side has length $2 \cdot (l + r)$, where l is defined as before. A sufficiently high number of random points is generated within the rectangle, in order to cover all its area (here, a compromise between calculation times and the coverage of the rectangle area for the bigger foci was needed, depending on the X-ray dose). The area of the focus is then obtained as:

$$A_{focus} = A_{rect} \cdot \frac{\text{nr. random points in all circles around DSBs}}{\text{total number of generated random points}} \tag{3.10}$$

  In the following, we will refer to this definition as "hit-or-miss" method.

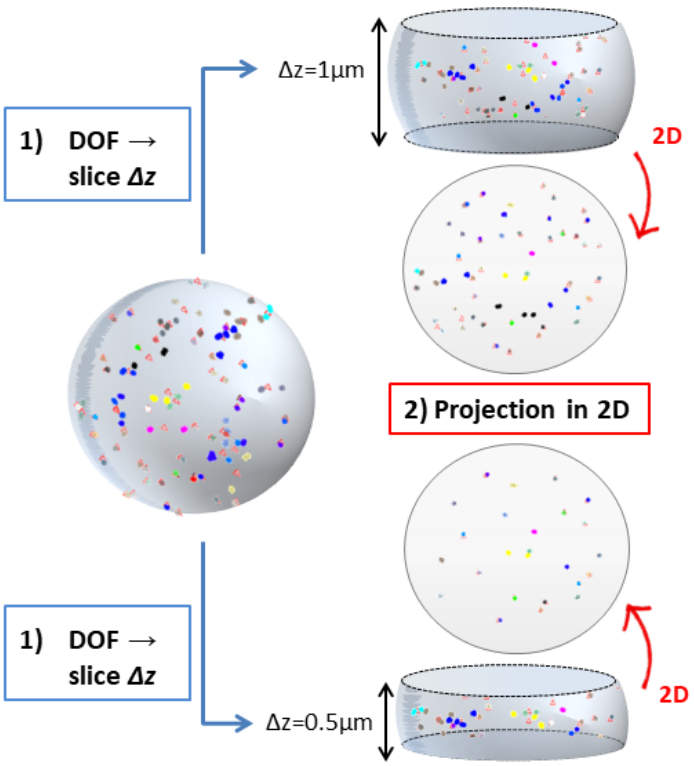

(a)

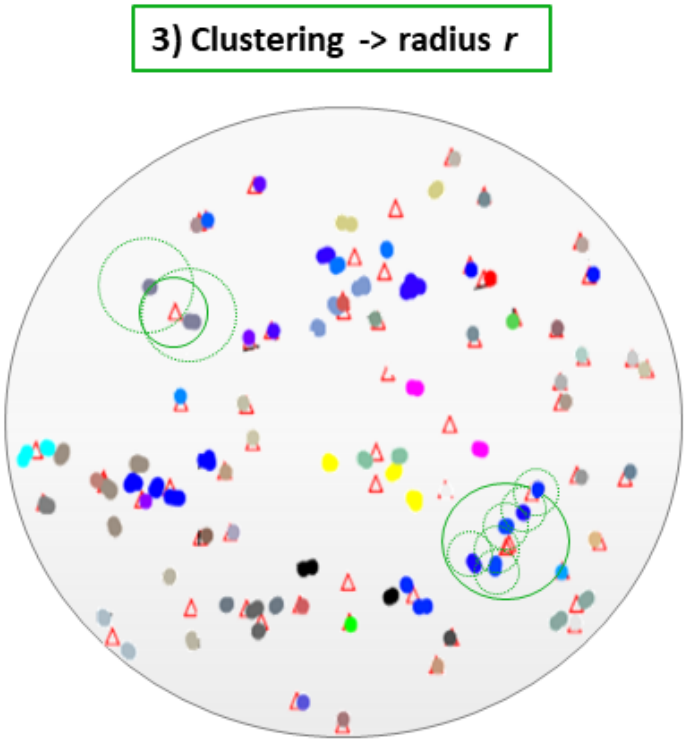

(b)

Figure 3.15: Principles of the clustering algorithm: (a) effect of the slicing of the nuclear volume and of the projection of DSBs onto a 2D plane. (b) Recursive clustering: starting from a random point, the algorithm looks for DSBs within a radius r (dotted circles); if at least one DSB lies within r, it becomes the centre of a new circle of radius r within which other DSBs are looked for, *etc...* Resulting foci are approximated as circles centred at the centre of mass of all merged DSBs, with radius l equal to the distance to the farthest DSB (solid circle).

3.2.4 Results and discussion

X-ray-induced foci To simulate γ-H2AX foci with the *ad hoc* developed clustering algorithm, DSBs and more complex damages had to be simulated with PARTRAC. PARTRAC results from the simulation of X-ray irradiation

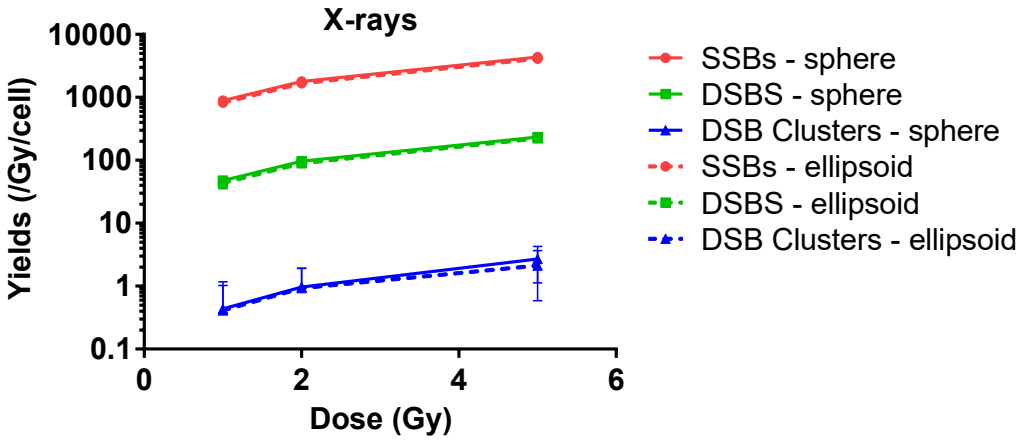

Figure 3.16: Yields of SSBs, DSBs, DSB clusters (per cell and per Gy) as a function of X-rays dose, induced in both the lymphocyte- and fibroblast-like nuclear models.

are shown in Fig.3.16, where the yields of different DNA damages have been reported as a function of the doses used for the irradiations at the RARAF facility, for both the spherical and ellipsoidal nuclear models. As expected, the yields for SSBs, DSBs and DSB clusters display an increasing trend with the dose. The number of SSBs and DSBs have been obtained at fixed doses and they are almost the same for the TS/A and IMR90 cell models. Fig.3.17 shows prediction of X-ray-induced foci from the clustering algorithm for the TS/A cell model, considering either the whole nucleus or a thin slice for the projection ($\Delta z = 0.75$ μm) and using three *clustering radii* r.
Results can be summarized as follows:

- by changing r: increasing the radius, more and more DSBs are merged in the same focus, yielding, for a fixed dose, less foci but with higher average multiplicity (average number of DSBs in a focus). The number of foci as a function of the dose is however not easily predictable, because there is an interplay between the *clustering radius* and the number of DSBs in the slice Δz. For a thin slice, the yield of foci increases for higher doses, while if the whole nuclear volume is considered, the trend saturates with the dose. The higher r, the more the curve bends, resulting in less and less (but bigger) foci, because of the close proximity of the damages. This is a signal of a saturation effect.

- By changing Δz: at a fixed dose, the selection of thinner slices implies fewer DSBs, meaning that also foci yields are reduced. This holds true

unless the decrease in the number of DSBs results into a better resolution of the same, hence of foci. This is true especially for high doses of X-rays, where the red lines for $\Delta z = 0.75$ μm lead to higher yields than the curves for $\Delta z = 10$ μm.

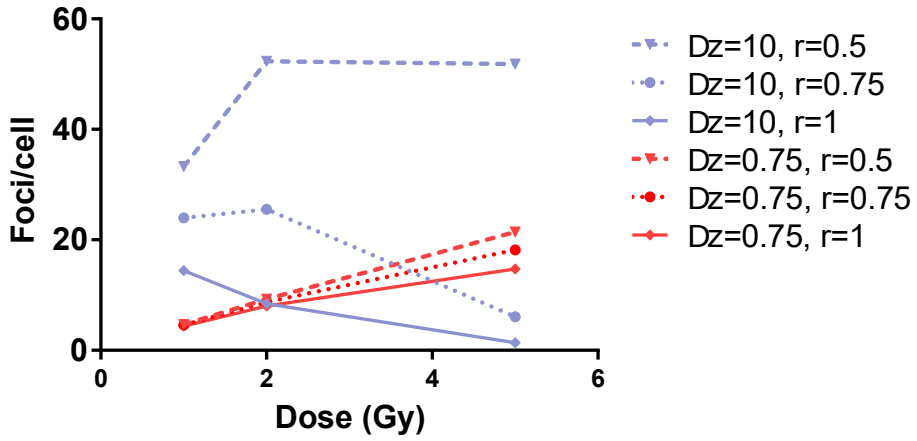

Figure 3.17: Yields of γ-H2AX foci/cell as a function of the X-ray dose, for the TS/A cell nuclear model. Different combinations of Δz (Dz in the plot) and r have been tested. The values for Δz and r are expressed in μm. The lines are drawn to guide the eye. Results are presented as mean $\pm$ SEM for different runs.

As explained in the "Material and Methods" Section, the choice of the values of Δz and r was driven by physical (foci radius in sham samples) or technical (conventional depths of field) observations. It has to be underlined that any read-out technique would introduce artefacts to be addressed with the introduction of particular parameters, as well as any set of experimental data would require a specific tuning of these. The benchmark of the code with experimental data sets is necessary to select the combination that better reproduces the biological outcome after detection with conventional fluorescence microscopy. Fig.3.18 shows the results for the prediction of X-ray-induced foci as a function of the dose and for different code parameters (coloured curves). Experimental points (TS/A cells, black line) for the foci scored 30 min post-irradiation are reported for comparison, since PARTRAC allows the simulation of the initial damage. It can be observed that all the curves with higher *clustering radius*, at high doses, show a certain degree of saturation in the yield of foci, previously largely discussed and shown to be characteristic following this kind of assay. Among the tested values, the best fit seems to be offered by the combination $\Delta z = 0.75$ μm and $r = 1$ μm.
It has to be recalled that while theoretical predictions with PARTRAC are for G_0/G_1 cells, the experimental yields are from averages of foci/cell in a population of cells that were not synchronized in a specific phase, which could

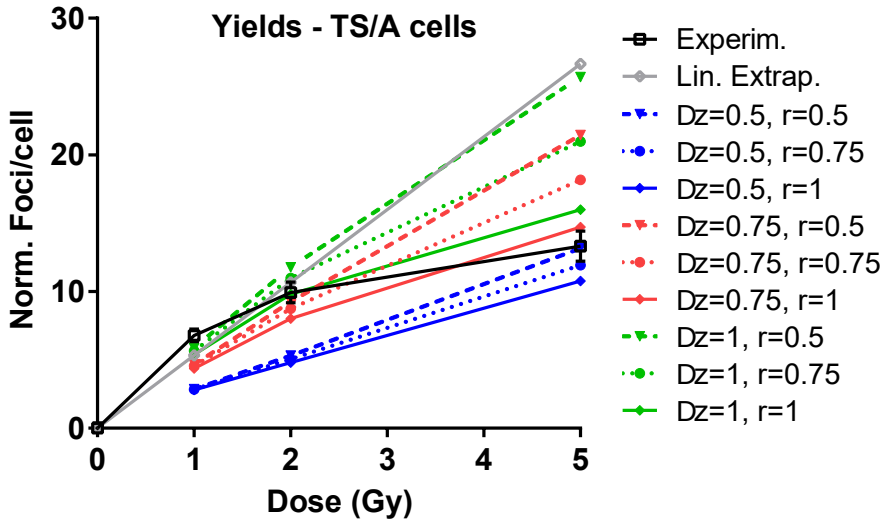

Figure 3.18: Yields of γ-H2AX foci/cell as a function of the X-ray dose, for the TS/A cell nuclear model [144]. Realistic combinations of Δz (Dz in the plot) and r have been tested (coloured curves). The values for Δz and r are expressed in μm. The lines are drawn to guide the eye. Results are presented as mean $\pm$ SEM for different runs. Experimental ΔFoci/cell (squares, black) following X-ray irradiation and the linear extrapolation of data up to 2 Gy (rhombi, grey) are also shown.

partially explain the differences with the calculations. However, S-phase usually implies an increase, more than a decrease, in the number of IRIF, due to the presence of DSBs caused by the endogenous processes during the replication of the DNA. Moreover, the difference in the yields can be justified by the following observations: 1)the first one is that calculated foci can be considered an upper limit for the number of nuclear γ-H2AX foci, because each single DSB (or DSB cluster) has been assumed to give rise to an IRIF; 2) cells with no foci in Δz were not taken into account in the foci distribution; 3) finally, even if experimentally the peak in the ICC signal is found 30 min post-irradiation, at that time some DSBs could have already been repaired, leading to a lower number of visible foci (as shown in Fig.3.2 [109, 186]).
In the plot, the gray curve represents the linear extrapolation from the first three data points available from the experiments (up to 2 Gy), in agreement with the theoretical expectation that sees the number of DSBs, and therefore of foci, linear with the imparted dose. The curve with the lower r (0.5 μm) and $\Delta z = 1$ μm is matching this extrapolation line very well. Ideally, for very low *clustering radii* and a random distribution of foci as the one from X-ray irradiation, it should be possible to distinguish foci arising from single DSBs.
As for the sizes, results of the two methods for the simulations with TS/A cells are shown in Fig.3.19. The "circular foci" method has firstly been used to have

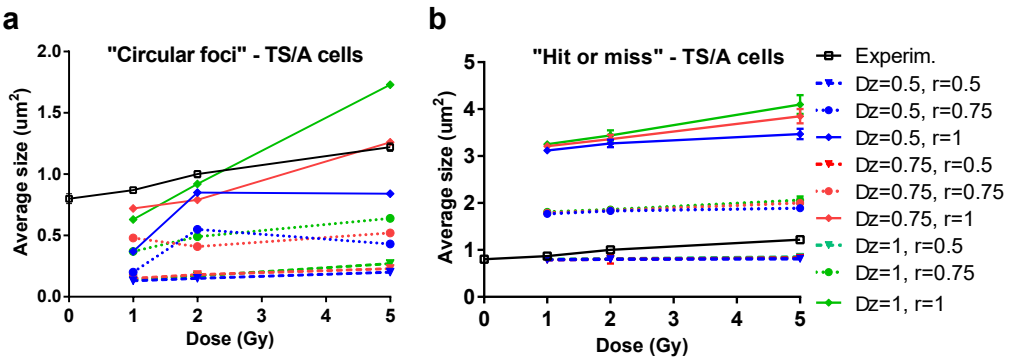

Figure 3.19: γ-H2AX foci size (in μm^2) as a function of the X-ray dose, for the TS/A cell nuclear model. (a) Results for the "circular foci" method [144]; (b) results obtained with the "hit or miss" method. Realistic combinations of Δz (Dz in the plot) and r have been tested (coloured curves). The values for Δz and r are expressed in μm. The lines are drawn to guide the eye. Results are presented as mean $\pm$ SEM for different runs. Experimental data for foci sizes (squares, black) following X-ray irradiation are also shown.

an approximated estimate of foci size. However, depending on the presence of at least 2 DSBs in a focus, it does not consider the spatial extension of foci due to single DSBs. This leads to an underestimation, as the values for low r may be dictated by two DSBs very close to each other, resulting in a circular area smaller than the one from a radius equal to r. For this first method, the combinations given by $r = 1$ μm are the closer to the experimental points, in particular the one with $\Delta z = 0.75$ μm. We can however conclude that this method does not provide reliable estimates for the size, and we will not further apply it to calculations for the high-LET radiations. The "hit or miss" method provides results that are highly dependent on the *clustering radius*. The values are almost independent on the dose and the *slice thickness* for $r =$ 0.5 and 0.75 μm, and they are approximately equal to the area of a circle with radius r ($\sim$ 0.9, 1.77 and 3.14 μm^2 for $r = 0.5$, 0.75 and 1 μm, respectively). This shows that, in any case, most of predicted foci are due to isolated single DSBs, except for $r = 1$ μm and 5 Gy X-rays. This is in agreement with what is expected from randomly distributed X-ray-induced DSBs/foci. With respect to experimental results, the choice of $r = 0.75$ and 1 μm overestimates the size for large r, and a better agreement is found for all curves with $r = 0.5$ μm.
Fig.3.20 shows instead the curves obtained with the ellipsoidal nuclear model used for IMR90 cell representation following X-ray irradiation. The yield of predicted foci is almost twice as the one foreseen for the TS/A cells. This is due to the fact the the longitudinal section of the ellipsoid has a planar area of 169.6 μm^2, almost the twice with respect to the spherical model (78.5 μm^2). IRIF are therefore distributed on a larger planar surface and better resolvable. The experimental ICC points show however a more enhanced saturation, which

is not reproduced by any combination of the tested parameters, even considering the larger r and the smallest Δz. The detected foci sizes are comparable to the values obtained using $r = 0.5$ μm, at least for the "hit or miss" method. Values from the "circular foci" method show less agreement for all the doses. A possible explanation for these discrepancies is that the geometrical shape for the software model of IMR90 cells might not be accurate enough. Together with the limitation of the options for source implementation in PARTRAC, that has been already mentioned and affects ellipsoidal nuclei, this leads the decision to focus on results for the TS/A cells in the rest of this Paragraph.

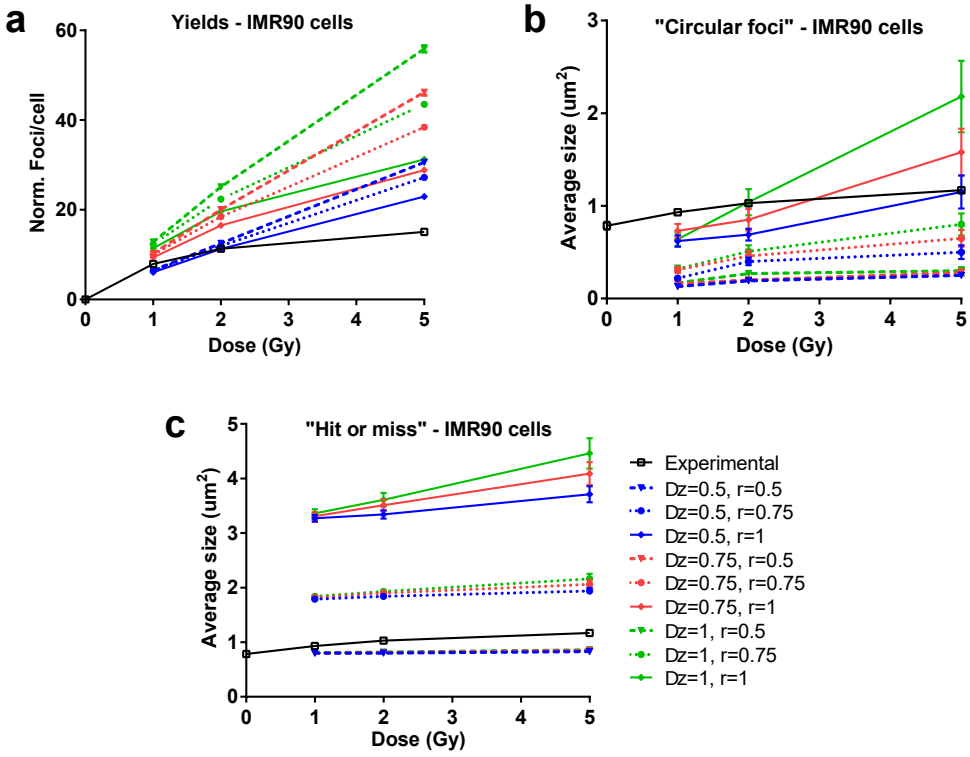

Figure 3.20: Yields of γ-H2AX foci/cell (a) and foci size (in μm^2) (b-c) as a function of the X-ray dose, for the IMR90 cell nuclear model. (b) Results for the "circular foci" method; (c) results obtained with the "hit or miss" method. Realistic combinations of Δz (indicated as Dz) and r have been tested (coloured curves). The values for Δz and r are expressed in μm. The lines are drawn to guide the eye. Results are presented as mean $\pm$ SEM for different runs. Experimental Δfoci/cell and foci sizes (squares, black) following X-ray irradiation are also shown.

Neutron-induced γ-H2AX foci We first present results from neutron transport calculations. Fig.3.21 reports the neutron fluence spectrum scored at the sample location (in the cell layers represented by the soft tissue), reproducing the one available at the RARAF irradiation facility, previously shown in Fig.3.14(b). The calculation of the $\overline{y}_D$ and of the relative dose can be easily

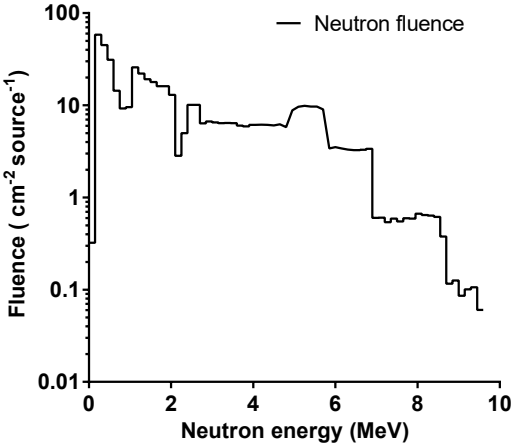

Figure 3.21: Neutron spectrum measured in PHITS with the [T-Track] tally in a region around the flask (cm^{-2} $source^{-1}$).

performed thanks to PHITS, as explained in Par.2.3. For example, Fig.3.22 shows in coloured scale the deposited dose due to all particles under investigation (a), and electrons (b) and protons (c) individually, in a planar slide of the setup (chosen only for graphic visualization). This information is the one used for the computation of the relative dose for each secondary particle.

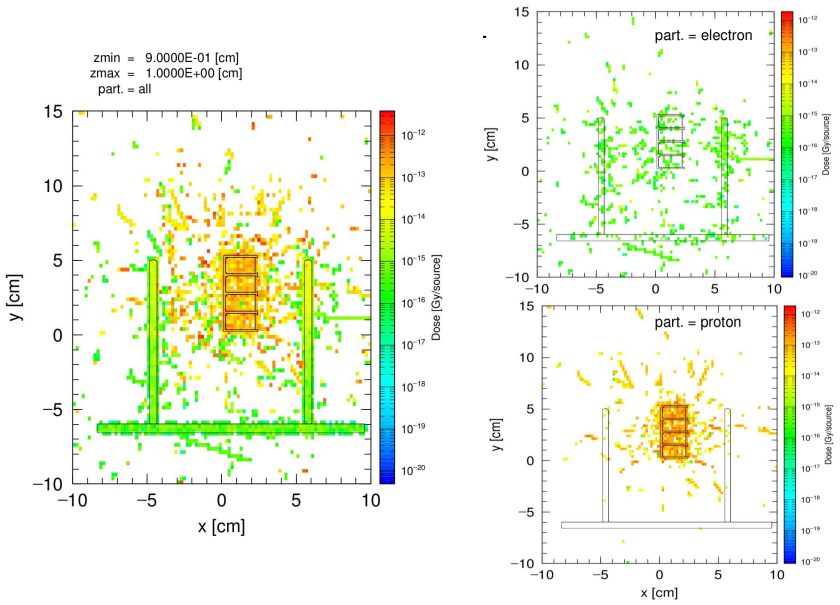

Figure 3.22: Distribution of dose depositions in a chosen slice of the setup of 1 mm thickness calculated in PHITS with the [T-Deposit] due to: (a) all the species under consideration; (b) electrons; (c) protons.

Tab.3.4 shows instead the calculated values for the dose-mean lineal energy $\overline{y}_D$ for the secondary species under investigation, in target 1, 2, 3, 4, representing the 4 thin soft tissue layers in the chambers of the flask (experimentally, they would correspond to the two IMR90 and the two TS/A cell layers respectively). As shown in the Tab.3.4, results have been averaged for the implementation of the parameters in PARTRAC. Eq.2.19 can be used to extract DSB clusters as a function of the species $\overline{y}_D$, as previously done in Par.2.3.5.

Table 3.4: Dose mean lineal energy $\overline{y}_D$ (keV/μm) and the relative dose D_{rel} for the different neutron-induced secondary particles under analysis, for the four soft tissue layers.

P.le / targ.	$\overline{y}_D$	Average $\overline{y}_D$	D_{rel}	Average D_{rel}
e^--1	2.01	2.01	0.12%	0.13%
e^--2	2.01		0.13%	
e^--3	2.01		0.14%	
e^--4	1.99		0.13%	
^{1}H-1	45.31	45.18	87.48%	87.58%
^{1}H-2	45.25		87.47%	
^{1}H-3	45.11		87.90%	
^{1}H-4	45.05		87.48%	
d-1	0.00	nan	0.00%	nan
d-2	0.00		0.00%	
d-3	0.00		0.00%	
d-4	0.00		0.00%	
α-1	192.11	191.40	1.07%	0.98%
α-2	191.29		0.98%	
α-3	192.49		0.88%	
α-4	189.72		1.01%	
^{12}C-1	378.66	376.68	3.06%	3.00%
^{12}C-2	378.25		2.88%	
^{12}C-3	375.25		2.98%	
^{12}C-4	374.55		3.08%	
^{14}N-1	363.81	380.21	0.38%	0.38%
^{14}N-2	395.07		0.40%	
^{14}N-3	377.79		0.38%	
^{14}N-4	384.18		0.38%	
^{16}O-1	346.33	349.49	7.69%	7.74%
^{16}O-2	351.84		7.96%	
^{16}O-3	348.69		7.55%	
^{16}O-4	351.10		7.79%	
neutron-1	82.30	82.11	100.00%	100.00%
neutron-2	82.74		100.00%	
neutron-3	81.08		100.00%	
neutron-4	82.32		100.00%	

The secondary particle contributions, weighted for their relative doses, are shown in Fig.3.23. A total number of 4.44 neutron-induced DSB clusters (Gy^{-1} $cell^{-1}$) has been found, providing a neutron RBE of 11.68 (using as a reference the Xstrahl-200 X-ray spectrum mentioned in Par.3.3.4). This value is reasonable if compared to the results shown in Fig.2.12(a), considering that the average neutron energy of the Hiroshima spectrum is of $\sim$ 2.4 MeV.

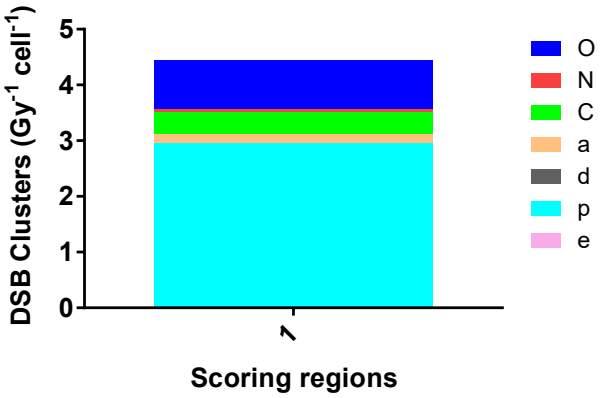

Figure 3.23: Yields of neutron-induced DSB clusters (Gy^{-1} $cell^{-1}$). The contributions due to neutron-induced secondary particles are also shown.

Track-structure simulations were performed for fixed numbers of particles (for simplicity, PARTRAC calculations were run only for ^{1}H, ^{12}C and ^{16}O ions, which contribute themselves to the 98.3% of the total dose), to study the IRIF dependence on the dose, for all the r and Δz under investigation. The conversion into dose per run conversion is provided as an output by PARTRAC.
Results for the yields of different initial damages due to these radiation qualities are in Fig.3.24. The same observations done for the case of X-rays can be made.

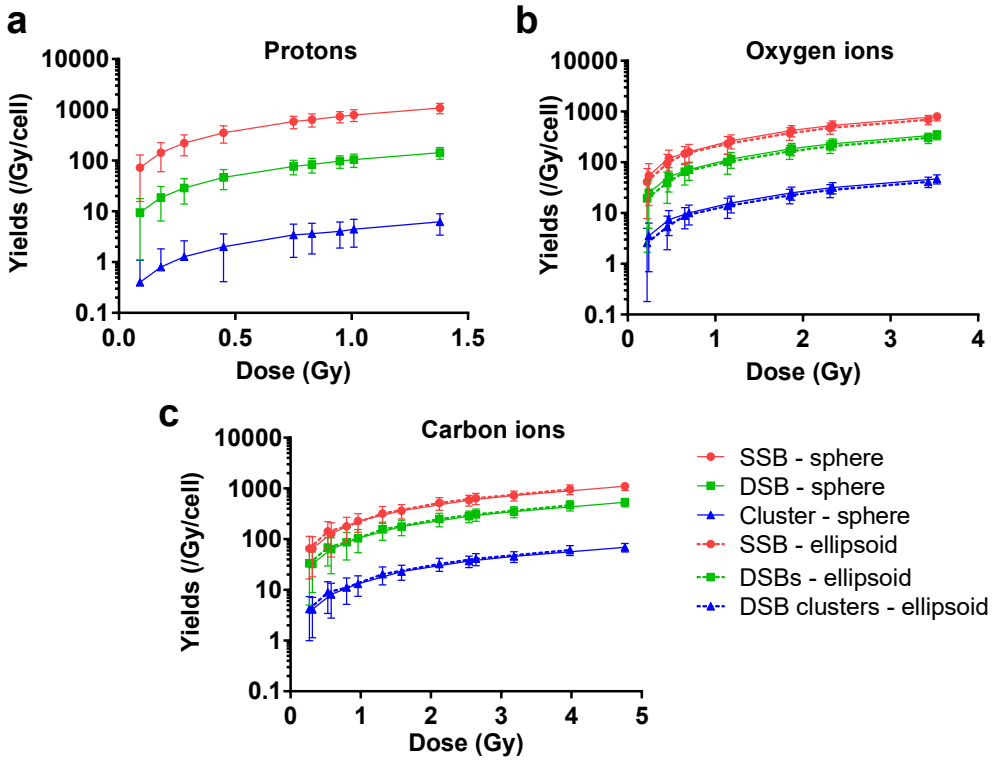

Figure 3.24: Yields of SSBs, DSBs and DSB clusters as a function of the dose of (a) ^{1}H, (b) ^{16}O and (c) ^{12}C ions. For protons, simulations in PARTRAC have been carried out only for the spherical nuclear model, while for ^{16}O and ^{12}C, the results from the exposure of the ellipsoidal model are also shown.

Results on the simulated γ-H2AX foci are shown in Fig.3.25 (for protons) and 3.26 (for ^{16}O and ^{12}C ions): it is evident that in the considered dose range, the yields of foci are linearly correlated with the dose for all the tested conditions. The plot on foci size (panels (b)), obtained with the "hit or miss" method, shows stable results as a function of the dose, and the better combinations are given for $r = 0.5$ μm.
Comparison with experimental data can be carried out only for the neutron-induced foci data (reported with the black curves in Fig.3.25), since no irradiations have been carried out with the singular species at these LETs. In order to do this, the different contributions of the secondary species have to be taken into account, weighted for their relative dose.

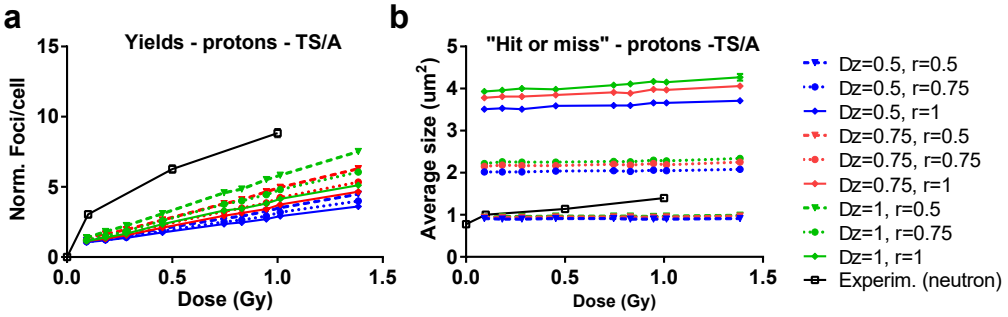

Figure 3.25: Yields of γ-H2AX foci/cell (a) and foci size (in μm^2, "hit or miss" method) (b) as a function of the proton dose, for the TS/A cell nuclear model. Realistic combinations of Δz (Dz in the plot) and r have been tested (coloured curves). The values for Δz and r are expressed in μm. The lines are drawn to guide the eye. Results are presented as mean $\pm$ SEM for different runs. Experimental Δfoci/cell and foci sizes (squares, black) following neutron irradiation are also shown.

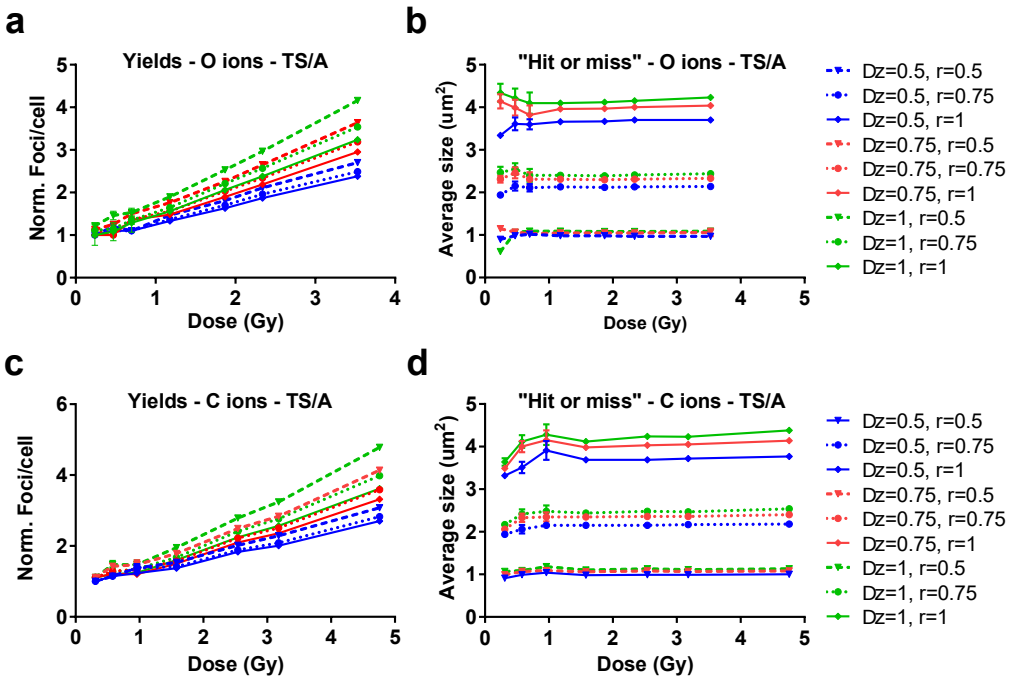

Figure 3.26: Yields of γ-H2AX foci/cell (a and c) and foci size (in μm^2, "hit or miss" method) (b-d) as a function of ^{16}O and ^{12}C ion doses, for the TS/A cell nuclear model. (a) Predicted yields following exposure to ^{16}O, while (c) is referred to exposure with ^{12}C. (b-d) Results for the "hit or miss" method, for ^{16}O and ^{12}C ions respectively. Realistic combinations of Δz (Dz in the plot) and r have been tested (coloured curves). The values for Δz and r are expressed in μm. The lines are drawn to guide the eye. Results are presented as mean $\pm$ SEM for different runs.

To account for the γ-ray contribution, the plot for X-ray predictions on foci for TS/A cells (Fig.3.18) has to be considered.
Experimentally, 1 Gy of (neutrons + γ-rays) from the Hiroshima nuclear spectrum produced at RARAF induces an average of 8-9 IRIF in TS/A cells. A $\sim$15% of the dose (0.15 Gy) is imparted by photons and it causes the onset of 1-2 foci, depending on the parameters, as extracted from Fig.3.18. The remaining $\sim$85% of the total dose is imparted by neutron-induced by-products, mainly protons (87.7%), ^{16}O ions (7.6%) and ^{12}C ions (3%), delivering individual doses of 0.75, 0.065 and 0.026 Gy, respectively (per Gy neutron).
From the plot in Fig.3.25, a number of 5 foci is extracted for protons (using $r = 0.5$ μm and $\Delta z = 1$ μm to have the higher yields obtained). For carbon and oxygen ions, the relative dose imparted to the soft tissue in PHITS is way lower than the dose imparted by single ions of those LETs (as calculated from PARTRAC), revealing that only a percentage of the nuclei is hit by maximum one particle: respectively, the $\sim$ 28% and the 8% for ^{16}O and ^{12}C ions. Summing up all the contributions, we obtain a value that is close to what found experimentally. For a summary of results obtained with this coupling scheme, refer to Fig.3.27. It has to be recalled here that calculated average values are

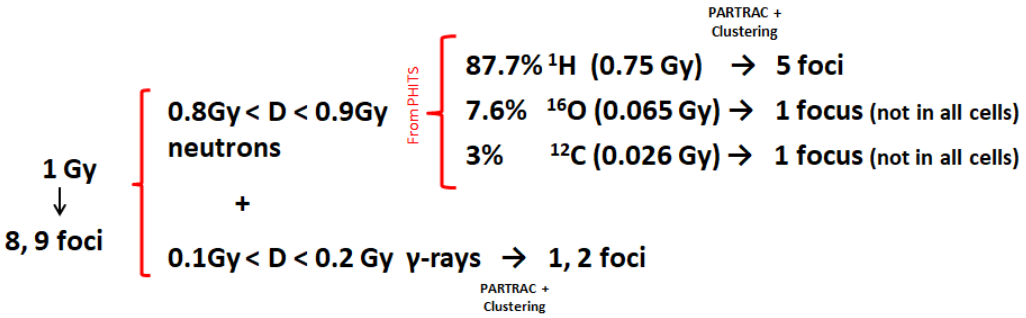

Figure 3.27: Summary of foci yields due to γ-rays and neutron-induced charged particles (^{1}H, ^{12}C, ^{16}O), weighted for the dose contributions to the total neutron dose of 1 Gy.

extracted from the analysis of cells where at least a focus survives the selection of the slice of the nucleus (*i.e.* from foci yield distribution with a minimum set to 1). A further refinement of the coupling would be necessary for a more quantitative comparison, also including cells with no foci in the analysis, possibly resulting in a lowering of the final reconstructed foci yields. Already at this stage however, the approach gives results close to experimental findings. If we compare the foci size, it can be observed that the combination of $r = 0.5$ μm and $\Delta z = 1$ μm for protons also nicely reproduces the observations from ICC for both methods (meaning that on average the morphology of neutron-induced foci is due to recoil protons), and it justifies the choice of these values for all radiations to sum up the yield contributions to estimate the total number of IRIF following neutron irradiation and conventional ICC.

3.3 An insight into read-out limitations: confocal *vs* conventional microscopy

3.3.1 Confocal microscopy to whole nucleus

Conventional fluorescence microscopy applied to ICC samples for DNA repair foci allows, with a good approximation, the quantification of the damage, the characterization of its spatial distribution and of the repair kinetics.
However, all the considerations made in previous Paragraphs have underlined the limitations introduced by this technique. In particular, as also anticipated, we observe a saturation of the signal as a function of dose also for the relative simple case of low-LET radiation, that leads to results for DNA damage far from expectations (30-40 DSBs/Gy). The same limitations are even more evident when studying high-LET radiation, in the end they hinder a comparison of radiation effectiveness based on foci as an endpoint. To bypass these limitations, a first step forward is represented by the use of the so called "Z stack" acquisition, that is the recursive acquisition of fields at the same x-y coordinates, but at different focal planes, incrementally stepping through the sample using a focal drive. These "Z stacks" are usually required for deconvolution of epi-fluorescence microscopy data to remove out-of-focus signal collected within each individual image. This method allows a "scan" of the whole nuclear volume, thus mitigating the artefacts due to selection of a single slice due to the microscope DOF. However, slices are usually thick (higher acquisition rate and reduced sample exposure), failing to provide a fine scanning of the events; besides, the spatial resolution is not enhanced.
The introduction of confocal microscopy represented a major breakthrough in the microscopy field. The concept behind confocal microscopy was patented by Minsky in 1957, and in the mid-1980s W. B. Amos and J. G. White built the first confocal beam scanning microscope at the Laboratory of Molecular Biology in Cambridge [187]. This technique allows to scan the sample at different depths with enhanced axial resolution (optical DOF), and it avoids most of the image limitations related to out-of-field light: it relies on spatial filtering that allows to neglect all the emission light from out-of-focus planes, that is instead detected in conventional microscopes. This is achieved thanks to the light selection guaranteed by two different pinholes, conjugated to the focal plane, one at the entrance of the electronic system of the microscope, and one positioned immediately before the detectors.
Fig.3.28 shows a schematics of the functioning of a confocal microscope.
In detail, while conventional microscopy uses a wide cone of light, that illuminates uniformly and simultaneously a large area of the sample and excites most of the fluorophores, confocal microscopy relies on laser light, which is collimated into a pencil-like beam by the first pinhole, and then sent through a dichroic mirror and to the sample. There, only a tiny spot of the sample is exposed, allowing to selectively excite the fluorophores in that portion of

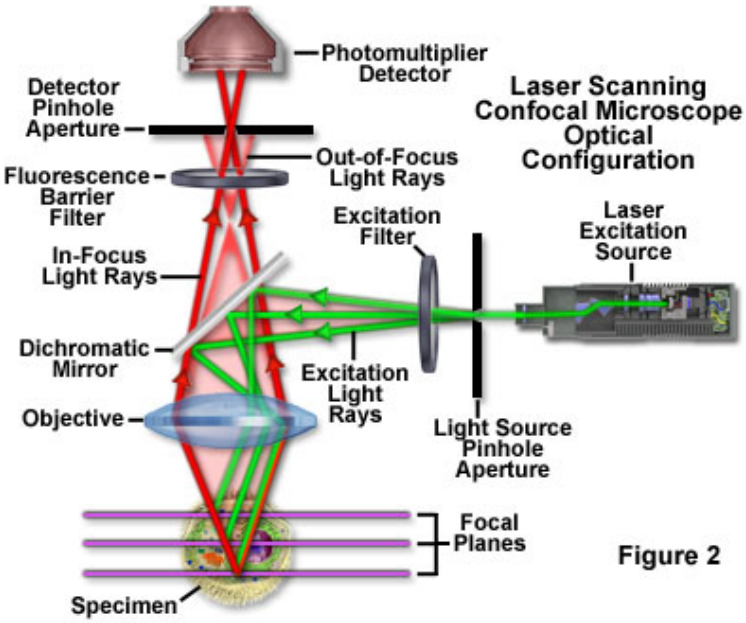

Figure 3.28: Schematics of a confocal microscope [188].

the specimen. The small spot is scanned over a defined area using the raster scanning to reconstruct the image point-by-point, following a definite pattern. Emitted light of a different wavelength travels back through the dichroic mirror and it reaches the second pinhole. This is the second main difference with conventional microscopy, where most of fluorescence emission light is gathered in the detector/camera, enhancing the background signal and resulting in a loss of image definition. In confocal microscopy, only photons coming from the plane at focus are perfectly aligned with the aperture and can reach the photomultipliers, while light from out-of-field planes is stopped by the metallic foil. This reduces the background signal and therefore the degradation of the image, offering better contrast and definition. Refocusing the objective shifts the excitation and the emission points to a new plane, therefore scanning the specimen in all its thickness. Moreover, the thickness of the focal plane is mostly defined by the inverse of the square of the numerical aperture of the objective lens, so the system has different pinholes apertures, to adjust this parameter. The resolution in the lateral plane x-y can be calculated as $d = \frac{0.37 \cdot \lambda}{NA}$ (for conventional microscopy: $d = \frac{0.61 \cdot \lambda}{NA}$), where NA is the numerical aperture and can vary between 0.6 and 0.15 μm, while on the z axis the minimum detectable thickness can easily be less than 500 nm.
In addition to other advantages, this technique reduces photo-bleaching, and does not require complicated sample preparation (protocols similar to the ones for conventional fluorescence microscopy can be used). Most importantly, the possibility to record different thin slices of the specimen opens the way for a 3D reconstruction, delivering a clear and realistic representation of the objects of interest.

As a drawback, costs of the machine are higher. The thickness of the samples that can be analysed is also limited by light penetration. Moreover, limited number of excitation wavelengths are available with common lasers.
Advanced microscopy techniques are available nowadays, usually falling into the category of *high-resolution* microscopy, such as stimulated emission depletion (STED) microscopy, and are currently being applied also to the study of radiation-induced DNA damage as done in this part of this thesis work (see *e.g.* the work by Reindl *et al.* [118]).

3.3.2 Objective

We present here results obtained by means of confocal microscopy for radiation-induced γ-H2AX foci. The first aim is to compare results coming from a 3D reconstruction of cell nuclei, that is possible with this kind of microscopy, to results obtained with 2D images, presented in the previous sections. To this aim, samples irradiated with X-rays and neutrons that underwent ICC staining have been acquired again with confocal microscopy. In addition, we here present a set of results coming from ^{12}C irradiations, as a representative case of high-LET exposures, for which conventional 2D microscopy can hardly give solid results. ^{12}C irradiations have been carried out at the National Centre of Oncological Hadrontherapy - CNAO, Pavia, Italy, as a pilot study on IMR90 cells only, and for a limited number of time-points (see "Material and Methods" Par.3.3.3). Image acquisition performed by means of confocal microscopy allows to visualize the streaks of very close foci generated by the high density of DSBs along the carbon track core.
In parallel with the new microscopy technique and the new set of data, we present an adaptation of the modelling approach, to relate the new experimental observations to actual predictions of DNA damage yields in 3D. In addition to possible artefacts coming from the scoring technique, in case of high-LET radiation a higher degree of clustering is found for the spatial distribution of initial damage, and what is experimentally counted as a single focus may contain more than one DSB. This has to be modelled or simulated, to provide information to *e.g.* compare the effectiveness of different radiation qualities.
In the long term, results from studies of this kind can potentially be collected in a database with yields of foci as a function of the particle, the dose, the LET, irradiation conditions and the read-out technique adopted for the scoring. Such a database could be queried for comparison to future experimental measurements and for biodosimetry purposes.

3.3.3 Material and methods

Culture protocols for experiments with IMR90 cells and carbon ions

The protocol for culturing IMR90 cells was the same as the one described in Par.3.1.5. For ^{12}C ion irradiations, the day prior the irradiation IMR90 cells were plated in 2 ml of complete medium in SlideFlasks (Thermo Fisher Scientific). For the γ-H2AX assay, $2 \cdot 10^5$ cells were plated, while 10^3 cells were plated in the same kind of flask and amount of medium for the survival experiment (see more detail below, Par.3.3.3, "Clonogenic assay").
Immediately before the experiments, the flasks had to be completely filled with medium, since they had to be placed vertically on the beamline. After the completion of the experiment, the whole amount of medium was completely discarded and it was changed with 2 ml of fresh complete one; afterwards flasks were placed back in the incubator for the endpoints of γ-H2AX foci induction or colony growth.

Carbon ion irradiation

^{12}C ion irradiations were carried out at the CNAO facility, Pavia, Italy. A dedicated treatment plan was developed by CNAO medical physicists for the irradiation, and different carbon energies were used to get a SOBP inside a cubic water phantom (in total 11 energies, from 186.9 to 213.8 MeV/u, each incrementing the penetration depth in water by 2 mm). The samples were positioned at a depth of 80 cm in the water box, for a total thickness in front of the biological material of: 6 mm plexiglass (phantom window) + 73 mm water + 1 mm plastic (flask bottom surface).
Active scanning was used to cover an area of 7×17 cm^2 in the transversal plane with respect to the beam direction, while the SOBP (constant physical dose) was of 2 cm width, with an average LET in the centre (at the sample position) of ~ 75 keV/μm.
The setup is shown in Fig.3.29. The doses used for the experiments (for both clonogenic and γ-H2AX foci assays) were of 0, 0.5, 1, 2 and 5 Gy, and the dose rate used is of ≈ 0.5 Gy/min. Non-irradiated samples were kept in a small container filled with water at the same temperature of that in the phantom ($\approx$ 21°C), for the duration of the longest irradiation (5 Gy).

Clonogenic assay

The preparation for the clonogenic assay following ^{12}C irradiations was carried out with the pre-treatment plating protocol: cells were directly plated at the right concentration for the growth of colonies the day before the experiment. Justification for the difference with respect to the previously adopted protocol (see Par.3.1.5 "Clonogenic Assay") lies in the different irradiation setup and experimental needs. We recall that, with such protocol, we do not have control of the number of cells that remain attached at the bottom of the flask because

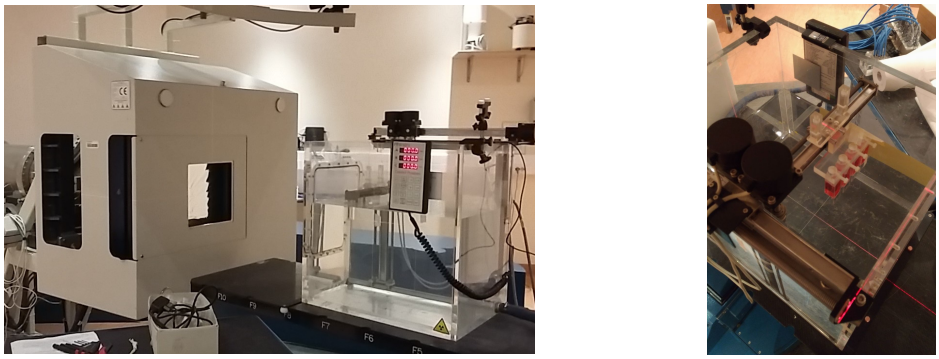

(a) (b)

Figure 3.29: Irradiation setup used for the ^{12}C ion irradiations at the CNAO facility. The water phantom is positioned on the beam line (a) and the biological samples are put at a depth in water of 80 cm (b).

of the stress induced by the long permanence outside the incubator. The same concentration of IMR90 cells was used, as the total area in a Petri dish and a SlideFlask is similar (10^3 cells for ~ 9 cm^2).
The protocol for staining the IMR90 colonies after the waiting time of 14 days (with a change of medium after one week) was the same as described in Par.3.1.5, "Clonogenic Assay". Unlike the irradiations with neutrons and X-rays, results are presented as mean ± SEM of two technical replicates and a biological duplicate.

ICC and confocal microscopy

The protocol for ICC treatment of the new samples irradiated with ^{12}C ions was maintained the same, except for the incubation with the secondary antibody (Abcam 555 anti-rabbit), performed at a concentration of 1:200 and for 1 hour. Cells were fixed at the following time-points: 30 min, 1 h, 3 h, 24 h post-exposure.
For what concerns the acquisition with a confocal microscopy, the Leica TCS SP5-II microscope available at the facilities of "Centro Grandi Strumenti" (University of Pavia) was used. Image acquisition of IMR90 cells was performed using an oil-immersion 63X objective and then applying a further digital magnification of 2.5X. Different focal planes were acquired at a distance of 200 nm from each other, for a total of 30-70 layers, depending on nuclei thickness. The spatial resolution in the longitudinal plane was of 200 nm. The bottom/top layers limiting the nuclear volume for the acquisition were selected using the DAPI signal, to be sure to consider all foci in the volume and to exclude non specific signals from possible debris in the fields.
A number of approximately 60 cells was acquired per condition, and pleomorphic and apoptotic cells were excluded from the analysis.
Results are presented as mean ± SEM from one single technical replicate of

each of the two biological replicates available for the ^{12}C-irradiated samples.

ImageJ analysis

The macro for the recognition and scoring of γ-H2AX foci in cells irradiated with X-rays and neutrons was adapted to consider the several slices acquired with the confocal microscope.
As a first step to evaluate the differences between the two microscopy techniques, and in particular to highlight the effect of considering only a slice at focus in conventional microscopy, we project all planes acquired with the confocal microscopy onto a single 2D image, and then apply the same macro that has been previously described for single images. The "Z-Projection" step was therefore done for of all the regions of interest (ROIs) for both the blue (DAPI) and the red (γ-H2AX foci) channels, and a final ROI recognition was performed in the same way as before (see Par.3.1.5). A further adjustment is needed for the parameters related to the size threshold, to take into account the different magnification of the images taken with the TCS SP5-II confocal microscope.
For a rigorous quantification of foci in the whole nuclear volume in 3D, the analysis of individual confocal images and of the spatial/intensity distribution of the objects therein contained will be needed. A fully 3D reconstruction algorithm is currently under development at the time this thesis is written. See *e.g.* the work by Jezckova *et al.* [189] for possible strategies for future improvements of the analysis presented in this part of the thesis.

PARTRAC simulations

In the experimental setup, the cell layer was positioned at the centre of the 2-cm SOBP. The full reproduction of the SOBP used for irradiation in water would require: the implementation of the different carbon-ion energies at the beamline exit, if known; otherwise, transport of ^{12}C ions in the accelerator, through the last passive elements, and in all elements before the target (mainly the water phantom) has to be simulated; finally the modelling of the scanning beam at different depths along the SOBP. Being the characterization of the CNAO ^{12}C ion beam out of the scopes of this thesis, we used the average LET of the ions at the target position. It is also reasonable to assume that primary ^{12}C ions play the major role in the induction of foci, and we neglect the possibility of secondary fragments hitting the cells.
We used a single energy of 310 MeV for the ^{12}C source implemented in the track-structure code PARTRAC, selected (based on SRIM/TRIM tables) such that the average LET expected in the cell nucleus is of ≈ 75 keV/μm, the same as in the experimental setup.
Since the experiments were carried out on IMR90 cells, the fibroblast-like nuclear model implemented in the code has been chosen for simulations, as done in Par.3.2. Particles are generated randomly from a plane attached to the

bottom surface of the cytoplasm, almost perpendicularly to the nucleus, until the desired doses (0.5, 1, 2, 5 Gy) are imparted to the nucleus.

Clustering algorithm for the results with confocal microscopy

Two different modelling approaches were developed, with two different aims:

- "Z-projection" method: reproducing the results from the ImageJ macro when applied to the single image obtained by projection and superimposition of all focal planes acquired by confocal microscopy. This is easily done by increasing the *slice thickness* parameter Δz to the total nuclear thickness of the nucleus. DSBs are then projected in a 2D plane, and then clustered with different values of r, following the algorithm presented in Par.3.2.3, "Development of an unsupervised clustering algorithm";

- "3D reconstruction" method: reconstructing foci in 3D, for the final correlation with confocal microscopy results. For this purpose, DSBs and more complex lesions were simulated, and their spatial distribution and coordinates in the whole nuclear volume kept for further analysis (as previously done). In the case of a 3D reconstruction, instead of projecting onto a plane before clustering, first-neighbour lesions are searched within spherical volumes, with a radius equal to the resolution parameter r intended as geometrical distance in space. DSBs densely packed along the track of a high-LET particle will be grouped together in a same streak of foci, as shown in Fig.3.30.

The same approaches have been adopted for simulations of X-rays and neutrons (*i.e.* their secondary particles), where the starting point has always been the set of simulation results previously obtained.

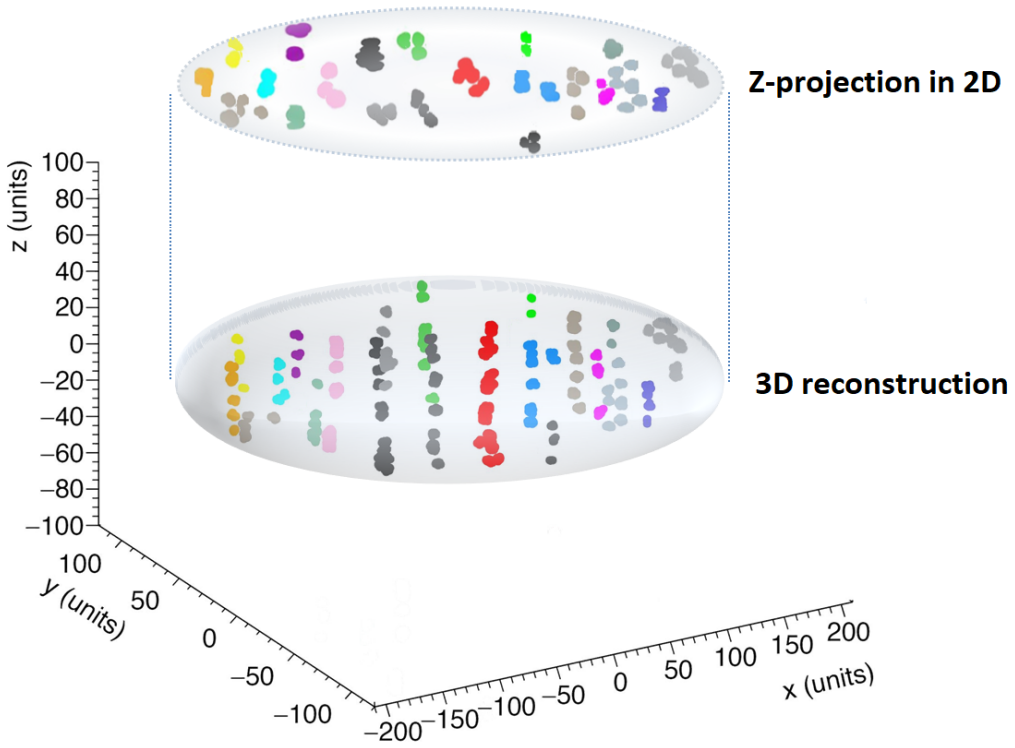

Figure 3.30: Illustration of the "3D reconstruction" method applied to distributions of DSBs due to 5 Gy of 300 MeV ^{12}C ions (bottom part of the figure). In the upper part, projection of the whole damage content onto a 2D plane, as it would result from the "Z-projection" method.

3.3.4 Results and discussion

Survival curves. The survival curve obtained by the analysis of colonies following ^{12}C irradiation is shown in Fig.3.31, along with the ones for X-rays and neutrons. Despite being seeded one day before the irradiation for practical

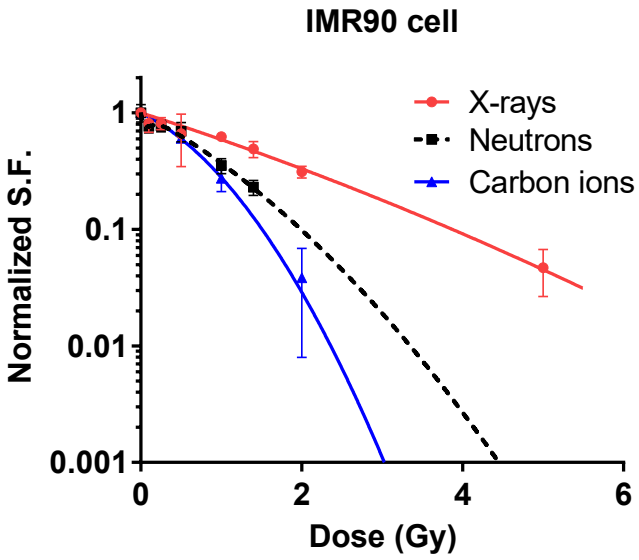

Figure 3.31: Survival curves for IMR90 cells exposed to X-rays and and neutrons (as in Fig.3.5(a)), with the addition of the new data for carbon ions. The fit of the latter has been obtained by means of the LQ model. Data related to carbon exposure are presented as mean values ± SEM values of two independent experiments.

reason, the change in the protocol is safely assumed to not alter the number of cells receiving the treatment, as the cell require some time (several hours) in order to attach to the bottom of the flask and their doubling time has been estimated to be around 36 h. Instead, as mentioned in Par.3.3.3, it is possible to have a loss in the cell during the handling of the flasks during the experiment at CNAO.
As already mentioned in Par.3.1.6 for the survival curves following neutron exposure, for high-LET radiation the role of potential lethal damage is less relevant than in case of low-LET exposure [157], because direct radiation action mainly conveys the induction of the damage, with lesions densely concentrated in same portion of DNA and therefore resulting in lethal damage. For instance, Autsavapromporn *et al.* (2011) reported that high-LET radiation (at similar initial damage level to low-LET-induced one) do not induce PLD repair, and toxicity increased with post-irradiation time [190]. Liu *et al.* (2013) confirmed the results following measurement of clonogenic death of confluent AG01522 fibroblasts: cells irradiated with X-rays and mid-LET Si ions (55 keV/μm) showed significant increase of cell survival, when allowed to repair

for 12 h, while for heavier-ions (200 and 500 MeV/u Fe ions, LET = 440 and 200 keV/μm respectively) no changes were observed [156].
Even if the IMR90 cells have been seeded the day before our experiments, the chosen seeding density was such that they cannot reach the confluence even 14 days post-irradiation, and they are grown in complete medium, meaning that cells should be proliferating. This allows to exclude the possibility of repair of potential lethal damage anyhow.
As it can be seen, ^{12}C is the most effective radiation quality for the induction of clonogenic death. The fit with the LQ model yields α and β values of 0.78 $\pm$ 0.04 Gy^{-1} and 0.50 $\pm$ 0.05 Gy^{-2}, respectively. The surviving fraction at 2 Gy (SF_2) is equal to 3%, while D_{10} = 1.5 Gy, D_{37} = 0.83 Gy, D_{60} = 0.49 Gy. This provides RBE values of 2.58, 2.18 and 1.96 respectively for the 10%, 37% and 60% survival levels, and $\alpha_C/\alpha_X = 1.53$ (using $\alpha_X = 0.51$, from Tab.3.1). The RBE is found to decrease for decreasing doses (higher survivals), unlike what usually found for RBE estimates from clonogenic assay. This is due to the shape of the curves resulting from the fit: an almost linear curve for the X-rays has been obtained, with $\beta \approx 0$ from the LQ model; on the other hand, the best fit for ^{12}C ions has a $\beta = 0.5$, which makes the curve bend down more steeply than the X-ray one. For this reason, the two functions are meant to diverge for higher doses and they will never intersect.
It can be also observed that these RBE values are slightly higher than neutron RBE values for IMR90 cells, when the LQ model is adopted to fit neutron data, but lower if the doses are extracted from the fit with the HS model.

γ-H2AX foci yields as a function of dose. We report in Fig.3.32 γ-H2AX foci yields in IMR90 cells for selected time-points as a function of dose, obtained analysing the superposition of all images acquired by confocal microscopy for irradiations with X-rays, neutrons and ^{12}C ions. For direct comparison, data obtained with conventional microscopy (a single 2D image) are also shown for X-rays and neutrons.

As expected, the use of confocal microscopy allows to count higher foci yields. Nevertheless, a saturation of the signal as a function of increasing dose (roughly after 2 Gy for X-rays and ^{12}C ions) is still observed, in particular for foci scored at the earliest time points, in the same dose range for the signal measured with conventional microscopy. The saturation is less evident for neutrons, but the maximal dose is lower in this case. At the latest time point (24 h), few foci persist after exposure with all radiation qualities, which means they are easier to count, and the signal as a function of dose seems to go back to linearity. Interestingly, a dose dependence for this late time point could not be assessed for neutrons from conventional microscopy, but becomes clear if confocal microscopy is used.

To discuss why the saturation trend appears also when confocal microscopy is used, we propose the following considerations (also supported by sample images shown later in this chapter).

We first recall that experimental findings presented here have not been analysed with a 3D reconstruction algorithm. The thickness of the slice from confocal microscopy is of about 200 nm. A single focus is likely to be sliced, and appear in more than one plane. This would be of concern when images from different planes are analysed separately, possibly leading to an overestimation, but this is not the case here, as we project and merge all planes before foci scoring. Therefore, this is not affecting our results. However, the projection and merging step itself can lead to the overlap of well-separated foci belonging to different planes. As a result, when the clustering according to the resolution parameter is applied on the final 2D image, foci will possibly include different sub-structures with individual morphologies, that are no more distinguished by the algorithm. This plays a role in the underestimation. For sparsely distributed damages resulting from low-LET radiation, this becomes more important the higher the number of damage sites in the nuclear volume is, thus leading to saturation for higher doses.

In the case of ^{12}C ions an additional factor comes into play: in our experimental irradiation setup, the beam is impinging perpendicularly onto the cell layer. Therefore, foci will be distributed in streak-like structures [191, 192] along the axis of the beam traversal in cell nuclei. By projecting along the same axis, a streak-like structure, ideally comprising many damage sites, will be seen and counted as a single focus (with higher intensity and transversal cross-section). This factor plays a major role in underestimation of foci yields following ^{12}C exposures.

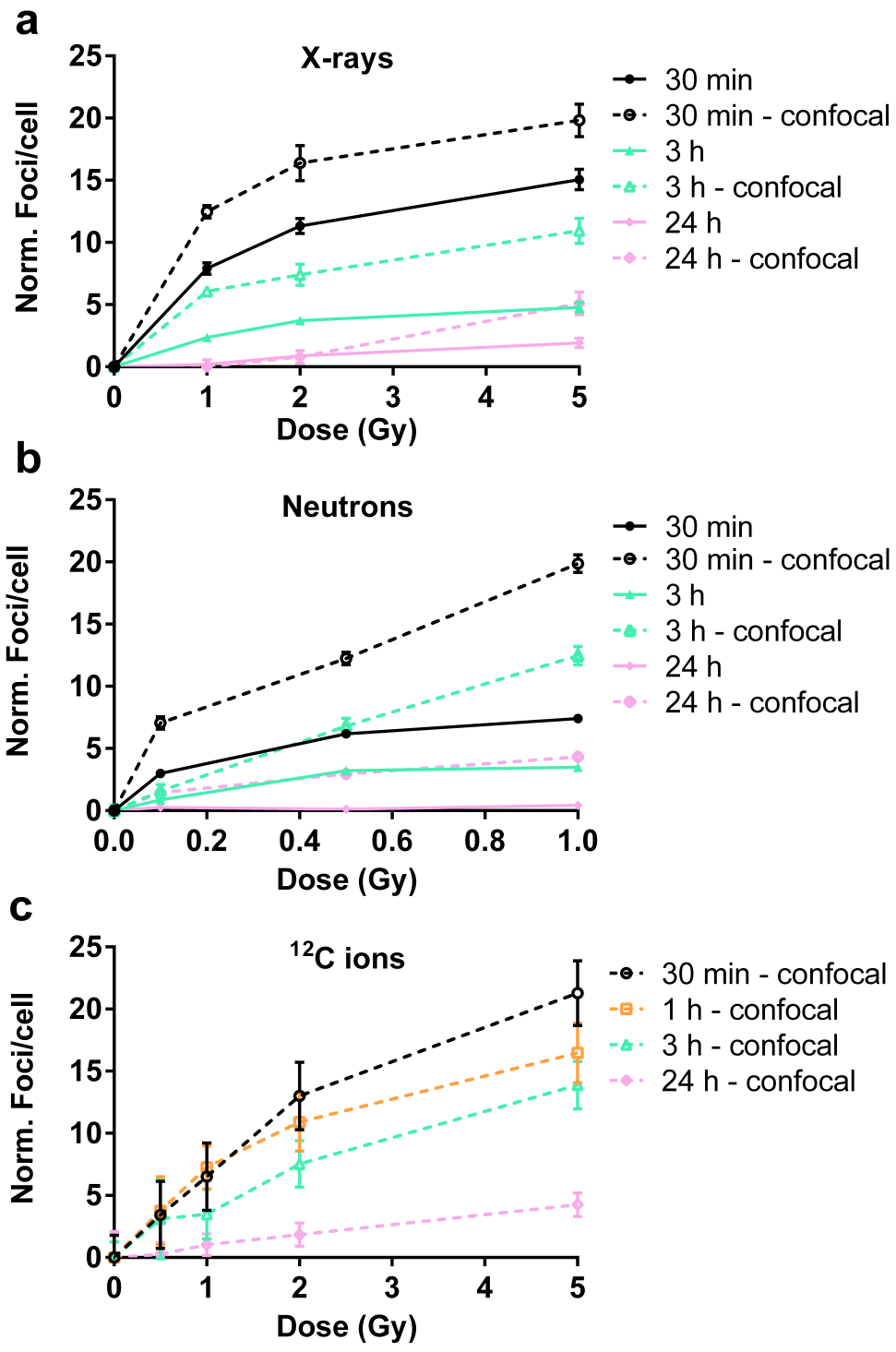

Figure 3.32: Dose dependence of yields of ΔFoci (above sham values) in IMR90 cells exposed to (a) X-rays, (b) neutrons and (c) carbon ions. Results from conventional microscopy are reported (solid lines). The lines are drawn to guide the line.

Finally, the neutron case (Fig.3.32(b)): for both neutrons and X-rays we expect a sparse distribution of events in the nuclear volume. Overlaps of well-separated foci belonging to different planes could occur as a consequence of the projection and merging steps. However, we also expect that neutron-induced foci will enclose highly clustered damage as that induced by slow recoiling ions, and possibly also show streak-like structures, corresponding to the track of the recoiling particle in the nucleus. Due to isotropy in the irradiation conditions, these (however short) streaks would be randomly oriented. If such a structure appear as a single focus (again, larger and with higher intensity), we underestimate foci yields. In conventional microscopy, both the selection of a single slice when the damage is sparse in 3D and the fact that damages can be clustered play a role in the underestimation of foci yields, with a clear saturation of the signal already below 1 Gy. The use of confocal microscopy seems to partially compensate for this, and the saturation is less evident (though, as already mentioned, the maximal dose is lower).
Overall, the use of confocal microscopy (though sub-optimal with the analysis strategy we applied here) makes possible the comparison in effectiveness between X-rays and neutrons from our datasets, at least up the maximal neutron energy of 1 Gy. Also, as already commented, it allows to recover a dose dependence for residual neutron-induced foci. On the contrary, yields for carbon-induced foci are largely underestimated, and the comparison in effectiveness with reference X-ray data is not possible: very similar foci yields are found 30 minutes after irradiation for the highest dose of the two radiation qualities, which would lead to a RBE of about one, not coherent with the survival data. Nevertheless, relative yields of foci cannot be straightforwardly correlated with the survival, because the loss of clonogenicity is not simply determined by the number of DSBs, but their complexity influences the cell fate: an increased complexity is usually translated in deficient repair, thus, greater biological effectiveness [193], as it was demonstrated experimentally by Jenner *et al.* (1993) [194] and Asaithamby *et al.* (2008) [195]. They showed a slowing-down of DSB repair for high-LET IR, eventually resulting in mutagenic (due to illegitimate recombination) or lethal consequences [196].
The best-fit curves for foci yields from confocal microscopy as a function of the dose are shown in Fig.3.33: Eq.3.8 generally provides a good fit for X-rays (a) and carbon-induced (b) foci yields but, in both cases, the trend seems to go back to linearity as a function of dose for residual foci at 24 hours. For neutrons, the fit has been performed using Eq.3.8 (c) or a simple linear function (d). Neutron data seem to be well described by linear trend, though neither Eq.3.8 nor the linear function seem to provide a satisfactory reproduction of data for the earliest time point. Overall, fit results confirm the considerations done discussing the data in Fig.3.32.

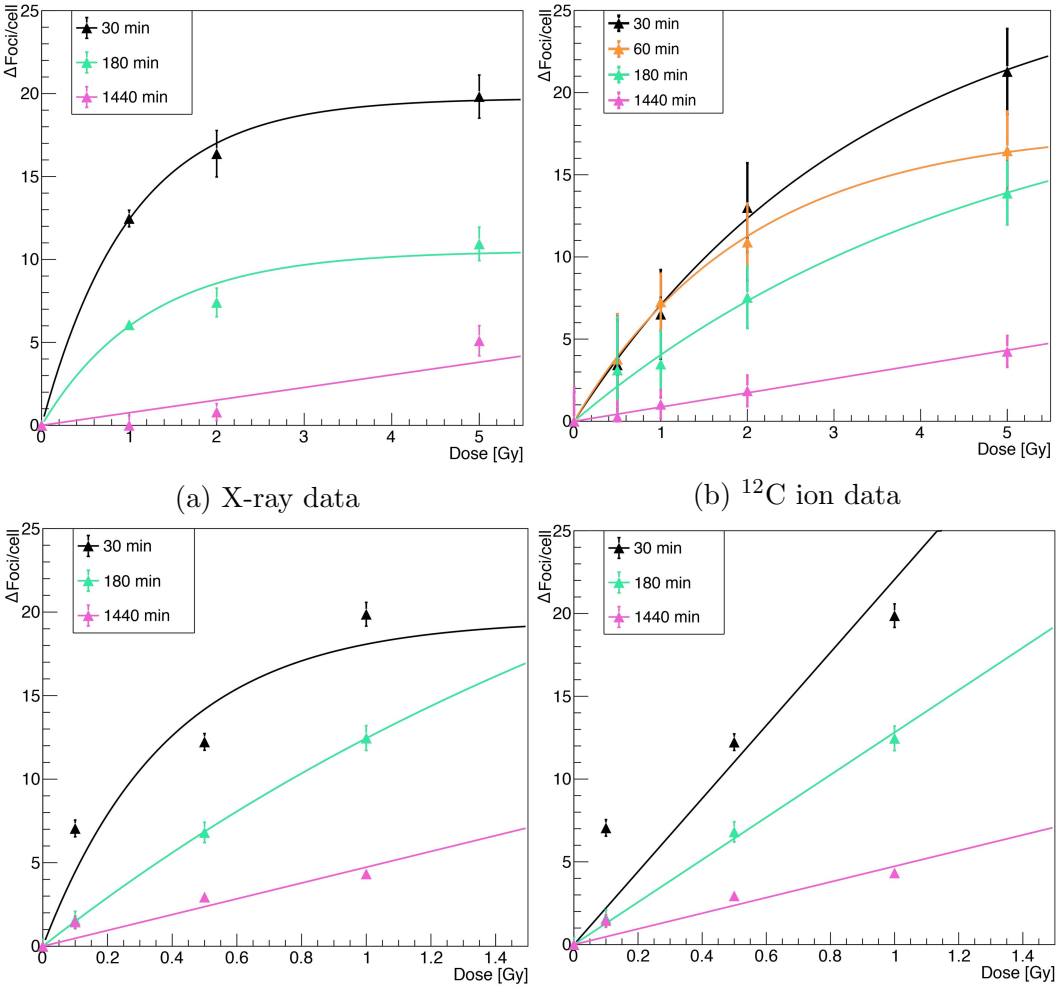

(a) X-ray data

(b) ^{12}C ion data

(c) Neutron data

(d) Neutron data - lin.

Figure 3.33: The yields of foci in IMR90 cells exposed to (a) X-rays, (b) carbon ions and (c-d) neutrons, scored following ICC and confocal microscopy have been fitted using Eq.3.8 for Figg.(a-c), while in Fig.(d) a linear fit has been performed, by means of the ROOT toolkit. Black - 30 min; orange -60 min; green - 180 min; pink - 24 h.

Fig.3.34 shows the detected foci size, always as a function of the dose. It can be observed that, at early time-points (30 min), there is a slight increase in foci dimensions for all radiation qualities as a function of the dose. This is more accentuated for 5 Gy of X-rays, while for ^{12}C ions the increase is much smoother, with a maximum at 2 Gy. This is due to the fact that foci are still well separated and countable in that dose range, shown by the almost linear trend in the yield of ^{12}C-ion-induced foci shown in Fig.3.32(c). For most conditions, the saturation in the number of foci is therefore compensated by an increase in foci size, justified by either the overlap of different foci or higher complexity. Another characteristic that can be observed is that foci dimensions are bigger for the early time-points for X-ray- and neutron-induced foci, even if in the latter case the curves are similar to each other. On the contrary, for ^{12}C ions the size is bigger 24 h post-irradiation. This is due to the fact that the residual damage following exposure to high-LET ^{12}C ions is more complex, and therefore more spatially extended, than the one from X-rays and neutrons. As mentioned before, this could also lead to the accumulation of heavily damaged sites in specific regions of the nucleus, for their processing in a single place where all the repair proteins are recruited to [170]. Comparing the plots for neutrons and ^{12}C ions in Fig.3.32(b-c) and Fig.3.34(b-c), we can see the level of the residual damage (yields) at 1 Gy is comparable, while the size of these IRIF is definitely smaller for neutrons ($\sim 0.75\ \mu m^2$) with respect to ^{12}C ions ($\sim 1.9\ \mu m^2$): this means that the higher damage complexity due to ^{12}C ions results in unsolved damage still after 24 h.
Moreover, the difference in morphology between both ^{12}C-ion- and neutron-induced foci, with respect to X-rays, can also be observed 30 minutes post-IR: following 1 Gy exposure, the foci sizes for the fist two radiation qualities are bigger than the one for X-ray foci, with values of respectively 1.30 and 1.26 μm^2 *vs* 0.85 μm^2.

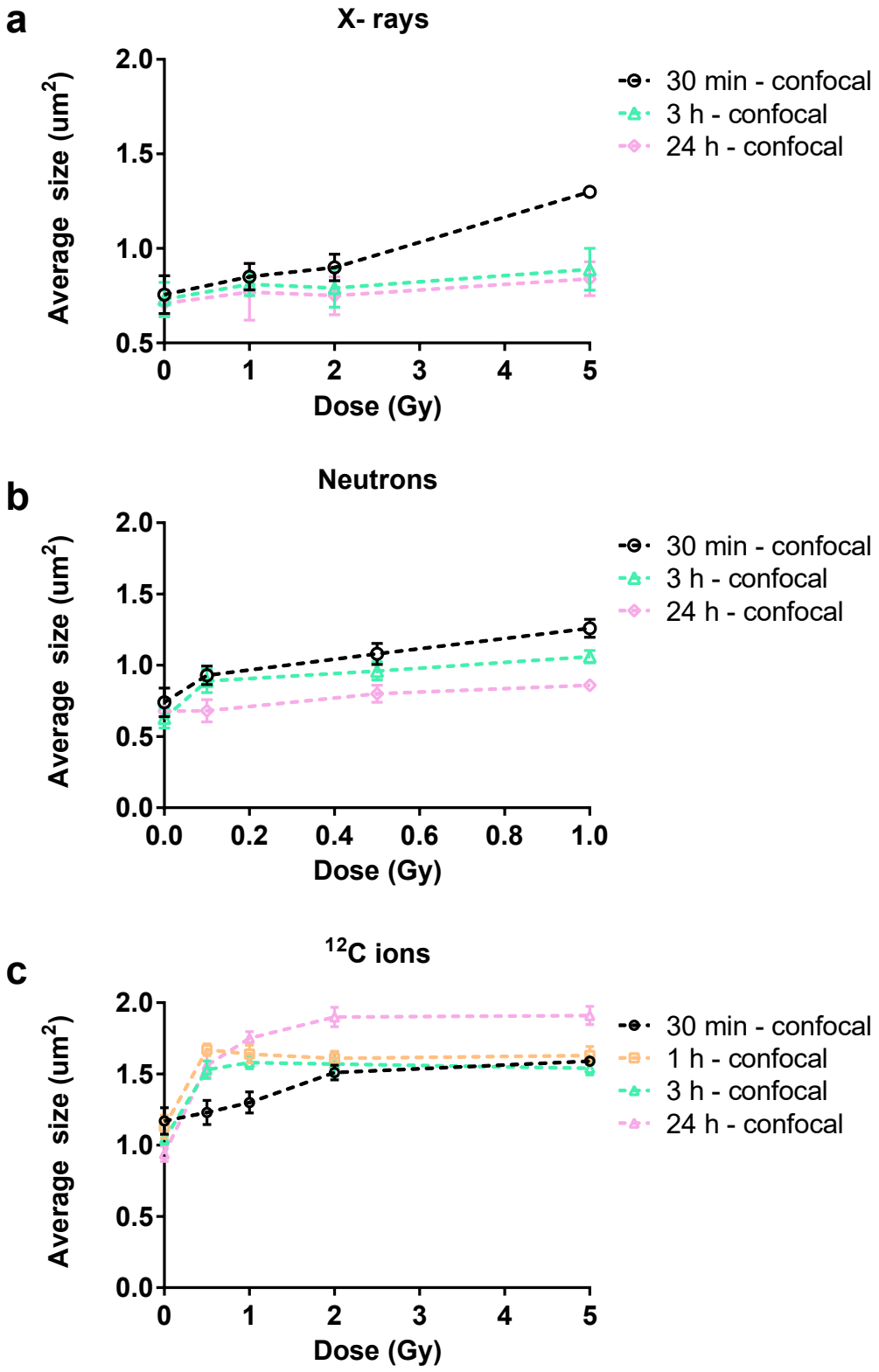

Figure 3.34: Dose dependence of foci size (μm^2) in IMR90 cells exposed to (a) X-rays, (b) neutrons and (c) carbon ions. The lines are drawn to guide the line.

γ-H2AX foci kinetics. Fig.3.35 shows the full kinetics for the three radiation qualities under study, also comparing foci yields obtained with conventional and confocal microscopy for X-rays and neutrons. As previously

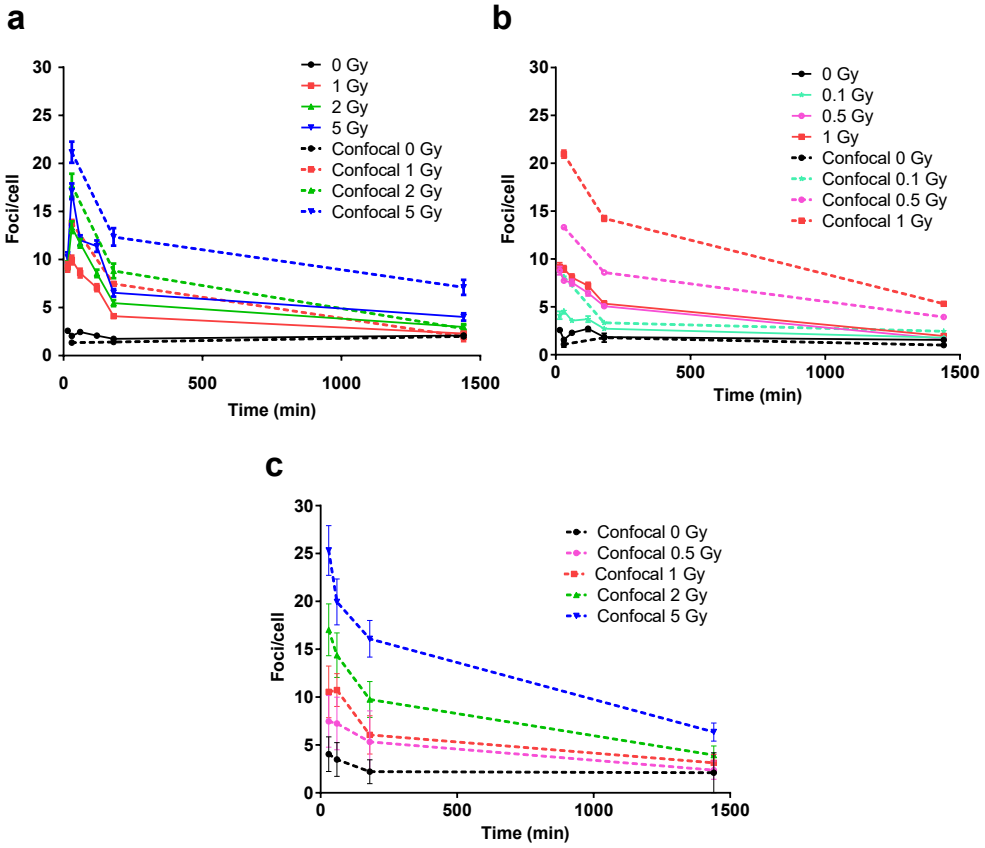

Figure 3.35: Repair kinetics of γ-H2AX foci for IMR90 cells, following irradiation with X-rays (a), neutrons (b) and carbon ions (c). Solid lines represent the data of Fig.3.1.6. The errors on the new experimental points (dotted) represent the SEM of a biological duplicate (1 technical replicate) for ^{12}C, and of 1 biological replicate (technical duplicate), for X-rays and neutrons. Lines are drawn to guide the eye.

observed, foci yields are higher when confocal microscopy is used.
As far as the kinetics is concerned, the overall shape of the curve remains unchanged, with the 30 min time-point corresponding to the maximum of the signal for all radiation qualities. In particular for neutrons, it is evident that the set of data obtained with confocal microscopy is necessary to conclude that after 24 h repair seems to be still ongoing, with residual foci data found to be dose-dependent above background levels. Though significantly affected by underestimation, carbon data show a clear kinetics and residual foci yields above background, again in a dose-dependent manner.

γ-H2AX foci topology from plane reconstruction from microscope images. The Leica LAS X software package [197] allows the reconstruction of foci in the transversal sections (x-z, y-z) of the nucleus for each single image. We here apply this to illustrate the difference in the topology of foci. In Fig.3.36 x-z views from carbon, X-ray and neutron irradiated (1 Gy) cells are shown: from these images it is easy to appreciate the differences between foci, with small streaks [198] of red-coloured foci going through the whole nucleus depth in the carbon case (a), more point-like structures for the X-ray case (b) and an intermediate situation for the neutron case (c). Even if not quantitative, this comparison provides a clear example of the differences in foci structure in case of exposure to different radiation qualities. This further underlines the importance of the analysis of spatial distribution of damage and its clustering in radiation-induced foci, for which modelling efforts as presented in what follows can be of great help.

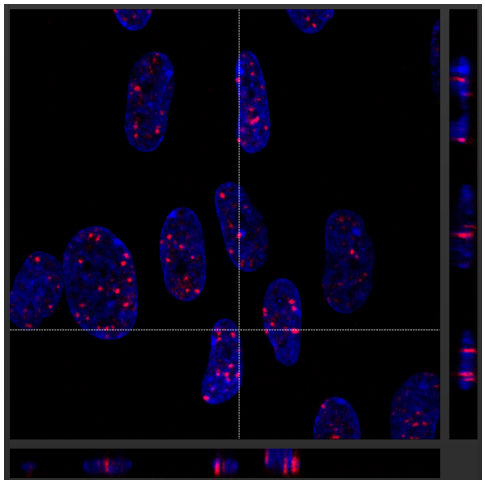

(a)

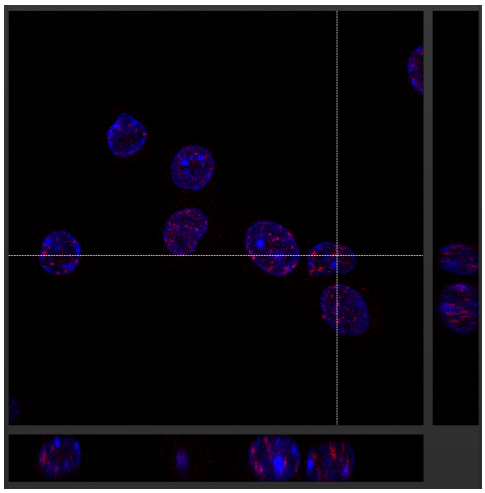

(b)

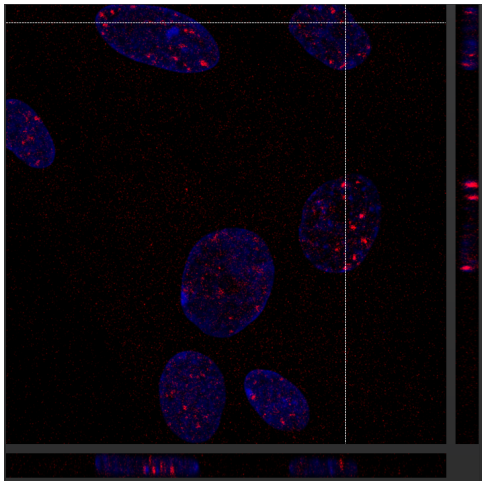

(c)

Figure 3.36: Images from the Leica LAS X software: IMR90 cells irradiated with 1 Gy (a) ^{12}C ions, (b) X-rays and (c) neutrons, 30 min post-IR. Laterally, x-z and y-z views of the morphology of the foci crossed by the viewfinder's dotted lines.

Monte Carlo simulations. Results obtained by the "Z-projection" method (Δz=5.4 μm) are shown in Fig.3.37, for X-rays and for the considered secondary species accelerated by neutrons (p, C, O). Experimental data are shown together with simulation results: in Fig.3.37(a-b) data and simulation points are from X-ray irradiations; in Fig.3.37(c-d) data for neutron-induced foci are shown together with calculations for secondary protons only; in Fig.3.37(e-h) we show simulation results for ^{16}O and ^{12}C ions. As done in Par.3.2.4, a weighted sum of damages induced by secondary particles is needed to directly compare neutron-induced damages and simulation results. This is done later also for this dataset acquired with confocal microscope. Unlike the 2D case, here no cells will be deprived of foci (even for low dose or few particle runs), as the whole cell nucleus is considered in the two reconstruction methods and at least 1 DSB is expected for the IRs under investigation.
For low doses of X-rays (Fig.3.37(a)), the yield of foci in fibroblast nuclei for the "Z-projection" method and $r = 0.5$ μm is consistently higher than what found experimentally for most of the conditions, and this remains true also increasing r. Increasing the dose, a larger *clustering radius* leads to either a saturation or even a decrease of foci yield, due to a significant clustering of the events. With the largest *clustering radius* (r=1 μm), expected yields are above the experimental data up to the maximum dose, but below the point for the highest dose. As far as the size is concerned (Fig.3.37(b)), $r = 0.5$ μm seems to best reproduce the experimental observation at all doses, and no dose dependence is observed or predicted with such *clustering radius*.
Experimental data for neutrons seem to be close to predictions for yields and size of foci induced at the same total dose by secondary protons only, with a clustering parameter of $r = 0.5$ μm, as it can be seen in Fig.3.37(c-d). However, it has to be recalled here that for protons it was impossible to run simulations with the same irradiation setup and the ellipsoidal nucleus: simulation results obtained for spherical nuclei are available (nucleus thickness of 10 μm instead of 5.4 μm) and shown in the Figure, as well as used for further analysis. We know already that the largest component of neutron-induced damage is due to secondary protons, but, to perform a direct comparison with experimental data, we need to sum all damages with a dose weight, as done hereafter for the same set of predictions at $r = 0.5$ μm. For 1 Gy neutron irradiation, around 20 foci are scored experimentally: proton-induced foci alone are estimated to be $\sim$ 18.5 foci for a dose of 0.75 Gy, 5 foci come from γ-rays, while $\sim$ 1.5 foci are induced by ^{16}O/^{12}C ions, in average in 28% and 8% of the cells, respectively. This scheme leads to a slight overestimation of predicted yields with respect to experimental data. As already mentioned when discussing results in Par.3.2.4, the geometrical shape for IMR90 cells might not be accurate enough for the reproduction of experimental data. Together with the need to mix different nuclear models for the prediction of neutron-induced yields, this might explain the observed discrepancy between predictions and experimental data.

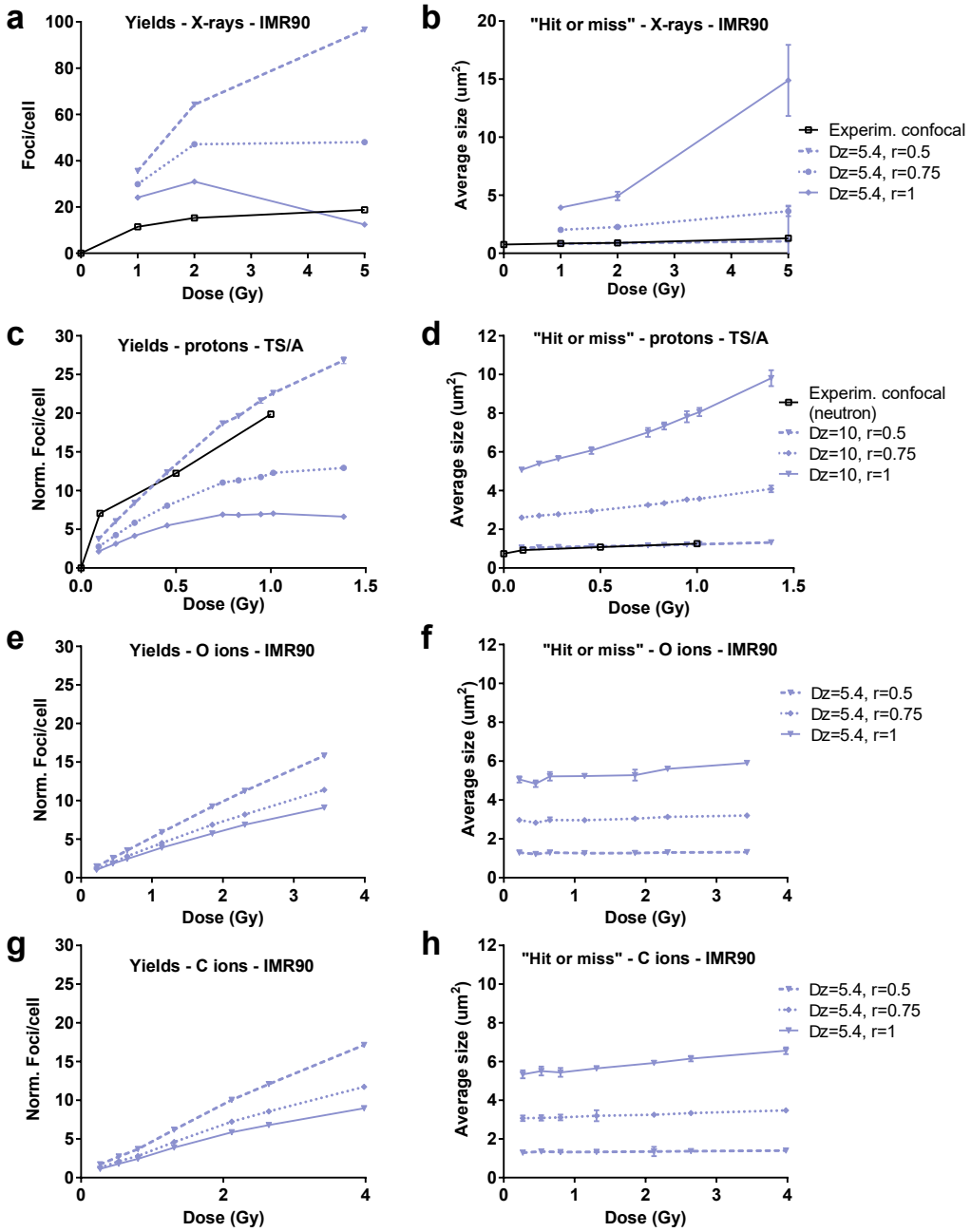

Figure 3.37: Yields of γ-H2AX foci/cell and foci size (in μm^2) as a function of the dose, for the IMR90 cell nuclear model. Results for X-rays irradiation: (a) yields, (b) size. Results for protons: (c) yields, (d) size. Results for ^{16}O ions:(e) yields, (f) size. Results for ^{12}C ions: (g) yields, (h) size. Δz is equal to 5.4 μm (except for protons, 10μm) and different r have been tested. The values for Δz and r are expressed in μm. The lines are drawn to guide the eye. Experimental results from exposure of IMR90 cells to X-rays and neutrons are also shown.

A summary of the coupling scheme is reported in Fig.3.38.
Fig.3.39 shows the predicted yields of ^{12}C-ion-induced foci obtained with

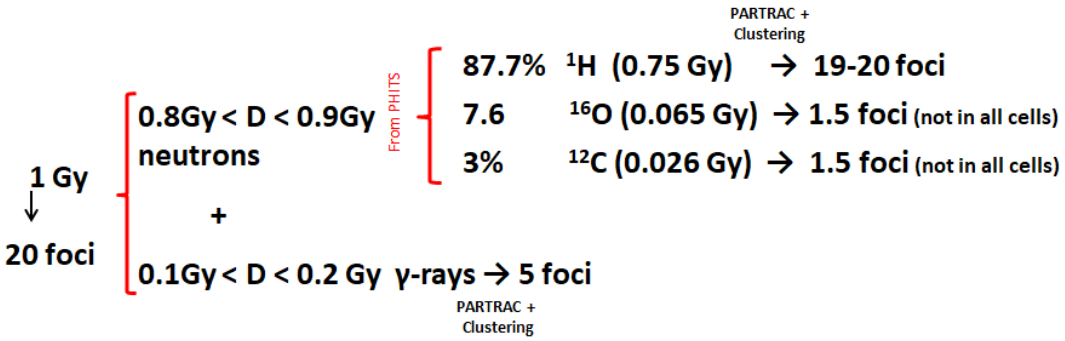

Figure 3.38: Summary of foci yields due to γ-rays and neutron-induced charged particles (^{1}H, ^{12}C, ^{16}O), weighted for the dose contributions to the total neutron dose of 1 Gy, when simulated considering the whole nuclear volume.

the "Z-projection" method. The best agreement for the foci yields seems to be achieved using a *clustering radius* of 1 μm, as shown in Fig.3.39(a). The simulated yield of foci is however slightly higher: in case of X-ray and neutron exposure, we justified this assuming that the experimental IRIF yield (30 min post-irradiation) did not reflect the number of initial DSBs, as the repair might have removed a fraction of them in the meanwhile.

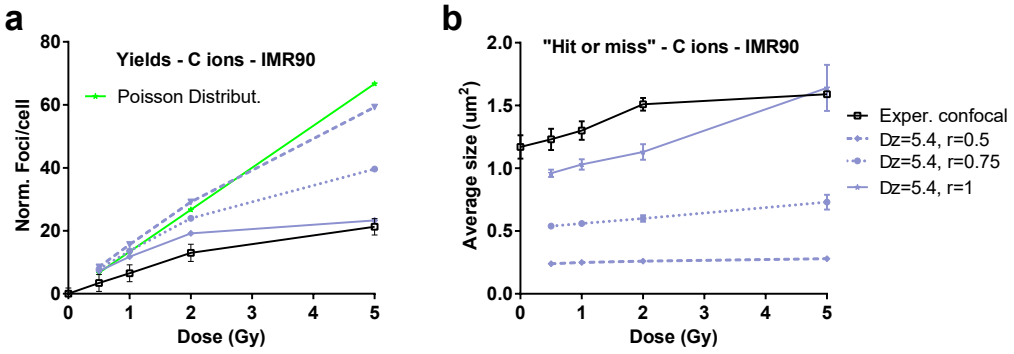

Figure 3.39: Yields of γ-H2AX foci/cell (a) and foci size (in μm^2) (b) as a function of the ^{12}C ion dose, for the IMR90 cell nuclear model. Reconstruction is done for Δz=5.4 μm and different values of r, expressed in μm. The lines are drawn to guide the eye. Results are presented as mean $\pm$ SEM for different runs. Experimental values for IMR90 cells irradiated with ^{12}C ions are also shown. Data in green are the number of expected particle hits (average of a Poisson distribution).

The simulations, instead, are built on the hypothesis that each initial DSB from PARTRAC gives rise to a focus, leading to a possible discrepancy of the IRIF number. However, for ^{12}C ions it can be reasonably stated that most DSBs are not repaired because of their higher complexity degree. The difference between calculations and the measurements could then be explained again by a pronounced saturation of yields due to technique-dependent limitations.
In the same Figure, we also show the expectation in terms of particle traversals based on Eq.2.4 (green curve labelled "Poisson Distribution"): given the geometric cross-section of the target (the nuclear surface), the dose and the particle LET, we can calculate the number of particles hitting the cell. In particular, we used a LET value of 75 keV/μm, doses of 0.5, 1, 2, 5 Gy, and nuclear axes as in PARTRAC (5.1 and 10 μm). Information on the number of tracks that will transverse the nucleus at a given radiation dose can be easily correlated with the number of foci seen in a 2D plane, as foci are the results from irradiation with a perpendicular beam in our setup. The agreement between the expected number of particles and the experimental foci yields is soon lost as the dose increases: the number of hits per nucleus does not take into account the spatial extension and distribution of the events, while foci resulting from different particle tracks can merge, leading to saturation of the signal. It can be observed the green curve is in agreement with the calculation results obtained using $r = 0.5$ μm. If the foci size is now considered, Fig.3.39(b) shows that, even with $r = 1$ μm, we do not have agreement with the experimental data until 5 Gy of ^{12}C. Overall, this shows that the "Z-projection" method is reconstructing more foci with smaller dimensions with respect to experimental observations, where a higher degree of clustering has been found.
Finally, we turn to an analysis of the DSB content in foci scored in whole nuclei, which is ultimately necessary for the evaluation of radiation effectiveness, as previously discussed. Fig.3.40 shows the yields of foci scored with the "3D reconstruction" method, together with the average total number of DSBs predicted by PARTRAC for X-rays, secondary protons (from the investigated neutron spectrum) and carbon ions. For low-LET radiation, the "3D reconstruction" method leads to small spheres representing the physical extension in space of single foci, that will be sparsely distributed in the nucleus. For high-LET particles, DSBs found in close spatial proximity will be enclosed in a single focus; possibly also streaks of foci will be formed by merging damages along the particle track, as it can be expected from what observed in microscope pictures (see Fig.3.36). The situation is expected to be similar for secondary-proton-induced foci.

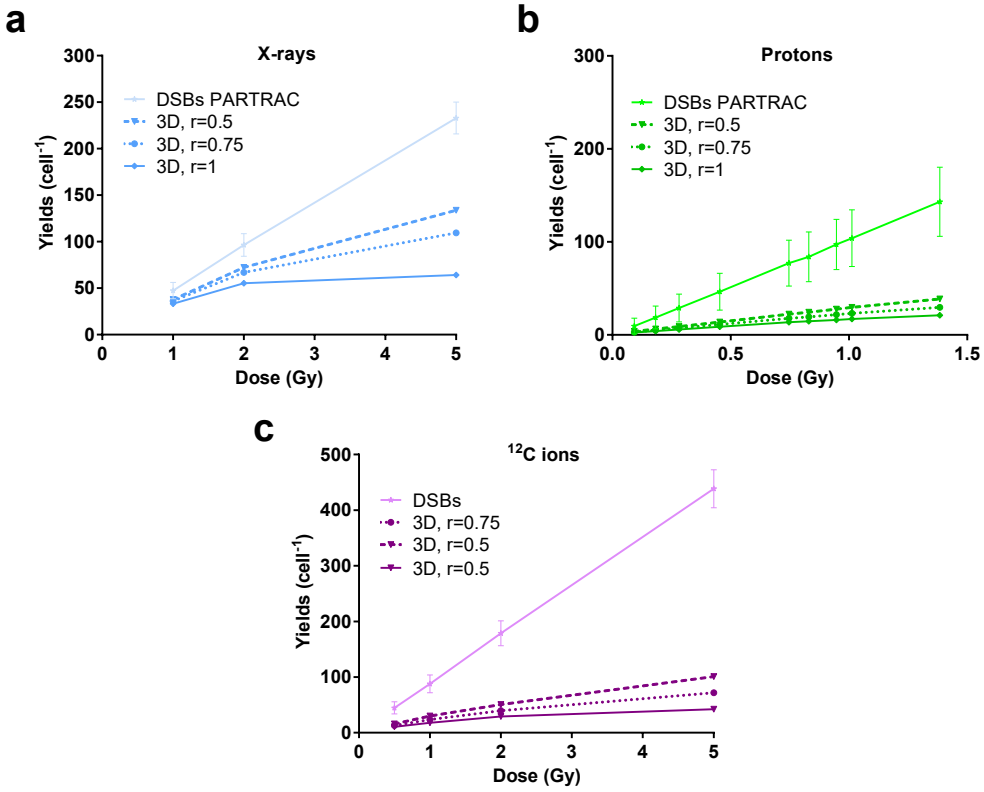

Figure 3.40: Comparison of the dose dependence of the DSBs predicted by PARTRAC and of the foci reconstructed in the whole nuclear volume for (a) X-rays (spherical), for (b) neutron-induced secondary protons (spherical) and (c) ^{12}C ions (ellipsoidal), as extracted from the "3D reconstruction" method.

DSB yields are always higher than foci yields, also for the case of X-rays, which brings to the conclusion that the 1:1 correspondence (assumed at least for low-LET radiations) can lead to a wrong evaluation of radiation effectiveness, also with a full 3D reconstruction of foci. DSB content information has also to be supplied, with the support of modelling, along with data on foci yields. To this aim, we can extract from the clustering algorithm the average number of DSBs within each focus, which we call DSB multiplicity. The amount of DSB in single focus depends on the dose, on the LET and the kind of clustering algorithm that has been used to simulate foci. Tab.3.5 shows the multiplicity of DSBs per focus for different doses of X-rays, protons, and ^{12}C ions and for different values of r.

Table 3.5: Average multiplicity obtained from the "3D reconstruction" (in the whole nuclear volume), as a function of the *clustering radius*. Results are shown for X-rays, protons and ^{12}C ions.

Dose (Gy)	r=0.5μm		r=0.75μm		r=1μm	
	Mult.	Δ Mult.	Mult.	Δ Mult.	Mult.	Δ Mult.
X-rays						
1.00	1.20	0.06	1.26	0.08	1.37	0.10
2.00	1.33	0.08	1.44	0.10	2.00	0.17
5.00	1.72	0.13	2.10	0.23	3.59	0.77
Protons						
0.09	3.85	0.08	4.72	0.10	5.86	0.13
0.18	3.10	0.08	3.80	0.11	4.80	0.14
0.28	3.16	0.12	3.87	0.15	4.92	0.21
0.45	3.22	0.12	3.97	0.16	5.10	0.23
0.75	3.30	0.12	4.16	0.18	5.44	0.25
0.83	3.28	0.09	4.14	0.13	5.48	0.19
0.95	3.36	0.13	4.29	0.75	5.82	0.29
1.01	3.35	0.13	4.27	0.19	5.79	0.30
1.38	3.54	0.14	4.63	0.22	6.06	0.62
^{12}C ions						
0.50	2.72	0.31	3.36	0.39	4.08	0.50
1.00	2.81	0.32	3.58	0.44	4.78	0.60
2.00	3.38	0.39	4.33	0.57	5.91	0.86
5.00	4.20	0.28	5.90	1.00	10.04	2.09

As expected, for a given radiation radiation quality, DSB multiplicity increases with increasing dose and *clustering radius*. A singularity has been found for 1 proton track, with multiplicities higher than for more particle traversals. Lowest DSB multiplicity values are found for X-rays, though always higher than one. At equal dose (1 Gy), DSB multiplicities and total DSB yields for secondary protons are slightly higher than for ^{12}C ions.
In perspective, by multiplying the simulated average DSB multiplicity for the experimental yields of foci, an estimation of the average number of DSBs in the whole nucleus due to a certain radiation quality can be extrapolated from measured data. As a 3D reconstruction analysis for experimental data from confocal microscopy is currently being studied at the time this thesis is written, we here test of this procedure on simulated data.
Results are shown in Fig.3.41, where a good agreement is found between PARTRAC predictions on the number of DSBs and reconstructed DSBs starting from foci yields multiplied by DSB multiplicity. As fewer foci but with a higher DSB multiplicity is found for higher r, the product of foci yields and DSB multiplicity is stable for different values of r. In Fig.3.41 we therefore show the average number of DSBs reconstructed for the three values of the *clustering radius* r.
The agreement observed for all radiation indicates that the average value of the DSB multiplicity distribution is a good indicator of the number of lesions in single foci. The little difference for higher LET particles may be explained considering that, with this approach, the intrinsic multiplicity (as the one defined in Tab.2.1) of DSB clusters from which foci originate has not been taken into account in this estimation: a focus from a DSB cluster is considered with a multiplicity equal to 1, even if it comprises more DSBs. DSBs from PARTRAC, instead, are obtained as the sum of "isolated" DSBs and the ones grouped in DSB clusters, as explained in Par.2.1.6. Moreover, while the morphology of foci created by randomly distributed DSBs is quite homogeneous (leading to IRIF with similar multiplicity for the same condition), for higher LETs, instead, the yields of DSBs in the streak-like foci might be more varied from case to case, and the average DSB multiplicity value might not adequately reflect the multiplicity distribution. It will be necessary to take this into account, if a similar procedure is applied to experimental data.

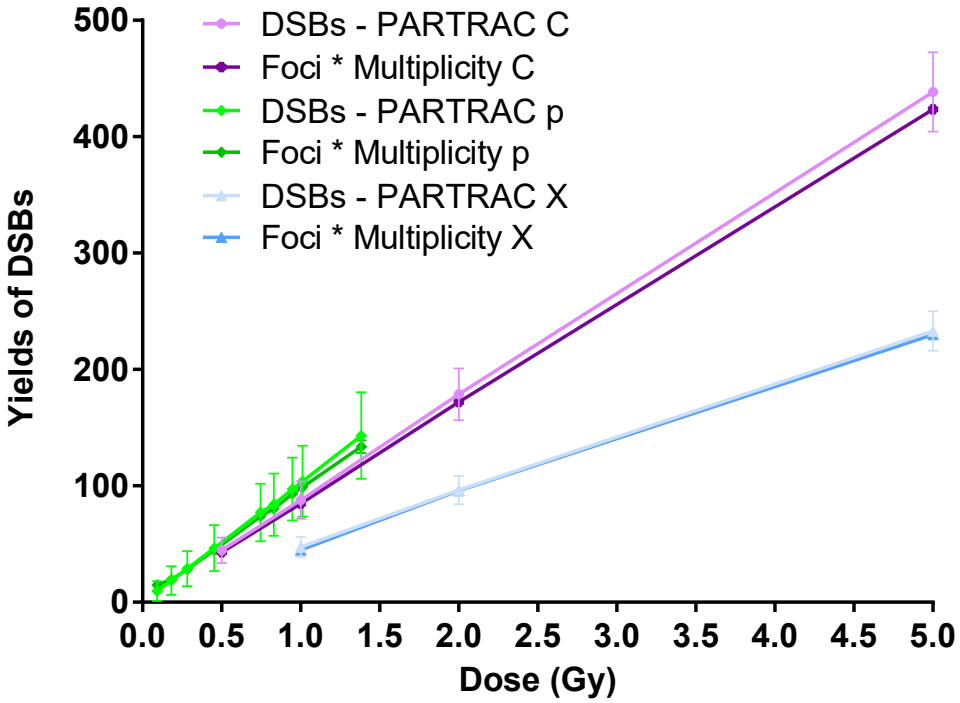

Figure 3.41: Comparison of the dose dependence, for different radiation qualities, of the DSBs predicted by PARTRAC and of the yields of DSBs reconstructed in the whole nuclear volume (ellipsoidal for ^{12}C ions, spherical for X-rays and neutrons), calculated as the product of the average multiplicity and the average number of reconstructed foci.

Chapter 4

Applications to the space radiation environment

4.1 Neutron biological effectiveness on Mars

4.1.1 Space radiation environment

Space radiation environment offers the opportunity to understand radiation effects and underlying biological mechanisms in the case of a highly mixed radiation field. On the International Space Station (ISS), a unique laboratory for research on space radiation effects, the Earth's magnetosphere still offers some protection, but astronauts are already exposed to a variety of particles and to dose levels that are much higher that what found on Earth due to the terrestrial radiation background. Exposure to space radiation increases the risk of long-term detrimental health consequences, that can appear even years after the astronaut's return to Earth. Also shorter-term and in-mission effects are possible, particularly in case of acute exposures, as it can happen as a consequence of phenomena maily related to the Sun (see later). Taken all togheter, this calls for research efforts to be able to evaluate the risk associated to human space exploration and, when possible, develop appropriate countermeasures [199].
The space radiation environment is mainly composed by a background of high energy particles, usually referred to as Galactic Cosmic Rays (GCRs) and by Solar Particle Events (SPEs). GCRs come from *e.g.* supernova shock waves or stellar wind/flares outside our solar systems. Hadrons represent the dominant contribution in GCR flux (98%), while the remaining 2% is due to electrons; among the hadrons, the 87% is due to protons, the 12% is due to ^{4}He ions, but species with higher Z and energy (HZE particles) can also be found (1%). GCR flux is very low (few particles/cm^2/s), and it has been shown to be in anti-correlation with the solar activity, that has an 11-year cycle. During solar maxima, GCR flux can decrease by a factor of 3-4. Fig.4.1(a) shows the

differential energy spectra for selected GCR particles (H, He, O, and Fe).

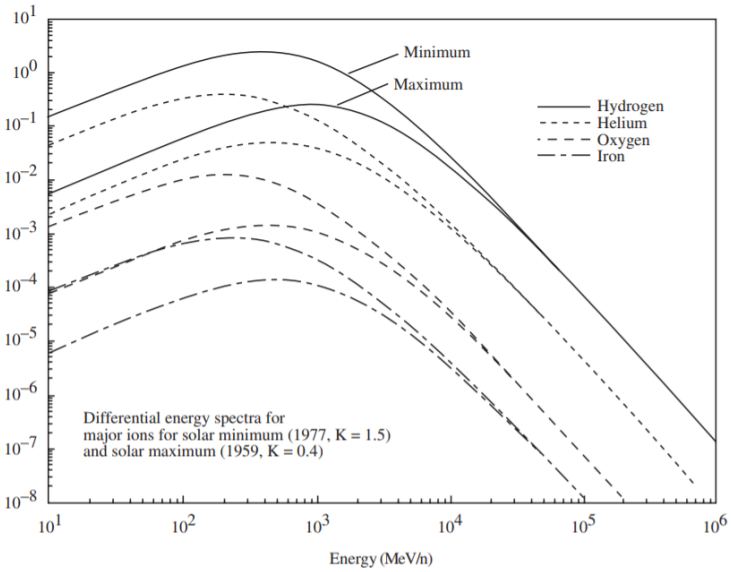

(a)

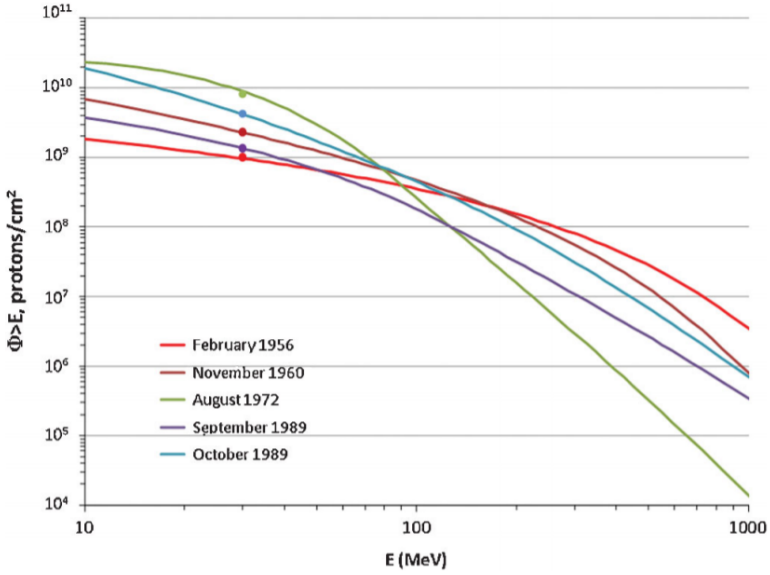

(b)

Figure 4.1: (a) Differential energy spectra for different GCR particles (H, He, O, and Fe) and their modification by solar activity at 1 AU [202, 203] and reproduced in NCRP (2000). (b) Integral energy spectra of intense solar particle events in the 20th century [Kim, Tylka, Atwell and Cucinotta] [204].

Notwithstanding the low flux, GCR particles are highly energetic (from tens to 10^{12} MeV/nucleon) and can easily transverse the spacecraft shielding and reach the astronaut body [200]. Their high LET leads to an increased probability of chromosomal aberrations [201], degenerative effects in tissues, initiation of cancer development and genomic instability [192].
The second major contribution to the space radiation environment is due to solar particle events: the Sun is continuously emitting low-energy particles (mainly protons and electrons in the so-called solar winds, with intensities from 10^{10} to 10^{12} particles/cm^2/s/sr), but sporadic and intense outbursts of higher energy protons (with a minor contribution of α particles and electrons, roughly 10% and 1% respectively) can also take place, originating from disturbed magnetic regions in the star. SPE particle energy can reach several GeV. In Fig.4.1(b) we report energy spectra for a selection of historical SPE events. Unlike GCRs, the high flux of SPE might cause the onset of severe early effects for high-dose exposures, including gastrointestinal symptoms, as nausea and diarrhea, skin burns, fatigue and damages to the heamatopietic system (all generally falling in the definition of Acute Radiation Syndrome, ARS), but also damages to the Central Nervous System (CNS). Short-term effects can appear from few hours to several days post-exposure, depending on the dose, the dose-rate and also individual radiation sensitivity [205].
In the last years, the perspective of a manned mission to Mars has attracted efforts of researchers and space agencies. To make this real, solutions will be needed to keep the risk of long-term health consequences below acceptable limits, as well as to provide astronauts with effective countermeasures against short-term effects related to solar particle events. Also in this context, large efforts have been already and are currently undertaken to characterize the radiation environment that will be encountered during the cruise to Mars and on the surface of the planet. In the framework of Mars Science Laboratory (MSL) mission, the Radiation Assessement Detector (RAD) was installed on board the rover Curiosity. MSL-RAD measured the equivalent dose rates during the cruise to Mars, which was found to be of 1.84 $\pm$ 0.30 mSv/day, and on the surface of the planet, giving a result of 0.64 $\pm$ 0.12 mSv/day during periods of solar maximum (0.92 mSv/day during solar minima) [206]. For comparison, the dose rate at the terrestrial surface due to the Earth's background radiation is of around 0.01 mSv/day, while dose-rate values as high as 0.4 - 1 mSv/day can be measured on board the ISS.

4.1.2 Reproducing space radiation exposure on Earth

Despite obvious technical limitations, ISS is a unique laboratory also for *in vitro* radiobology research. It has to be kept in mind however that, in addition to space radiation, microgravity conditions also play a major role in inducing stress to biological systems on board the ISS. Microgravity itself has been demonstrated to impact on the cell repair machinery, inflammatory pathways and induction of ROS [207]), as well as on body functions [208, 209].

The stress induced by microgravity represents an inevitable confounding factor when studying space radiation effects in space. More generally however, the low dose and dose-rate characteristic of a space radiation environment always makes it difficult to draw clear-cut conclusions on dose-response relationship. To make an example of a radiobiological endpoint that is also investigated in part of this thesis work, the γ-H2AX foci assay has been used to detect and quantify DNA damage in samples that were exposed on board the ISS [210, 211, 212, 213], and a recent work discusses the application of this assay to space-related exposures [169].
Ground-based experiments can be performed in accelerator facilities to investigate the biological effectiveness of space radiation in *in vitro* (and also *in vivo*) systems [214, 215], and analogues exist to recreate microgravity conditions in the lab[207]. A plethora of studies addressing biological effects induced by particle species found in space (such as α particles, iron, proton) are available in the literature. More recently, more attention has been devoted to the development of ground-based facilities for irradiations with a mixed particle field [216], providing for a more adequate representation of what is found in space. However, a chronic prolonged exposure to a low dose rate of mixed particles can hardly be reproduced with ground-based measurements.
The characterization of the effectiveness of the space radiation exposure remains a hot topic of research and a major objective in the research agenda of space agencies. As already mentioned, this is of compelling importance in view of long-term expeditions towards Mars (or the Moon), and it drives the development of countermeasures or specific mitigations for the different mission scenarios.
Modelling approaches by means of Monte Carlo simulations, can give an essential contribution in many aspects, as *e.g.*: (i) the characterization of the radiation environment; (ii) the understanding of biological mechanisms, starting from energy depositions at the sub-cellular level; (iii) risk estimation; (iv) prediction of the effectiveness and development of countermeasures. Modelling also comes to help for the interpretations of biological data from groud-based or space measurements, in light of the many difficulties and specifities related to the space radiation environment [24, 217].

4.1.3 Neutrons on Mars

The issue of radiobiological effectiveness of neutrons in space deserves a special discussion: there are essentially no neutrons in the primary space radiation environment. Instead, neutrons are produced by GCR (and SPE) interactions with spacecraft walls, other habitat materials and body tissues. As a GCR particle with $Z > 1$ interacts with a target nucleus, it can fragment releasing neutrons with high energies. The interaction may also induce fragmentation of the target nucleus, or a variety of nuclear reactions can occurr, as a result of which neutrons can be emitted by the hit material, generally with lower energies (below 20 - 30 MeV) [218]. The final neutron energy spectrum in

the habitat will therefore depend both on the incident radiation, and on the type and thickness of the target material. Although neutrons contribution to the total dose received by astronaut during an interplanetary journey might be not high, neutron biological effectiveness varies enormously with the energy, reaching values as high as 20 in the energy region around 1 MeV (see the "Discussion" in Par.2.3.5 and Fig.2.12). The biological impact of the neutron component of the radiation environment in a space habitat (a vehicle or a planetary habitat) therefore deserves careful investigation. From an experimental point of view, newly planned ground-based mixed-field simulators will likely not be able to reproduce the neutron component of the space radiation inside a habitat [216]. Also, neutron data from radiobiological measurements are much varied among different experiments, and often available in the few MeV region, while space radiation requires dedicated studies also at hundreds of MeV. Modelling becomes therefore essential in this respect.
Recent data on neutron fluxes during a cruise to Mars and on the surface of the planet are now available thanks to MSL-RAD [219, 220]. The detector sensitivity window allows to characterize the neutron environment between energies of 8 and 740 MeV. The neutron equivalent dose rate on Mars has been measured to be 61 ± 15 μSv/day (almost 9% of the total) [221]. The total neutron spectrum at the surface is composed by backscattered neutrons, generated by the interactions of GCRs with the planetary regolith, and by neutrons directly produced by GCR interactions in the upper Martian atmosphere. By means of MC simulations, it is possible to distinguish and estimate the entity and characteristics of these two components.

4.1.4 Objective

In this part of the thesis we adopt the modelling approach, previously developed for the study of neutron biological effectiveness as a function of energy (see Par.2.3), for the investigation of the biological effectiveness of the neutron field as predicted at the surface of Mars. Neutron effectiveness is quantified (with respect to a reference low-LET radiation) in terms of induction of cluster damage to the cellular DNA. Results presented in the following offer the chance of a direct comparison with results obtained for the effectiveness of mono-energetic neutron beams (Chap.2) and for the Hiroshima neutron spectrum (Chap.3).

4.1.5 Material and methods

Simulation of clustered DNA damage due to neutrons on Mars

In Fig.4.2(a) we report neutron spectra predicted at the surface of Mars: neutrons are produced by GCR interactions with the Martian atmosphere (downward component) and soil (upward component). Simulations are done with GEANT4 PLANETOCOSMICS. The lower neutron energy scored for both

components is 1 MeV. The atmospheric profile was adapted from the Mars climate database (MCD) at the location of Gale Crater, under a surface pressure of about 830 Pascal [222]. The input GCR spectrum (protons and helium ions) was calculated using the Badwahr–O'Neill model (BON10) [223] with a modulation potential $\Phi = 1500$ MV, representing the solar maximum period.

For the purpose of this work, we used the same coupling between transport

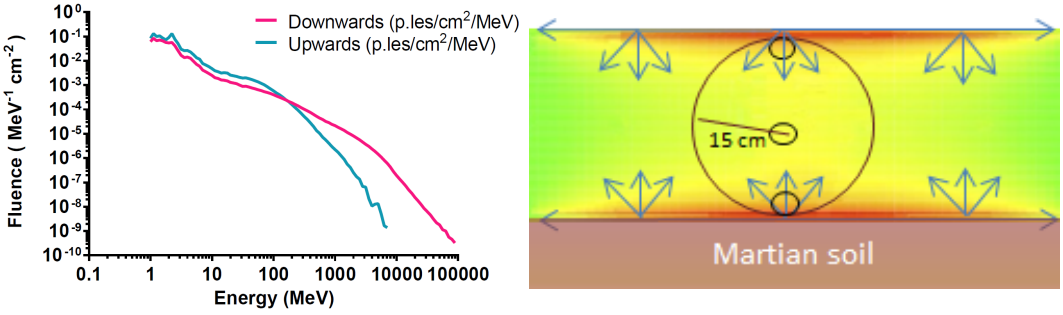

(a) (b)

Figure 4.2: (a) Neutron spectra (upward and downward) on the surface of Mars obtained via the GEANT4 - PLANETOCOSMICS simulations of GCRs transported through the Martian atmosphere [222]. (b) Schematics of the target phantom in PHITS calculations, superimposed to the neutron fluence spectra, calculated with the [T-Track] tally.

and track-structure calculations introduced in Par.2.3.4. We implemented in PHITS a source of neutrons with energy distributions shown in Fig.4.2(a): two sources have been considered, each in form of a disk of radius equal to 60 cm. The disks are parallel with each other, positioned at the opposite sides of a spherical (30-cm-diameter) ICRU44 phantom (same phantom geometry as in Par.2.3.4), both tangential to the phantom surface. The top disk is emitting neutrons isotropically downwards, and the bottom one isotropically upwards, each with the corresponding neutron spectrum shown in the Figure. The whole (phantom and disks) are put in void. We perform neutron transport and characterize the secondary charged particle field induced by neutron interactions, namely: p, d, α, ^{12}C, ^{14}N, ^{16}O, e$^-$. For each species we score the dose-mean lineal energy and the relative contribution to the total neutron dose in different scoring sites (1.5-cm-radius spheres) in the phantom: one in the middle of the phantom, one at the top towards the atmosphere and one at the bottom towards the soil. The simulation setup is shown in Fig.4.2(b). Calculations are done for 10 millions of neutrons, averaged over 3 runs, errors on scored quantities are given as standard deviations from the different runs.

After that, the analytical function reported in Eq.2.19 derived in Par.2.3.5 from PARTRAC calculations is used to predict complex DNA lesions (DSB clusters) given by secondary particle $\overline{y}_D$. Damages by all particles are weighted by their contribution to the neutron dose and summed to obtain a neutron-induced

damage yield (Gy^{-1} $cell^{-1}$). Neutron RBE has been calculated as the ratio of damage induced by neutrons to that induced by X-rays. The low-LET reference radiation is the 220 kVp X-ray spectrum used before.

4.1.6 Results and discussion

Tab.4.1 reports, for all neutron-induced secondary species, the values of $\overline{y}_D$ and relative dose for the 3 different scoring regions obtained by PHITS. The overall $\overline{y}_D$ associated to the neutron field is also reported.
The sum of the relative doses for the considered secondary species is $\sim 91\%$ for

Table 4.1: $\overline{y}_D$ (keV/μm) and D_{rel} for the three scoring regions inside the spherical phantom. The $\overline{y}_D$ of the total neutron field is also reported.

	e^-		^1H		d		α	
	$\overline{y}_D$	D_{rel}	$\overline{y}_D$	D_{rel}	$\overline{y}_D$	D_{rel}	$\overline{y}_D$	D_{rel}
central	2.01	5.14%	11.79	68.66%	11.51	6.97%	132.34	6.28%
atmosp.	1.95	2.22%	16.66	69.82%	12.67	6.27%	126.03	8.59%
soil	1.94	7.21%	19.19	73.59%	10.96	5.42%	138.78	7.94%
	^{12}C		^{14}N		^{16}O		neutron	
	$\overline{y}_D$	D_{rel}	$\overline{y}_D$	D_{rel}	$\overline{y}_D$	D_{rel}	$\overline{y}_D$	D_{rel}
central	654.12	1.77%	614.49	0.42%	449.46	1.30%	43.53	100.00%
atmosp.	633.06	2.35%	624.80	2.06%	459.50	1.99%	59.86	100.00%
soil	618.34	2.71%	775.01	0.77%	462.43	2.60%	65.79	100.00%

the central sphere, and of $\sim 93\%$ and 100% for respectively the sphere towards the atmosphere and the one towards the soil. The missing component might be due to pions and electromagnetic cascades, that have not been considered in the calculations, or heavier ions (Z>8). In Fig.4.3 we report the yields of DNA DSB clusters per cell per Gy predicted for the three scoring regions, also distinguishing the contribution of the different secondary species in the neutron-induced mixed field. We obtain 1.47, 2.26 and 2.42 DSB clusters Gy^{-1} $cell^{-1}$ respectively for cells in the central scoring region, in the external one facing the atmosphere and in the one towards the Martian soil.

DSB cluster yields can be converted into RBE values, by dividing them for the yield of DSB clusters expected after X-ray irradiations at the same 1 Gy dose (0.38): this gives RBE values of 3.87, 5.95 and 6.37, again respectively for the three regions (central; towards the atmosphere; towards the soil).
Some simple considerations can be done to interpret data presented in this part of the thesis and are reported in what follows. As expected, results both in terms of neutron $\overline{y}_D$ and effectiveness vary as a function of the position in the phantom. Neutrons in the two external scoring regions, the one facing the

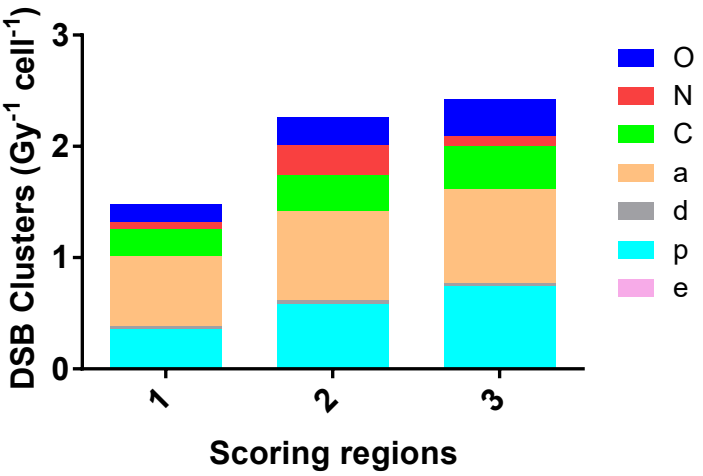

Figure 4.3: Yields of DSB clusters (Gy^{-1} $cell^{-1}$) due to neutron-induced secondary particles, for the three scoring regions inside the spherical phantom (1 - central sphere, 2 - facing the atmosphere, 3 - facing the soil.

atmosphere and the one facing the soil, seem to be characterized by a higher effectiveness. Neutrons coming from the atmosphere are, on average, more energetic, hence a lower effectiveness is found for the scoring region at the top with respect to the one at the bottom of the phantom. Some self-shielding is offered by the tissue sphere itself, when we consider the central scoring region, and the overall $\overline{y}_D$ is lower. If we consider neutrons at 1 MeV, abundant in both the upward source and the downward one and characterized by a maximal effectiveness, it is likely that this energy is decreased when such neutrons reach the center of the sphere. Hence, the lower effectiveness found for the central scoring region. This is coherent with what observed in Fig.2.11(b), comparing the different scoring regions at a fixed neutron energy of 1 MeV. All these considerations are somewhat simplified, as the presence of multiple sources means that *e.g.* neutrons from above might very well reach the bottom of the phantom and vice versa, and makes the situation more complex.
Moreover, a comparison can be made with the average value of the neutron quality factor Q (based on RBE values, it is used to account for different radiation qualities), as estimated from the ratio of the equivalent dose to the absorbed dose due to neutrons on the surface of Mars, as measured by the RAD detector. Being the neutron equivalent dose H = 61 $\pm$ 15 μSv/day, while the absorbed dose D = 14 $\pm$ 4 μGy/day, the resulting <Q> is equal of 4.36, quite similar to what found with our approach.
Results presented in this section are to be considered a first application of this modelling approach to the neutron component of space radiation. Different input neutron spectra can be tested, as the one at the surface of Mars under different conditions (*e.g.* input GCR spectrum, pressure profile for the atmosphere, solar cycle conditions, etc.), as well as the one expected in a space

vehicle due to GCR interactions with the shielding walls. The model allows, in perspective, to obtain a full mapping of neutron RBE for all sites of interest in all phantoms, including realistic voxel phantoms.

4.2 Countermeasures to Solar Particle Events

4.2.1 Risk estimation and limitations

Astronauts are considered exposed workers by the U.S. NASA regulations, therefore dose limits have been established to keep the risk associated to space radiation below acceptable levels [224, 225]. To obtain a risk estimate, models are needed to first predict absorbed physical doses in Gy, then to convert such doses in effective dose levels (Sv), taking into account the effectiveness of different radiation qualities and the radiosensitivity of different tissues or organs. MC simulation tools to predict exposure levels have to be benchmarked with dosimetric measurements, whenever possible, and useful information come from the use of anthropomorphic phantoms [226, 227]. In the course of a mission, both exposures occurring during Intra- and Extra-Vehicular Activity (IVA/EVA) have to be considered. Finally, this information has to be translated into risk, currently conventionally expressed in terms of risk of exposure-induced death (REID), *i.e.* the risk of occurrence of a cancer with lethal consequences in the course of the astronaut's life, that can be ascribed to the space environment. Levels of exposure are acceptable only if REID stays below a threshold of the 3%, with a 95% confidence level [228].
Short-term non-cancer effects, as those possibly related to acute exposures in case of SPEs, are not currently included in this risk evaluation. To prevent this kind of effects NASA has set thresholds on permissible doses to specific tissues and organs at risk, over different time periods (from 30 days to 1 year, and over the astronaut's career) [229]. Such dose limits are given in Gy-Eq, that is the product of the physical dose in Gy and a RBE factor that is particle, energy (and effect) dependent. Such dose thresholds are reported in Tab.4.2. At

Table 4.2: Dose Limits for Short-Term or Career Non-Cancer Effects (in mGy-Eq., or mGy for CNS). ($\star$) Lens limits are intended to prevent early (<5 yr) severe cataracts, *e.g.*, from a solar particle event. ($\star\star$) Circulatory system doses calculated as average over heart muscle and adjacent arteries. (***) CNS limits should be calculated at the hippocampus. [229]

Tissue/Organ	**30-day limits**	**1-year limits**	**Career**
Lens (*)	1000	2000	4000
Skin	1500	3000	6000
BFO	250	500	Not applicable
Circulatory system (**)	250	500	1000
Central nervous system (***)	500	1000	15000

present, dose limits for short-term non-cancer effects are given only for missions near low Earth orbit (LEO). Thresholds are agreed upon for blood forming organs (BFO), skin, circulatory system, lens and central nervous system (CNS).

The limit for the CNS is given in mGy, as the RBE is largely unknown [229]. BFO are a particularly sensitive target: acute radiation exposure can heavily damage the hematopoietic system, compromising the spontaneous regeneration of the bone marrow. As it can be seen from the Table, dose thresholds for the skin, CNS and lenses are indeed set to higher levels than those for BFO (even if BFO benefit from higher shielding provided by body tissues).

4.2.2 Countermeasures to space radiation.

A first solution to limit the risk associated to space radiation exposure is quite obviously to restrict the mission duration. However, recent estimates for future deep-space missions at the study of space agencies, as that to Mars, seem to indicate that current limits for the REID will be exceeded, also for the shortest mission duration.
Since operational countermeasure cannot account for the problem alone [230], many complementary strategies have to be put in place to reduce as much as possible such risk. How to improve habitat shielding strategies [231], as far as this is possible for high energy GCRs, *e.g.* with innovative materials, or how to develop active shielding strategies, deserve separate discussions, outside the scope of this thesis. In what follows we focus on the development of countermeasures to prevent life-threatening health risks, as possibly caused by acute exposures due to SPEs. Such risks add to the concern of the cumulative health risk associated to chronic exposure to GCRs, but, given the lower energy of solar particles, shielding strategies can be successful, and, as it will be discussed, there is still large room for improvement and optimization.
Currently, the main mitigation to the risk of a SPE is the inclusion in the habitat design of a radiation shelter, *i.e.* a region of the habitat with increased wall thickness, where astronauts can take shelter when warned for a SPE and where they can stay for the duration of the event. Given the obvious limitations in terms of mass and cost associated to material launch in space, small shelter solutions are usually adopted in the habitat design. Nevertheless, complex operational scenarios in future missions might make crew direct interventions outside a small shelter highly probable even during SPEs, and fast complementary shielding solutions need to be available, possibly relying on resources already available on board. Personal radiation protection devices are a promising complementary countermeasure for astronauts during deep-space missions [232, 233].
In the framework of the PERSEO ("PErsonal Radiation Shielding for intErplanetary missiOns") project [1], an innovative concept for a wearable water-fillable radiation-shielding garment was developed, specifically aiming at the

[1]PERSEO was funded by the Italian Space Agency (ASI), Contract n. 2016-3-U.0. and coordinated by Dr. Giorgio Baiocco and Prof. Andrea Ottolenghi, University of Pavia (UniPv).

protection of astronauts' most radiosensitive organs in case of emergency interventions outside the shelter during a SPE (for Intra-Vehicular Activity). Previous feasibility studies [2] had demonstrated the validity of the choice of water as a shielding material against solar protons, based on a trade-off analysis between shielding performances and availability of resources on board [234]. A prototype of the PERSEO garment demonstrator has been manufactured and tested on board the ISS.

4.2.3 Objective

In this part of the thesis we present results from MC simulations of radiation transport in a space radiation environment. Such calculations have supported the validation of the shielding efficacy of the PERSEO garment. In particular, we present an analysis based on results of Geant4-GRAS for doses to target organs of an anthropomorphic phantom in a simplified space Al habitat (for walls of different thickness), when exposed to solar protons with and without the additional protection offered by water layers. The focus is on SPEs as they deliver high doses in short time intervals, contributing to the onset of acute non-cancer syntoms. From this analysis we derive dose reductions to BFO and the heart, achievable when a system like the PERSEO garment is used. For the solar proton radiation environment, we used as a reference the ESP model [235], and finally compared results to two of the worst historical SPEs energy spectra (1972 and 1989).

Publications for the topic.

- "Innovative solutions for personal radiation shielding in space". G. Baiocco, L. Bocchini, M. Giraudo, **S. Barbieri**, L. Narici, C. Lobascio, A. Ottolenghi. Radiation Protection Dosimetry, online ahead of print,2018.
- "A water-filled garment to protect astronauts during interplanetary missions tested on board the ISS", G. Baiocco, M. Giraudo, L. Bocchini, **S. Barbieri**, I. Locantore, E. Brussolo, D. Giacosa, L. Meucci, S. Steffenino, A. Ballario, B. Barresi, R. Barresi, L. Ravagnolo, M. Benassai, L. Narici, A. Rizzo, E. Carrubba, F. Carubia, G. Neri, M. Crisconio, S. Piccirillo, G. Valentini, S. Barbero, M. Giacci, C. Lobascio, A. Ottolenghi. Life Sciences in Space Research, 2018.
- "Exploring innovative radiation shielding approaches in space: a material and design study for a wearable radiation protection spacesuit", M. Vuolo, G. Baiocco, **S. Barbieri**, L. Bocchini, M. Giraudo, T. Gheysens, C. Lobascio, A. Ottolenghi. Life Sciences in Space Research, 2017.

[2]This work was supported by the Contract n. 4000111396/14/NL/MV in the framework of the tender: http://dx.doi.org/10.13039/501100008702 interaction with academia on advanced research topics – Ariadna call for ideas on INNOVATIVE RADIATION SHIELDING APPROACHES

4.2.4 Material and methods

SPE model

To describe an average test energy distribution for solar protons, the ESP (Emission of Solar Protons) model was selected, with a 90% confidence level for a 1 year mission [235]. This model is available on the ESA SPace ENVironment Information System (SPENVIS) website (2015). ESP predicts an initial solar proton fluence distribution given by a truncated power law, neglecting the role of the Earth magnetic shielding. Data from IMP (Interplanetary Monitoring System) and GOES (Geostationary Operational Environmental Satellite) from the last 3 complete solar cycles (20–22) are used. For the normalization to the fluence of a single SPE event, the OMERE (Outil de Modélisation de l'Environnement Radiatif Externe) tool was used. OMERE provides the SPE flux in particles/cm^2/h, using the worst-case solar event flux model realized by the space environment department at ONERA (Office national d'études et de recherches aérospatiales, Toulouse-France). For each energy and time scale, the ONERA model gives the highest flux measured by IMP8 and GOES during the years from 1974 to 2002. The normalization yields the integrated (over the whole energy range) flux of $1.3 \cdot 10^{11}$ protons/cm^2/h for the worst hour.
As a term of comparison, two historical SPEs (August 1972 and October 1989) were considered, using as normalization factor the integral fluxes for evaluation of short-term effects, as given by SPENVIS (CREME86 for August 1972 and CREME96 for October 1989).
Input energy spectra used in this work are plotted in Fig.4.4.

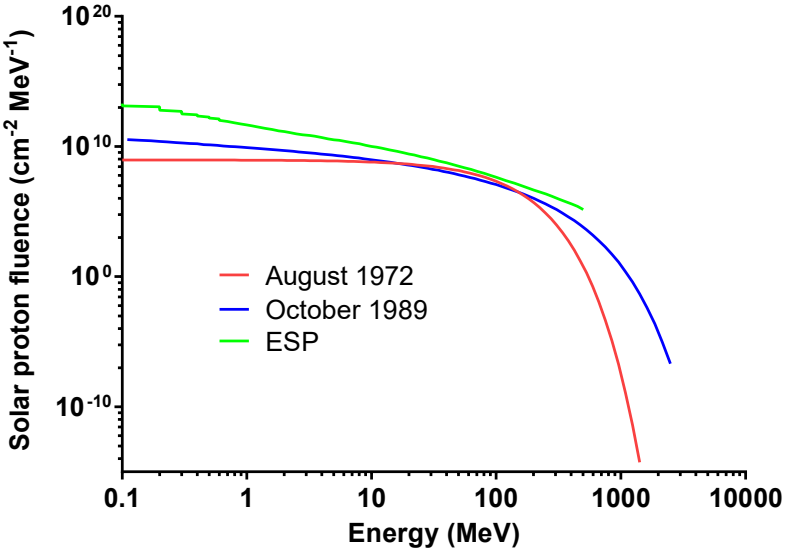

Figure 4.4: Energy spectra for solar protons used for dose calculations: the average spectrum calculated with ESP for a 1-year mission, and spectra from historical events (August 1972 and October 1989) [236].

3D calculations of radiation transport with an anthropomorphic phantom

All simulations were performed using the GRASv3.3 tool [237] based on Geant v.4.9.6.p03 [238]. The physics list QBBC was used, dedicatedly created for radiation biology, radiation protection and for space applications; it includes combinations of selected interaction models to reach higher precision in a wide energy range [239]. 3D simulation setups were built using GDML (Geometry Description Markup Language) [240], and a simplified software replica of the phantom and the garment model were implemented including elemental composition and density of materials.
The mathematical phantom available in Geant4 was used for the evaluation of dose reduction to target organs (see Fig.4.5(a)). In this phantom, each organ is represented using surfaces described by mathematical functions. The total mass of the phantom body is $\approx$ 70 kg. For the garment, the thickness of the water elements was set to 7 cm, plus a 2.5 mm layer of polyurethane for their containment. Bags were positioned around the torso of the geometrical phantom and lateral dimensions were scaled to cover it, as shown in the right picture of (Fig.4.5(b)).
The phantom, with and without the protecting elements, was positioned at

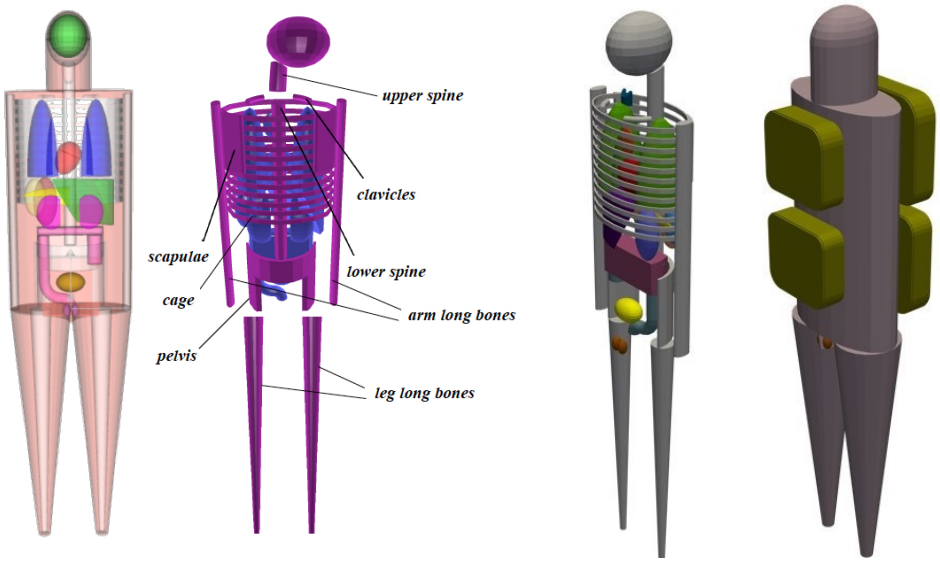

(a) (b)

Figure 4.5: Geant4-GRAS simulation setups for preliminary validation of the shielding effectiveness of the PERSEO garment. (a) Mathematical phantom with internal organ distribution and skeletal system [234]. (b) Positioning of water protection elements around the torso of the phantom [241].

the center of an Al module (2.25 m radius, 6 m length), to simulate exposure conditions during IVA. Increasing thickness values were tested for the module

walls: 1.5, 5 and 10 cm, equal to the thickness of the lateral cylindrical surface (with thinner conical surfaces and thicker caps).
The module was immersed in an isotropic proton source, generated by a spherical surface, with emission energies sampled according to the three chosen different input spectra. A representation of the habitat with the phantom is shown if Fig.4.6(a), while in Fig.4.6(b) the module is shown in the isotropic proton field.
Two different positions were also considered for the phantom inside the mod-

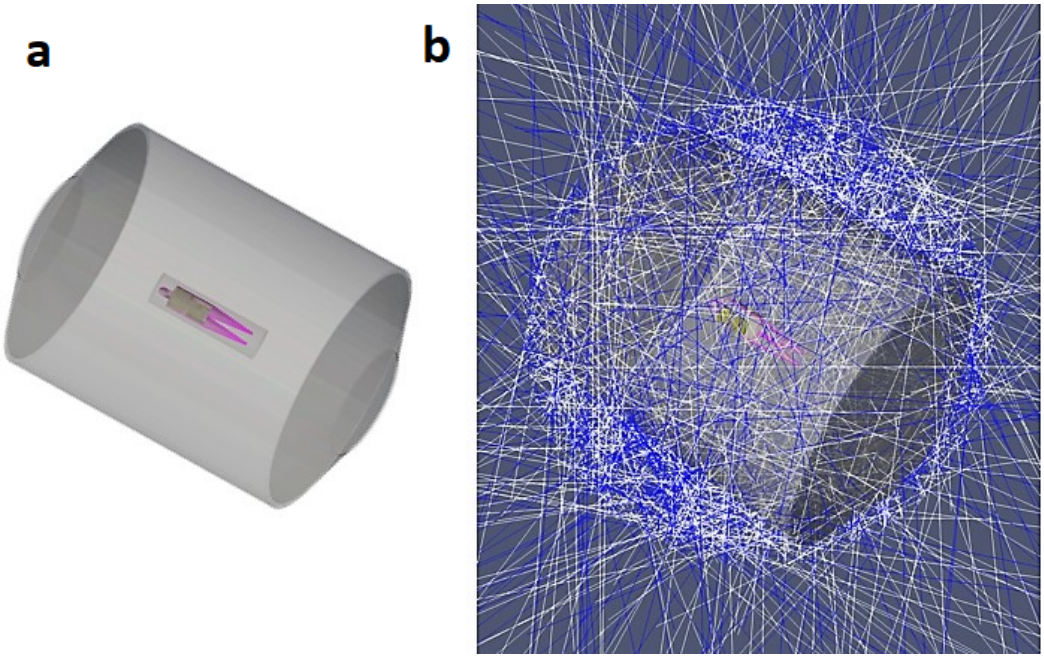

Figure 4.6: Geant4-GRAS simulation of habitat and exposure to protons. (a) Phantom wearing protection elements in the Al module. (b) Example of proton events generated isotropically from a spherical surface source around the Al module [241].

ule, namely with the cranio-caudal axis parallel to the module axis, or rotated of 90°, to evaluate variations in the dose reduction due to the Al thickness.
The dose to BFO was obtained with a weighted sum of doses to the phantom bone structures, taking into account their red bone marrow (RBM) content. RBM weights were derived from ICRP, Publication 110 [242]. The expression for the physical dose to BFO with RBM weights reads:

$$Dose_{BFO-rbm} = \frac{\sum_i rbm_i \cdot D_i}{\sum_{i=1} rbm_i} \tag{4.1}$$

where D_i is the dose to the i-th bone (Gy), the sum takes place over bone structures in the phantom (upper and lower spine; cage; pelvis; right and left leg/arm bones, scapulae and clavicles) and rbm_i weights are given in Tab.4.3,

together with RBM to bone mass ratio.

Different bones listed in ICRP 110 were grouped in corresponding phantom

Table 4.3: Bone components in the GRAS anthropomorphic phantom and red bone marrow content. For each bone structure the red bone marrow mass rbm_i in kg is reported, together with the corresponding ratio (%) to the total mass_i of the bone [241].

Bone	$\mathbf{rbm}_i$	$\mathbf{rbm}_i/\mathbf{mass}_i$ [%]
Upper spine	0.05	25.8
Lower spine	0.36	32.2
Pelvis	0.17	19
Leg bone (right/left)	0.01	0.3
Arm bone (right/left)	0.03	2.6
Scapula (right/left)	0.01	4
Clavicle (right/left)	0	4.7
Cage	0.21	23.6

bone structures for the derivation of RBM weights: phantom lower spine includes thoracic and lumbar spine and sacrum in ICRP 110; phantom leg and arm bones are taking into account femora/humeri upper halves only, with relative weight from ICRP 110; phantom cage includes ribs and sternum in ICRP 110.

The $Dose_{BFO-rbm}$ was calculated for the phantom in the module with and without the garment, and the shielding performance was measured in terms of dose reduction to the BFO:

$$Dose_{Red}(\%) = 100 \cdot \frac{Dose_{\text{ phantom in module}} - Dose_{\text{ phantom with garment in module}}}{Dose_{\text{ phantom in module}}} \tag{4.2}$$

Among the other organs for which NASA established short-term dose limits, only the circulatory system is partially protected by the suit. We also evaluated dose reduction to the heart as an indicator of dose reduction to the circulatory system, which is defined as an average over heart muscle and adjacent arteries. Statistical uncertainties on dose reduction values were obtained from propagation of uncertainties in primary dose quantities, and dictated by the statistics for incoming protons (up to several millions in 3D calculations).

4.2.5 Results and discussion

For the ESP model and the simplified garment geometry implemented in this work, the achievable dose reduction to BFO is: 43 ± 3 % for the lowest-shielded condition (1.5 cm Al module); 34 ± 3 % for 5 cm Al; 31 ± 3 % for the highest shielding considered (10 cm Al). These values are obtained with the phantom axis parallel to the module axis. If the phantom is rotated of 90°,

dose reduction values differ at maximum by a few percent, and even less for increasing thickness (within error bars for the thickest-shielding).
For the worst-hour condition, dose-rate values to BFO are of 0.099, 0.035 and 0.014 Gy-Eq/h for the naked phantom in Al modules of thickness 1.5, 5 and 10 cm.
If the 250 mGy-Eq limit to BFO is taken as a reference, and a constant dose rate equal to the worst-hour condition in the low-shielded scenario is assumed for the event, the dose limit would be reached in $\approx$ 2.5 h if the astronaut is not wearing any protection garment. On the contrary, considering the 43% dose reduction offered by the garment, the limit is reached in almost double of this time.
Fig.4.7(a) shows results for dose reduction (in %) to BFO in no shielding environment (phantom with and without the garment but free in space, as a reference condition), in a 1.5-cm- and 5-cm-thick Al habitat, following exposure to the different proton spectra under consideration. The comparison indicates that, though absolute values of dose reduction obviously depend on the specific spectrum, dose reduction values are always similar and the shielding strategy is justified.
Results for D_{red} to the circulatory system (heart) are summarized in Fig.4.7(b)

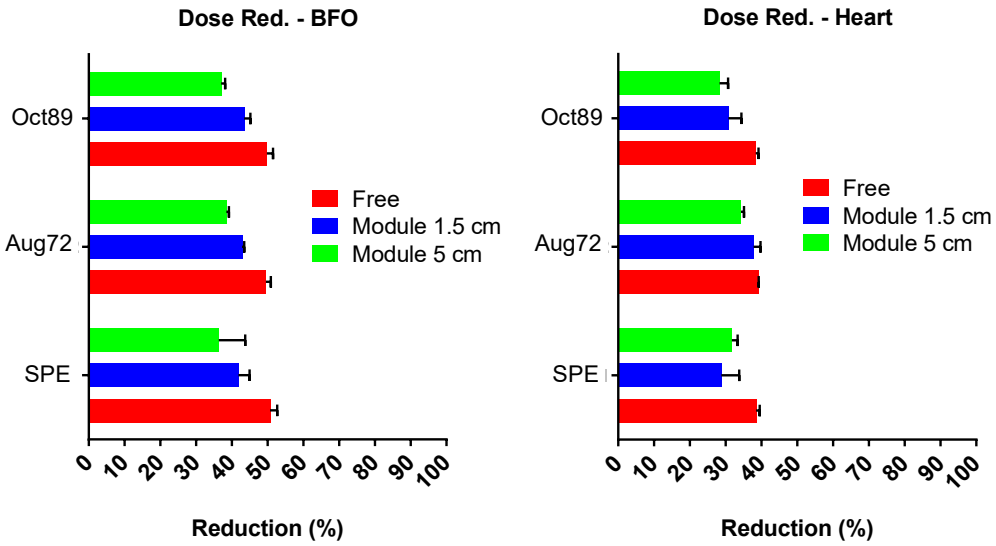

(a) (b)

Figure 4.7: Dose reduction to (a) BFO and to (b) heart when the phantom is wearing water protection elements in no shielding environment and inside the Al module (1.5 and 5 cm thick walls), and the module is immersed in different solar proton spectra [236].

for the different shielding conditions. Dose reduction values to the heart show slightly higher variations for different solar particle events than in the BFO case, which is justified if we think that BFO is more distributed and more

shielded by body tissues. A dose reduction value of 33% dose reduction has been found for the heart for the low-shielding condition, with respect to the 43% for the BFO. In case of thicker habitat shielding, average dose reduction values are reduced (of up to 5%), but still remain significant.
It has to be noted that the difference in the shielding performance for the two shielding conditions is due to the interplay of two effects: i) thicker walls stop lower energy protons that would have been stopped by the water containers, decreasing the efficacy; ii) they slow down protons from the external source to an energy range in which they can be stopped in the water thickness offered by protection elements.
Dose rate values to BFO and circulatory system for the phantom without the suit in both shielding conditions are summarized in Tab.4.4 and in Tab.4.5.

Table 4.4: Dose rate values to BFO for the phantom without protection elements [236].

Dose rate (Gy-Eq/h)	ESP	August 1972	October 1989
1.5-cm module	0.1	0.06	0.09
5-cm module	0.04	0.01	0.03

Table 4.5: Dose rate values to the circulatory system for the phantom without protection elements [236].

Dose rate (Gy-Eq/h)	ESP	August 1972	October 1989
1.5-cm module	0.06	0.03	0.05
5-cm module	0.03	0.01	0.02

Overall, Monte Carlo radiation transport results presented in this last Paragraph supported the validation of the shielding efficacy against solar protons of a personal radiation protection garment made of water elements. With such a system, dose to organs subject to the occurrence of short-term effects (BFO and the heart) can be significantly reduced during worst-hour fluxes of solar protons even if the astronaut is in a low-shielded area of the habitat. Results here presented are necessarily affected by the use of simplified phantom, garment and habitat geometries, and are not to be intended as of general validity but as a proof-of-concept of the shielding strategy [241].
The achievable dose reduction can be translated into an increase of the time the astronauts can be exposed, either accidentally or because obliged to work outside a radiation shelter, before the dose thresholds for the onset of short-term effects are reached. The decrease in absorbed dose also translates into an

overall decrease of detrimental long-term effects, though this is not explicitly modelled here.
This modelling activity was of support in the general development of the PERSEO project, that led to the manufacturing and test on board the ISS of a first garment prototype, with the joint efforts of many industrial and academic partners. A full description of the project development and final test can be found in the work by Baiocco *et al.* [241].

Chapter 5

Conclusions and future perspectives

The work presented in this Ph.D. thesis has been carried out with the aim of a comprehensive characterization of radiation-induced effects to the DNA, both at the nanoscopic level, by using approaches that start from the *ab-initio* description of the physical event distribution of energy depositions to the genetic make-up, and at the "visible" scale, getting to the study of detectable DNA damage endpoint as γ-H2AX foci.
The nanoscopic detail of the events has been investigated by means of the Monte Carlo code biophysical code PARTRAC, a powerful tool to simulate particle tracks, to predict the resulting initial DNA damage and correlate it to radiation effectiveness. The radiation field at the cellular scale is the product of radiation interactions at a macroscopic scale, and for this the transport code PHITS has been used. In this thesis work, a modelling approach is presented, based on the coupling of transport and track-structure calculations, that allows to unravel the dependence of neutron relative biological effectiveness on how neutron-induced DNA lesions vary with neutron energy and location in the target. Neutron effectiveness is predicted to have two peaks at around 1 MeV and 20 MeV neutron energy, in agreement with what concluded by the US-NRC for the neutron radiation weighting factor. Also an RBE model based on the saturation-corrected dose-mean lineal energy was proposed, showing the same feature for a saturation parameter of 200 keV/μm. For both models, the maximum RBE at around 1 MeV is $\sim$ 17. Neutrons can be much more effective in inducing biological damage than photons or other charged particles, with a non-trivial dependence on the geometry of the target.
In the following Chapters, neutron biological effectiveness is further investigated, also with an extension of the modelling approach from initial DNA damage to detectable γ-H2AX foci, that represents a main advancement achieved in this thesis work. In Chap.3, the RBE for the induction of DSB clusters following exposure to the analogue of the Hiroshima neutron spectrum available at RARAF is found to be $\approx$ 11.68, which is coherent with what expected

for neutrons of energy around 2.5 MeV (the average energy of the spectrum). Software replica of the exposure with reference X-rays and neutrons at RARAF have been integrated with dedicated experimental data from γ-H2AX foci detection by means of ICC and different microscopy techniques. Physical and read-out artefacts alter the quantification of the real damage content, and a dedicated modelling approach was developed to take this into account. In particular, the physical extension of foci and the use of different detection techniques (conventional fluorescence microscopy and confocal microscopy) have been modelled using geometrical parameters, finally allowing to reproduce the point of view of the observer in the analysis of pictures taken at the microscope. This approach has been successful in the reproduction of experimental data from different radiation qualities, and it has been shown to have the potential to deliver results for an actual quantification of damage (e.g. DSB contents) behind detected foci, which is essential for the comparison of radiation effectiveness with this assay. In addition to reference irradiations with low-LET X-rays, irradiations with carbon ions have also been performed and simulated, to extend the application of the modelling approach to a different example of high-LET radiation. The modelling of γ-H2AX foci has been extended in 3D, while a 3D reconstruction algorithm for experimental data from confocal microscopy is under development at the time this thesis is written.
Future developments of this study could address the modelling of the biochemical mechanisms leading to the formation of γ-H2AX foci, by considering the key molecules playing a role in the pathway. Moreover, DNA repair kinetics could also be followed, by modelling NHEJ and HR repair processes starting from the initial damage distribution as predicted by a track-structure code as PARTRAC.
The final neutron spectrum considered is the one expected at the surface of Mars: we present neutron RBE values for the induction of clustered DNA damage in different regions of the same geometrical phantom used in Chap.2, extracting values around 6 for the regions at the boundary of the spherical phantom (facing the Martian atmosphere or soil), and a lower value of ~ 4 for the most internal phantom region. In this case, the non-symmetric nature of the neutron source (with an upward component due to GCR interacting with the atmosphere, and a downward component due to GCR interactions with the soil) and the interplay with the phantom geometry make the interpretation of results not trivial. The average neutron energy is higher that what measured for the analogue of the Hiroshima spectrum at RARAF, and the RBE is coherently found to be much lower. The application of the MC approach to space radiation represents an example of possible predictive results that can be used for the estimation of the DNA damage in a scenario where experimental data are still lacking. This information, coupled with the characterization of the secondary particle fields generated by radiation in a space environment, could be also exploited for the optimization of countermeasures (both passive, but also biological), for future manned missions.

Taken all together, the RBE model for neutron-induced DNA damage and the modelling approach for neutron-induced foci allow the investigation of all neutron spectra of interests, delivering theoretical prediction of effectiveness as well as, when possible, predictions to be compared with experimental data on γ-H2AX foci. The same approaches can very well be extended to the study of any mixed field, as *e.g.* the one generated by nuclear reactions induced by a particle therapy beam or by the full GCR spectrum in space, with the same strategy of disentangling the effectiveness of the different components in the produced mixed field. Results presented in this thesis, both for initial DNA damage yields and γ-H2AX foci induced as a function of particle type, energy, LET, irradiation conditions, etc. could concur to the creation of a large database to be queried for practical applications such as bio-dosimetry following *e.g.* accidental exposure, optimization of radiation therapy and space radiation protection.

Bibliography

[1] M. E. Lomax, L. K. Folkes, and P. O'Neill. Biological consequences of radiation-induced DNA damage: relevance to radiotherapy. *Clinical Oncology*, 25(10):578 – 585, 2013. Advances in Clinical Radiobiology.

[2] N. Shikazono, M. Noguchi, K. Fujii, A. Urushibara, and A. Yokoya. The yield, processing, and biological consequences of clustered DNA damage induced by ionizing radiation. *Journal of Radiation Research*, 50(1):27–36, 2009.

[3] B. M. Sutherland, P. V. Bennett, O. Sidorkina, and J. Laval. Clustered DNA damages induced in isolated DNA and in human cells by low doses of ionizing radiation. *Proceedings of the National Academy of Sciences*, 97(1):103–108, 2000.

[4] D. Alloni, F. Ballarini, W. Friedland, M. Liotta, S. Molinelli, et al. Role of DNA/chromatin organisation and scavenging capacity in USX- and proton-induced DNA damage. *Radiation Protection Dosimetry*, 122:141–6, 2006.

[5] M. A. Hill. Track to the future: historical perspective on the importance of radiation track structure and DNA as a radiobiological target. *International Journal of Radiation Biology*, 0:1–10, 2017.

[6] D. Alloni, A. Campa, W. Friedland, L. Mariotti, and A. Ottolenghi. Track structure, radiation quality and initial radiobiological events: considerations based on the PARTRAC code experience. *International Journal of Radiation Biology*, 88(1-2):77–86, 2012.

[7] H. Nikjoo, S. Uehara, I. Khvostunov, F. Cucinotta, W. E Wilson, et al. Monte Carlo track structure for radiation biology and space applications. *Physica medica*, 17:38–44, 2001.

[8] D. E. Charlton, H. Nikjoo, and J. L. Humm. Calculation of initial yields of single- and double-strand breaks in cell nuclei from electrons, protons

and alpha particles. *International Journal of Radiation Biology*, 56(1):1–19, 1989.

[9] P. Howard-Flanders. Physical and chemical mechanisms in the injury of cells by ionizing radiations. volume 6 of *Advances in Biological and Medical Physics*, pages 553 – 603. Elsevier, 1959.

[10] T. Brustad. Heavy ions and some aspects of their use in molecular and cellular radiobiology. volume 8 of *Advances in Biological and Medical Physics*, pages 161 – 224. Elsevier, 1962.

[11] G. W. Barendsen. Impairment of the proliferative capacity of human cells in culture by α-particles with differing linear-energy transfer. *International Journal of Radiation Biology and Related Studies in Physics, Chemistry and Medicine*, 8(5):453–466, 1964.

[12] D. T. Goodhead, R. J. Munson, J. Thacker, and R. Cox. Mutation and inactivation of cultured mammalian cells exposed to beams of accelerated heavy ions. *International Journal of Radiation Biology and Related Studies in Physics, Chemistry and Medicine*, 37(2):135–67, 1980.

[13] A. Mozumder and J. L. Magee. Model of tracks of ionizing radiations for radical reaction mechanisms. *Radiation Research*, 28(2):203–214, 1966.

[14] J. J. Butts and R. Katz. Theory of rbe for heavy ion bombardment of dry enzymes and viruses. *Radiation Research*, 30(4):855–871, 1967.

[15] K. Sax. Chromosome aberrations induced by X-rays. *Genetics*, 23(5):494–516, 1938.

[16] H. J. Muller. Artificial transmutation of the gene. *Science*, 66(1699):84–87, 1927.

[17] R. M. Anderson, D. L. Stevens, and D. T. Goodhead. M-FISH analysis shows that complex chromosome aberrations induced by α-particle tracks are cumulative products of localized rearrangements. *Proceedings of the National Academy of Sciences*, 99(19):12167–12172, 2002.

[18] Maria P. S., Liudmila V. S., and Nikolai V. T. Application of new methods for detection of DNA damage and repair. In *International Review of Cell and Molecular Biology*, volume 277 of *"International Review of Cell and Molecular Biology*, pages 217 – 251. Academic Press, 2009.

[19] G. Figueroa-González and C. Pérez-Plasencia. Strategies for the evaluation of DNA damage and repair mechanisms in cancer. *Oncology LETters*, 13(6):3982–3988, 2017.

[20] K. M. Prise, M. Pinto, H. C. Newman, and B. D. Michael. A review of studies of ionizing radiation-induced double-strand break clustering. *Radiation Research*, 156(5):572–576, 2001.

[21] I. Plante and F. A. Cucinotta. Monte-Carlo simulation of ionizing radiation tracks. In *Applications of Monte Carlo methods in biology, medicine and other fields of science*. InTech, 2011.

[22] T. Friedrich, U. Scholz, T. Elsässer, M. Durante, and M. Scholz. Calculation of the biological effects of ion beams based on the microscopic spatial damage distribution pattern. *International Journal of Radiation Biology*, 88(1-2):103–107, 2012.

[23] Y. Zhang, Y. Feng, W. Wang, C. Yang, and P. Wang. An expanded multiscale Monte Carlo simulation method for personalized radiobiological effect estimation in radiotherapy: a feasibility study. *Scientific Reports*, 7:1–11, 2017.

[24] H. Nikjoo, S. Uehara, D. Emfietzoglou, and F. A. Cucinotta. Track-structure codes in radiation research. *Radiation Measurements*, 41(9-10):1052–1074, 2006.

[25] G Baiocco, G Babini, S Barbieri, J Morini, W Friedland, C Villagrasa, H Rabus, and A Ottolenghi. What roles for track-structure and microdosimetry in the era of -omics and systems biology? *Radiation Protection Dosimetry*, page ahead of print, 2018.

[26] M. Dingfelder. Track-structure simulations for charged particle. *Health Physics*, 103(5), 2012.

[27] H. Nikjoo, P. O'Neill, W. E. Wilson, and D. T. Goodhead. Computational approach for determining the spectrum of dna damage induced by ionizing radiation. *Radiation Research*, 156(5):577–583, 2001.

[28] W. Friedland, M. Dingfelder, P. Kundrát, and P. Jacob. Track structures, DNA targets and radiation effects in the biophysical Monte Carlo simulation code PARTRAC. *Mutation Research*, 711(1):28–40, 2011.

[29] Z. Francis, S. Incerti, R. Capra, B. Mascialino, G. Montarou, et al. Molecular scale track structure simulations in liquid water using the GEANT4-DNA Monte-Carlo processes. *Applied Radiation and Isotopes*, 69(1):220–226, 2011.

[30] M. A. Bernal, M. C. Bordage, J. M.C. Brown, M. Davídková, E. Delage, et al. Track structure modeling in liquid water: A review of the GEANT4-DNA very low energy extension of the GEANT4 Monte Carlo simulation toolkit. *Physica Medica*, 31(8):861–874, 2015.

[31] S. Incerti, M. Douglass, S. Penfold, S. Guatelli, and E. Bezak. Review of GEANT4-DNA applications for micro and nanoscale simulations. *Physica Medica*, 32(10):1187–1200, 2016.

[32] S. Meylan, S. Incerti, M. Karamitros, N. Tang, M. Bueno, et al. Simulation of early DNA damage after the irradiation of a fibroblast cell nucleus using GEANT4-DNA. *Scientific Reports*, 7(1):1–15, 2017.

[33] W. Friedland, H. G. Paretzke, F. Ballarini, A. Ottolenghi, G. Kreth, et al. First steps towards systems radiation biology studies concerned with DNA and chromosome structure within living cells. *Radiation and Environmental Biophysics*, 47(1):49–61, 2008.

[34] E. Schmitt, W. Friedland, P. Kundrát, M. Dingfelder, and A. Ottolenghi. Cross-section scaling for track structure simulations of low-energy ions in liquid water. *Radiation Protection Dosimetry*, 166(1-4):15–18, 2015.

[35] D. Alloni. Radiation biophysics modeling: track structure theoretical bases and Monte Carlo simulations of DNA damage. *Scientifica Acta*, 1(1):164 – 169, 2007.

[36] P. Siegmund, A. Schinner, and H. Paul. Errata and addenda for ICRU report 73, stopping of ions heavier than helium. *Journal of the ICRU*, 5(1):311–315, 2009.

[37] J. Valentin. Relative biological effectiveness (RBE), quality factor (Q), and radiation weighting factor (w_R)). A report of the International Commission on Radiological Protection. *Annals of the ICRP*, 33(4):1 – 121, 2003.

[38] E. J. Hall and A. J. Giaccia. *Radiobiology for the radiologist*, volume 119. Lippincott Williams and Wilkins, 2006.

[39] J. F. Ziegler. Interactions of ions with matter. `http://www.srim.org/`, 2013.

[40] A. Valota, F. Ballarini, W. Friedland, P. Jacob, A. Ottolenghi, et al. Modelling study on the protective role of OH radical scavengers and DNA higher-order structures in induction of single- and double-strand break by gamma-radiation. *International Journal of Radiation Biology*, 79(8):643–653, 2003.

[41] J. F. Ward. Factors controlling the radiosensitivity of cellular DNA. In D. T. Goodhead, P. O'Neill, and H. G. Menzel, editors, *Microdosimetry – An Interdisciplinary Approach*, pages 57–64. Royal Society of Chemistry, 1997.

[42] B. D. Michael and P. O'Neill. A sting in the tail of electron tracks. *Science*, 287(5458):1603–1604, 2000.

[43] M. Ljungman, S. Nyberg, J. Nygren, M. Eriksson, and G. Ahnstrom. DNA-bound proteins contribute much more than soluble intracellular compounds to the intrinsic protection against radiation-induced DNA strand breaks in human cells. *Radiation Research*, 127(2):171–176, 1991.

[44] W. Friedland, M. Dingfelder, P. Jacob, and H. G. Paretzke. Calculated DNA double-strand break and fragmentation yields after irradiation with He ions. *Radiation Physics and Chemistry*, 72(2):279 – 286, 2005.

[45] W. Friedland, P. Jacob, H. G. Paretzke, A. Ottolenghi, F. Ballarini, et al. Simulation of light ion induced DNA damage patterns. *Radiation Protection Dosimetry*, 122(1-4):116–120, 2006.

[46] M. S. Kreipl, W. Friedland, and H. G. Paretzke. Interaction of ion tracks in spatial and temporal proximity. *Radiation and Environmental Biophysics*, 48(4):349, 2009.

[47] P.H. Bernhardt, W. Friedland, P. Jacob, and H.G. Paretzke. Modeling of ultrasoft X-ray induced DNA damage using structured higher order DNA targets. *International Journal of Mass Spectrometry*, 223-224:579 – 597, 2003.

[48] W. Friedland, P. Jacob, and P. Kundrat. Stochastic simulation of DNA double-strand break repair by non-homologous end joining based on track structure calculations. *International Journal of Mass Spectrometry*, 173(5):677 – 688, 2010.

[49] Graphpad prism 7. `https://www.graphpad.com/`, 2018.

[50] W. Friedland, E. Schmitt, P. Kundrát, M. Dingfelder, G. Baiocco, et al. Comprehensive track-structure based evaluation of DNA damage by light ions from radiotherapy-relevant energies down to stopping. *Scientific Reports*, 7:1–15, 2017.

[51] M. J. Berger, M. Inokuti, H. H. Andersen, and H. Bichsel. Stopping powers and ranges for protons and alpha particles ICRU report 49. *Journal of the ICRU*, 1993.

[52] D. Alloni, A. Campa, M. Belli, G. Esposito, A. Facoetti, et al. A Monte Carlo study of the radiation quality dependence of DNA fragmentation spectra. *Radiation Research*, 173:263–271, 2010.

[53] H. Nikjoo, P. O'Neill, D. T. Goodhead, and M. Terrissol. Computational modelling of low-energy electron-induced DNA damage by early physical and chemical events. *International Journal of Radiation Biology*, 71(5):467–483, 1997.

[54] H. Nikjoo, C. Bolton, R. Watanabe, M. Terrissol, P. O'Neill, et al. Modelling of DNA damage induced by energetic electrons (100 eV to 100 keV). *Radiation protection dosimetry*, 99:77–80, 2002.

[55] H. Nikjoo, D. Emfietzoglou, T. Liamsuwan, R. Taleei, D. Liljequist, et al. Radiation track, DNA damage and response—a review. *Reports on Progress in Physics*, 79(11):116601, 2016.

[56] H. Nikjoo and T. Liamsuwan. Biophysical basis of ionizing radiation. *Comprehensive Biomedical Physics*, 9:65–104, 2014.

[57] J. F. Ward. The complexity of DNA damage: Relevance to biological consequences. *International Journal of Radiation Biology*, 66(5):427–432, 1994.

[58] D. T. Goodhead. Initial events in the cellular effects of ionizing radiations: Clustered damage in DNA. *International Journal of Radiation Biology*, 65(1):7–17, 1994.

[59] A. G. Georgakilas, P. O'Neill, and R. D. Stewart. Induction and repair of clustered DNA lesions: What do we know so far? *Radiation Research*, 180(1):100–109, 2013.

[60] H. G. Paretzke. Radiation track structure theory. In Freeman G. R., editor, *Kinetics of nonhomogeneous processes*, pages 89–170. Wiley, 1987.

[61] D. E. Charlton and J. L. Humm. A method of calculating initial DNA strand breakage following decay of incorporation. *International Journal of Radiation Biology*, 53(3):353–365, 1988.

[62] D. E. Charlton, H. Nikjoo, and D. T. Goodhead. Energy deposition in sub-microscopic volumes. In W. C. Dewey, M. Edington, R. J. M. Fry, E. J. Hall, and G. F. Whitmore, editors, *Radiation research: a twentieth century prospective*, volume 2, pages 421 – 426. Academic Press, 1985.

[63] S. Uehara, H. Nikjoo, and D. T. Goodhead. Cross-sections for water vapour for the Monte Carlo electron track structure code from 10 eV to the MeV region. *Physics in Medicine and Biology*, 38(12):1841–1858, 1993.

[64] A. Ottolenghi, M. Merzagora, L. Tallone, M. Durante, H. G. Paretzke, et al. The quality of DNA double-strand breaks: a Monte Carlo simulation of the end-structure of strand breaks produced by protons and alpha particles. *Radiation and Environmental Biophysics*, 34(4):239–244, 1995.

[65] A. Campa, D. Alloni, F. Antonelli, F. Ballarini, F. Belli, et al. DNA fragmentation induced in human fibroblasts by ^{56}Fe ions: experimental data and Monte Carlo simulations. *Radiation Research*, 171(4):438–445, 2009.

[66] D. Alloni, A. Campa, W. Friedland, L. Mariotti, and A. Ottolenghi. Integration of Monte Carlo simulations with PFGE experimental data yields constant RBE of 2.3 for DNA double-strand break induction by nitrogen ions between 125 and 225 keV/μm LET. *Radiation Research*, 179(6):690–697, 2013.

[67] E. Höglund. DNA fragmentation in cultured cells exposed to high linear energy transfer radiation. *Acta Universitatis Upsaliensis, Comprehensive Summaries of Uppsala Dissertations from the Faculty of Medicine*, 960, 2000.

[68] E. Höglund, E. Blomquist, J. Carlsson, and B. Stenerlow. DNA damage induced by radiation of different linear energy transfer: initial fragmentation. *International Journal of Radiation Biology*, 76:539–547, 2000.

[69] A. Campa, F. Ballarini, M. Belli, R. Cherubini, V. Dini, et al. DNA DSB induced in human cells by charged particles and gamma rays: experimental results and theoretical approaches. *International Journal of Radiation Biology*, 81(11):841–854, 2005.

[70] A. Lühr, C. von Neubeck, M. Krause, and E. G. C. Troost. Relative biological effectiveness in proton beam therapy – current knowledge and future challenges. *Clinical and Translational Radiation Oncology*, 9:35–41, 2018.

[71] M. Biaggi, F. Ballarini, W. Burkard, E. Egger, A. Ferrari, et al. Applications and possible generalisations of a method tested at the OPTIS facility, for analysing physical and radiobiological properties of therapeutic proton beams. *Physica Medica*, XVII:63–66, 2001.

[72] T. Matsuura, Y. Egashira, T. Nishio, Y. Matsumoto, M. Wada, et al. Apparent absence of a proton beam dose rate effect and possible differences in RBE between Bragg peak and plateau. *Medical Physics*, 37(10):5376–5381, 2010.

[73] C. R. Peeler, D. Mirkovic, U. Titt, P. Blanchard, J. R. Gunther, et al. Clinical evidence of variable proton biological effectiveness in pediatric patients treated for ependymoma. *Radiotherapy and Oncology*, 121(3):395–401, 2016.

[74] J. Unkelbach and H. Paganetti. Robust proton treatment planning: physical and biological optimization. *Seminars in Radiation Oncology*, 28(2):88 – 96, 2018.

[75] N. Bassler, O. Jäkel, C. S. Søndergaard, and J. B. Petersen. Dose- and LET-painting with particle therapy. *Acta Oncologica*, 49(7):1170–1176, 2010.

[76] E. Malinen and Å. Søvik. Dose or LET painting – what is optimal in particle therapy of hypoxic tumors? *Acta Oncologica*, 54(9):1614–1622, 2015.

[77] M. A. Cortés-Giraldo and A. Carabe. A critical study of different Monte Carlo scoring methods of dose average linear-energy-transfer maps calculated in voxelized geometries irradiated with clinical proton beams. *Physics in Medicine and Biology*, 60(7):2645–2669, 2015.

[78] A. M. Kellerer. Fundamentals of microdosimetry. In Kenneth R. Kase, Bengt E. Bjärngard, and Frank H. Attix, editors, *The Dosimetry of Ionizing Radiation*, pages 77 – 162. Academic Press, 1985.

[79] S. E. Anderson, K. M. Furutani, L. T. Tran, L. Chartier, M. Petasecca, et al. Microdosimetric measurements of a clinical proton beam with micrometer-sized solid-state detector. *Medical Physics*, 44(11), 2017.

[80] T. T. Böhlen, F. Cerutti, M. P. W. Chin, A. Fassò, A. Ferrari, et al. The fluka code: Developments and challenges for high energy and medical applications. *Nuclear Data Sheets*, 120:211 – 214, 2014.

[81] C. Y. Pan, Y. W. Huang, K.H. Cheng, T. C. Chao, and C. J. Tung. Microdosimetry spectra and relative biological effectiveness of 15 and 30 Mev proton beams. *Applied Radiation and Isotopes*, 97:101 – 105, 2015.

[82] T. B. Borak, T. Doke, T. Fuse, S. Guetersloh, L. Heilbronn, et al. Comparisons of LET distributions for protons with energies between 50 and 200 Mev using a spherical tissue equivalent proportional counter (TEPC) and a position sensitive Si-spectrometer (RRMD-III). *Radiation Research*, 162:687–692, 2004.

[83] A. Lühr, D. C. Hansen, R. Teiwes, N. Sobolevsky, O. Jäkel, et al. The impact of modeling nuclear fragmentation on delivered dose and radiobiology in ion therapy. *Physics in Medicine and Biology*, 57:5169–5185, 2012.

[84] M. De Napoli, C. Agodi, G. Battistoni, A. A. Blancato, G. A. P. Cirrone, et al. Carbon fragmentation measurements and validation of the GEANT4 nuclear reaction models for hadrontherapy. *Physics in Medicine and Biology*, 57(22):7651–7671, 2012.

[85] G. De Lellis, S. Buontempo, F. Di Capua, A. Di Crescenzo, P. Migliozzi, et al. Measurement of the fragmentation of carbon nuclei used in hadrontherapy. *Nuclear Physics A*, 853(1):124–134, 2011.

[86] K. Gunzert-Marx, H. Iwase, D. Schardt, and R. S. Simon. Secondary beam fragments produced by 200 Mev u^{-1} ^{12}C ions in water and their dose contributions in carbon ion radiotherapy. *New Journal of Physics*, 10, 2008.

[87] S. F. Kry, M. Salehpour, D. S. Followill, M. Stovall, D. A. Kuban, et al. The calculated risk of fatal secondary malignancies from intensity-modulated radiation therapy. *International Journal of Radiation Oncology * Biology * Physics*, 62(4):1195 – 1203, 2005.

[88] W. D. Newhauser and M. Durante. Assessing the risk of second malignancies after modern radiotherapy. *Nature Reviews Cancer*, 11(6):438–448, 2011.

[89] D. J. Brenner and E. J. Hall. Secondary neutrons in clinical proton radiotherapy: a charged issue. *Radiotherapy and Oncology*, 86(2):165 – 170, 2008.

[90] H. Jiang, B. Wang, X. G. Xu, H. D. Suit, and H. Paganetti. Simulation of organ-specific patient effective dose due to secondary neutrons in proton radiation treatment. *Physics in Medicine and Biology*, 50(18):4337, 2005.

[91] D. Followill, P. Geis, and A. Boyer. Estimates of whole-body dose equivalent produced by beam intensity modulated conformal therapy. *International Journal of Radiation Oncology * Biology * Physics*, 38(3):667 – 672, 1997.

[92] S. F. Kry, M. Salehpour, D. S. Followill, M. Stovall, D. A. Kuban, et al. Out-of-field photon and neutron dose equivalents from step-and-shoot intensity-modulated radiation therapy. *International Journal of Radiation Oncology * Biology * Physics*, 62(4):1204 – 1216, 2005.

[93] D. Satoh, F. Takahashi, A. Endo, Y. Ohmachi, and N. Miyahara. Calculation of dose contributions of electron and charged heavy particles inside phantoms irradiated by monoenergetic neutron. *Journal of Radiation Research*, 49(5):503–508, 2008.

[94] Nrc regulations title 10, code of federal regulations: 10 cfr. `https://www.nrc.gov/reading-rm/doc-collections/cfr/part020/part020-1004.html`, 2014.

[95] A. Ottolenghi, G. Baiocco, V. Smyth, and K. Trott. The ANDANTE project: a multidisciplinary approach to neutron RBE. *Radiation Protection Dosimetry*, 166(1-4):311–315, 2015.

[96] T. Sato, K. Niita, N. Matsuda, S. Hashimoto, Y. Iwamoto, et al. Particle and heavy ion transport code system, PHITS, version 2.52. *Journal of Nuclear Science and Technology*, 50(9):913–923, 2013.

[97] T. Sato, Y. Kase, R. Watanabe, K. Niita, and L. Sihver. Biological dose estimation for charged-particle therapy using an improved PHITS code coupled with a microdosimetric kinetic model. *Radiation Research*, 171(1):107–117, 2009.

[98] H. Horiguchi, T. Sato, H. Kumada, T. Yamamoto, and T. Sakae. Estimation of relative biological effectiveness for boron neutron capture therapy using the PHITS code coupled with a microdosimetric kinetic model. *Journal of Radiation Research*, 56(2):382–390, 2014.

[99] G. Baiocco, D. Alloni, G. Babini, L. Mariotti, and A. Ottolenghi. Reaction mechanism interplay in determining the biological effectiveness of neutrons as a function of energy. *Radiation Protection Dosimetry*, 166(1-4):316–319, 2015.

[100] L. Mariño-Ramírez, M. G. Kann, B. A. Shoemaker, and Landsman D. Histone structure and nucleosome stability. *Expert Review of Proteomics*, 2(5):719–729, 2005.

[101] D. Rossetto, A. W. Truman, S. J. Kron, and J. Côté. Epigenetic modifications in double-strand break DNA damage signaling and repair. *Clinical Cancer Research*, 16(18):4543–4552, 2010.

[102] R. J. Carter, C. M. Nickson, J. M. Thompson, A Kacperek, M. A. Hill, et al. Complex DNA damage induced by high linear energy transfer alpha-particles and protons triggers a specific cellular DNA damage response. *International Journal of Radiation Oncology*Biology*Physics*, 100(3):776 – 784, 2018.

[103] I. Chiolo, J. Tang, W. Georgescu, and S. V. Costes. Nuclear dynamics of radiation-induced foci in euchromatin and heterochromatin. *Mutation Research*, 750(1):56 – 66, 2013.

[104] S. Barnard, S. Bouffler, and K. Rothkamm. The shape of the radiation dose response for DNA double-strand break induction and repair. *Genome Integrity*, 4(1):1, 2013.

[105] A. Georgoulis, C. E. Vorgias, G. P. Chrousos, and E. P. Rogakou. Genome instability and γH2AX. *International Journal of Molecular Sciences*, 18(9):1–10, 2017.

[106] J. Her and S. F. Bunting. How cells ensure correct repair of DNA double-strand breaks. *Journal of Biological Chemistry*, 293(27):10502–10511, 2018.

[107] G. Iliakis. Backup pathways of NHEJ in cells of higher eukaryotes: cell cycle dependence. *Radiotherapy and Oncology*, 92(3):310 – 315, 2009.

[108] E. P. Rogakou, D. R. Pilch, A. H. Orr, V. S. Ivanova, and W. M. Bonner. DNA double-stranded breaks induce histone H2AX phosphorylation on serine 139. *Journal of Biological Chemistry*, 273(10):5858–5868, 1998.

[109] A. Kinner, W. Wu, C. Staudt, and G. Iliakis. γ-H2AX in recognition and signaling of DNA double-strand breaks in the context of chromatin. *Nucleic Acids Research*, 36(17):5678–5694, 2008.

[110] W. M. Bonner, C. E. Redon, J. S. Dickey, A. J. Nakamura, A. Olga, et al. γ-H2AX and cancer. *Nature Reviews Cancer*, 8(12):957–967, 2011.

[111] L. J. Mah, A. El-Osta, and T. C. Karagiannis. γH2AX: a sensitive molecular marker of DNA damage and repair. *Leukemia*, 24(4):679–686, 2010.

[112] O. Fernandez-Capetillo, A. Lee, M. Nussenzweig, and A. Nussenzweig. H2AX: the histone guardian of the genome. *DNA Repair*, 3(8-9):959–967, 2004.

[113] M. Fink, D. Imholz, and F. Thoma. Contribution of the Serine 129 of histone H2A to chromatin structure. *Molecular and Cellular Biology*, 27(10):3589–3600, 2007.

[114] E. Unal, A. ARBEl-Eden, U. Sattler, R. Shroff, M. Lichten, et al. DNA damage response pathway uses histone modification to assemble a double-strand break-specific cohesin domain. *Molecular Cell*, 16:991–1002, 2004.

[115] A. Celeste, S. Petersen, P. J. Romanienko, O. Fernandez-Capetillo, H. T. Chen, et al. Genomic instability in mice lacking histone H2AX. *Science*, 296(5569):922–927, 2002.

[116] T. T. Paull, E. P. Rogakou, V. Yamazaki, C. U. Kirchgessner, M. Gellert, et al. A critical role for histone H2AX in recruitment of repair factors to nuclear foci after DNA damage. *Current Biology*, 10(15):886–895, 2000.

[117] H. van Attikum and S. M. Gasser. Crosstalk between histone modifications during the DNA damage response. *Trends in Cell Biology*, 19(5):207–217, 2009.

[118] J. Reindl, G. A. Drexler, S. Girst, C. Greubel, C Siebenwirth, et al. Nanoscopic exclusion between RAD51 and 53BP1 after ion irradiation in human hela cells. *Physical Biology*, 12(6):066005, 2015.

[119] J. Reindl, S. Girst, D. W. M. Walsh, C. Greubel, B. Schwarz, et al. Chromatin organization revealed by nanostructure of irradiation induced γ-H2AX, 53BP1 and RAD51 foci. *Scientific Reports*, 7:1–11, 2017.

[120] V. Savic, B. Yin, N. L. Maas, A. L. Bredemeyer, A. C. Carpenter, et al. Formation of dynamic γ-H2AX domains along broken DNA strands is distinctly regulated by ATM and MDC1 and dependent upon H2AX densities in chromatin. *Molecular Cell*, 34(3):298–310, 2009.

[121] C. Lukas, F. Melander, M. Stucki, J. Falck, S. Bekker-Jensen, et al. MDC1 couples DNA double-strand break recognition by NBS1 with its H2AX-dependent chromatin retention. *The EMBO journal*, 23(13):2674–2683, 2004.

[122] M. Stucki, J. A. Clapperton, D. Mohammad, M. B. Yaffe, S. J. Smerdon, et al. Mdc1 directly binds phosphorylated histone H2AX to regulate cellular responses to DNA double-strand breaks. *Cell*, 123(7):1213–1226, 2005.

[123] T. Banerjee and D. Chakravarti. A peek into the complex realm of histone phosphorylation. *Molecular and Cellular Biology*, 31(24):4858–4873, 2011.

[124] F. A. Cucinotta, J. M. Pluth, J. A. Anderson, J. V. Harper, and P. O'Neill. Biochemical kinetics model of DSB repair and induction of γ-H2AX foci by non-homologous end joining. *Radiation Research*, 169(2):214–222, 2008.

[125] L. G. Mariotti, G. Pirovano, K. I. Savage, M. Ghita, A. Ottolenghi, et al. Use of the γ-H2AX assay to investigate DNA repair dynamics following multiple radiation exposures. *PLoS ONE*, 8(11), 2013.

[126] G. Gruel, C. Villagrasa, P. Voisin, I. Clairand, M. Benderitter, et al. Cell to cell variability of radiation-induced foci: relation between observed damage and energy deposition. *PLOS ONE*, 11(1):1–20, 2016.

[127] X. Huang and Z. Darzynkiewicz. Cytometric assessment of histone H2AX phosphorylation: a reporter of DNA damage. *Methods in Molecular Biology*, 314:73–80, 2006.

[128] N. Desai, E. Davis, P. O'Neill, M. Durante, F. A. Cucinotta, and H. Wu. Immunofluorescence detection of clustered γ-H2AX foci induced by HZE-particle radiation. *Radiation Research*, 164(4 Pt 2):518–22, 2005.

[129] G. Du, G. A. Drexler, W. Friedland, C. Greubel, V. Hable, et al. Spatial dynamics of DNA damage response protein foci along the ion trajectory of high-LET particles. *Radiation Research*, 176(6):706–715, 2011.

[130] P. R. BaRBEr, R. J. Locke, P. G. Pierce, K. Rothkamm, and B. Vojnovic. Gamma-H2AX foci counting: image processing and control software for high-content screening. *Proceedings of SPIE*, 6441:64411–1605, 2007.

[131] R. Runge, R. Hiemann, M. Wendisch, U. Kasten-Pisula, K. Storch, et al. Fully automated interpretation of ionizing radiation-induced γ-H2AX foci by the novel pattern recognition system aklides. *International Journal of Radiation Biology*, 88(5):439–447, 2012.

[132] A. Willitzki, S. Lorenz, R. Hiemann, K. Guttek, A. Goihl, et al. Fully automated analysis of chemically induced γ-H2AX foci in human peripheral blood mononuclear cells by indirect immunofluorescence. *Cytometry Part A*, 83(11):1017–1026, 2013.

[133] Haberthur K. The difference between an image, flow, time-lapse and cell-sorting cytometer. https://bitesizebio.com/33459/image-flow-time-lapse-sorting-cytometer/, 2017.

[134] S. A. Marino. 50 years of the Radiological Research Accelerator Facility (RARAF). *Radiation Research*, 187(4):413–423, 2017.

[135] M. Z. Dewan, A. E. Galloway, N. Kawashima, J. K. Dewyngaert, J. S. Babb, et al. Fractionated but not single-dose radiotherapy induces an immune-mediated abscopal effect when combined with anti-CTLA-4 antibody. *Clinical Cancer Research*, 15(17):5379–5388, 2009.

[136] A. Rosato, S. Dalla Santa, A. Zoso, S. Giacomelli, G. Milan, et al. The cytotoxic T-lymphocyte response against a poorly immunogenic mammary adenocarcinoma is focused on a single immunodominant class i epitope derived from the gp70 Env product of an endogenous retrovirus. *Cancer Research*, 63(9):2158–2163, 2003.

[137] P. L. Chen, D. J. Brenner, and R. K. Sachs. Ionizing radiation damage to cells: effects of cell cycle redistribution. *Mathematical Biosciences*, 126(2):147 – 170, 1995.

[138] M. A. Chaudhry. Base excision repair of ionizing radiation-induced DNA damage in G1 and G2 cell cycle phases. *Cancer Cell International*, 7(1):15, 2007.

[139] Y. Xu, G. Garty, S. A. Marino, T. N. Massey, G. Randers-Pehrson, et al. Novel neutron sources at the Radiological Research Accelerator Facility. *Journal of Instrumentation*, 7(3), 2012.

[140] Y. Xu, G. Randers-Pehrson, S. A. Marino, G. Garty, A. Harken, et al. Broad energy range neutron spectroscopy using a liquid scintillator and a proportional counter: application to a neutron spectrum similar to that from an improvised nuclear device. *Nuclear Instruments and Methods in Physics Research Section A*, 2016.

[141] T. T. Puck and P. I. Marcus. Action of X-rays on mammalian cells. *Journal of Experimental Medicine*, 103(5):653–666, 1956.

[142] J. Schindelin, I. Arganda-Carreras, E. Frise, V. Kaynig, M. Longair, et al. Fiji: An open source platform for biological image analysis. *Nature Methods*, 9(7):676–682, 2012.

[143] T. J. Collins. ImageJ for microscopy. *BioTechniques*, 43(1 Suppl):25–30, 2007.

[144] S. Barbieri, G. Baiocco, G. Babini, J. Morini, W. Friedland, et al. Modelling γ-h2ax foci induction to mimic limitations in the scoring technique. *Radiation Protection Dosimetry*, page ahead of print, 2018.

[145] N. Otsu. A threshold selection method from gray-level histograms. *IEEE Transactions on Systems, Man, and Cybernetics*, 9(1):62–66, 1979.

[146] P. Lambin, B. Fertil, E. P. Malaise, and M. C. Joiner. Multiphasic survival curves for cells of human tumor cell lines: induced repair or hypersensitive subpopulation? *Radiation Research*, 138(1 Suppl):S32–6, 1994.

[147] M.C. Joiner and B. Marples. The response of chinese hamster V79 cells to low radiation doses: evidence of enhanced of the whole cell population sensitivity. *Radiation Research*, 133(1):41–51, 1993.

[148] S. ChanDNA, B. S. Dwarakanath, D. Khaitan, T. L. Mathew, and V. Jain. Low-dose radiation hypersensitivity in human tumor cell lines: effects of cell-cell contact and nutritional deprivation. *Radiation Research*, 157(5):516–525, 2002.

[149] F. A. Azooz. Survival curves models of neutron irradiation data and evidence for hypersensitivity phenomena. *Bulgarian Journal of Physics*, 37:123–131, 2010.

[150] F. A. Azooz and S. K. Hashim. A logarithmic formula to describe the relationship between the increased radiosensitivity at low doses and the survival at 2 Gray. *Sultan Qaboos University Medical Journal*, 13:560–566, 2013.

[151] J. S. Bedford and D. Phil. Sublethal damage, potentially lethal damage, and chromosomal aberrations in mammalian cells exposed to ionizing radiations. *International Journal of Oncology Biology Physics*, 21(6):1457–1469, 1991.

[152] C. Liu, T. Kawata, N. Shigematsu, F. Cucinotta, K. George, et al. A comparison of chromosome repair kinetics in G_0 and G_1 reveals that enhanced repair fidelity under noncycling conditions accounts for increased potentially lethal damage repair. *Journal of Radiation Research*, 174:566–73, 2010.

[153] R. Cox, W. K. Masson, R. R. Weichselbaum, J. Nove, and J. B. Little. The repair of potentially lethal damage in X-irradiated cultures of normal and Ataxia Telangiectasia human fibroblasts. *International Journal of Radiation Biology and Related Studies in Physics, Chemistry and Medicine*, 39(4):357–365, 1981.

[154] C. F. Arlett and A. Priestley. Deficient recovery from potentially lethal damage in some gamma-irradiated human fibroblast cell strains. *The British journal of cancer. Supplement*, 6:227—232, 1984.

[155] G. Iliakis. Radiation-induced potentially lethal damage: DNA lesions susceptible to fixation. *International journal of radiation biology*, 53:541–84, 1988.

[156] C. Liu, T Kawata, G. Zhou, Y. Furusawa, R. Kota, et al. Comparison of the repair of potentially lethal damage after low- and high-LET radiation exposure, assessed from the kinetics and fidelity of chromosome rejoining in normal human fibroblasts. *Journal of Radiation Research*, 54:989–997, 2013.

[157] E. A. Blakely, P. Y. Chang, and L. Lommel. Cell-cycle-dependent recovery from heavy-ion damage in G_1-phase cells. *Radiation Research*, 104(2):S145–S157, 1985.

[158] M. Suzuki, Y. Kase, T. Kanai, and K. Ando. Change in radiosensitivity with fractionated-dose irradiation of carbon-ion beams in five different human cell lines. *International Journal of Radiation Oncology Biology Physics*, 48(1):251 – 258, 2000.

[159] R. Stewart. Two-lesion kinetic model of DSB rejoining and cell killing. *Radiation Research*, 156:365–378, 2001.

[160] G. Iliakis, H. Wang, A. R. Perrault, W. Boecker, B. Rosidi, et al. Mechanisms of DNA double strand break repair and chromosome aberration formation. *Cytogenet Genome Research*, 104:14–20, 2004.

[161] R. Brun and F. Rademakers. ROOT : an object oriented data analysis framework. *Nuclear Instruments and Methods in Physics*, A389:81–86, 1997.

[162] D. Juerß, M. Zwar, U. Giesen, R. Nolte, S. Kriesen, et al. Comparative study of the effects of different radiation qualities on normal human breast cells. *Radiation Oncology*, 12(1):159, 2017.

[163] P. W. Nagle, N. A. Hosper, L. Barazzuol, A. L. Jellema, M. Baanstra, et al. Lack of DNA damage response at low radiation doses in adult stem cells contributes to organ dysfunction. *Clinical Cancer Research*, 2018.

[164] E. Staaf, K. Brehwens, S. Haghdoost, J. Czub, and A. Wojcik. Gamma-H2AX foci in cells exposed to a mixed beam of X-rays and alpha particles. *Genome Integrity*, 3:8, 2012.

[165] D. Ding, Y. Zhang, J. Wang, X. Wang, D. Fan, et al. γ-H2AX/53BP1 /pKAP-1 foci and their linear tracks induced by in vitro exposure to

radon and its progeny in human peripheral blood lymphocytes. *Scientific Reports*, 6:1–11, 2016.

[166] D. Avondoglio, T. Scott, W. J. Kil, M. Sproull, P. J. Tofilon, and K. Camphausen. High throughput evaluation of γ-H2AX. *Radiation Oncology*, 4:31, 2009.

[167] A. N. Ivashkevich, O. A. Martin, A. J. Smith, C. E. Redon, W. M. Bonner, et al. γ-H2AX foci as a measure of DNA damage: a computational approach to automatic analysis. *Mutation Research*, 711(1-2):49–60, 2011.

[168] F. Tommasino, T. Friedrich, B. Jakob, B. Meyer, M. Durante, and M. Scholz. Induction and processing of the radiation-induced gamma-H2AX signal and its link to the underlying pattern of DSB : a combined experimental and modelling study. *PLoS ONE*, 10(6):1–25, 2015.

[169] D. M. Sridharan, A. Asaithamby, S. R. Blattnig, S. V. Costes, P. W. Doetsch, et al. Evaluating biomarkers to model cancer risk post cosmic ray exposure. *Life Sciences in Space Research*, 9:19 – 47, 2016.

[170] S. V. Costes, A. Ponomarev, J. L. Chen, D. Nguyen, F. A. Cucinotta, and M. H. Barcellos-Hoff. Image-based modeling reveals dynamic redistribution of DNA damage into nuclear sub-domains. *PLoS Computational Biology*, 3(8):1–12, 2007.

[171] S. Roch-Lefèvre, M. Valente, P. Voisin, and J. F. Barquinero. Suitability of the γ-H2AX assay for human radiation biodosimetry. In Mitsuru Nenoi, editor, *Current Topics in Ionizing Radiation Research*, chapter 2. IntechOpen, Rijeka, 2012.

[172] C. E. Redon, A. J. Nakamura, O. Sordet, J. S. Dickey, K. Gouliaeva, et al. γ-H2AX detection in peripheral blood lymphocytes, splenocytes, bone marrow, xenografts, and skin. *Methods in Molecular Biology*, 682:249–70, 2011.

[173] D. Heylmann and B. Kaina. The γ-H2AX DNA damage assay from a drop of blood. *Nature Publishing Group*, 6(February):1–9, 2016.

[174] C. E. Redon, J. S. Dickey, W. M. Bonner, and O. A. Sedelnikova. γ-H2AX as a biomarker of DNA damage induced by ionizing radiation in human peripheral blood lymphocytes and artificial skin. *Advances in Space Research*, 43(8):1171–1178, 2009.

[175] A. Sak, S. Grehl, P. Erichsen, M. Engelhard, A. Grannass, et al. Gamma-H2AX foci formation in peripheral blood lymphocytes of tumor patients after local radiotherapy to different sites of the body: dependence on the dose-distribution, irradiated site and time from start of treatment. *International Journal of Radiation Biology*, 83(10):639–652, 2007.

[176] J. Wang, L. He, D. Fan, D. Ding, X. Wang, et al. Establishment of a γ-H2AX foci-based assay to determine biological dose of radon to red bone marrow in rats. *Nature Publishing Group*, 6(July):1–11, 2016.

[177] A. Ivashkevich, C. E. Redon, A. J. Nakamura, R. F. Martin, and O. A. Martin. Use of the γ-H2AX assay to monitor DNA damage and repair in translational cancer research. *Cancer LETters*, 327(1-2):123–133, 2012.

[178] P. M. Sharma, B. Ponnaiya, M. Taveras, I. Shuryak, H. Turner, and D. J. Brenner. High throughput measurement of γH2AX DSB repair kinetics in a healthy human population. *PLoS ONE*, 10(3):1–18, 2015.

[179] S. Oeck, N. M. Malewicz, S. Hurst, J. Rudner, and V. Jendrossek. The Focinator - a new open-source tool for high-throughput foci evaluation of DNA damage. *Radiation Oncology*, pages 1–11, 2015.

[180] J. Feng, J. Lin, P. Zhang, S. Yang, Y. Sa, et al. A novel automatic quantification method for high-content screening analysis of DNA double strand-break response. *Scientific Reports*, 7(1):1–10, 2017.

[181] A. Jucha, A. Wegierek-Ciuk, Z. Koza, H. Lisowska, A. Wojcik, et al. FociCounter: a freely available pc programme for quantitative and qualitative analysis of gamma-H2AX foci. *Mutation Research*, 696(1):16–20, 2010.

[182] C. Villagrasa, S. Meylan, G. Gonon, G. Gruel, U. Giesen, et al. GEANT4-DNA simulation of DNA damage caused by direct and indirect radiation effects and comparison with biological data. *EPJ Web of Conferences*, 153:04019, 2017.

[183] H. Rabus, S. Barbieri, G.o Baiocco, A. Ottolenghi, and U. Giesen. Investigation into the probability for miscounting in foci-based assays. *Radiation Protection Dosimetry*, page ahead of print, 2018.

[184] International Commission on Radiation Units and Measurments. Tissue substitutes in radiation dosimetry and measurement., 1989.

[185] G. Baiocco, S. Barbieri, G. Babini, J. Morini, D. Alloni, et al. The origin of neutron biological effectiveness as a function of energy. *Scientific Reports*, 6:1–14, 2016.

[186] M. Gulston, C. de Lara, T. Jenner, E. Davis, and P. O'Neill. Processing of clustered DNA damage generates additional double-strand breaks in mammalian cells post-irradiation. *Nucleic Acids Research*, 32(4):1602–9, 2004.

[187] J. G. White, W. B. Amos, and M. Fordham. An evaluation of confocal versus conventional imaging of biological structures by fluorescence light microscopy. *Cell*, 105(1):41–48, 1987.

[188] Introduction to confocal microscopy. https://www.olympus-lifescience.com/en/microscope-resource/primer/techniques/confocal/confocalintro/, 2015.

[189] L. Jezkova, M. Zadneprianetc, E. Kulikova, E. Smirnova, T. Bulanova, et al. Particles with similar LET values generate DNA breaks of different complexity and reparability: a high-resolution microscopy analysis of γH2AX/53BP1 foci. *Nanoscale*, 10(3):1162–1179, 2018.

[190] N. Autsavapromporn, S. M. de Toledo, J. B. Little, J. P. Jay-Gerin, A. L. Harris, et al. The role of gap junction communication and oxidative stress in the propagation of toxic effects among high-dose α-particle-irradiated human cells. *The British journal of cancer. Supplement*, 175(3):347—357, 2011.

[191] S. Goto, M. Watanabe, and F. Yatagai. Delayed cell cycle progression in human lymphoblastoid cells after exposure to high-LET radiation correlates with extremely localized DNA damage. *Radiation Research*, 158(6):678–686, 2002.

[192] F. A. Cucinotta and M. Durante. Cancer risk from exposure to Galactic Cosmic Rays: implications for space exploration by human beings. *The Lancet Oncology*, 7:431–5, 2006.

[193] D. T. Goodhead, J. Thacker, and R. Cox. Weiss Lecture. Effects of radiations of different qualities on cells: molecular mechanisms of damage and repair. *International Journal of Radiation Biology*, 63:543–556, 1993.

[194] T.J. Jenner, C. M. deLara, and D. L. O'Neill, P. Stevens. Induction and rejoining of DNA double-strand breaks in V79-4 mammalian cells following gamma- and alpha-irradiation. *International Journal of Radiation Biology*, 64(3):256–73, 1993.

[195] A. Asaithamby, A. Uematsu, N. anf Chatterjee, M. D. Story, S. Burma, et al. Repair of HZE-particle-induced DNA double-strand breaks in normal human fibroblasts. *Radiation Research*, 169(4):437–446, 2008.

[196] T. A. Dobbs, P. Palmer, Z. Maniou, M. E. Lomax, and P. O'Neill. Interplay of two major repair pathways in the processing of complex double-strand DNA breaks. *DNA repair*, 7(8):1372—1383, 2008.

[197] Software for life science research: LAS X life science. https://www.leica-microsystems.com/it/prodotti/software-per-microscopi/dettagli/product/leica-las-x-ls/, 2018.

[198] N. I. Nakajima, H. Brunton, R. Watanabe, A. Shrikhande, R. Hirayama, et al. Visualisation of γH2AX foci caused by heavy ion particle traversal; distinction between core track versus non-track damage. *PLoS ONE*, 8(8):1–14, 2013.

[199] F. A. Cucinotta, M. Y. Kim, and L. Ren. Space radiation: the number one risk to astronaut health beyond Low Earth Orbit. *Life*, 4(3):491–510, 2014.

[200] T. Ohnishi, A. Takahashi, A. Nagamatsu, K. Omori, H. Suzuki, et al. Detection of space radiation-induced double strand breaks as a track in cell nucleus. *Biochemical and Biophysical Research Communications*, 390(3):485–488, 2009.

[201] M. A. Hill. Fishing for radiation quality: chromosome aberrations and the role of radiation track structure. *Radiation Protection Dosimetry*, 166(1-4):295–301, 2015.

[202] G. D. Badhwar and P. M. O'Neill. Galactic Cosmic Ray model and its applications. *Advances in Space Research*, 17(2):7 – 17, 1996.

[203] G. D. Badhwar and P. M. O'Neill. Long-term modulation of galactic cosmic radiation and its model for space exploration. *Advances in Space Research*, 14(10):749 – 757, 1994.

[204] M. Durante and F. A. Cucinotta. Physical basis of radiation protection in space travel. *Rev. Mod. Phys.*, 83:1245–1281, 2011.

[205] A. R. Kennedy. Biological effects of space radiation and development of effective countermeasures. *Life Sciences in Space Research*, 1:10–43, 2014.

[206] D. M. Hassler, C. Zeitlin, R. F. Wimmer-Schweingruber, B. Ehresmann, S. Rafkin, et al. Mars' surface radiation environment measured with the Mars Science Laboratory's Curiosity rover. *Science*, 119, 2013.

[207] M. Moreno-Villanueva, M. Wong, T. Lu, Y. Zhang, and H. Wu. Interplay of space radiation and microgravity in DNA damage and DNA damage response. *Microgravity*, 3(1):14, 2017.

[208] J. B. West. Historical perspectives: physiology in microgravity. *Journal of Applied Physiology*, 89(25):2483–2489, 2000.

[209] D. Williams, A. Kuipers, C. Mukai, and R. Thirsk. Acclimation during space flight: effects on human physiology. *Canadian Medical Association Journal*, 180(13):1317–1323, 2009.

[210] M. Mognato, C. Girardi, S. Fabris, and L. Celotti. DNA repair in modeled microgravity: double strand break rejoining activity in human lymphocytes irradiated with γ-rays. *Mutation Research*, 663(1):32 – 39, 2009.

[211] T. Ohnishi, A. Takahashi, A. Nagamatsu, K. Omori, H. Suzuki, et al. Detection of space radiation-induced double strand breaks as a track in cell nucleus. *Biochemical and Biophysical Research Communications*, 390(3):485 – 488, 2009.

[212] T. Lu, Y. Zhang, M. Wong, A. Feiveson, R. Gaza, et al. Detection of DNA damage by space radiation in human fibroblasts flown on the international space station. *Life Sciences in Space Research*, 12:24 – 31, 2017.

[213] T. Lu, Y. Zhang, Y. Kidane, A. Feiveson, L. Stodieck, et al. Cellular responses and gene expression profile changes due to bleomycin-induced DNA damage in human fibroblasts in space. *PLoS ONE*, 12(3):1–19, 2017.

[214] W. Hu, H. Pei, H. Li, N. Ding, J. He, et al. Effects of shielding on the induction of 53BP1 foci and micronuclei after Fe ion exposures. *Journal of Radiation Research*, 55(1):10–16, 2014.

[215] A. Ottolenghi, F. Ballarini, and M. Biaggi. Mechanistic bases for modelling space radiation risk and planning radiation protection of astronauts. *Physica Medica*, 17 Suppl 1:272–7, 2001.

[216] J. W. Norbury, W. Schimmerling, T. C. Slaba, Azzam E. I., F. F. Badavi, et al. Galactic Cosmic Ray simulation at the NASA space radiation laboratory. *Life Sciences in Space Research*, 8:38 – 51, 2016.

[217] S. Trovati, F. Ballarini, G. Battistoni, F. Cerutti, A. Fasso, et al. Human exposure to space radiation: role of primary and secondary particles. *Radiation Protection Dosimetry*, 122(1-4):362–366, 2006.

[218] L. H. Heilbronn, T. B. Borak, L. W. Townsend, P. E. Tsai, C. A. Burnham, and R. A. McBeth. Neutron yields and effective doses produced by Galactic Cosmic Ray interactions in shielded environments in space. *Life Sciences in Space Research*, 7:90–99, 2015.

[219] J. Köhler, B. Ehresmann, C. Zeitlin, R. F. Wimmer-Schweingruber, D. M. Hassler, et al. Measurements of the neutron spectrum in transit to Mars on the Mars Science Laboratory. *Life Sciences in Space Research*, 5:6 – 12, 2015.

[220] J. Guo, C. Zeitlin, R. Wimmer-Schweingruber, D. M. Hassler, J. Köhler, et al. Measurements of the neutral particle spectra on Mars by MSL/RAD from 2015-11-15 to 2016-01-15. *Life Sciences in Space Research*, 14(June):12–17, 2017.

[221] J. Köhler, C. Zeitlin, B. Ehresmann, D. M. Hassler, G. Reitz, et al. Measurements of the neutron spectrum on the martian surface with

MSL/RAD. *Journal of Geophysical Research: Planets*, 119:594–603, 2014.

[222] J. Guo, C. Zeitlin, R. F. Wimmer-Schweingruber, T. McDole, P. Kühl, et al. A generalized approach to model the spectra and radiation dose rate of Solar Particle Events on the surface of Mars. *The Astronomical Journal*, 155(1):49, 2018.

[223] P. O'Neill. Badhwar–O'neill 2010 Galactic Cosmic Ray flux model—revised. *IEEE Transactions on Nuclear Science*, 57:3148 – 3153, 2011.

[224] F. A. Cucinotta. Evaluating shielding approaches to reduce space radiation cancer risks. In *TM-2012-217361*, 2012.

[225] F. A. Cucinotta, M. Y. Kim, and L. Ren. Evaluating shielding effectiveness for reducing space radiation cancer risks. *Radiation Measurements*, 41:1173–1185, 2006.

[226] L. Sihver, T. Sato, M. Puchalska, and G. Reitz. Simulations of the Matroshka experiment at the international space station using PHITS. *Radiation and Environmental Biophysics*, 49(3):351–357, 2010.

[227] K. Gustafsson, L. Sihver, D. Mancusi, T. Sato, G. Reitz, et al. PHITS simulations of the Matroshka experiment. *Advances in Space Research*, 46(10):1266–1272, 2010.

[228] F. A. Cucinotta. Radiation risk acceptability and limitations. `https://three.jsc.{NASA}.gov/articles/AstronautRadLimitsFC.pdf`, 2010.

[229] National Aeronautics and Space Administration. Space flight human-system standard. *NASA Standard 3001*, 1(A: Crew Health), 2018.

[230] P. Spillantini, M. Casolino, M. Durante, R. Mueller-Mellin, G. Reitz, et al. Shielding from cosmic radiation for interplanetary missions: active and passive methods. *Radiation Measurements*, 42:14–23, 2007.

[231] M. Durante. Physical and biomedical countermeasures for space radiation risk. *Zeitschrift fur Medizinische Physik*, 18(4):244–252, 2008.

[232] J. W. Wilson, B. M. Anderson, F. A. Cucinotta, J. Ware, and C. J. Zeitlin. Spacesuit radiation shield design methods. *SAE Technical Papers*, 2006.

[233] D. W. Murrow, R. Gaza, B. Lytle, S. Anderson, O. Milstein, et al. ASTRORAD: personal radiation shield for deep space exploration. *IAC-15-A5.1.13*, 2015.

[234] M. Vuolo, G. Baiocco, S. Barbieri, L. Bocchini, M. Giraudo, et al. Exploring innovative radiation shielding approaches in space: a material and design study for a wearable radiation protection spacesuit. *Life Sciences in Space Research*, 15:69 – 78, 2017.

[235] M. A. Xapsos, G. P. Summers, J. L. Barth, E. G. Stassinopoulos, and E. A. Burke. Probability model for worst case solar proton event fluences. *IEEE Transactions on Nuclear Science*, 46:1481 – 1485, 2000.

[236] G. Baiocco, L. Bocchini, M. Giraudo, S. Barbieri, L. Narici, et al. Innovative solutions for personal radiation shielding in space. *Radiation Protection Dosimetry*, page ahead of print, 2018.

[237] G. Santin, V. Ivanchenko, H. Evans, P. Nieminen, and E. Daly. GRAS: a general-purpose 3-D modular simulation tool for space environment effects analysis. *IEEE Transactions on Nuclear Science*, 52(6):2294–2299, 2005.

[238] S. Agostinelli, J. Allison, K. Amako, J. Apostolakis, H. Araújo, et al. GEANT4 - a simulation toolkit. *Nuclear Instruments and Methods in Physics Research Section A Accelerators Spectrometers Detectors and Associated Equipment*, 506:250, 2003.

[239] A. V. Ivantchenko, V. N. Ivanchenko, J. M. Molina, and S. L. Incerti. GEANT4 hadronic physics for space radiation environment. *International Journal of Radiation Biology*, 88(1-2):171–175, 2012.

[240] R. Chytracek, J. McCormick, W. Pokorski, and G. Santin. Geometry description markup language for physics simulation and analysis applications. *IEEE Transactions on Nuclear Science*, 53:2892 – 2896, 2006.

[241] G. Baiocco, M. Giraudo, L. Bocchini, S. Barbieri, I. Locantore, et al. A water-filled garment to protect astronauts during interplanetary missions tested on board the iss. *Life Sciences in Space Research*, 18:1 – 11, 2018.

[242] ICRP. Adult reference computational phantoms, 39, 2009.

[243] International Commission on Radiation Units and Measurments. Linear energy transfer, 1970.

[244] F. Tommasino, T. Friedrich, U. Scholz, G. Taucher-Scholz, M. Durante, et al. A DNA double-strand break kinetic rejoining model based on the local effect model. *Radiation Research*, 180(5):524–538, 2013.

[245] L. W. Townsend. Critical analysis of active shielding methods for space radiation protection. In *2005 IEEE Aerospace Conference*, pages 724–730, 2005.

[246] S. Barnard, E. A. Ainsbury, J. Al-Hafidh, V. Hadjidekova, R. Hristova, et al. The first gamma-H2AX biodosimetry intercomparison exercise of the developing european biodosimetry network RENEB. *Radiation Protection Dosimetry*, 164(3):265–270, 2015.

[247] M. Gerić, A. Štraser, G. Gajski, J. Nunić, and B. Žegura. Use of γ-H2AX foci assay on human peripherala blood lymphocytes as sensitive biomarker of exposure. *Proceedings of the National Academy of Science*, pages 166–171, 1988.

[248] F. A. Cucinotta, M. Kim, and L. Chappell. Space radiation cancer risk projections and uncertainties-2010. *NASA Tech. Pap.*, pages 1–132, 2011.

[249] L. W. Townsend. Critical analysis of active shielding methods of space radiation protection. *IEEE Aerospace Conference 2005*, 2005.

[250] F. A. Cucinotta and M. Durante. Risk of radiation carcinogenesis. *Human Research Program Requirements Document*, pages 119–170, 2009.

[251] National Aeronautics and Space Administration. Understanding space radiation. *NASA Facts*, page 3, 2002.

[252] L. Heilbronn. Neutron properties and definitions. `http://three.usra.edu/articles/NeutronPropertiesDefinitions.swf`, 2015.

[253] F. A. Cucinotta. Space radiation organ doses for astronauts on past and future missions. *Space Physiology and Medicine*, 5(2), 2007.

[254] J. Rask, W. Vercoutere, B. Navarro, and A. Karuse. The Radiation Challenge - Space Faring. *NASA*, Module 3(Module 3):36, 2008.

[255] A. R. Kennedy. Biological effects of space radiation and development of effective countermeasures. *Life Sciences in Space Research*, 1(1):10–43, 2014.

[256] P. Spillantini, M. Casolino, M. Durante, R. Mueller-Mellin, G. Reitz, L. Rossi, V. Shurshakov, and M. Sorbi. Shielding from cosmic radiation for interplanetary missions: active and passive methods. *Radiation Measurements*, 42(1):14–23, 2007.

[257] T. B. Borak, L. H. Heilbronn, L. W. Townsend, R. A. McBeth, and W. De Wet. Quality factors for space radiation: a new approach. *Life Sciences in Space Research*, 1(1):96–102, 2014.

[258] W. R. Holley and A. Chatterjee. Clusters of DNA damage induced by ionizing radiation: formation of short DNA fragments. Theoretical modeling. *Radiation Research*, 145(2):188–199, 1996.

[259] G. Baiocco, S. Barbieri, G. Babini, J. Morini, W. Friedland, et al. At the physics-biology interface: the neutron affair. *Radiation Protection Dosimetry*, 180(1-4):278–281, 2018.

[260] D. Schardt, T. Elsässer, and D. Schulz-Ertner. Heavy-ion tumor therapy: Physical and radiobiological benefits. *Reviews of Modern Physics*, 82:383–425, 2010.

[261] M. Kan'o, T. Kawata, H. Ito, N. Shigematsu, C. Liu, et al. Repair of potentially lethal damage in normal cells and Ataxia Telangiectasia cells; consideration of Non-Homologous End-Joining. *Journal of Radiation Research*, 48(1):31–38, 2007.

Publications

Publications in peer-reviewed ISI-indexed journals:

1. **S. Barbieri**, G. Baiocco, G. Babini, J. Morini, W. Friedland, M. Buonanno, V. Grilj, D. J. Brenner, A. Ottolenghi. Modelling γ-H2AX foci induction to mimic limitations in the scoring technique. Radiation Protection Dosimetry, online ahead of print, 2018. DOI: 10.1093/rpd/ncy217

2. H. Rabus, **S. Barbieri**, G. Baiocco, A. Ottolenghi, U. Giesen. Investigation into uncertainty contributions in foci-based assays. Radiation Protection Dosimetry, online ahead of print, 2018. DOI: 10.1093/rpd/ncy251

3. J. Morini, G. Babini, **S. Barbieri**, G. Baiocco, M. Ciocca, G. B. Ivaldi, M. Liotta, S. Molinelli, P. Tabarelli de Fatis, A. Ottolenghi. A comparison between X-rays and carbon ions irradiation in human neural stem cells. Radiation Protection Dosimetry, online ahead of print, 2018. DOI: 10.1093/rpd/ncy231

4. G. Baiocco, G. Babini, **S. Barbieri**, J. Morini, W. Friedland, C. Villagrasa, H. Rabus, A. Ottolenghi, What roles for track structure and microdosimetry in the era of –omics and systems biology? Radiation Protection Dosimetry, online ahead of print, 2018. DOI: 10.1093/rpd/ncy221

5. G. Baiocco, L. Bocchini, M. Giraudo, **S. Barbieri**, L. Narici, C. Lobascio, A. Ottolenghi. Innovative solutions for personal radiation shielding in space. Radiation Protection Dosimetry, online ahead of print, 2018. DOI: 10.1093/rpd/ncy216

6. J. Schuemann, A. McNamara, J. W. Warmenhoven, N. T. Henthorn, K. Kirkby, M. J. Merchant, S. Ingram, H. Paganetti, K. D. Held, J. Ramos-Mendez, B. Faddegon, J. Perl, D. Goodhead, I. Plante, H. Rabus, H. Nettelbeck, W. Friedland, P. Kundrat, A. Ottolenghi, G. Baiocco, **S. Barbieri** et al. A new Standard DNA Damage (SDD) data format. Radiation Research, online ahead of print, 2019. DOI:10.1667/RR15209.1

7. G. Baiocco, M. Giraudo, L. Bocchini, **S. Barbieri**, I. Locantore, E. Brussolo, D. Giacosa, L. Meucci, S. Steffenino, A. Ballario, B. Barresi, R. Barresi, L. Ravagnolo, M. Benassai, L. Narici, A. Rizzo, E. Carrubba, F. Carubia, G. Neri, M. Crisconio, S. Piccirillo, G. Valentini, S. Barbero, M.

Giacci, C. Lobascio, A. Ottolenghi. A water-filled garment to protect astronauts during interplanetary missions tested on board the ISS. Life Science in Space Research (18), 1-11, 2018. DOI:10.1016/j.lssr.2018.04.002

8. G. Babini, J. Morini, **S. Barbieri**, G. Baiocco, G. B. Ivaldi, M. Liotta, P. Tabarelli de Fatis, A. Ottolenghi. A Co-culture Method to Investigate the Crosstalk Between X-ray Irradiated Caco-2 Cells and PBMC. Journal of Visualized Experiments (131), 2018. e56908, DOI:10.3791/56908, WOS:000426095700101

9. G. Baiocco, **S. Barbieri**, G. Babini, J. Morini, W. Friedland, P. Kundrát, E. Schmitt, M. Puchalska, U. Giesen, R. Nolte, A. Ottolenghi. At the physics-biology interface: the neutron affair. Radiation Protection Dosimetry, 1-4, 2017. DOI:10.1093/rpd/ncx222

10. G. Baiocco, M. Vuolo, **S. Barbieri**, L. Bocchini, M. Giraudo, T. Gheysens, C. Lobascio, A. Ottolenghi. Exploring innovative radiation shielding approaches in space: a material and design study for a wearable radiation protection spacesuit. Life Sciences in Space Research (15), 69-78, 2017. DOI:10.1016/j.lssr.2017.08.003, WOS:000416873500009

11. W. Friedland, E. Schmitt, P. Kundrát, G. Baiocco, **S. Barbieri**, A. Ottolenghi. Comprehensive track-structure based evaluation of DNA damage by light ions from radiotherapy relevant energies down to stopping. Scientific Reports (7), 45161, 2017. DOI:10.1038/srep45161, WOS:000397824900001

12. J. Morini, G. Babini, **S. Barbieri**, G. Baiocco, A. Ottolenghi. The interplay between radioresistant Caco-2 cells and the immune system increases epithelial layer permeability and alters signaling protein spectrum. Frontiers in Immunology, 2017. doi:10.3389/fimmu.2017.00223, WOS:000395332600001

13. G. Baiocco, **S. Barbieri**, G. Babini, J. Morini, D. Alloni, W. Friedland, P. Kundrát, E. Schmitt, M. Puchalska, L. Sihver, A.Ottolenghi. An ab initio approach to trace back the origin of neutron biological effectiveness as a function of energy. Scientific Reports, 2016. DOI:10.1038/srep34033, WOS:000383697500001

Contributions to conferences

Invited talks:

1. **S. Barbieri**, G. Baiocco, G. Babini, J. Morini, W. Friedland, M. Buonanno, V. Grilj, D. J. Brenner, A. Ottolenghi."An ab-initio approach to predict DNA damage foci following exposure to Earth and space radiation". COSPAR General Assembly, 18/07/2018, Pasadena, USA.

2. **S. Barbieri**. "Physical and radiobiological bases of hadron biological effectiveness, and its dependence on ion type and energy", Hadrontherapy school funded by CNAO, FranceHADRON and the University of Lyon, 22/09/2016, CNAO, Pavia, Italy.

Other contributions:

1. **S. Barbieri**, G. Baiocco, G. Babini, J. Morini, W.Friedland, M. Buonanno, V. Grilj, D. Brenner, A. Ottolenghi. "A Monte Carlo approach to simulate results from DNA damage foci scoring according to the chosen detection technique". RRS Annual Meeting, Chicago, Illinois, USA, September 2018.

2. G. Baiocco, **S. Barbieri**, J. Guo, G. Babini, J. Morini, W. Friedland, R. Wimmer-Schweingruber, A. Ottolenghi. "Radiobiological effectiveness of neutrons in space". COSPAR General Assembly 2018, Pasadena, USA, July 2018.

3. G. Babini, G. Baiocco, **S. Barbieri**, J. Morini, A. Ottolenghi. "The hurdles and promises of systems biology approaches in space radiation research". COSPAR General Assembly 2018, Pasadena, USA, July 2018.

4. G. Baiocco, M. Giraudo, L. Bocchini, **S. Barbieri**, L. Narici, M. Crisconio, S. Piccirillo, V. Giovanni, C. Lobascio, A. Ottolenghi, "Personal radiation shielding for space exploration: the PERSEO experience", COSPAR General Assembly 2018, Pasadena, USA, July 2018.

5. **S. Barbieri**, G. Baiocco, G. Babini, J. Morini, W. Friedland, M. Buonanno, D. Brenner, A. Ottolenghi. "Track-structure based simulation of the observer for the scoring of radiation-induced DNA damage foci". EURADOS Annual Meeting 2018, Lisbon, Portugal, February 2018.

6. **S. Barbieri**, G. Babini, G. Baiocco, J. Morini, W. Friedland, M. Buonanno, D. Brenner, A. Ottolenghi. "Mechanistic study of low- and high-LET radiation induced DNA damages: benchmarking Monte Carlo simulations with experimenta results". MICROS Microdosimetry Symposium 2017, Venice, Italy, November 2017.

7. A. Ottolenghi, G. Babini, G. Baiocco, **S. Barbieri**, J. Morini. "What roles for track structure and microdosimetry in the era of omics, systems biology and holistic approaches?". MICROS Microdosimetry Symposium 2017, Venice, Italy, November 2017.

8. J. Morini, G. Babini, G. Baiocco, **S. Barbieri**, M. Ciocca, G. B. Ivaldi, M. Liotta, S. Molinelli, P. Tabarelli de Fatis, A. Ottolenghi. "A comparison between X-ray and carbon ion irradiation in human neural stem cells". MICROS Microdosimetry Symposium 2017, Venice, Italy, November 2017.

9. **S.Barbieri**, M. Buonanno, G. Baiocco, G. Babini, J. Morini, W.Friedland, D.Brenner, A.Ottolenghi. "Kinetics of γ-H2AX foci formation in cancer cells exposed to radiation of different LET". RRS Annual Meeting, Cancun, Mexico, October 2017.

10. **S. Barbieri**, G. Babini, G. Baiocco, J. Morini, W. Friefland, M. Buonanno, A. Ottolenghi. "Track-structure simulation of γ-H2AX foci and comparison with experimental results: unravelling the role of radiation quality". ERRS Annual Meeting, Essen, Germany, September 2017.

11. A. Ottolenghi, G. Babini, G. Baiocco, **S. Barbieri**, J. Morini. "From track structure to systems biology: How many roads must a man walk down...". ERRS, Essen, Germany, September 2017.

12. W. Friedland, E. Schmitt, P. Kundrát, A. Ottolenghi, G. Baiocco, **S. Barbieri**, D. Alloni, M. Dingfelder. "Modelling DNA damage at light ions' track ends". Radiation Research Society Annual Meeting, Hawaii, USA, October 2016.

13. W. Friedland, E. Schmitt, P. Kundrát, A. Ottolenghi, G. Baiocco, **S. Barbieri**, D. Alloni, M. Dingfelder. "Simulations tracking DNA damage along ion tracks". Biological Radiation Research – GBS2016, Erlangen, Germany, September 2016.

14. G. Baiocco, **S. Barbieri**, G. Babini, J. Morini, D. Alloni, W. Friedland, P. Kundrát, E. Schmitt, M. Puchalska, L. Sihver, A. Ottolenghi. "An ab-initio approach to trace back the physical origin of neutron biological effectiveness as a function of energy". Radiation Protection Week, Oxford, UK, September 2016.

15. G. Baiocco, **S. Barbieri**, G. Babini, J. Morini, D. Alloni, W. Friedland, P. Kundrát, E. Schmitt, M. Puchalska, L. Sihver, A. Ottolenghi. "Neutron induced DNA damage using transport and track structure calculations". EURADOS Annual Meeting - AM2016, Milan, Italy, February 2016.

16. G. Baiocco, **S. Barbieri**, G. Babini, J. Morini, D. Alloni, W. Friedland, P. Kundrát, E. Schmitt, M. Puchalska, L. Sihver, A. Ottolenghi. "Neutron biological effectiveness as a function of energy with transport and track structure calculations". DoReMi's final meeting, Budapest, Hungary, December 2015.

17. W. Friedland, P. Kundrát, E. Schmitt, G. Baiocco, **S. Barbieri**, D. Alloni, A. Ottolenghi. "TREND - TRacking damage at ion track ENDs - Task 5.6 ad-hoc extension". DoReMi's final meeting, Budapest, Hungary, December 8, 2015.

18. A. Ottolenghi, G. Baiocco, M. Siragusa, D. Alloni, G. Babini, **S. Barbieri**, J. Morini. Proposal for an organisation of the task on "dosimetry", including track structure and links with radiobiology. Crosscutting support to improved knowledge on tritium management in Fission&Fusion facilities. International Workshop, Bruxelles, 8-9 October 2015.

Acknowledgements

It would have been impossible to accomplish all this work without the support and the help of many people, to whom I express here my gratitude.
The warmest thank you is for my family, whose endless support and wise suggestions have been the reason of my perseverance; and for Edoardo, I am happy to have you by my side, and I thank you for your patience and affectionate way of encouraging me every day.

Foremost, I would like to thank my supervisor, Prof. Andrea Ottolenghi for encouraging my research and giving me the opportunity to work with brilliant people both in Pavia and all over the world. I thank him also for financially supporting my research.
I would also like to express my deepest gratitude to Giorgio Baiocco, Gabriele Babini and Jacopo Morini, for their invaluable help, good advice and friendship you offered throughout these 3 years.

I would like to thank Dr. David J. Brenner, who accepted me for the 6-month project in his team at CRR and made this amazing experience come true, and all the colleagues at RARAF, where I spent some of the most enjoyable and scientifically fruitful months of this Ph.D. program: Andrew Harken, Guy Garty, Charles Geard, Brian Ponnaiya, Gerhard Randers-Pehrson, David Welch and Dennis Farrell.
But the warmest thank goes to my friend Manuela Buonanno, whose kindness and guidance supported me and motivated my research at RARAF.
Thanks to Malek, Veljko, Ljubica and Christian for the unforgettable moments spent together in NYC.

I express my gratitude to all the people who provided assistance during my Ph.D. work: to Werner Friedland, who shared his experience with PARTRAC; to Marco Liotta and Paola Tabarelli, for allowing me to irradiate at the "ICS Salvatore Maugeri" Foundation for my first experimental attempts; to Mario Ciocca, who also kindly allowed my experiments at CNAO and provided insightful suggestions for the irradiations; to Andrea Mairani and Davide Maestri, for their technical assistance during the beamtime at CNAO; to Patrizia Vaghi ("Centro Grandi Strumenti"), for making all the hours spent at the confocal microscope enjoyable and for her practical hints on some aspects

of my project.

Thanks to all the people who made the PERSEO project reality, in particular the colleagues from Thales Alenia Space - Italy (TAS-I) S.p.A.; Società Metropolitana Acque Torino (SMAT) S.p.A.; AVIOTEC S.p.A.; Advanced Logistic Technology Center (ALTEC) S.r.l.; University of Rome Tor Vergata (UniRMToV). In particular, I want to acknowledge Martina Giraudo, Luca Bocchini and Cesare Lobascio for their contribution to the Monte Carlo simulations.

I thank Dr. Mark Hill and Dr. Carmen Villagrasa for the availability and the efforts in reviewing my Ph.D. thesis. I have found much food of thought by reading all their valuable comments and suggestions.

The work presented in Chap.2, Par.2.1 of this thesis was supported by the FP7-Euratom INITIUM and TREND projects (Project n. 249689), within the Network of Excellence "Doremi"; the work described in Par.2.3 was instead supported by the FP7-Euratom project ANDANTE (Project n. 295970).
The work shown in Chap.3, Par.3.1, performed at the RARAF facility was partially funded by the NIBIB (National Institute for Biomedical Imaging and Bioengineering) (Grant n. 5P41EB002033).
The work presented in Chap.4, Par.4.2, was funded by the Italian Space Agency (Contract n. 2016-3-U.0) and supported by the ESA ARIADNA call for ideas (Contract n. 4000111396/14/NL/MV).